Doctoral theses at NTNU, 2022:190

Jarle Vinje Kramer

# Hydrodynamic Aspects of Sail-Assisted Merchant Vessels

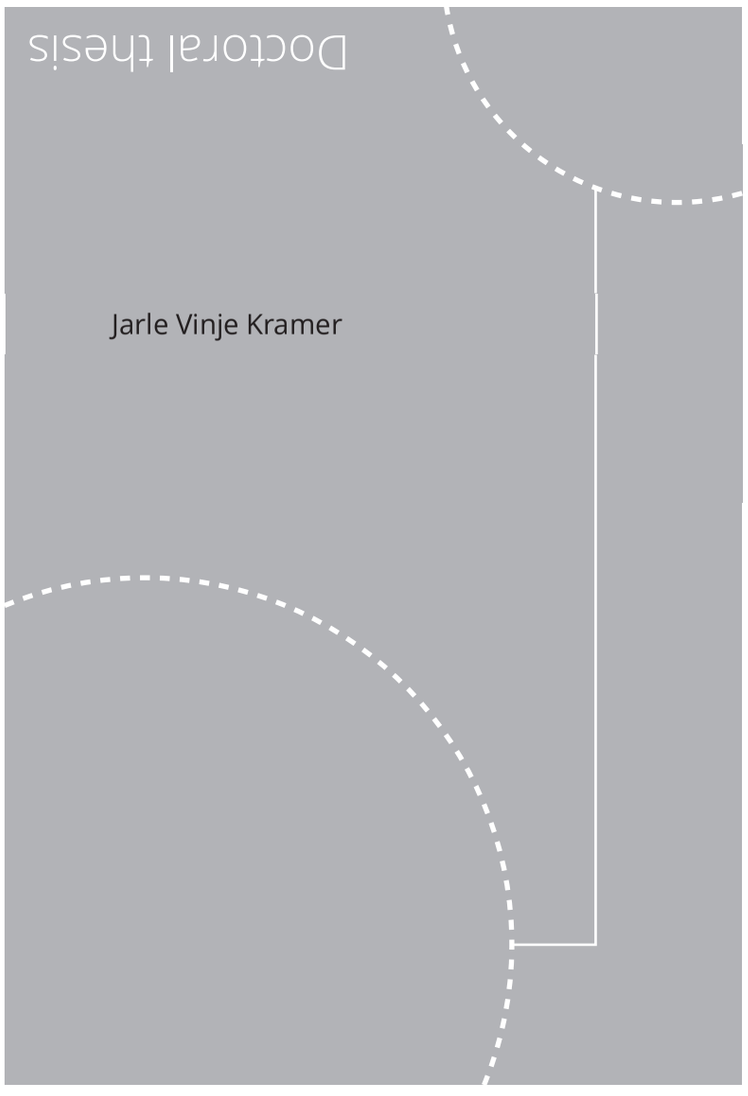


ISBN 978-82-326-5293-8 (printed ver.)
ISBN 978-82-326-5848-0 (electronic ver.)
ISSN 1503-8181 (printed ver.)
ISSN 2703-8084 (electronic ver.)

NTNU
Norwegian University of
Science and Technology

**NTNU**
Norwegian University of
Science and Technology
Thesis for the degree of
Philosophiae Doctor
Faculty of Engineering
Department of Marine Technology

**Doctoral theses at NTNU, 2022:190**

NTNU

NTNU
Norwegian University of
Science and Technology

Jarle Vinje Kramer

# Hydrodynamic Aspects of Sail-Assisted Merchant Vessels

Thesis for the degree of Philosophiae Doctor

Trondheim, June 2022

Norwegian University of Science and Technology
Faculty of Engineering
Department of Marine Technology

NTNU
Norwegian University of
Science and Technology

**NTNU**
Norwegian University of Science and Technology

Thesis for the degree of Philosophiae Doctor

Faculty of Engineering
Department of Marine Technology



ISBN 978-82-326-5293-8 (printed ver.)
ISBN 978-82-326-5848-0 (electronic ver.)
ISSN 1503-8181 (printed ver.)
ISSN 2703-8084 (electronic ver.)

Doctoral theses at NTNU, 2022:190

PRINTED IN NORWAY
NO - 1598

NORDIC SWAN ECOLABEL
Printed matter
2041 0731

Printed by Skipnes Kommunikasjon AS

# Preface

This PhD project was performed at the Department of Marine Technology (shortened to "the department" later in the text) at The Norwegian University of Science and Technology (NTNU). Financial support was given from the Norwegian Research Council and industry partners through the research programs Low Energy and Emission Design of Ships (LEEDS) and SFI Smart Maritime. The goal was to investigate the use of wind-power in commercial shipping to further push the technology towards large scale industrial use. I will get back to the detailed research questions later.

The project originally started in 2014 and continued full-time for approximately 2.5 years. This work laid the foundation for the development and results presented in this report. However, after that time, I ended up – almost accidentally – being involved in another project at the department which did research on hydrofoil vessels. This project was led by my colleague, John Martin Kleven Godø, who has the same PhD supervisor as me, Professor Sverre Steen. My involvement was first intended as a short break from my PhD project to assist in the development of simulation tools for hydrofoil vessels. Due to a long and complicated story, it soon turned into a much larger break, and I ended up as a founding partner in a spin-off company called Flying Foil. The company was started with the support from the Technology Transfer Office (TTO) at NTNU, and with the university, John Martin, Sverre and me as the main shareholders. The goal was to develop hydrofoil technology that could drastically reduce the energy consumption of high-speed passenger ferries and thereby facilitate the use of zero-emission energy sources on such vessels.

We used many of the software tools that I developed as part of this PhD in Flying Foil, such as software to automate and test hydrofoil designs with CFD and custom simulation tools to rapidly optimize the lift distribution on the wings and the pressure distribution around foil profile geometries. We also did extensive work on other topics, such as structural design, control algorithm development and physical prototyping. The company ended up being fully operational for more than 3 years with 4 employees at the peak, before we eventually decided to shut it down due to lack of further funding. There were many underlying reasons for this decision, but it can be summarized as a slightly sub-optimal business strategy, some technical difficulties with a physical prototype, and a significant dose of bad luck and poor timing.

However, I am very proud of the work we did and happy to have learned a lot through the process. The lessons from Flying Foil have also been valuable in the final stage of this PhD. Primarily, it gave me insight into the real world outside academia, and how practical problems sometimes differ from academic problems. Although it was sad to shut down our company, it gave me an opportunity to go back and complete the project that is presented in this report. It was always the plan to finish my PhD, but it turned out to be tremendously difficult to combine that with the work in a start-up company. I was back fulltime on this project from June 2020 and was finished with this report in early January 2022.

# Acknowledgments

Several people have been instrumental in this project. Two important examples are my supervisors, Professor Sverre Steen and Dr. Luca Savio. I would like to thank Sverre for the guidance, advice, and patience – especially when I have chosen to follow paths that where not the most efficient for completing this project. Luca has also been a valuable resource for practical discussions and help with experimental work.

I would also like to thank my friend, colleague, and former business partner John Martin Kleven Godø. I learned a lot from trying to start a business with him, and he is also a formidable resource for discussing and understanding hydrodynamics. Eirik Bøckmann is another friend and former colleague that has given much advice on both the research in this thesis and life in academia in general. Even though his specialty is wave-powered ships, I sometimes suspect he is secretly even more interested in wind-power (which is saying something, because he is very devoted to wave-power).

Finally, I would like to thank my wife, Berit Vinje Kramer. I suspect it is not always fun being the spouse of someone trying to complete their PhD project, especially not in the final stages where there is a lot of long working hours and frustration. She has been nothing but supportive. For that – and countless other reasons – I love her.

# Abstract

Modern sail technology is a potential solution for reducing the fuel consumption for merchant ships. This can be used to either reduce the emission of greenhouse gasses with conventional fuels, or the cost related to zero-emission fuels. This thesis explores wind-power for commercial shipping, with particular focus on the additional hydrodynamic challenges related to such vessels. These challenges primarily arise because a sail does not only push a ship forward, but often also strongly sideways. For a wind-powered vessel to move with a steady speed and direction, this aerodynamic side force must be balanced by opposing hydrodynamic forces and moments. A conventional ship will do this by moving with steady drift, rudder, and heel angles. As a direct consequence, the resistance of the ship will increase, and therefore remove some of the positive effect of the sails. The added resistance on a ship due the sails are labeled the *sail-induced resistance* in this report.

The research work was divided into three main questions related to the negative hydrodynamic effects: how can we accurately and practically model a wind-powered ship when the negative hydrodynamic effects are a concern? How important are these negative effects for merchant ships? What can be done to reduce the negative effects to a minimum?

The project started by exploring the drift-induced forces on simple foil-like ship geometries with different aspect-ratios and bottom edge shapes based on towing tank experiments. This was done to explore the accuracy of simplified methods for low aspect-ratio lifting surfaces and to see how much the lift and lift-induced drag are sensitive to design details. It was found that simplified theories where not able to capture the physics with acceptable accuracy, and that relatively small changes to the bottom edge shape could have a large impact on the results. The cross-flow drag experienced by the ship was found to not only affect the non-linear lift, but also the linear lift and lift-induced drag.

Because of these complicated physical effects, the details in the geometry are important when the goal is to create an accurate hydrodynamic model. An automated and scriptable framework for setting up CFD simulations using the open-source library OpenFOAM was therefore developed. This was used to simulate the forces acting on ship hulls with both rudders and keels, at various speeds, drift angles, rudder angles, and propeller loadings. Different simplifications were tested for the simulation strategy, including neglecting the free surface and performing the simulations in model scale. These simplifications were found to give acceptable accuracy, although with some important limits on both model size and Froude number. The assumptions in established maneuvering theory for predicting the forces due to drift angle, rudder angle, and propeller thrust were evaluated with the purpose of reducing the necessary test matrix for a given ship design to a minimum. Most simplifications in the MMG maneuvering model were found to be acceptable, including the models for the rudder-hull interaction. However, an update to the rudder force model was suggested to better estimate the lift-induced resistance. In addition, heel was found to affect the drift-induced forces significantly when the drift angle was large, but much less for small drift angles. The most likely explanation is that heel is mainly affecting the cross-flow drag on a merchant ship geometry, while the circulatory lift is less affected.

Although the focus of this thesis is hydrodynamic effects, some attention was also given to the aerodynamics of wind-power devices. A custom discrete lifting line method was developed specially to model wingsails. This method includes the interaction effects between multiple sails and viscous effect on both lift and drag. The lifting line model was compared against CFD simulations for both single wings and for multiple wings as a function of wind-direction. The accuracy was found to be good, especially considering the computational speed and simplicity of the method.

The importance of the negative hydrodynamic effects due to the sails was evaluated by performing route simulations of two different case study ships representing a 5 000 DWT general cargo ship. The necessary software for performing such simulations was developed as part of this project. The exact

magnitude of the sail-induced resistance depends on several factors, such as total sail area, ship speed, hydrodynamic design, and control strategy for the sails. In general, the relative importance of the sail-induced resistance is highest for low ship speeds and for cases with large fuel savings. As an example, at 8 knots ship speed, and three 56 m tall sails, the fuel savings without hydrodynamic effects were estimated to approach 70% based on route simulations with weather data from the north Atlantic. When the hydrodynamic effects where included, the fuel savings were reduced to right below 60%. In other words, around 10 percentage points – which corresponds to 14% of the sail thrust – was lost due to the sail-induced resistance. The source of the added resistance was found to be a combination of drift-induced forces on the hull and lift-induced resistance on the rudder. The rudder was found to often be the largest source of resistance, depending on the sail-placement. One way to reduce the lift-induced resistance on the rudder was to balance more of the side force with the hull. This could be achieved by adding either a fixed high-aspect ratio keel to the hull or bilge keels. A surprising result was that low-aspect ratio bilge keels essentially gave the same improvement as a high-aspect ratio keel. The reason was that the lift coefficient and the resulting lift-induced drag on the hull was small, despite the small aspect ratio of the geometry. The best design solution tested in this project was a dynamic high-aspect ratio keel that was both rotatable and retractable. This allowed the lift on the keel to be adjusted independently of the drift angle on the hull. The loss of fuel savings due to hydrodynamic effects were reduced to right above 6 percentage points at 8 knots with this design solution.

Another important solution for managing the negative hydrodynamic effects was to alter the control strategy for the sails. The case studies showed that the side force from the sails can be significantly limited in unfavorable weather conditions without significant loss of fuel savings. This allowed the ship to operate with smaller rudder angles and heel angles. This is therefore a simple way to ensure safe and comfortable operation of wind-powered ships without any physical design changes to the system. Although the thrust from the sails is reduced along with the side force, the reduction in sail-induced resistance was almost equal in magnitude, depending on the exact ship design. A simple control algorithm designed to maximize thrust but with strict hydrodynamic limits was found to be comparable to the more advanced control algorithms that optimized the operation of the sails including hydrodynamic effects.

In short, the work presented in this report shows that the negative hydrodynamic effects on wind-powered merchant vessels are important to consider if accurate fuel savings are the goal of the analysis. Practical and efficient computational methods for analyzing these effects are suggested. However, the magnitude of sail-induced resistance is not so large that it should be considered as a major problem for the concept of wind-propulsion for merchant ships. The negative hydrodynamic effects can be managed quite easily with either simple design changes, modifications to the control algorithm of the sails, or both.

# Content

# 1 Introduction

## 1.1 Background and motivation

People must be predominantly procrastinators. Although the negative consequences of releasing greenhouse gasses into the atmosphere have been documented and discussed for more than one and a half century [1], humanity has only recently decided to be ambitious about solving the problem. As a result of the Paris climate agreement, the nations of the world are planning to reduce emissions by 50% within a single decade and 100% within three [2]. Although some details are yet to be figured out, these goals will also extend to international shipping for instance through regulations from The International Maritime Organization (IMO) [3] and the European Union (EU) [4]. While the new ambitions are exclusively a good thing, the delay of action for so long has put us in an unprecedented hurry to transform the way we propel ships forward, from entirely fossil-based fuels in conventional engines to something new without emissions at all. This is a huge challenge that creates exciting opportunities for new technologies!

There is actually no lack of potential solutions to this challenge. For instance, there are several types of zero emission fuels that can easily power a merchant ship, even when operating on long routes. They can also be used with engine technologies that are either already available on the market or that require only minor modifications to existing products. Examples include hydrogen, ammonia, methanol, and synthetic fuels – at least when they are produced using zero-emission energy sources. However, as for instance highlighted in the recent DNV energy outlook report [5], zero emission fuel types come with substantial challenges related to both cost and availability. There is a severe lack of available green energy sources in the world, both today and probably also in the future. As a result, the cost of energy is likely to rise for ships that starts to use green fuel types. This has resulted in an increased interest in technological solutions that either reduce the energy consumption of ships or make it possible to harvest its own energy at sea.

This thesis is about one possible way to harvest energy at sea: modern versions of sails. In the recent years, many companies developing different variants of this technology have emerged all over the world. Through research projects, prototype tests, and real-life installments, wind-power has been shown to have a significant potential to reduce the fuel consumption of the merchant fleet. More details on different wind-power devices and the current market will be given in Section 1.2. Obviously, wind-power is nothing new in the shipping world. It used to be the only source of ship propulsion for millennia – perhaps except for human power. We therefore know for a fact that wind-powered ships are possible, and that they could be powered 100% by the wind if needed – at least if the logistics in the operation allowed for enough flexibility. The real interesting question for wind-power as a solution for the future is how competitive this energy source is relative to the other alternatives for low or zero emission shipping. To figure this out, there are several sub-questions that must be answered. One of the primary ones are: how much fuel – and therefore cost – can you save with a wind-power device without significantly changing the logistics of the shipping operation?

To quantify this, an aerodynamic analysis of the wind-power device is necessary and perhaps the most important task. This has therefore been the primary goal of many other research projects in the past, some of which will be highlighted further in Section 1.2. However, using wind-power also introduces new hydrodynamic effects on the ship. While a propeller mainly provides a thrust force that only pushes the ship forward, a sail will very often push the ship both forward and sideways at the same time, depending on the wind direction. This is because the wind can come from any direction and the sails create thrust mainly from lift – the force component that acts normal to the incoming wind. In addition, as the ship is always moving with a forward velocity, the experienced wind – also known as apparent wind – will always be rotated towards the bow relative to the true wind direction. This usually results in increased side force from the sails. This effect is illustrated in Figure 1. Depending on the placement and the height of the sails, the side force also generates a heel and yaw moment on the ship. To move with a steady heading and direction, the aerodynamic side force and the moments

must be balanced with opposite hydrodynamic forces and moments. The ship must therefore be operated with a steady drift, heel, and rudder angle during transit. This will in general increase the resistance and the required energy for moving the ship forward. As a result, some of the positive effect of the wind-power device is lost due to hydrodynamic effects. If the benefit of wind-power is analyzed with only aerodynamics in mind, the positive contributions are likely overestimated.

These negative hydrodynamic effects have been well known for a long time and there has been much work on the hydrodynamics of conventional sail boats in the past. However, there are some important differences between them and a modern cargo ship. The most important one is that sailboats are usually specifically designed to balance the unwanted forces from the sails, often by using a deep high-aspect-ratio keel. This reduces the importance of the hydrodynamic effects and can to a certain extent allow for simpler modelling approaches. A normal merchant ship is often designed with a very low aspect-ratio hull, which complicates the drift-induced flow. In addition, there is usually a more complex configuration of the rudder and propeller relative to sailboats. On the other hand, since a modern merchant ship with wind-power is generally a hybrid vessel, where only some of the power comes from the wind, the relative importance of the hydrodynamic effects could be smaller than for conventional sailboats.

The importance of the hydrodynamic effects on wind-powered ships was generally uncertain before starting this project. The goal of this PhD was therefore to investigate these effects specifically for merchant ships. If any challenges where discovered, the next task was to look for solutions. To achieve this, significant work had to be done on creating tools to model wind-powered ships. This included hydrodynamic analysis through simulations, simplified but accurate hydrodynamic models, aerodynamic modelling of wind-power devices, and route simulation with realistic weather conditions. More on the specific research questions explored in this thesis will be given in chapter 2. Before that, an overview of the previous work on wind-power for merchant ships will be given in section 1.2, while section 1.3 gives an overview of the content in the rest of the thesis.

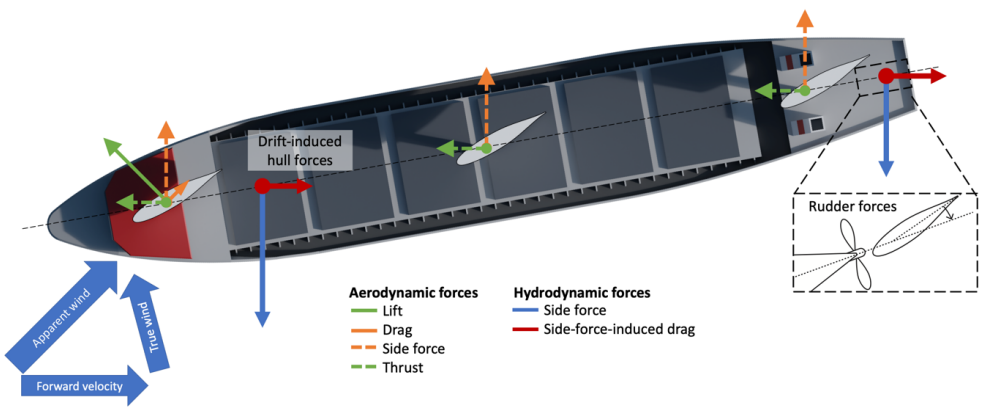


*Figure 1: Illustration of aerodynamic and hydrodynamic forces on a wind-powered ship. The magnitude of the drift angle is somewhat exagerated for clearity.*

## 1.2 Previous work

This overview of previous work is primarily limited to “modern” wind propulsion, meaning the type of solutions suggested for merchant ships today. The solutions generally differ from the traditional sail rigs in that they are both more efficient at extracting energy from the wind and substantially less labor intensive for the crew. The word modern was put in quotations marks, as all these technologies have a long history. The oldest form of the modern sail types discussed in this section was invented in the 1920s. The “newest” idea is from the 1970s. However, although the ideas behind the different concepts are old, there has been significant development in making the technologies available in an industrial setting in the recent years.

I will first go through the five main categories of modern sail technologies that are either already available for merchant ships today or likely to be so in the near future. This includes automated soft sails, wingsails, rotor sails, suction sails, and kites. The references provided are both for academic papers, and for relevant industry projects. Then, an overview of literature relevant for the hydrodynamic modelling of wind-powered ships is provided. This includes the topics of drift-induced forces on hulls, rudder modelling, and route simulations. The references for these topics are a mix between previous work on wind-powered ships – including conventional sail boats – and modelling related to ship maneuvering – a field that involve much of the same physics. For a more in-depth overview of aerodynamic modelling of wind-power devices, I recommend the recent PhD thesis found in reference [6].

### 1.2.1 Soft sails

Soft sails are still an option for modern cargo ships. It is also important to remember that traditional sail rigs for commercial shipping were used for a long time after the introduction of the steam engine. One of the last – and perhaps most famous – commercial ships to exclusively use soft sails for propulsion was the vessel known as Cutty Sark, built in 1869. Wind-power was still a competitive solution for some types of trade at this time even though this was long after the first steam powered ship had crossed the Atlantic in 1819. Another example of a ship partly powered by the wind around the same time was the luxury ocean liner RMS Oceanic that was built in 1875. Traditional sails eventually lost to ships propelled only by engines in the early 1900s. However, the idea had a revival in the 1970s because of high oil prices. For instance, a soft sail rig was installed on two commercial vessels with the support from the Asian Development Bank to evaluate the reduction of fuel consumption with this technology. An analysis of the fuel consumption for these ships can be found in reference [7]. Although the study is somewhat limited, the reported fuel savings due to the sails was around 37% in the test period.


*Figure 2: Examples of old and new soft sails solutions*

A current example of a soft sail for commercial shipping is the product known as Dynarig [8]. This sail type is also studied experimentally in the PhD-thesis in reference [6]. Although the fundamental aerodynamic principle of these sails is similar to older square rigs, the modern version is improved by being highly automated. The masts are rotated by a control system to achieve control over the forces, and the sail cloth can be automatically retracted or deployed without manual labor. The product has been installed on at least two larger yachts and suggested as a wind propulsion device for a concept cargo ship – known as the WASP Ecoliner – from Dykstra naval architects [9]. Photographs comparing the modern Dynarig against the traditional square rig used on the Cutty Sark is shown in Figure 2

### 1.2.2 Wingsails

Wingsails are rigid streamlined structures that create thrust by having an angle of attack relative to the apparent wind direction. In other words, they are wings – primarily with symmetrical foil profiles – that are placed vertically on the ship's deck. Although the exact origin of this technology is unclear, it was at least suggested in the early 1920s by Anton Flettner [10], who also invented the rotor sail. However, Flettner seemingly never built a wingsail himself. The first real life example of a vessel powered by a wingsail that I know of is a small Norwegian boat built by Fin Utne sometime around 1940 [11]. Already at that time, the sail was automatically adjusted relative to the wind by using a tail mechanism. Unfortunately, the craft was destroyed by invading forces from Germany during the second world war. Several people have experimented with small wingsail powered crafts since then, as for instance outlined in the report from 1957 found in reference [12].

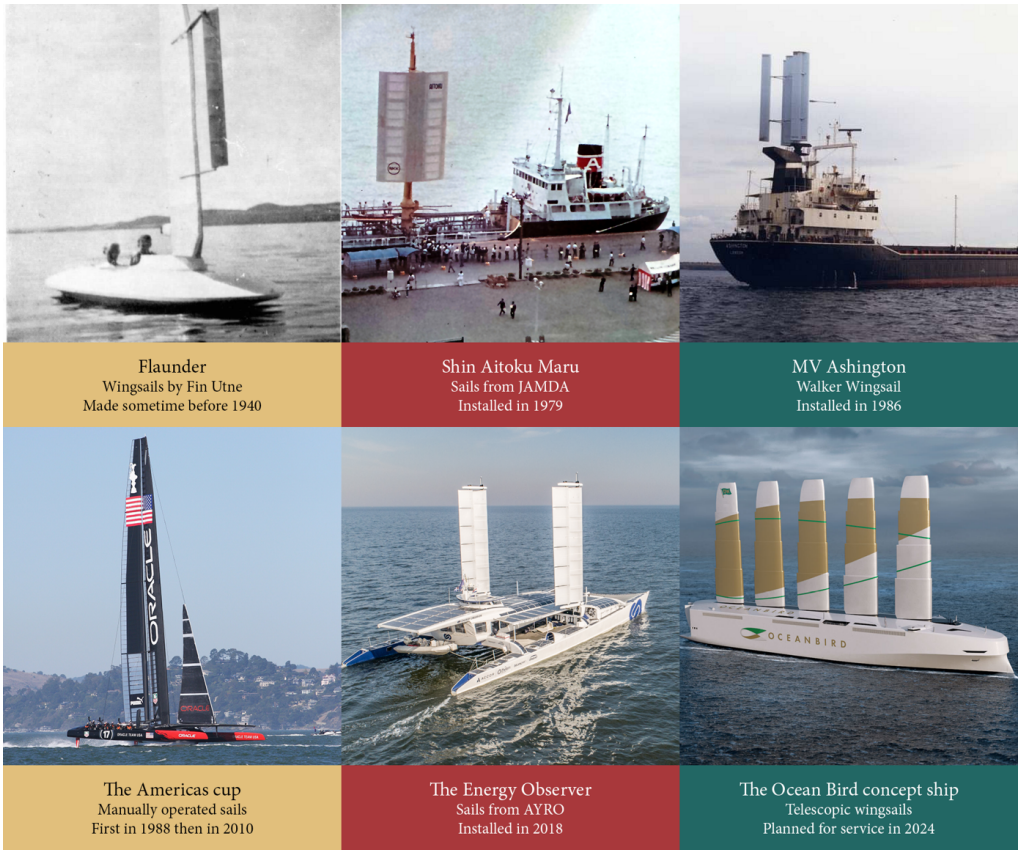


*Figure 3: Examples of wingsails*

The technology gained renewed interest from the late 1960s which increased further in the 1980s. Significant efforts were made by John G. Walker to introduce this technology to commercial shipping [13]. A prototype of the Walker Wingsail was installed on the cargo ship MV Ashington in 1986. A similar effort was made by the Japanese Machinery Development Association (JAMDA) in the late 70s and early 80s, and at least 10 different commercial ships were equipped with wingsails in this period [14]. Although the commercial interest in wind-power seemingly followed the same decline as the oil price in the late 1980s, wingsails continued to be explored in the sail racing community. The primary reason was that wingsails were found to offer better performance than soft sails [15]. One of the more famous competitions featuring wingsails is the Americas Cup. Wingsails were first introduced for a short period in 1988 and then reintroduced for a longer period in 2010. Although the technical details of the wingsails used in the Americas cup have changed quite a lot, it is still used today. Renewed interest in wingsails for commercial shipping started in the late 2000s, as for instance shown in the papers that explore the topic in reference [16] and [17].

Today there are several companies developing wingsail products for commercial shipping. Some versions have multiple elements – also known as flaps – where the backwards elements are made to have larger angles relative to the wind than the foremost elements. Examples include the products from the companies BAR Technologies [18] and AYRO [19]. Different mechanisms are used to take the sails down when they are not needed. The previous example from BAR Technology comes with a tilting mechanism while the wingsails from the company Bound4Blue [20] can be mechanically folded together. Another idea comes from the company WISAMO [21] – a spinoff from the tire producer Michelin – who are developing inflatable wingsails. One of the largest wind-power projects in the industry today is the Ocean Bird project by Wallenius-Wilhelmsen [22]. They plan to install several 80 m tall sails on a car carrier that can be lowered by a telescopic mechanism. All wingsail systems are marketed with automatic operation, which require little input from the crew. The angle of the sails and the flaps are adjusted based on the wind direction to maximize thrust. As of writing this, modern full-scale testing of wingsails has primarily been limited to smaller vessels, such as the Energy Observer project [23]. However, several of the already mentioned companies claim that full-scale installments of the technology will be achieved in 2022-2024, and there is also substantial practical experience with the technology from the projects in the 1980s and from sail racing.

The main benefit with wingsails relative to soft sails is increased performance and easier control. The lift coefficient of a wingsail and a soft sail is similar for single element sails. However, the drag can be reduced as rigid structure makes it easier to create efficient planforms, and the viscous drag on soft sails can sometimes be high if the wind pressure adjusts the shape of sails in a suboptimal way. By using multiple elements, a wingsail can also be made to have higher lift coefficients than soft sails. This is achieved by deflecting the air more gradually, and by allowing some air to leak in between the different elements, and thereby delay stall. They can be easier to control than soft sails as the forces acting on the wing are more predictable and follow simple equations as a function of the control parameters. While the shape of a soft sail will vary depending on both wind direction and speed, the shape of a wingsail is completely fixed.

### 1.2.3 Rotor sails

Rotor sails are spinning cylinders which can create lift due to the Magnus effect. When the wind flows over the cylinders, the flow on one side is accelerated – due to the rotating motion and no-slip conditions on the wall – and slowed down on the other side. This creates a pressure difference, and therefore lift. Spinning the cylinder requires energy, but usually much less than the energy extracted from the wind. The first to explore this concept was Anton Flettner in the early 1920s. The sails are therefore sometimes referred to as Flettner rotors. Two very famous names in aerodynamics were involved in the early theoretical analysis of rotor sails: Ludwig Prandtl [24] – one of the inventors of the lifting line – and Albert Betz [25] – famous for “Betz’s law” that predicts the max energy that can be extracted from a wind turbine. They figured out how to calculate the lift from a spinning cylinder with potential theory. The involvement of these two people suggests that there must have been great

interest in the technology at the time. Even Albert Einstein has publicly stated that he was a fan of rotor sails [26]. The first vessel to be equipped with rotor sails was the Buckau, which crossed the Atlantic in 1926 with the assistance of two 15 m tall sails.


*Figure 4: Examples of rotor sails*

The interest in the technology seemingly disappeared a few years after its introduction. Unlike wingsails, rotor sails are not usable in sail racing as it requires input power to operate. There has therefore been little interest outside commercial shipping. As with other wind-power technologies, the interest in rotor sails increased again during the oil crisis in the late 70s, and rotor sails were again suggested by many as a possible solution. Examples can be found in reference [27] [28] and [14]. At least one physical prototype was tested in the same period, shown in reference [29]. The modern interest in rotor sails started in the late 2000s, and the wind turbine installation vessel E-ship 1 was equipped with 4 rotor sails developed by Enercon. Examples of two rotor sail companies today are Norse Power [30] and Anemoi [31]. Based on information from the web sites of the two companies, there have been at least 8 installments of full-scale rotor sails on merchant ships during the period 2015 – 2021. One of the later ones where the installation of two 35 m tall tiltable sails on the Norwegian ship SC Connector, shown in Figure 4.

The main benefit of rotor sails is extremely high lift forces even with a small sail area. The lift coefficient on wingsails is typically limited to values between 1.5 and 3.5 – depending on the exact configuration – while the rotor sails can reach values of 8-12 [6]. However, this enormously concentrated lift comes at the cost of high drag coefficients. Since the shape of a rotor sail is a cylinder, the drag is high both when producing lift and without rotation. This means that the rotor sails are efficient for apparent wind directions straight from the side – where the drag does not reduce the thrust – but much less efficient for apparent wind directions towards the bow of the ship. Because of this effect, rotor sails can utilize some wind directions much more efficiently than wingsails, and some less efficient. If the sails are not retractable, they will be a large source of added resistance in head wind conditions. The forces acting on a rotor sail are controlled by changing the rotational speed.

### 1.2.4 Suction sails

Suction sails are often referred to by brand names such as Turbo sails or Ventifoils. They are in general wingsails that use some form of fluidic control mechanism to delay the onset of stall and therefore increase both the angle of attack and the lift. The most common mechanism is boundary layer suction. This sail type was developed and popularized by Jacques Cousteau, a famous filmmaker and conservationist, together with several other partners in the late 1970s [32]. Full scale devices were installed on at least two research vessels in the early 1980s. The newest, the Alcyone, is shown in Figure 5.


*Figure 5: The original turbo sail compared with a modern implementation*

The original device was constructed as almost elliptical cylinders with a triangular flap that could be rotated depending on the wind direction. Inside the cylinders, there were fans that sucked air through slots on the surface of the sail. Like rotor sails, the operation of the fan system requires energy, but much less than the energy extracted from the wind. How much the lift is increased due to the boundary layer suction is very dependent on the suction rate. Experimental test indicated that the protypes where able to achieve lift coefficients as high as 8.5 for two-dimensional foil profiles and around 7 for a three-dimensional wing [32]. Unlike a rotor sail, the drag on a suction sail can be made to be very low when the suction is turned off. This is possible due to the more streamlined shape of the wing, as opposed to a circular cylinder. In some sense, a suction sail is an attempt to get the best from both wingsails and rotor sails at the same time. It can create lift forces comparable to rotor sails for wind directions directly from the side but can reduce both the lift and the drag to be similar to wingsails when the ships course is approaching head wind conditions. From a pure fluid dynamic point of view, it seems like the perfect sail. However, the mechanical complexity and number of moving parts is somewhat higher than both rotor sails and wingsails.

Although boundary layer suction is the most common type of fluid control mechanism for sails, there are also other potential methods for fluidic control. This is for instance explored in reference [33] which explores both boundary layer suction and blowing. With the latter mechanism, a thin jet of air is blown into the boundary layer close to the leading edge of a foil profile. This energizes the boundary layer and therefore delays stall. By combining blowing and suction on the same profile, the lift coefficients can reach values of 16. Today there are at least two companies offering suction sail on the commercial market: Bound4Blue [20] – which also makes normal wingsails – and Econowind [34]. Both companies have done physical tests of their systems, and at least 7 different commercial ships have been equipped with suction sail devices.

### 1.2.5 Kites

Kites are flying wings that utilize the larger wind speeds high up in the atmosphere. There are several different types of kites, which in theory could be used for ship propulsion. This includes parachute-like kites, inflatable wings known as ram kites, and rigid kites. It was at least considered by some researchers from the late 1970s [35], although the exact origin of this idea is unclear. At the same time, in a review paper regarding wind propulsion from 1985 [10], kites are not mentioned at all, suggesting it was not as well established as the rest of the modern sail types at that time. Although small scale prototype testing was done in the early 1980s, there were seemingly no large-scale installations.

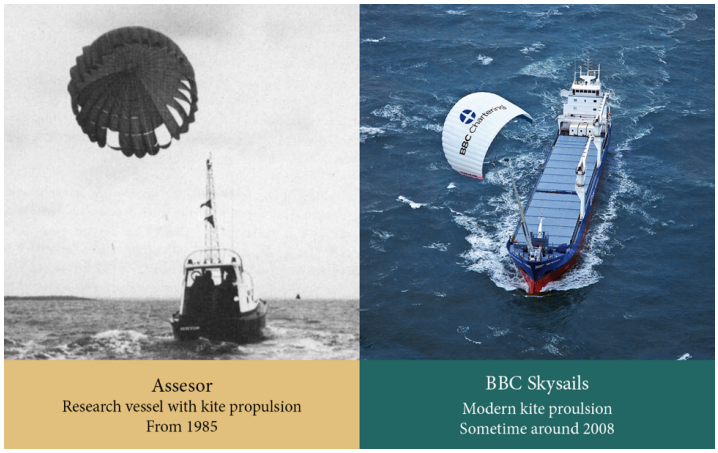


*Figure 6: Examples of old and new kite systems*

Several researchers were interested in the idea from around the mid 2000s and forward. The analysis of kites is devoted to both aerodynamic modelling and control principles. Examples of papers can be found in [36], [37] and [38]. The control principles are important as kites can utilize dynamic movement to extract more energy from the wind than what would be possible with static structures. In 2008 the company SkySails installed the first full scale kite for commercial ship propulsion on the ship MS Beluga [39]. The same company is still offering towing kites for ships today [40]. Another company with similar products is a spin-off from Airbus, called Airseas [41].

### 1.2.6 Drift-induced forces on hulls

When the sails force the ship to move with a drift angle, it becomes a "lifting" surface. The lift refers to the force normal to the ship's velocity, i.e., the side force. The physics of lifting surfaces are in general well known, as they occur for many different applications. However, different applications come with their own challenges and modeling techniques. The primary difference between ship hulls and other types of lifting surfaces is the aspect-ratio. That is, the ratio of the ship length to the depth, or the span of a wing relative to the mean chord. This variable is typically one to two orders of magnitude smaller for ships than for other types of lifting surfaces. Although this is only a simple change in the relationship between the main dimensions of the geometry, the physics of the flow changes quite a lot. When discussing this difference, it is useful to divide the lift into two different types: circulatory lift and cross-flow drag.

The first type occurs even for small drift angles and can be described by potential theory. For high-aspect ratio lifting surfaces, the lift and lift-induced drag are often well described by classical lifting line equations, originally developed independently by Prandtl [42] and Lanchester [43]. However, for low aspect-ratio surfaces, a different simplified analysis is often used, known as slender body theory [44]. The difference between the two simplifications is the assumptions about the dominating dimension. In lifting line theory, the span of the wing is assumed to be much larger than the chord. For slender body theory, it is the other way around – the length of a ship is much larger than the depth. The different theories end up with different equations for the lift. Both predict that the lift is linearly dependent on the angle of attack, but slender body theory gives a smaller slope than lifting line theory for aspect ratios typical for ship hulls. Another important difference is the yaw moment. While the lift on high aspect ratio wings is generally assumed to act at the quarter chord – depending on the exact pressure distribution of the foil – the lift on low-aspect ratio surfaces will be destabilizing and create what is known as a "Munk moment". That is, the center of pressure for the lift on low aspect-ratio surfaces are often predicted to be in front of the bow of the ship – depending on the depth-distribution along the length of the hull. The third difference between high and low aspect-ratio surfaces is the equations for the lift-induced drag. Classical lifting line theory predicts that the lift-induced drag is

proportional to the lift coefficient squared, and inversely proportional to the aspect-ratio. Classical slender body theory does not concern itself with the topic of resistance at all.

The second type of lift on low aspect-ratio bodies is the cross flow drag. This refers to the phenomenon where the flow separates around the bottom of the ship hull due to the drift angle. This can create large forces normal to the ships center line. Although this is often referred to as a drag force – due to the flow separation – it will mostly act in the same direction as the circulatory lift, and therefore contribute to the side force. This source of side force is negligible for high-aspect ratio wings but can be significant for ship hulls. It results in a non-linear behavior of both the lift and yaw moment as a function of angle of attack, and a complex flow field that is highly affected by the separated flow. This is therefore an effect that complicates the simulation and modelling of low aspect-ratio lifting surfaces considerably, especially for larger drift angles.

The way these two effects have been modeled in ship hydrodynamics varies between different researchers and throughout history. In the early history of ship maneuvering theory, it used to be common to neglect all higher order effects and assume that a drift angle only creates a linear sway force – the force normal to the longitudinal direction of the ship. If this sway force is translated to lift and drag – and small angles are assumed – it would result in roughly a linear lift force and a second order drag force on the ship as a function of drift angle. This is for instance the case in the historically important lecture notes from Abkowitz from 1964 [45]. The lecture notes start by introducing how a general hydrodynamic force model can be created of a ship by doing a Taylor expansion of the state variables around an initial condition. The state variables are all variables that can change in the simulations, such as drift angle, sway velocity, rudder angle, yaw rate, acceleration, etc. The initial condition is the ship moving straight ahead at the design speed. The order of the model and number of cross coupling terms can in principle be increased until satisfactory accuracy is achieved. However, to simplify and to ease the mathematical analysis of a maneuvering ship, it is suggested to linearize the model. For conventional sail boats it has sometimes also been common to model the ship as a high aspect-ratio lifting surface, such as in the early Velocity Prediction Program (VPP) found in reference [46].

Today, most maneuvering simulations are done with higher order methods. An example of a modern high order implementation of an Abkowitz model can for instance be found in [47]. Another popular maneuvering model is the MMG model [48]. The expressions for the hull forces in this model is inspired by the principles of Abkowitz models, but the MMG model differ in that it attempts to model the hull and the rudder in a modular way. More on this topic in the next section. The drift-induced sway force and yaw moment on the hull is modeled with terms proportional to the sway velocity to the first and third order, while the drift-induced surge force depends on second and fourth order terms. The MMG model has also been suggested for route simulation of wind-powered ships, for instance in [49]. Similar methods were also suggested for wind-powered cargo ships as early as the 1980s, for instance in [10], [50] and [51]. The papers present different polynomial models for the hydrodynamic forces, which depend on several empirical coefficients that must be set based on either simplified theory or experimental data. Higher order terms are also usually included in modern implementations of VPP programs for conventional sailboats [52].

The principal challenge for modelling the drift-induced forces on a hull is less about the exact order of the polynomials, but more on how to set the coefficients in the models so that they predict correct forces for different ship geometries. There are three main methods for doing this: with empirical and theoretical expressions, with physical experiments, or with simulations.

Several empirical methods for maneuvering coefficients exist. A comprehensive overview over expressions suitable for the MMG model is for instance presented in [53]. However, most expressions are regression models tuned on a very limited set of experimental data. The accuracy for general ship geometries is therefore somewhat uncertain. As for instance highlighted in the SIMMAN workshop, maneuvering simulations based on empirical methods differ quite a lot between different researchers

and much more than simulations based experimental data or CFD data [54]. This is, however, the only way to quickly estimate the maneuvering characteristics or the added resistance due to a side force for a ship. The route simulation framework for wind-powered ships presented in [55] is therefore devoted to using empirical expressions for every part of the ship, including the drift induced forces on the hull.

Experimental studies of the drift induced forces on ship hulls can be found in many papers. A non-exhaustive list of examples include [56], [57], [58], [59], [60] and [61]. Although an experiment is guaranteed to give a physically correct flow around the ship model, there are primarily two issues with this methodology. First, it is generally expensive and time consuming to perform experiments. Second, the drift-induced flow around a ship shows tendencies to being significantly Reynolds number dependent. The non-dimensional force coefficients predicted in model scale are therefore not necessarily the same as for a full-scale ship. This is for instance explored in [62], [63], [64], and [65]. Unlike for normal calm water resistance prediction, we currently have no established method to scale maneuvering coefficients from one scale to another.

A method for estimating forces in full scale without building the ship is Computational Fluid Dynamic (CFD) simulations. This was also the tool used to study the effect of Reynolds number in most of the scaling studies mentioned above. Simulations do however introduce new challenges related to both turbulence modelling and simulation setup in general. A large investigation of optimal mesh design and different turbulence models for drift-induced forces on wind-powered ships can be found in reference [66]. The results from the CFD simulations were compared against experiments and it was concluded that CFD simulations could capture the drift-induced effects with acceptable accuracy. Another method for simulating ship hydrodynamics of historic importance is potential methods for lifting flow, including Boundary Element Methods (BEM) and Vortex Lattice Methods (VLM). This type of simulation is for instance suggested as a method to test sailboat hulls with appendages in an overview of VPP programs from 1990 [67]. Potential theory can still be an option for vessels with high aspect ratio keels today, although it is important to be aware that the validity of the analysis is limited to small drift angles.

### 1.2.7 Rudder modelling

Rudders are generally high aspect ratio lifting surfaces, at least compared to ship hulls. Therefore, the lift and drag should be better captured by the simple equations from lifting line theory. However, a rudder is usually placed both in the wake of the hull and right in the jet stream from the propeller. This complicates the incoming flow field to the rudder and therefore the requirements for the modelling framework. This is especially true when the ship starts to operate with a drift angle. An important effect to capture is the phenomenon known as flow straightening. The flow field in the wake behind a ship geometry is generally more aligned with the ships center line than the external flow. How much depends on the ship geometry and propeller thrust. There are different models in the literature to capture this effect. The simplest approach is to assume that the effective drift angle of the rudder is proportional to the drift angle of the hull. This approach is for instance tested experimentally in [68] and [69]. The proportionality factor depends on the propeller thrust in this case. The MMG maneuvering model [48] use a similar approach, although with slightly more corrections for effective surge velocity at the rudder.

The effect of the propeller jet stream is also treated with different methods. The MMG model use a theoretical expression based on actuator disk theory to estimate the increase in the surge velocity due to the propeller, which also affects the flow straightening. Other expressions use pure empirical corrections with the propeller thrust as the only input variable [70], and do not consider the drift angle at all. An option is to simulate the interaction between the rudder and propeller with computationally fast methods based on potential theory. This is for instance done in [71], [72] and [73]. The propeller can either be an actuator disk, a lifting line model, or a boundary element method (BEM). The rudder is either represented by a lifting line or a BEM simulation. The interaction is captured by the induced velocities between the different lifting surfaces in the simulation. The method in these references do

not include the effect of the hull, which is a significant simplification. However, some suggests modeling the rudder and propeller as a unit, which experience the same influence of the hull [74]. I.e., the wake and effective drift angle experienced both by the propeller and the rudder is assumed to be the same in this approach. This could therefore simplify the experimental setup for tuning the hull-rudder-propeller interaction model.

The final interaction effect to consider between rudders and hulls is the lift induced by the rudder on the hull. This interaction is assumed to be linearly dependent on the rudder sway force in the MMG model. With an Abkowitz model, this effect can be built into the coefficients for the rudder force.

In the same way as for the hull forces, there exists several empirical expressions for the maneuvering coefficients related to rudder and hull interaction [53]. However, the only way to get accurate values for a specific ship is to either test it experimentally or by using simulation methods that can accurately capture the wake behind the ship. In practice, this means including viscous effects in the simulation. CFD simulations for capturing the rudder-hull interaction are for instance done in reference [75].

The importance of the rudder for wind-powered merchant ships are explored previously. One early example is reference [76] that explores the necessary rudder angles to achieve steady yaw moment balance for different placement of two sails. The model is based on empirical maneuvering coefficients of both the hull and the rudder. The results show the added resistance due to both drift and rudder angle, which illustrates that the rudder resistance is the largest source of added resistance for the case study ship. Another example is a similar study, but more recent, found in reference [77]. The paper provides results from a wind-powered ship modeled with the MMG model, where the coefficients are set based on experimental results. The rudder and drift angle are compared, but there is no presentation of the of added resistance due to the sails.

### 1.2.8 Hydrodynamic design solutions

Design solutions for managing the side force from wind-powered devices are usually focused on the design and placement of different keels or fins. An example of a design study for conventional sailboats can be found in reference [78] that investigates the performance of different keel forms experimentally. In reference [79] a keel with winglets – also known as a winged keel - is investigated and compared against conventional keels. The goal of the winglets is both to reduce the lift-induced drag on the keel directly, but also to increase the side force at a given drift angle and thereby reduce the resistance on the hull. This can be achieved by increasing the effective aspect ratio of the keel. Reference [80] investigates the shape of the bulb on the bottom edge of a keel. The bulb contains counterweights to minimize the heel angle of the boats, but the required volume for the weight increases the drag. The shape should therefore be optimized. Reference [81] investigates how different keel shapes and placement affect the yaw balance of a sailboat. The goal was to find a suitable balance between drift and rudder angles.

It is perhaps obvious that the exact shape of a keel is an important design parameter for the performance of sailboats. However, the design question is somewhat different for merchant ships. For one, a deep keel introduces significant disadvantages for a vessel that is intended to operate in commercial harbors that usually have limited depth relative to typical merchant ships. Second, the added friction due to a keel will always be negative for the fuel consumption when there is no side force from the sails. While a sailboat is mainly used when there is wind to push the ship forward, a merchant ship will operate even on days when the condition for sailing is poor. Thus, design explorations typically investigate smaller and simpler keel shapes, that results in only limited increase in depth and wetted surface area.

An example can be found in reference [82] which investigates the placement of several very shallow keels on a cargo ship equipped with wingsails. The goal was both to offload the rudder – so that steering could be maintained even in challenging weather conditions – but also to see if the fuel savings could be improved. A specified concern by the authors was that the added surface of the keels would lead to larger fuel consumption for the ship. They conclude that the fins reduced the necessary

rudder angle, as wanted. The difference in fuel savings due to the keels were found to be minimal. Consequently, the positive and negative effects of the keels where approximately equal in magnitude. The hydrodynamic properties of the ship were determined experimentally. Reference [61] investigates the effect of different bilge keels where both placement and size is varied. The bilge keels were found to move the center of effort for the side force significantly backwards, and therefore be positive for the sailing performance. However, the exact effect on the fuel consumption of a wind-powered ship was not covered by the work. Reference [83] outline a test program for testing various appendages for a wind-powered cargo ship using CFD. The study covers both conventional keels, bilge keels and rudders. They present the ratio of drag to side force for the different configurations, but no results on how this affects the fuel savings of a wind-powered ship.

### 1.2.9 Route simulation of merchant ships

To analyze the fuel savings due to wind-power devices, at least three different parts are needed: an aerodynamic model of the wind-power device, a hydrodynamic model of the ship, and weather data. The analysis can also be extended with additional models for other parts of the ship and the operation – such as engine models, various control systems, and route optimization. The complexity and details in how these things are modeled varies a great deal, both between different researchers and throughout history.

Complete route simulations are seemingly a relatively new thing in the marine community. This is probably due to the availability of weather data. For instance, in both reference [10] and [32] from 1985, a framework for route simulations of different wind-powered cargo ships is explained, including models for the added resistance due to the side force from the sails. However, the fuel savings are only discussed for a limited set of example wind conditions. In other words, they had models of the physics of sailing ships, but seemingly not usable data for the wind conditions on the actual routes. This is not a problem today. Many metrological institutions provide global hindcast data for several decades back in time. Most data sources are free of cost for non-commercial use. A popular example – used by most of the following references – is data from the European Center for Medium Range Weather Forecast [84].

At the simplest level used in recent academic papers, the hydrodynamics and the aerodynamics is modeled completely independently from each other. Conventional methods in calm water ship hydrodynamics can be used for the ship resistance model, such as empirical expressions, CFD simulations, or towing tank experiments. The aerodynamic model can be based on relatively simple expressions for the lift and drag coefficients for a single sail. Interaction effects between either multiple sails or the sails and the rest of the ship is often completely neglected. An example of such a simple modelling approach can be found in reference [85]. In this paper, a kite and a rotor sail are compared, by assuming they both produce a constant lift and drag coefficient independent of the wind conditions. The resulting propulsion power from the sails is compared against the required propulsion power from existing ships, which give a rough estimation of the fuel savings. The primary new contribution of the paper is the use of high resolution hindcast data for modelling the weather conditions. In other words, the weather data is in focus, while the rest of the ship is treated with as simple models as possible.

From this first level there are several ways to add more complexity. Different researchers tend to focus on different aspects and therefore improve different parts of the modelling framework. For instance, reference [86] improves the model by introducing a more detailed calm water resistance model, a simple control policy for the sails, and added resistance in waves. The paper also investigates how the wave energy can be utilized for propulsion. Reference [87] and [88] do not include added resistance in waves, but instead focus on better modelling of the engine dynamics. They investigate whether there is a difference between gas turbines and diesel engines when using wind propulsion and compare different wind propulsion technologies – rotor sails and vertical axis wind-turbines – using simplified aerodynamic models. They also include explicit estimation of the fuel price and can therefore quantify the cost savings. Reference [89] focus on improving the aerodynamic modelling of

the sails by using CFD-simulations that include interaction effects between both the rest of the ship and multiple sails. Otherwise, the route simulation is similar to the other references. Reference [90] and [91] is back to using very simple models for the ship but focus on methods for optimizing the route for wind-powered vessels. This includes simple models for the added resistance in waves and increased air resistance on the superstructure. A final example of simplified route simulations is reference [92] which compare rotor sails against air lubrication of the hull. The analysis is focused on doing a rough comparison between the two very different technologies for reducing the energy consumption of different ships. To get realistic operational profiles, they used Automatic Identification System (AIS) data to get the actual location of the case study ships throughout the test period.

Although all the above references are published between 2013 and 2019, none of the mentioned examples so far include the added resistance due to the side force from the sails. Exactly why the effect is neglected is not clear; it could be due to the added complexity of including the effect, or an implicit assumption that the effect is not very important. Whatever reason, it is not discussed directly in the papers.

However, there has been an increased interest in these negative hydrodynamic effects recently. An example is the articles presented in reference [93] and [94] that use the same route simulation framework to analyze different merchant ships. Both papers analyze rotor sails, while reference [94] also include a study of a soft sail and a wingsail. The framework consists of empirical models for different parts of the ship, including all necessary maneuvering coefficients, the engine, and the propeller. It also includes a control system where sails are adjusted to avoid too large heel and rudder angles. The ship resistance is modeled as a function of speed, side force, and weather conditions, including added resistance in waves. However, as every model is empirical, the framework can only test "typical" ships. The results from the calculations are primarily based on the main dimensions, and not the actual geometry of the hull and rudder. Reference [95] also investigates the reduction in fuel consumption due to rotor sails, but in this case, the ship hull is analyzed with CFD to estimate the drift-induced forces. The exact modelling strategy for the rudder and propeller is not clear from the text. There is also at least one older reference that performs route simulations with both weather data and added resistance due to the side force [96], but the hydrodynamic model is not explained in detail.

Neither of the references that include hydrodynamic effects focus on the importance of the effect. It is therefore not clear from the results whether it is necessary to include the added resistance due to the side force from the sails, or whether this is an advanced effect that can be safely neglected for merchant ships. The results are mainly presented as the final output of the complete route simulation framework which is a composite of many models. In other words, it is not possible to tell directly from the papers whether the hydrodynamic effect is a problem for wind-powered merchant ships or not.

Many of the references above provide numbers for the fuel savings due to wind-power. A collection of these numbers is plotted in Figure 7. The references included were those that provide clear data on fuel savings, sail dimensions, and ship particulars. This included 30 data points from the references [85], [88], [89], [92], [93], [94], and [95]. In addition, some of the results from the final paper in this project – labeled paper 5 in the plot – is added as a comparison. The figure is divided in two; a full view that shows all data points, and a zoomed view that focus on the smaller sail areas. As can be seen in the figure, the data points from the final paper in this project are for a case with large sails relative to the ship speed and wetted surface. Most of the other papers mentioned in this section focuses on smaller sails.

The variable on the x-axis is the installed sail area, $A_{sail}$, divided by the case study ships wetted surface, $S$, and the non-dimensional velocity of the ship, $U$, to the second power. The non-dimensional velocity is calculated by dividing the actual velocity by the average velocity of all the included cases, $U_{ref}$, which corresponds to 13.3 knots. This is an attempt to compare data from different sources in a structured manner. The average thrust from the sails should be roughly proportional to the sail area, and the resistance of the ship is roughly proportional to the wetted surface and the velocity squared.

For most of the cases, the exact value for wetted surface of the ships was not available. The empirical expression from the Holtrop method was therefore used to get a rough estimate [97]. Estimated fuel savings range from almost nothing to 47% for the external papers, and up to 70% when the result from this project is included. The average value is around of 20%. The installed sail area is between 0,3% and 86% of the ships wetted surface, with and average value of 28%.

The data show a tendency of significant scatter. This is due to a combination of different modelling strategies between the different papers, as well as different routes and ship types. Some data points are clear outliers. For instance, there is one data point from reference [92] that claims 47% fuel savings with relatively small rotor sails. This datapoint was estimated with weather data from a route in the North Atlantic during a short period between November and December. The large fuel savings is therefore likely a result of very good wind conditions in the route simulation. Most of the data points from the external papers that include hydrodynamic effects have relatively low values for the estimated fuel savings – generally less than 10%. However, it is not clear whether this is specifically due to the sail-induced resistance as all external cases with hydrodynamic effects are simulated with small sails. Both the importance of hydrodynamic effects and the question of which wind-power device has the largest potential are unclear based on the external papers. The data points from this project indicate a clear effect of the sail-induced resistance. This is further discussed later in this report and in the actual paper itself.

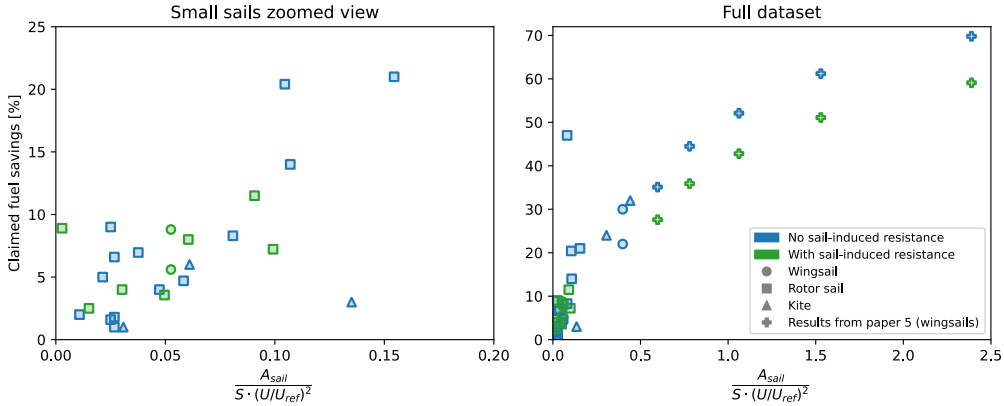


*Figure 7: Fuel saving claims from many of the different sources presented in this section, as well as the final paper in this report, sorted based on sail type. The reference velocity on the x-axis, $U_{ref}$, is 13.3 knots*

## 1.3 Thesis structure

This thesis is written as a collection of **five** articles. Two of them are published in the journal Ocean Engineering, while one is currently sent to review as of February 2022. In addition, there are two shorter conference papers with relevant results. The rest of the chapters are primarily meant to give a broader overview of the work. An outline of the different chapters is presented below.

- **Chapter 2** presents the main research questions for this work, along with the background.
- **Chapter 3** gives a summary of each of the papers**.**
- **Chapter 4** gives my conclusions and recommendations for future work.

A short overview of the papers is given below:

**Paper 1**

| **Title** | **Experimental study of the effect of drift angle on a ship-like foil with varying aspect ratio and bottom edge shape** |
|---|---|
| **Authors** | Jarle Vinje Kramer, Sverre Steen, and Luca Savio |
| **Published in** | Journal of Ocean Engineering, July 2016 |
| **Content** | Paper 1 presents results from towing tank experiments where a special foil-like ship geometry was tested with different aspect ratios and varying shape on the bottom edge. The purpose was both to produce validation data for CFD simulations and to explore the effect of simple geometry changes when it comes to lift and lift-induced drag. |

**Paper 2**

| **Title** | **Drift Forces – Wingsails vs Flettner Rotors** |
|---|---|
| **Authors** | Jarle Vinje Kramer, Sverre Steen, and Luca Savio |
| **Published in** | The High-Performance Marine Vehicles conference (HiPER), October 2016 |
| **Content** | Paper 2 presents result from a case study of a general cargo ship with wingsails and rotor sails. It explores how the estimated fuel savings depend on the modelling framework, geometry, and control algorithm of the sails. |

**Paper 3**

| **Title** | **Hydrofoil simulations – non-linear lifting line vs CFD** |
|---|---|
| **Authors** | Jarle Vinje Kramer, John Martin Kleven Godø, Sverre Steen |
| **Published in** | The Numerical Towing Tank Symposium (NuTTS), October 2018 |
| **Content** | Paper 3 is a short article about a numerical lifting line method. The accuracy of the method is compared against CFD simulations for single wings. |

**Paper 4**

| | |
|---|---|
| **Title** | **Simplified test program for hydrodynamic CFD simulations of wind-powered cargo ships** |
| **Authors** | Jarle Vinje Kramer and Sverre Steen |
| **Published in** | Journal of Ocean Engineering, December 2021 |
| **Content** | Paper 4 presents results from several numerical experiments that explored different simplifications for modelling the hydrodynamics of a wind-powered merchant ship using CFD and maneuvering theory. |

**Paper 5**

| | |
|---|---|
| **Title** | **Sail-induced resistance on a wind-powered cargo ship** |
| **Authors** | Jarle Vinje Kramer and Sverre Steen |
| **Published in** | Submitted to Journal of Ocean Engineering in January 2022 and first round of reviews were completed in April 2022. The preprint from April 2022 which include the changes based on the feedback from the reviewers is included in this report |
| **Content** | Paper 5 is in some ways an updated version of paper 2. It contains a similar case study, but both the modelling framework and the practical details in the study have been updated. The results show how the sail-induced resistance affects the performance of a ship with wing-sails, as a function of speed, number of sails, control algorithm and keel geometries. |

# 2 Research questions and objectives

The background for this project was a general suspicion that the negative hydrodynamic effects due to the side force from the sails could be important for wind-powered merchant vessels. Consequently, it would imply that the ship design should be modified to be well suited for wind-assistance. As highlighted in the literature review in Section 1.2, most recent papers on the topic neglected the negative hydrodynamic effects entirely, which we – myself and my supervisors – thought was strange. The papers in Section 1.2 that do include hydrodynamic effects in the analysis are mostly published after the start of this project. There was also an uncertainty regarding which effects that were most important. We knew that the wind-power devices would affect the drift angle, heel angle, rudder angle and the thrust from the propeller. However, we did not know which of these effects that would have the largest impact on the fuel savings for a merchant ship. Our first hypothesis when starting the project was that the drift angle would be the largest problem – which is why this effect was the focus in the beginning – but we did not know this for sure. As will be shown later, the initial hypothesis was at least somewhat wrong.

To answer these questions, it was necessary with some method for testing different ships and sail configurations and measure the magnitude of the potential problems. A very large portion of my work has therefore been on the topic of modeling wind-powered ships. In the beginning, it was an open question how this should be done, as there are several ways to approach this problem. It was decided that an ideal modelling framework should be both relatively fast and practical to use, but still capable of testing different design solutions with reasonable accuracy. The goal was to make something that could potentially be useful in the design phase of wind-powered ships. The first requirement is at odds with experimental work or very time-consuming simulations. The last requirement is at odds with purely empirical or theoretical approaches, as they are only capable of giving rough values based on the main dimensions of the ship. The most promising method was identified to be industrial CFD simulations, i.e., Reynolds-Averaged Navier-Stokes (RANS) turbulence modelling, combined with some form of route simulation models. The purpose of the route simulation models is to generalize the results from a limited set of CFD simulations to model the forces acting on the ship for arbitrary values of the state variables. It is important that the models are simple enough to not require too many CFD simulations to tune the coefficients in the expressions. However, too simple models would not be able to capture the physics with acceptable accuracy. To create these tools, I needed to explore both CFD strategies and different models to be used in route simulation framework.

The research questions can be summarized by the three points below:

- How can we accurately and practically model a wind-powered ship, when the negative hydrodynamic effects are a concern?
- How important are these negative effects for merchant ships?
- What can be done to minimize the negative effects?

These questions were in general explored together in a loop. For instance, to know how to simplify the modelling and how to reduce the negative effects, it is necessary to know which physical effects that are important. To know which physical effects that are important, it is necessary with some modelling method that include all effects of interest. Due to time and practical considerations, the project ended up focusing on some effects more than others. The limitations of the work and potential future improvements are highlighted in Section 4.2, after an overview of the conclusions.

Significant software development was done as part of this project. This includes software for route simulations, computationally efficient modelling of lifting surfaces, and automated and scriptable CFD-setup software. The theory behind these tools is described in the different papers, and some software packages are currently in use by other researchers at the department of Marine Technology at NTNU.

# 3 Overview of papers

This section contains an overview of the papers included as parts of this thesis. The original abstract of each paper is given along with the rest of the article text later in this report. This overview therefore focusses on giving a short explanation of the content of each paper and the background for why the research questions were relevant for the overall project. The conclusion from each paper is further covered in Section 4, discussed together with the conclusion from the project as a whole. The papers are explained in chronological order.

## 3.1 Paper 1: Experimental study of the effect of drift angle on a ship-like foil with varying aspect ratio and bottom edge shape

### 3.1.1 Content of the paper

The first paper gives results from an experimental study where the drift induced forces on a simple foil-like ship geometry – referred to as a "foil-ship" – was tested with different aspect-ratios, Froude numbers, and bottom edge shapes. The waterline geometry of this ship was a foil profile with 17% thickness which was extruded with straight sides to an aspect-ratio – or draught / length ratio – similar to typical merchant ships. That is, the actual model had a large aspect-ratio, but the depth could be changed by varying the number and size of the ballast weights placed in the model. For low Froude numbers, when surface wave-making is limited, it is commonly accepted as an approximation to model the surface as rigid, so that flow pattern is effectively mirrored about the surface. This means that the underwater part is modelled as a double body in infinite fluid. Assuming a double body across the free surface, we tested aspect ratios equal to 0.1, 0.2 and 0.3. The Froude numbers tested were 0.1 and 0.2. As a final geometry variation, the bottom edge geometry was tested both as perfectly sharp, and with a rounded edge.

The results present the resistance, side force, and yaw moment as a function of drift angles for all speeds and geometry variations. The uncertainty in the experiment is quantified. To facilitate ease of use of the experimental data, polynomial models are generated, and the coefficients are presented in tables. The results are compared against classical theoretical equations for lifting surfaces – both for small and large aspect ratios – with discussions.

### 3.1.2 Background and comments

The purpose of this experiment was threefold.

First, it was performed to generate validation data that could be used to test the accuracy of CFD simulations. Similar data existed for other ship geometries in the literature, and the data in reference [59] is for instance used in later work. However, it is always good to have a variety in validation data, and we believed new data sources could be beneficial both for us and others.

Second, we were interested in the validity of classical simplified models of lifting surfaces. The accuracy of these models for large aspect-ratio surfaces has been well documented previously, but less so for ship-like aspect ratios. We therefore wanted to test similar geometries with varying aspect ratios to see how the lift and lift-induced drag varied. An important point was to keep the geometry as simple as possible. The idea was that the drift-induced forces were more likely to be well described by simplified methods if the geometry was kept simple. If the experiment showed a good match between simplified theories, we could go further with more complex models for further validation. If the accuracy was poor, it is likely that it would be even worse for more complex geometries, and the validity of simplified methods would be disproven. All simplified methods for lifting surfaces use the aspect-ratio of the geometry as an input variable. Having a ship geometry where it was easy to change the aspect-ratio was therefore an important point.

Third, we wanted to see how important the bottom edge shape was for the results. This was also a fundamental test of simplified methods. Classical lifting line equations and empirical models for ship maneuvering theory only considers the main dimensions of the ship. Or in other words, they implicitly

assume that the details of the geometry are not that important. By comparing two almost identical shapes where only the bottom edge shape was varied, we could get a first test of how important geometrical details are for the drift-induced forces.

The result from this paper was a better understanding of drift-induced forces on low aspect ratio surfaces. Based on the results, we concluded that simplified methods had severe limits, and that more advanced methods for estimating the drift-induced forces on ships are necessary.

## 3.2 Paper 2: Drift Forces – Wingsails vs Flettner rotors

### 3.2.1 Content of the paper

The second paper contains a case study of a general cargo ship with multielement wingsails and rotor sails. The hull, rudder, and sails were all analyzed using CFD, but with simplified relationship between them. That is, all parts were analyzed separately without including interaction effects. Everything was combined with an early version of the route simulation framework. We varied both the complexity of the models and the control algorithm of the sails to see how much the fuel savings were affected by the variations. The base line results were from route simulations where no negative hydrodynamic effects were included. Then, the model complexity was gradually increased to include drift and rudder angles. Finally, we included hydrodynamic effects to the control algorithm and tested the effect of a simple keel.

### 3.2.2 Background and comments

The overall purpose of the paper was both to see the importance of the drift-induced forces, but also to see if there was any significant difference between a wingsail and a rotor sail. To a certain extent, this was an exploration of almost all research questions in this thesis. It was performed to get an early hypothesis of what the results of this project would be. However, it should be noted that significant simplifications were used, and improved methods were applied in later papers. An overview of the main limitations in this paper is listed below:

- The rudder was analyzed using a simplified model that did not include any interaction with the hull, and only a simplified interaction with the propeller. Although the rudder was tested with CFD, it was standing alone on a symmetry plane to represent the ship hull. Based on later results, this likely overestimated the effective aspect-ratio, and therefore underestimate the lift-induced drag on the rudder.
- The drift-induced resistance was evaluated using a small model scale at a relatively low Reynolds number. Although the model size was within what is typical for physical towing tank tests of ship geometries, it was later found that small scale testing overestimates the drift-induced resistance for full-scale ships.
- The control algorithm of the sails was not entirely realistic. It optimized the sails for every wind condition by evaluating the performance of the model. However, there were no limits on the rudder angle or heel angle, and therefore no explicit control of whether the ship was analyzed within realistic operating conditions. As can be seen in some of the plots in the paper, the rudder angle was at times very large during the simulations, and most likely above where stall would occur.

These simplifications have the effect that the drift-induced resistance is likely overestimated, while the rudder resistance is underestimated. The max thrust control algorithm without any limits on the rudder and heel angle is also a somewhat extreme condition that would not have been used in real life. For instance, if the sail-control algorithm is pushing the ship sideways to such an extent that the rudder is stalling, the captain on board would likely understand that the thrust from the sails should be reduced. This type of practical limits on the sail operation were not fully appreciated in this study but is included in paper 5.

The results from this paper were still useful. It showed that performance of rotor sail can suffer from very large drag forces in some wind conditions. This was largely solved by introducing retractable sails to the model. The study also showed that the control mechanism of the sails can be very important for the results. Although the exact relationship between the rudder and the hull was slightly wrong, it gave a clear indication that it is important to include both effects in the route simulation model. Finally, it also indicated that the effect of a fixed keel is limited for the sail-induced resistance.

## 3.3 Paper 3: Hydrofoil simulations – non-linear lifting line vs CFD

### 3.3.1 Content of the paper

The third paper is a short validation study of the discrete lifting line method developed as part of this PhD. As explained further in the next section, this paper focus on hydrofoil geometries. The implementation of the method is described with equations and relevant references to other similar methods in the literature. The accuracy of the method is evaluated, both in terms of integrated values for lift and drag, but also for local distribution of the lift over the span of different wing geometries. We tested different forms of non-planar wing shapes, with varying chord distribution, and evaluated a simple model for including high-speed free surface effects. The CFD simulations in the paper is set up with same software framework as the other papers in this thesis.

### 3.3.2 Background and comments

It may appear strange to include a paper about hydrofoil simulations in a PhD thesis about wind-powered merchant ships. However, this paper is relevant, as it was the first presentation and validation of the tool that is used to simulate wingsails in the final paper of this thesis.

The inspiration for the discrete lifting line came from my teaching duties at the department of marine technology, where I supervised a student project about lifting line methods for propellers. The students were tasked with implementing classical models from the literature and evaluate the accuracy. The combination of simplicity and accuracy offered by lifting line methods, even for relatively complex geometries such as propellers, are fascinating. I therefore wanted to test an advanced lifting line method for wingsails. The method ended up being developed as part of a hydrofoil research project – the background of which is shortly explained in the preface of this report – and then further developed specifically for wingsails after that. Although slightly on the side of the topic in this project, the model for the high-speed free surface effects explained in this article is very simple but provides a surprisingly good match for the lift distribution when compared with CFD simulations.

The results from this paper indicated that the discrete lifting line was capable of very accurate predictions of forces acting on single wings, even when the wings had relatively complex shapes. This made us believe that there was a good chance that the method would work for interaction effects between multiple sails as well, which was further explored in paper 5.

## 3.4 Paper 4 – Simplified test program for hydrodynamic CFD simulations of wind-powered cargo ships

### 3.4.1 Content of the paper

The fourth paper test four different simplifications for setting up hydrodynamic route simulation models of wind-powered ships using CFD. The simulations include both the hull and the rudder while the propeller is represented as an actuator disk. The simplifications consist of neglecting the free surface, testing the ship geometry in model scale, neglect the effect of heel on the drift-induced forces, and use the general assumptions in the MMG maneuvering model to reduce the test matrix to a minimum. That is, a slight modification to the rudder model is suggested, as it was found to be necessary to capture the rudder resistance. The logic in the setup of the CFD simulations is thoroughly described, including details in the mesh design. Systematic mesh refinement studies are performed to quantify the numerical uncertainty in the results. The results from the CFD setup are compared against several other experiments in the literature, including the results from paper 1. Recommendations for

each simplification are made based on the results. We also discuss the importance of different parts of the model by decomposing the resistance into hull and rudder components.

### 3.4.2 Background and comments

This paper represents a thorough test of the CFD strategy developed as part of this thesis. The goal was to find a setup that offered a good balance between accuracy and practicality. Due to the sheer number of settings in a CFD simulation, and the time it takes to run them, this paper is the result of much trial and errors throughout the PhD project. The paper also lays the foundation for the case study presented in paper 5. The results demonstrated the importance of the rudder forces in the modelling of wind-powered ships. In short, it was shown to be much more important than what we had previously believed.

## 3.5 Paper 5: Sail-induced resistance on a wind-powered cargo ship

### 3.5.1 Content of the paper

The fifth paper performs a similar case study as the one in paper 2, but with the final analysis framework, a different design of the ship and sails, and slightly different research questions. A general cargo ship is tested with varying number of sails, different design speeds, four different design configurations and with two different control algorithms. The design configurations consist of a bare hull, the same hull with bilge keels, a normal high aspect-ratio keel and a dynamic keel that is both rotatable and retractable. The control algorithms include practical limits for the rudder angle, heel angle and the side force on the sails. We document how much the fuel savings are dependent on the sail-induced resistance for the different design configurations and variations in the control strategy. The results are used to discuss the importance of the negative hydrodynamic effects on wind-powered vessels, and to quantify the effect of potential solutions to the problem. We also divide the resistance of the vessel into different components to highlight the source of energy loss. This includes the normal calm water straight ahead components, as well as added resistance due to waves, and the sail-induced resistance.

### 3.5.2 Background and comments

This is the final evaluation of the research questions in this project. To an extent, this paper can therefore be read as a summary of the work in this thesis. The modelling strategy for the vessel is based on the results from the previous papers, and this case study answers the two other research questions: how important are the negative hydrodynamic effects for a wind-powered vessels, and is there anything we can do about them?

The conclusions from both this paper and the rest are further discussed Section 4.

# 4 Conclusions and future work

## 4.1 Conclusions

The conclusions from my work are structured into different topics in the following subsections.

### 4.1.1 Modeling the hydrodynamics of wind-powered merchant ships

An early and important conclusion in this project was based on the experimental tests that were performed for the first paper in this thesis: simplified methods for estimating the side-force induced resistance on ship geometries are not necessarily very accurate. This conclusion is different than for high aspect-ratio wings, where the classical theoretical equations often give good results. For instance, when the lift-induced drag on straight wings with different taper ratios are estimated with elliptical wing theory, the errors are typically less than 10%, as for instance shown in reference [98], chapter 5. The first paper in this thesis showed that the lift and lift-induced drag on the tested low-aspect ratio geometries differed greatly from the same classical models. The exact magnitude of the difference varied between the tested cases. As an example, for the ship geometry with the rounded bottom edge, an aspect-ratio of 0.2, and a drift angle of 5 degrees, the lift-induced drag was roughly twice as high as what would be expected with lifting-line theory. The variation between the geometries with different bottom edge shapes, but the same aspect-ratio, were also significant. This implies that it is impossible to find a simplified theory that matches both shapes at the same time – at least if only the main dimensions of the geometry are used as the input. The reason for the large difference is the flow separation around the bottom of the hull. Although it was expected that the cross-flow drag would be affected by the bottom edge shape, it was surprising to see that the flow separation also affected the circulatory lift significantly. This was identified through a difference in the linear part of a polynomial model that was fitted to the experimental data. For the lowest aspect-ratio tested, the linear lift was close to twice as high for the ship with the sharp bottom edge as for the ship with the rounded bottom edge. The experiment tested geometries that on purpose were constructed to be as simple as possible. When simplified theories do not work for these geometries, it is also unlikely that it will work for more complex geometries. Similar conclusions can be made from the design study in paper 5. It showed that adding bilge keels to a ship hull has a large effect on both the side force and the side-force induced resistance. This effect is not captured by simplified models or existing empirical methods for estimating maneuvering coefficients. It should be noted that this is a potential difference between merchant ships and conventional sailing vessels. As for instance demonstrated in paper 5, the lift and drag on a high aspect ratio keel can be modeled relatively accurately using classical lifting line equations. Sailing vessels where a high aspect-ratio keel is balancing a large portion of the side force should therefore be more suitable for simplified methods than conventional merchant ship designs with a low aspect-ratio hull.

As this project was focused on merchant ships, a method for testing the actual geometry was necessary. The inclusion of viscous effects is essential since the drift-induced forces consist of both circulatory lift and cross flow drag. The standard method for doing such simulations is finite volume RANS CFD. Although this method simulates the actual geometry of the ship, it still introduces simplifications, for instance through the turbulence model and the discretization of the equations. Setting up practical CFD simulations can be a cumbersome task, especially if low computational time is of interest. Significant work was therefore done in this project to develop a CFD simulation setup that was both practical and accurate. This was achieved through a custom developed software framework for setting up ship simulations in OpenFOAM automatically, where the choice of settings where adjusted based both on published work from others and tests done specifically for this project. The result of this work is primarily presented in paper 4. A major question was how accurate one can estimate the drift-induced forces on a ship hull with CFD. This was explored by comparing CFD simulations against different benchmark experiments of ship hulls – both from other researchers and the experimental work presented in paper 1. This included validation tests of both the straight-ahead resistance and the drift-induced resistance. The results showed that the straight-ahead resistance is

captured significantly more accurately than the drift-induced forces. The straight-ahead resistance was compared against three different benchmark ships, over a wide range of Froude numbers, which resulted in an average error of only 1.2%. The error in the drift-induced forces was highly dependent on the drift angle, but several cases had errors around and above 10%. To achieve these results, we ended up using slightly unconventional settings for some of the discretization schemes. We found that the LUST scheme in OpenFOAM – which is a combination of linear and linear upwind interpolation – gave more accurate results than the more conventional linear upwind scheme typically used in RANS simulations. Although the LUST scheme is less dissipative, and therefore could be more unstable in certain situations, it was found to be stable for all tested cases in this project. This discovery was a result of much trial and error with different settings in OpenFOAM. The general conclusion is that hydrodynamic simulations of wind-powered ships is less accurate than the typical resistance test for conventional ships, due to the more complex flow structures around the hull. However, we still concluded that the magnitude of the error was acceptable with appropriate settings and mesh resolution.

Improving the accuracy of the CFD simulations can likely be achieved, for instance by using more physically correct turbulence models – which will also increase the computational time – such as Large Eddy Simulations or Algebraic Stress Models. This is partly commented on in paper 4, based on results presented in reference [66]. It is not, however, given that experimental evaluation of wind-powered ships is more accurate than CFD simulations. In attempt to find an efficient CFD setup, the effect of model scale on the drift-induced forces was evaluated. This showed that the Reynolds number had a large effect on the drift-induced forces, something that is also indicated in other papers. Since the flow separation around the bottom of the ship is such an important effect, this is perhaps not that strange. It is, however, important to be aware of when using results from towing tank experiments to evaluate wind-powered ships. For a drift angle of 9 degrees, the drift-induced drag was overestimated with more than 50% in a model scale of 1:20 for the ship geometry teste in paper 4. This model scale corresponds to a model length of 6 m, which is a typical size for physical towing tanks. The scaling error in the drift-induced forces was found to decrease with increasing Reynolds number. A model scale of 1:4 was found to give drift-induced forces close to the estimated full-scale values. This corresponds to a model length of 30 m and Reynolds number close to 70 million. Although this is a model size that is way too large to test in a physical towing tank, it is still small enough that practical CFD simulations are possible. That is, even though the Reynolds number is high, the required mesh resolution is acceptable for time efficient CFD simulations. The conclusion is therefore that it is possible to evaluate the drift-induced forces accurately at a reduced Reynolds number and practical mesh resolutions, but it is important to be aware of the errors when testing very small models, such as physical towing tank models.

Another trick for reducing the computational time of CFD simulations is to neglect the free surface. This was also evaluated in paper 4. The free surface was found to have a relatively small effect on the drift-induced forces for Froude numbers below 0.25. This corresponds to a speed slightly above 16 knots for a cargo ship with 120 m length. For larger Froude numbers, there was a significant effect. However, it is also important to consider the relative importance of the drift-induced forces. With increasing Froude number, the wave resistance naturally becomes more and more important. Consequently, at Froude numbers where the drift-induced forces are highly affected by the free surface, the relative importance of the drift-induced resistance is decreased, due to the relative increase of the wave resistance. Free surface effects were therefore concluded to be of secondary importance for the drift-induced forces on a wind-powered ship. That is, at least in an early design-loop where quick simulations are of great importance.

The effect of heel on the drift-induced forces was of interest, as it is a common and practical simplification to neglect heel in existing maneuvering models. Based on the experiments performed in paper 4, the effect of heel on the drift-induced forces was found to be significant for larger drift angles – such as 9 degrees – but negligible for smaller drift angles – such as 6 degrees and smaller. The

explanation is, again, connected to the cross-flow drag on the ship. The results showed that a heel angle could alter the amount of separation around the bottom edge of the ship. Whether or not to include heel in the modelling framework is therefore both a question about how large the heel angles are – which depends on the ship stability – and the magnitude of the drift angles – which depends on the center of effort of the hull and placement of the sails. If the sails are placed towards the front of the ship, much of the side force must be balanced by drift-induced forces. However, with sails placed towards the middle or the stern of the ship, drift-induced forces become less important, as the rudder is balancing a large portion of the total side force. As a result, in the final case study in this thesis, heel was neglected, as we found that both the heel angle and the drift angle was relatively small for the case study ship.

Although the beginning of this project was very much focused on drift-induced hull forces, the rudder was also identified to be a very important part of the total hydrodynamic model. In the case studies performed in paper 4 and paper 5, it was typically balancing around 50% of the total side force from the sails. The reason was that the center of effort for the hydrodynamic side force was placed either in front of or very close to the bow of the ship. Large rudder angles are therefore necessary to achieve yaw moment balance and the rudder model deserves just as much attention as the hull model. Although rudders are high-aspect ratio surfaces – which should make them good candidates for simplified models – they are usually placed in the wake of the hull and in the jet stream of the propeller. This complicates the physics considerably. The interaction between the hull, rudder, and propeller was therefore tested by simulating them together at various rudder angles, drift angles and propeller loadings in paper 4 and paper 5. The expressions in the MMG maneuvering model were found to generally predict the interaction effects well. However, this was not the case for the rudder resistance. This was mostly fixed by switching the default rudder model to the classical lifting line equations. The accuracy was also reduced when the drift angle, rudder angle, and propeller loading was large at the same time. This is important to be aware of for ships where this condition occurs often. The drift angles experienced by the case study ships in this project were limited, and the MMG model was therefore found to be suitable. The model includes simple polynomial expressions for the drift-induced forces, which were found to give a very good fit with the CFD data. This was the case even when the model was tuned based on minimal amount of data points.

### 4.1.2 Modelling the aerodynamics of wind-powered merchant ships

The topic of aerodynamic modelling is slightly outside the core topic of this PhD but was still given significant attention during my work. A custom discrete lifting line method was made and tested for various lifting surfaces. The implementation is relatively simple, and the computational speed is many orders of magnitude smaller than full three-dimensional CFD simulations. The details of this method along with validation experiments is covered in paper 3 and paper 5. The lifting line method has been widely used in the fluid dynamic community for a long time, and the accuracy of the method for single straight wings are therefore not that surprising. It is, however, more surprising that the accuracy is maintained even for the relatively complex cases tested in the papers, which includes curved wings, with and without free surface effects, and two wingsails in close proximity.

### 4.1.3 Importance of hydrodynamic effects

The importance of the negative hydrodynamic effects for wind-powered merchant vessels is primarily explored in paper 2 and paper 5, where the latest paper is using the final and therefore most accurate modelling framework. As mentioned in Section 3.2.2, the simplifications used in paper 2 are likely causing a slight overestimation of the drift-induced resistance and an underestimation of the rudder resistance. Paper 5 is therefore the main source of the conclusions on this topic.

The exact importance of the hydrodynamic effects will naturally depend on the size and number of sails, the speed of the ship, and the hydrodynamic design. All these things were varied in paper 5, which includes detailed presentations of the effect on the fuel savings. As an example, the effective thrust from the sails was reduced by around 10 percentage points – or 14% of the sail thrust – for a case with 8 knots ship speed, 3 sails and no keels. This was a case where the estimate fuel savings

were around 60%. The results also showed that increasing the speed results in greater relative reduction of the fuel savings. The explanation is likely that higher ship speeds cause the apparent wind angle to be closer to the bow. Another way of evaluating the same effects is to compare the sail-induced resistance – defined as the added resistance due to the side force from the sails – to the other resistance components in the route simulations. The relative value of this resistance component is roughly corresponding to the reduction in thrust. Paper 5 used a simplified model of the propeller to estimate the change in advance ratio and propeller efficiency. This modelling showed that the advance ratio was generally close to the design conditions. Although the topic of propellers for wind-powered ships certainly could deserve more investigation than what is done in this project, the current results indicate that the increased resistance is the main source of loss of fuel savings. As a comparison of the magnitude, the sail-induced resistance was shown to be comparable to the added resistance in waves for our case study ship. This indicate that both effects deserve equal attention when estimating the fuel consumption of a wind-powered ship.

The source of the sail-induced resistance is in general a combination of drift-induced forces on the hull and lift-induced resistance on the rudder. As explored in paper 4, the main source of resistance depends on the placement of the sails. If the sails are placed towards the bow, the main source is the drift-induced resistance. For sails placed towards the middle of the ship or further back, the rudder becomes the most important source. For the case study in paper 5, the rudder was the main source of sail-induced resistance for most of the cases, even though the hull was balancing slightly more of the side force. It was initially surprising to find that the rudder contributed so much to the total resistance. After all, the lift-induced drag on a lifting surface is inversely proportional to the aspect-ratio, according to classical lifting line theory. The aspect-ratio of the rudder in paper 4 was around 30 times higher than the aspect-ratio of the hull. However, the explanation was straightforward when the lift coefficient of the hull and the rudder was compared. The lift coefficient of the rudder was found to be close to 77 times as high as the lift coefficient on the hull when both the side force and the yaw moment were balanced at the same time. This is important as the lift-induced resistance is roughly proportional to the lift coefficient squared. Because of this high loading, the rudder ends up as the main source of the sail-induced resistance. The hull, on the other hand, was found to be relatively efficient at balancing the side forces from the sails, due to the very low lift coefficient. The main issue was achieving yaw balance with drift-induced forces alone. This is difficult with a large sail area as the center of effort for the drift-induced forces are usually either in front of the bow or close to it. In other words, large rudder angles are necessary for achieving yaw moment balance unless the sails are placed close to the bow.

The effect of heel on the drift-induced forces was neglected in paper 5, as the ship was mostly experiencing small drift angles. This simplification was based on the results in paper 4. The heel angle was, however, still calculated based on hydrostatic theory, to investigate whether large heel angles could be an issue related to safety or comfort for the crew. The ship was on purpose assumed to be relatively stable, with a metacentric height of 1.5 m. For low speeds, the heel angle was very small, and therefore found not to be important at all. This changes with increasing speed, and at 16 knots, the heel angle would sometimes approach the maximum limit in the study of 10 degrees. Still, the conclusion is that heel angles were usually not a problem, both from a safety and comfort point of view and for using simplified modelling of the forces.

As already mentioned, large rudder angles where often necessary for achieving yaw moment balance in the case studies performed for this project. In paper 5, the rudder angle was explicitly controlled to have a safety margin against stall. If the sails were operated to maximize thrust, this limit was reached quite often. This means that a control system for wind-powered ships should monitor the rudder angle, and make sure to reduce the thrust and side force from the sails if too large rudder angles are experienced. Otherwise, this could be a safety issue related to loss of maneuvering capabilities.

Whether or not the negative hydrodynamic effects due to sails should be considered important depends on the viewpoint. In cases where accurate estimation of fuel savings is the goal, it should certainly be included in the analysis. Otherwise, the positive effect of the wind-power device is going to be overestimated. However, the negative hydrodynamic effects can't be claimed to be a large problem. The case study in paper 5 showed that fuel savings close to 60% are possible with a conventional ship design. The sail-induced resistance does therefore not appear as a major showstopper for the concept of wind-propulsion for merchant shipping.

### 4.1.4 What can be done about the negative effects?

The main problem to be solved regarding negative hydrodynamic effects is to reduce the sail-induced resistance. Throughout this project I was actively trying to come up with new ideas to reduce this resistance component. Some of these ideas were tested in simplified ways – with quick and coarse CFD simulations – but not published in any articles. The reason they were not published was that most of those ideas turned out to have little to no effect on the results. For instance, I did experiment with different variations for the skeg and the rudder design, without finding any solutions that significantly reduced the sail-induced resistance. The only geometric design that was found to provide a large impact was the obvious solution: add some form of keel to the ship.

The simplified view of the effect of a keel is that it helps reduce the sail-induced resistance by balancing the side force with a high aspect ratio lifting surface. However, paper 5 showed that adding bilge keels to the hull was essentially just as efficient as adding a fixed high-aspect ratio keel. The main reason the keel is reducing the sail-induced resistance in this case is by offloading the rudder. The rudder was experiencing a very large lift coefficient and therefore large lift-induced resistance. The reason was a center of effort on the hull that was far ahead of the bow, such that a large rudder angle was necessary for yaw balance. Designing the ship to have a better balance between the rudder and the hull was therefore the first trick to reduce the sail induced resistance. However, the reduction in the sail-induced resistance with the bilge keels was not large enough to make up for the increase in friction. This illustrates that it is not simple to find a solution that drastically increase the fuel savings. Reducing one resistance component may increase another.

A fixed high aspect ratio keel will always experience the same angle of attack as the hull. Unless a very large keel is used, the hull will therefore always contribute to a large portion of the side force. By making the keel rotatable, as shown in paper 5, the balance between the hull, the keel, and the rudder could be improved. By making the keel retractable, the problem with the added friction was solved. This was therefore the best solution tested in this project. Although this will introduce some added complexity, it could be a solution for ships with very large sails.

The final strategy tested for managing the side force induced resistance was to modify the control algorithm of the sails to include the negative hydrodynamic effects in the objective function. This solution was first found to be very effective in paper 2. When similar strategies were tested in paper 5 – with updated and better models – the effect of this solution found to be relatively small. The reason was that the updated models in paper 5 predicted less sail-induced resistance than the early models in paper 2. However, the results in paper 5 still showed an interesting aspect for the control strategy. The side force from the sails could be limited to quite small values without significant reduction in fuel savings from the sails. When the side force is limited, so will the thrust – as they are both a result of the same angle of attack of the sails. However, in cases where the side force is large, the fuel savings are usually small. It is therefore not a problem to reduce the angle of attack in these cases. In other words, a very simple way to avoid large drift, heel, and rudder angles is to avoid using the sails in unfavorable weather conditions. This did not reduce the fuel savings from the sails significantly in the cases tested in paper 5, and even increased it slightly in some cases.

## 4.2 Limitations and future work

Although the goal of this project was to increase the complexity and accuracy of the hydrodynamic modelling, it was still necessary with several simplifications. A potential area for future work is to increase the accuracy of the modelling framework further. The most important simplifications are listed below:

- The propeller was modeled using a simplified approach throughout the project. CFD simulations were performed with the propeller as an actuator disk, and empirical open water data was used in route simulations. Performing more accurate simulations or experiments of the interaction between the rudder, hull, and propeller could offer better modeling. However, it is important to be aware that this is also a challenging topic. The results in this study indicated that the propeller was usually operating close to design conditions, even with significant fuel savings from the sails. A simplified approach may therefore be sufficient.
- The effect of heel was generally simplified in this study, primarily based on the results in paper 4. The simplification was likely acceptable for the type of ship tested in paper 5. However, there are other types of ships where this simplification might not be acceptable. Examples could include car carriers with very tall sails – such as the Ocean Bird project [22] – and cruise ships.
- The seakeeping of the ships was not tested in this thesis. Based on for instance the work presented in [99], there are reasons to expect that a wind-powered ship will experience less motions in waves than a conventional ship. Consequently, it could be that the added resistance in waves is reduced. This would be a positive hydrodynamic effect, which could be interesting to explore further.
- I did not explore the interaction between the sails and the superstructure. This effect is likely to be important at least for some ships.

As illustrated in the literature review in the beginning of this report, there is currently a wide range of different modelling approaches for wind-powered ships and several researchers are working on the topic from different angles. It is therefore difficult to compare the results from one paper directly to another. Is the difference in fuel savings due to differences in the sail technology, the ship details, or the modelling framework? A general improvement on this topic for the larger marine community could therefore be to introduce some amount of standardization for route simulation of ships. This could both be standard models and routes and more general recommendations regarding which effects to include and which to neglect. For both calm water hydrodynamics and maneuvering applications, it is common with standardized cases for comparing different models. This approach could be used for comparing different route simulation models as well. For instance, a standardized ship case, including geometry, route, and weather data. It would also be useful with standardized arrangements of sails or other fuel savings technologies of interest.

Finally, this report is mainly concerned about fuel savings, a topic that many researchers tend to focus on. However, there is also another important part of the equation for the analysis of wind-powered ships: the investment cost. Reducing this factor could very well be more important than maximizing the fuel savings. Research on solutions that reduce the cost of wind-power would be very interesting.

# Bibliography


[1] S. Arrhenius, "On the influence of Carbonic Acid in the Air upon the Temperature of the Ground," *The London, Edinburgh, and Dublin Philosophical Magazin and Journal of Science,* vol. 41, no. 251, 1886.

[2] United Nations, "Paris agreement," 2015. [Online]. Available: https://treaties.un.org/pages/ViewDetails.aspx?src=TREATY&mtdsg_no=XXVII-7-d&chapter=27&clang=_en.

[3] International Maritime Organization, "Cutting GHG emission from shipping - 10 years of mandatory rules," [Online]. Available: https://www.imo.org/en/MediaCentre/PressBriefings/pages/DecadeOfGHGAction.aspx.

[4] Europeean commission, "Reducing emissions from the shipping sector," [Online]. Available: https://ec.europa.eu/clima/eu-action/transport-emissions/reducing-emissions-shipping-sector_en. [Accessed 15 Novemeber 2021].

[5] DNV, "Maritime forceast to 2050," DNV, 2021.

[6] G. Bordogna, "Aerodynamics of Wind-Assisted Ships," Delft Univeristy of Technology, Delft, The Netherlands, 2020.

[7] C. J. Satchwell, "Preliminary Analysis of log data from the Fiji Windship 'Cagidonu'," University of Southampton, 1986.

[8] Southern Spars, "Dynarig information page," [Online]. Available: https://southernspars.com/dynarig/. [Accessed 3 November 2021].

[9] Dykstra Naval Architetcs, "Wasp Ecoliner," [Online]. Available: https://www.dykstra-na.nl/designs/wasp-ecoliner/. [Accessed 3 November 2021].

[10] P. Schenzle, "Estimation of wind assistance potential," *Journal of Wind Engineering and Industrail Aerodynamics,* vol. 20, pp. 97-110, 1985.

[11] P. V. MacKinnon, "A Canoe Wing Sail," Amateur Yacht Research Society, 1957.

[12] Amateur Yacht Research Society, "Wingsails," Amateur Yach Research Socity, 1957.

[13] J. G. Waker, "A High Performance Automatic Wingsail Axuiliary Propulsion System for Commercial Ships," *Journal of Wind Engineering and Industrial Aerodynamics,* vol. 20, pp. 83-96, 1985.

[14] B. Clayton, "Wind-assisted ship propulsion," *Physics and Technology,* vol. 18, 1987.

[15] P. J. Richards, A. Johnson and A. Stanton, "America's Cup downwind sails - vertical wings or horizontal parachutes," *Journal of Wind Engineering,* vol. 89, pp. 1565-1577, 2001.

[16] P. C. Shukla and K. Ghosh, "Revival of the Modern Wing Sails for the Propulsion of Commercial Ships," *Interntional Journal of Mathematical, Computational, Natural and Physical Engineering,* vol. 3, no. 3, 2009.

[17] T. Miyasaka, T. Nakashima, Y. Nihei and Y. Doi, "Prediction and Improvement of Propulsive Performance of Wing Sails Considering Their Aerodynamic Interaction," in *Proceedings of the Twenty-third International Offshore and Polar Engineering*, Anchorage, Alaska, USA, 2013.

[18] BAR Technologies, "WindWings," [Online]. Available: https://www.bartechnologies.uk/project/windwings/. [Accessed 17 October 2021].

[19] AYRO, "AYRO homepage," [Online]. Available: https://ayro.fr/. [Accessed 17 October 2017].

[20] Bound4Blue, "Bound4Blue homepage," [Online]. Available: https://bound4blue.com/en/. [Accessed 2021 October 2021].

[21] Michelin, "2021 Movin'On: Michelin presents two innovations to accelerate the development of sustainable mobility," 1 June 2021. [Online]. Available: https://www.michelin.com/en/press-releases/2021-movinon-michelin-presents-two-innovations-to-accelerate-the-development-of-sustainable-mobility/. [Accessed 17 October 2021].

[22] Wallenius Marine and Alfa Laval, "Ocean Bird homepage," [Online]. Available: https://www.theoceanbird.com/. [Accessed 17 October 2021].

[23] Energy Observer, "Energy observer homepage," [Online]. Available: https://www.energy-observer.org/. [Accessed 17 October 2021].

[24] L. Prandtl, "Applications of the Magnus Effect to the Wind Propulsion of Ships," National Advisory Committee for Aeronautics, Washington, USA, 1926.

[25] A. Betz, "The Magnus Effect, The Principle of the Flettner Rotor," National Advisory Committee for Aeronautics, Washington, USA, 1925.

[26] Bailey, "One thing that Einstein got wrong," 10 October 2018. [Online]. Available: https://historynewsnetwork.org/article/170158. [Accessed 2021 October 18].

[27] J. F. Wellicome, "Some comments on the relative merits of various wind propulsion devices," *Journal of Wind Engineering and Industrial Aerodynamics,* vol. 20, pp. 111-142, 1985.

[28] C. J. Satchwell, "Aerodynamics Design of Marine Aerofoils," *Journal of Wind Engineering and Industrial Aerodynamics,* vol. 20, pp. 1-22, 1985.

[29] L. Bergeson and K. C. Greenwal, "Sail Assist Developments," *Journal of Wind Engineering and Industrial Aerodynamics,* vol. 19, pp. 45-114, 1985.

[30] Norse power, "Norse power home page," [Online]. Available: https://www.norsepower.com/. [Accessed 18 October 2021].

[31] Anemoi Marine, "Anemoi Marine Web Page," [Online]. Available: https://anemoimarine.com/rotor-sail-technology/. [Accessed 18 October 2021].

[32] B. Charrier, J. Constans, J.-Y. Cousteau, A. Daif, L. Malavard and J.-L. Quinio, "Fondation Cousteau and windship propulsion 1980-1985," *Journal of wind engineering and industrial aerodynamics,* vol. 20, pp. 39-60, 1985.

[33] J. Cairns, M. Vezza, R. Green and D. MacVicar, "Numerical optimisation of a ship wind-assisted propulsion system using blowing and suction over a range of wind conditions," *Ocean Engineering,* vol. 240, 2021.

[34] Econowind, "Econowind homepage," [Online]. Available: https://www.econowind.nl/. [Accessed 17 November 2021].

[35] R. Duckworth, "The application of elevated sails (kites) for fuel saving auxiliary propulsion of commercial ships," *Journal of Wind Engineering and Industrial Aerodynamics,* vol. 20, pp. 297-315, 1985.

[36] B. Houska and M. Diehl, "Optimal control of towing kites," in *Proceedings of the 45th IEEE Conference on Decision and Control*, 2006.

[37] P. Naaijen and V. Koster, "Performance of auxiliary wind propulsion for merchant ships using a kite," in *2nd International Conference on Marine Research and Transportation*, 2007.

[38] R. Leloup, K. Roncin, M. Behrel, G. Bles, J. B. Leroux, C. Jochum and Y. Parlier, " A continuous and analytical modeling for kites as auxiliary propulsion devoted to merchant ships, including fuel saving estimation," *Renewable Energy,* vol. 86, pp. 483-496, 2016.

[39] C. Willyard, "The answer is blowing in the wind," Geotimes, 2008. [Online]. Available: http://www.geotimes.org/mar08/article.html?id=nn_wind.html.

[40] SkySails, "SkySails homepage," [Online]. Available: https://skysails-marine.com/index.html. [Accessed 21 Novemeber 2021].

[41] AirSeas, "AirSeas homepage," [Online]. Available: https://www.airseas.com/. [Accessed 21 November 2021].

[42] L. Prandtl, Tragflügeltheorie, Königliche Gesellschaft der Wissenschaften zu Göttingen, 1918.

[43] F. W. Lanchester, Aerodynamics: constituting the first volume of a complete work on aerial flight, Constable, 1907.

[44] J. N. Newman, Marine Hydrodynamics, Cambridge, Massachusetts, USA: The MIT Press, 1977.

[45] M. A. Abkowitz, "Lectures on Ship Hydrodynamics Steering and Manoeuvrability," Technical Univeristy of Denmark, Lyngby, Denmark, 1964.

[46] J. E. Kerwin, "A Velocity Prediction Program for Ocean Racing Yachts," Ocean Race Handicapping Project, 1975.

[47] Y. Liu, L. Zou, Z. Zou and H. Guo, "Predictions of ship maneuverability based on virtual captive model tests," *Engineering Applications of Computational Fluid Mechanics,* vol. 12, no. 1, pp. 334-353, 2018.

[48] H. Yasukawa and Y. Yoshimura, "Introduction of MMG standard method for ship maneuvering predictions," *Journal of Marine Science and Technology,* vol. 20, no. 1, pp. 37-52, 2015.

[49] I. M. Viola, M. Sacher, J. Xu and F. Wang, "A numerical method for the design of ships with wind-assisted propulsion," *Ocean Engineering,* vol. 105, pp. 33-42, 2015.

[50] A. Fiorention, L. Lecce, A. D'Antonio, G. Del Core, A. Maglione and F. Marulo, "Proposal of a sail system for the propulsion of a 25.000 DWT Bulk-carrier," *Journal of Wind Engineering and Industrial Aerodynamics,* vol. 19, pp. 115-137, 1985.

[51] C. J. Satchwell, "Aerodynamic Design of Marine Aerofoils," *Journal of Wind Engineering and Industrial Aerodynamics,* vol. 20, pp. 1-22, 1985.

[52] K. Roncin and J. Kobus, "Dynamic simulation of two sailing boats in match racing," Laboratory of Fluid Mechanics, Ecole Centrale de Nantes, Nantes, France, 2004.

[53] O. F. Sukas, O. K. Kinaci and S. Bal, "Theoretical background and application of MANSIM for ship maneuvering simulations," Faculty of Naval Architecture and Ocean Engineering, Istanbul Technical University, Istanbul, Turkey, 2019.

[54] F. Quadvlieg, F. Stern, C. D. Simonsen and J. F. Otzen, "SIMMAN 2014 Workshop on Verification and Validation of Ship Manoeuvering Simulation Methods," 2017.

[55] F. Tillig and J. W. Ringsberg, "A 4 DOF simulation model developed for fuel consumption prediction of ships at sea," *Ships and offshore structures,* vol. 14, no. 51, pp. 112-120, 2019.

[56] J. B. Van den Brug, W. Beukelman and G. J. Prins, "Hydrodynamic forces on a surface piercing flat plate," Delft Univeristy of Technology, Delft, The Netherlands, 1971.

[57] W. M. S. Bradbury, "An experimental investigation of the flow past hulls at leeway," *Journal of Wind Engineering and Industrial Aerodynamics,* vol. 20, pp. 227-265, 1985.

[58] J. Longo and F. Stern, "Effects of drift angle on model ship flow," *Experiments in Fluids,* vol. 32, pp. 558-596, 2002.

[59] K. Kume, J. Hasegawa, Y. Tsukada, J. Fujisawa, R. Fukasawa and M. Hinatsu, "Measurements of hydrodynamic forces, surface pressure, and wake for obliquely towed tanker model and uncertainty analysis for CFD validation," *Journal of Marine Science and Technology,* vol. 11, pp. 65-75, 2006.

[60] N. J. van der Kolk, J. A. Keuning and R. H. M. Huijsmans, "Part 1: Experimental validation of a RANS-CFD methodology for the hydrodynamics of wind-assisted ships operating at leeway angles," *Ocean Engineering,* vol. 178, pp. 375-387, 2019.

[61] N. J. van der Kolk, I. Akkerman, J. A. Keuning and R. H. M. Huijsmans, "Low-aspect ratio appendages for wind-assisted ships," *Journal of Marine Science and Technology,* pp. 1-18, 2021.

[62] M. Renilson and T. Mak, "Scale effect on manoeuvring coefficients for a modern full-form vessel," in *International Symposium and Workshop on Forces Acting on a Manoeuvring Vessel*, Val de Reuil, France, 1998.

[63] K.-H. Kim, R. M. Joseph Gorski, R. Wilson, F. Stern, M. Hyman and C. Burg, "Simulation of Surface Ship Dynamics," in *Proceedings of the 2003 User Group Conference*, 2003.

[64] S. Bhushan, T. Xing, P. Carrica and F. Stern, "Model- and Full-Scale URANS Simulations of Athena Resistance, Powering, Seakeeping, and 5415 Maneuvering," *Journal of Ship Research,* vol. 53, no. 4, pp. 179-198, 2009.

[65] Y. Jin, J. Duffy, S. Chai, C. Chin and N. Bose, "URANS study of scale effects on hydrodynamic manoeuvring coefficients of KVLCC2," *Ocean Engineering,* vol. 118, pp. 93-106, 2016.

[66] N. J. van der Kolk, I. Akkerman, J. A. Keuning and R. H. M. Huijsmans, "Part 2: Simulation methodology and numerical uncertainty for RANS-CFD for the hydrodynamics of wind-assisted ships operating at leeway angles," *Ocean Engineering,* vol. 201, 2020.

[67] L. Larsson, "Scientific Methods in Yacht Design," *Annual review of fluid mechanics,* vol. 22, pp. 349 - 385, 1990.

[68] A. F. Molland and S. R. Turnock, "Wind tunnel tests on the effect of a ship hull on rudder-propeller performance at different angles of drift," University of Southampton, Southampton, England, 1995.

[69] A. F. Molland and S. R. Turnock, "Flow straightening effects in a ship rudder due to upstream propeller and hull," *International Shipbuilding Progress,* vol. 49, no. 3, pp. 195-214, 2002.

[70] H. Söding, "Limits of potential theory in rudder flow predictions,," *Ship Technology Research,* vol. 45, no. 3, 1998.

[71] A. F. Molland, "The prediction of rudder-propeller interactions using blade element-momentum theory and modified lifting line theory," University of Southamptopn, Southampton, England, 1992.

[72] L. He and S. A. Kinnas, "Numerical simulation of unsteady propeller/rudder interaction," *International Journal of Naval Architecture and Ocean Engineering,* vol. 9, pp. 677-692, 2017.

[73] B. Carstensen, "A Method for Rudder Force Calculation in the Design Process Considering Rudder-Propeller-Interaction," in *Sixth International Symposium on Marine Propulsors*, Rome, Italy, 2019.

[74] A. F. Molland and S. R. Turnock, "Developments in modelling ship rudder-propeller interaction," *Transaction on the Built Environment,* vol. 5, 1994.

[75] C. E. Badoe, A. B. Phillips and S. R. Turnock, "Influence of drift angle on the computation of hull–propeller–rudder interaction," *Ocean Engineering,* vol. 103, pp. 64-77, 2015.

[76] A. Skogman, "The practical meaning of lateral balance for a sail-assisted research vessel," *Journal of wind engineering and industrial aerodynamics ,* vol. 20, pp. 201-226, 1985.

[77] T. Fujiwara, G. E. Hearn, F. Kitamura, M. Ueno and Y. Minami, " Steady sailing performance of a hybrid-sail assisted bulk carrier," *Journal of Marine Science and Technology,* vol. 10, pp. 131-146, 2005.

[78] J. A. Keuning and B. J. Binkhorst, "Appendage resistance of a sailing yacht hull," in *SNAME 13th Chesapeake Sailing Yacht Symposium*, 1997.

[79] P. Van Oossanen and P. N. Joubert, "The development of the winged keel for twelve-metre yachts," *Journal of Fluid Mechanics,* vol. 173, pp. 55-71, 1986.

[80] B. Axfors and H. Tunander, "Investigation of Keels Bulbs for Sailing Yachts," Chalmers Univeristy of Technology, Gothenburg, Sweden, 2011.

[81] J. A. Keuning and K. J. Vermeulen, "The Yaw Balance of Sailing Yachts Upright and Heeled," in *SNAME 16th Chesapeake Sailing Yacht Symposium*, 2003.

[82] Y. Minami, T. Nimura, T. Fujiwara and M. Ueno, " Investigation into Underwater Fin Arrangement Effect on Steady Sailing Characteristics of a Sail Assisted Ship," in *Proceedings of The Thirteenth International Offshore and Polar Engineering Conference*, Honolulu, Hawaii, USA, 2003.

[83] L. Marimon Giovannetti, M. Alexandersson, F. Olsson and S. Werner, "Appendages investigation and their effects on maneuvering coefficients for applications in wind assisted ships," in *Innovasail proceedings*, Gothenburg, Sweden, 2020.

[84] H. Hersbach, B. Bell, P. Berrisford and S. Hirahara, "The ERA5 global reanalysis," *Quarterly Journal of the Royal Meteorological Society,* 2020.

[85] M. Traut, P. Gilbert, C. Walsh, A. Bows, A. Filippone, P. Stansby and R. Wood, "Propulsive power contribution of a kite and a Flettner rotor on selected shipping routes," *Applied Energy,* vol. 113, pp. 362-372, 2014.

[86] E. Bøckmann, S. Steen and D. Myrhaug, "Performance of a ship powered purely by renewable energy," in *International Conference on Ocean, Offshore and Arctic Engineering*, San Fransisco, California, USA, 2014.

[87] L. Talluri, D. Nalianda, K. Kyprianidis, T. Nikolaidis and P. Pilidis, "Techno economic and environmental assessment of wind assisted marine propulsion systems," *Ocean Engineering,* vol. 121, pp. 301-311, 2016.

[88] L. Talluri, D. Nalianda and E. Giuliani, "Techno economic and environmental assessment of Flettner rotors for marine propulsion," *Ocean Engineering,* vol. 154, pp. 1-15, 2018.

[89] K. Ouchi, K. Uzawa, A. Kanai and M. Katori, "Wind challenger" the next generation hybrid sailing vessel," in *The third international Symposium on Marine Propulsors*, Launceston, Tasmania, Australia, 2013.

[90] L. Yuankui, Z. Yingjun and Z. Feixiang, "Minimal time route for wind-assisted ships," *Marine Technology Society Journal,* vol. 48, no. 3, pp. 115-124, 2014.

[91] M. Bentin, D. Zastrau, M. Schlaak, D. Freye, R. Elsner and S. Kotzur, "Bentin, Marcus, et al. "A new routing optimization tool-influence of wind and waves on fuel consumption of ships with and without wind assisted ship propulsion systems," *ransportation Research Procedia,* vol. 14, pp. 153-162, 2016.

[92] B. Comer, C. Chen, D. Stolz and D. Rutherford, "Rotors and bubbles: Route-based assessment of innovative technologies to reduce ship fuel consumption and emissions," The international council on clean transportation.

[93] F. Tillig, J. W. Ringsberg, H. N. Psaraftis and T. Zis, "Reduced environmental impact of marine transport through speed reduction and wind assisted propulsion," *Transportation Research Part D,* vol. 83, 2020.

[94] R. Lu and J. W. Ringsberg, "Ship energy performance study of three wind- assisted ship propulsion technologies including a parametric study of the Flettner rotor technology," *Ships and Offshore structures,* vol. 15, no. 3, pp. 249-258, 2020.

[95] N. J. van der Kolk, G. Bordogna, J. C. Mason, P. Desprairies and A. Vrijdag, "Case study: Wind-assisted ship propulsion performance prediction, routing, and economic modelling," in *Power & Propulsion Alternatives for Ships*, London, UL, 2019.

[96] G. Clauss, H. Sickmann and B. Tampier, "Simulation of the Operation of Wind-Assisted Cargo Ships," Hauptversammlung der Shiffbautechnischen Gesellschaft, Berlin, germany, 2007.

[97] J. Holtrop and G. G. J. Mennen, "An approximate power prediction method," *International Shipbuilding Progress,* vol. 29, no. 335, pp. 166-170, 1982.

[98] J. D. Anderson, Fundamentals of Aerodynamics, McGraw-Hill, 1991.

[99] J. Tranell, "Seakeeping capabilities of sailing cruise and passenger vessels," Norwegian University of Science and Technology, Trondheim, Norway, 2021.

[100] ESI-group, "OpenFOAM homepage," [Online]. Available: https://www.openfoam.com/.

[101] Blender Foundation, "Blender homepage," [Online]. Available: https://www.blender.org/.

## Paper 1: Experimental study of the effect of drift angle on a ship-like foil with varying aspect ratio and bottom edge shape

Written by Jarle Vinje Kramer, Sverre Steen and Luca Savio

Published in Journal of Ocean Engineering, July 2016

Ocean Engineering 121 (2016) 530–545

Contents lists available at ScienceDirect

Ocean Engineering

journal homepage: www.elsevier.com/locate/oceaneng

# Experimental study of the effect of drift angle on a ship-like foil with varying aspect ratio and bottom edge shape

Jarle A. Kramer [a,*], Sverre Steen [a], Luca Savio [b]

[a] Department of Marine Technology, Norwegian University of Science and Technology (NTNU), Trondheim, Norway
[b] The Norwegian Marine Technology Research Institute (MARINTEK), Trondheim, Norway

ARTICLE INFO

*Article history:*
Received 1 December 2015
Received in revised form
3 May 2016
Accepted 5 June 2016

*Keywords:*
Experiment
Drift-induced forces
Very small aspect ratio
Varying bottom edge shape
Froude effects

ABSTRACT

A ship-like foil geometry with different aspect ratios and bottom edge shapes are tested experimentally with several drift angles (0–10°), and two Froude numbers (0.1 and 0.2). The geometry is a modified version of the foil Eppler E836 that is extruded in the span direction to make it a 3D geometry. The aspect ratios are 0.1, 0.2 and 0.3. Two different bottom edge shapes are tested: a perfectly sharp bottom edge and a rounded bottom edge. Lift, drag and yaw moment is measured. The result is presented both as raw data and data fitted polynomial functions. The experimental results are compared to simplified models for lifting surfaces, along with some discussion regarding the physics of a drift-induced forces. The simplified models do not fit the experimental data very well, but the comparison is used to discuss the importance of different physical effects. The result from the experiments show that both the aspect ratio and the shape of the bottom edge is very important. Froude number effects on lift and lift-induced drag are seen to be very small, for the two Froude numbers tested in this experiment, while the yaw moment and center of pressure is affected.



## 1. Introduction

When a ship moves with a drift angle, it becomes a lifting surface. The "lift" is the force pushing the ship sideways, or in a direction normal to the traveling direction. The drift-induced effects on the global forces are of interest in several practical situations. Two examples are maneuvering and ships that use wind assisted propulsion devices, such as sails. Maneuvering simulations requires the global forces for several types of ship movements, including static drift angles. For instance, this is the case when vessels are in a turning maneuver. Ships that use wind propulsion devices will, depending on the wind direction, travel with a steady drift angle in order to balance the side force from the sails. The overall purpose of this paper is to aid in the prediction of global forces on a ship traveling with a steady drift angle. This is done by giving experimental data that can be used as Computational Fluid Dynamics (CFD) validation data, study the importance of different parameters that are known to affect lifting surfaces, and by comparing the measured forces to simple lifting surface theory. In order to do this, a "ship-like" foil geometry traveling with varying drift angles is tested experimentally in the MARINTEK (Marintek Homepage,) towing tank. The geometry is simpler than modern cargo ships, with a straight trailing edge, straight sides, and a rounded nose. The purpose of this simple geometry is to make geometry variations simple. The parameters varied are the aspect ratio of the foil, the shape of the bottom edge, and the Froude number. Three different aspect ratio values are tested: 0.1, 0.2 and 0.3. These aspect ratios are within the range of "normal" ship aspect ratios. Two different bottom edge shapes are tested: one perfectly sharp edge and one rounded edge. The purpose of this is to quantify the importance of the cross sectional shape. The cross sectional shape affects how the flow moves around the bottom edge of the geometry. The Froude numbers 0.1 and 0.2 are tested in order to get an idea of the importance of the free surface on the global forces. The Froude number is defined as $Fr = U/\sqrt{gL}$, where $U$ is the speed of the model, $L$ is the length of the model and $g$ is the gravitational acceleration. At Froude number equal to 0.1 there were virtually no waves, while there were significant waves at Froude number equal to 0.2. The results presented in Section 6 consist of lift, drag, and yaw moment coefficients for the geometries tested. In addition, sinkage and trim are plotted, although the values are small, and somewhat uncertain. A series of pictures of the wave pattern around the model is used for qualitative discussion. In order to give numerical values, the experimental data is fitted to polynomials, and the polynomial coefficients are given in tables, so that the forces and moments for an arbitrary drift angle can be calculated. Both raw measurements and polynomial data are plotted. The specific form of the

* Corresponding author.
*E-mail address:* jarle.a.kramer@ntnu.no (J.A. Kramer).

http://dx.doi.org/10.1016/j.oceaneng.2016.06.004
0029-8018/

polynomial functions is based on trial and error, with some help from simplified models of lifting surfaces. Detailed description of the geometries tested, as well as why these geometries were chosen is explained in Section 3. How the experiment is performed and how the results are post-processed is explained in Section 4. Uncertainty of the results, with main focus on the precision limit, is estimated in Section 5.

Drift-induced effects on global forces have been studied experimentally before. Validation experiments intended for CFD has primarily been done on traditional ship geometries. Longo and Stern (2005) contains data for the ship geometry Series 60 for several Froude numbers between 0.1 and 0.35, and drift angles between 0° and 10°. The model had a length of 3.048 m, and was tested at the IIHR-Hydroscience & Engineering, University of Iowa, towing tank. The data shows that the side force on the ship is a non-linear function of drift angle. Changes in the side force due to varying Froude number are small, at least for Froude numbers below 0.3. The SIMMAN 2008 workshop (Stern et al., 2011) used towing tank test data for several types of ship movement, and several hull geometries, from several towing tank facilities. The purpose of the experiments was validation of manoeuvring simulations. Some of the tests were static drift angles, although only a few drift angles were tested for each hull geometry. The hull geometries used was KVLCC1, KVLCC2, KCS and the DTMB 5415. The KVLCC2 was also the geometry used in reference (Kume et al., 2006) where a 4.97 m long model was tested in the "National Maritime Research Institute" towing tank, Japan, for several drift angles between 0° and 12°. The Froude number was 0.142, which corresponds to the design speed of the KVLCC2. Reference (Van Den Brug et al.,) studies a flat plate with different aspect ratios, for both static and oscillating drift angles. The experiment is done in the Shipbuilding laboratory, at the University of Technology, Delft. The aspect ratios tested are 0.08, 0.4, 0.7 and 1. The shapes of both the leading and trailing edge is varied, as well as the inclination of the bottom edge.

## 2. Simplified models for lifting surfaces

Lifting surfaces in general have been studied many times before. In particular, many simplified models exist that attempts to predict the forces and moments that act on a lifting surface. The results from the experiment described in this paper have been compared with some of these models. The classical lifting surface models are in general well known, and although there is no reason to expect them to be very accurate for a ship-like geometry, a comparison between real life and simplified mathematical models is interesting. There are models for both large and small aspect ratios, but none of the models include free surface effects. A short review of these models will be given below, in order to use them in further discussion. The theories mentioned will be linear foil theory, elliptic wing theory, slender body theory, and methods for estimating cross-flow effects.

### 2.1. Lift

The basic textbook (Anderson, 1985) knowledge of lifting surfaces consist of, among other things, linear foil theory and simplified evaluation of 3D effects by lifting line theory (Prandtl). In linear foil theory, the lift coefficient for a symmetric 2D foil profile is predicted to be linearly dependent on the drift angle, or angle of attack ($\alpha$ [rad]), by the following function:

$$C_{L,2D} = 2\pi\alpha \tag{1}$$

Three-dimensional effects are very important for lifting surfaces. Tip vortices decreases the lift compared to the 2D case, and creates lift-induced drag. The aspect ratio ($Asp$) is an important parameter for the 3D effects on lifting surfaces and is defined as the span of the lifting surface ($s$) squared, divided by the planform area ($A$). For a perfectly rectangular lifting surface, this can be simplified to the span divided by the chord ($c$). The free surface can be approximated as a symmetry plane, so that the aspect ratio for a ship is two times the depth ($D$), divided by the length ($L$). If the circulation distribution on the wing is elliptically distributed, it is possible to calculate 3D effects analytically. The reduction in lift due to 3D-effects can be calculated as follows:

$$Asp = \frac{s^2}{A} \approx \frac{s}{c} \overset{\text{ship}}{=} \frac{2D}{L} \tag{2}$$

$$C_L = \frac{C_{L,2D}}{1 + 2/Asp} \tag{3}$$

For a wing without an elliptic circulation distribution, the aspect ratio used in the equation can be changed to an effective aspect ratio. The effective aspect ratio can be calculated with a span efficiency factor, $e$, as $Asp{\cdot}e$. For planar wings, $e$ is usually less than 1 (Anderson, 1985, chapter 5). For non-planar wings, such as wings with winglets, box wings, biplane wings, etc., $e$ can be larger than 1 (Kroo). These equations are useful and accurate when the lifting surface have a large aspect ratio, and small angle of attack. However, this is not the case for ships, which have very small aspect ratios, compared to traditional wings. "Slender body theory" attempts to give a better estimate of the 3D effects for very low aspect ratio lifting surfaces (Newman, 1977, chapter 7). Slender body theory assumes the longitudinal length dimension to be much larger than all the others, and that the flow can be described by potential theory. The lift on a slender body is evaluated by dividing the body into strips along the longitudinal axis, and evaluate the 2D potential on each strip, with some simplifications introduced by the slenderness assumption. The result is that the lift on an infinitesimal small cross section is dependent on the local cross-sectional velocity and the infinite-frequency added-mass of the strip. More information can be found in reference (Newman, 1977, chapter 7). The resulting equation for the lift coefficient for a planar lifting surface, with very small aspect ratio is then as follows:

$$C_L = \frac{1}{2}\pi Asp\alpha = \frac{1}{4}C_{L,2D}Asp \tag{4}$$

Even if Eq. (4) attempts to estimate the lift on a low aspect ratio surface, it does so by assuming potential flow with the Kutta condition. This means that it only consider the separation at the trailing edge, which is a good assumption for large aspect ratio surfaces. However, for a lifting surface with a small aspect ratio, this is not always the case. The phenomenon known as cross-flow can be a major contributor to the lift as discussed in reference (Faltinsen, 2005, Section 10.6). Cross-flow refers to the separation of the flow around the bottom edge of the ship. The separation can happen due to sharp corners or adverse pressure gradients in the viscous boundary layer. In the context of a ship, with velocity U and a constant drift angle, the cross-flow velocity, $V$, can be calculated as $V = U\sin\alpha$. If the drift angle, and thereby the cross-flow velocity, is large, one can think of this cross-flow lift as a steady state viscous drag force on the cross section of the ship, in the cross-sectional plane, due to the cross-flow velocity. If at the same time the drift angle is small enough so that the simplification $\sin\alpha \approx \alpha$ holds true, simplified theory predicts a lift force that is approximately dependent on the drift angle squared (Faltinsen, 1993, Chapter 6). However, when the drift angle is very small, the ship velocity is much larger than the cross-flow velocity, and the

assumption that the cross-flow force can be approximated as a steady state drag force on the cross-section is not valid. More advanced methods are needed to estimate the effect, such as CFD. Another way of doing this is the 2D+t approach which is described in reference (Faltinsen, 2005, Section 10.6). In the 2D+t method, a 3D steady problem is transformed into a transient 2D problem. The time in the 2D problem becomes the third spacial dimension in the 3D problem. The cross-flow drag on a specific cross-section is only affected by the upstream cross-sections. The 2D+t method is for instance used in reference (Ommani and Faltinsen,), where the forces on a flat plate moving with a drift angle is estimated by decomposing the problem into a tail-separated forward flow part and a bottom-tip cross flow part. The 2D+t method is used to estimate the cross-flow lift, independent of free surface effects, and the tail separated part is estimated with a Boundary Element Method (BEM) code. Although the 2D+t theory could be a good candidate for estimating the effect of cross-flow for this case, it demands time dependent data for the drag coefficient for a large number of cross-sectional shapes. The geometries used in this paper has a varying cross-sectional shape along the length of the model. Drag coefficients for suddenly accelerated cross-sections, for all the necessary cross-sectional shapes, as a function of time, are not available, and it is therefore hard to use this method for simple calculations of lift. Instead, only Eqs. (3) and (4) will be used for comparison. Cross-flow effects will be discussed by considering the non-linearity in the experimental results, and deviations from low aspect ratio theory.

### 2.2. Lift-induced drag

Any surface that creates lift will also create additional drag, known as lift-induced drag. This additional drag comes from both viscous and potential flow phenomenons, and are often assumed to be proportional to the lift squared (Anderson, 1985, chapter 5). The potential lift-induced drag, ($C_{D,i}$), assuming an elliptic lifting surface,can be calculated as follows:

$$C_{D,i} = \frac{C_L^2}{\pi Asp} \tag{5}$$

To our knowledge, no simplified theories exists that attempts to estimate lift-induced drag on a very small aspect ratio surface, such as a ship. However, as Eq. (5) is very well known and is considered as a minimum value of the lift induced drag for a large aspect ratio lifting surface, it has still been used to compare the lift induced drag measured in the experiment.

### 2.3. Yaw moment

A lifting surface will experience a yaw moment about its leading edge. If the lift force on the geometry is represented by a single vector rather than a distributed load, it must be placed such that it produces a moment equal to the actual yawing moment on the geometry. This location is known as the center of pressure, $x_{xp}$. The center of pressure is predicted to be located at the quarter chord for a symmetric foil according to linear foil theory (Anderson, 1985, chapter 4). Slender body theory can also be used to estimate the moment. This will result in the Munk moment. For a non-lifting ship-like body in a potential flow, with a drift angle, there will be a low pressure region in the nose and tail region, which generates a moment. This moment can be estimated if the added mass of the ship is known, which is explained in for instance reference (Faltinsen, 1993, chapter 6; Newman, 1977, chapter 7). However, the Munk moment alone will not predict correct moments, as viscous moment due to cross-flow is also an important effect, and the separation at the trailing edge must be considered. As this quickly becomes complicated calculations, only linear foil theory has been used as a comparison model in this paper. Specifically, the center of pressure will be calculated, in order to see how it relates to the quarter chord assumption from linear foil theory.

## 3. Model geometry

The geometry used in this experiment was based on a 2D foil profile, extruded to a 3D body with very small aspect ratio. Since the aspect ratio is known to be an important parameter, aspect ratios within the normal range of ship aspect ratios were chosen. Ref. (IHS) contains a large ship database. Data from 47,282 ships were extracted from this database in order to calculate normal aspect ratios for cargo ships. This number represent all the ships in the categories “general cargo”, “container”, “dry bulk”, “oil tankers” and “chemical tankers” from the database. The aspect ratio is calculated as two times the depth of the ship divided by the length. The result can be seen in Fig. 1. Aspect ratios 0.1, 0.2 and 0.3 were chosen as the test aspect ratios. As can be seen in Fig. 1, most of

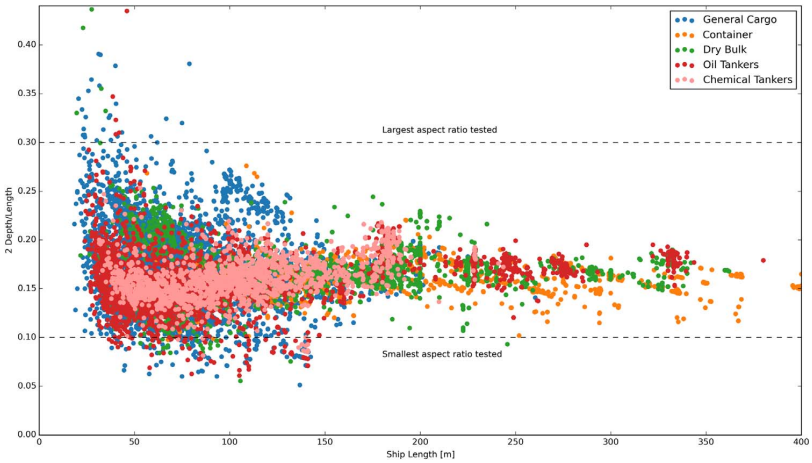


**Fig. 1.** Aspect ratios for several ships, of different type and length.

the data points are scattered between these values, with some exceptions, in particular for smaller ships. The average values for the cargo ship types “general cargo”, “container”, “dry bulk”, “oil tankers” and “chemical tankers” are 0.164, 0.158, 0.172, 0.162, and 0.172 respectively.

A 2D foil profile geometry was chosen due to three requirements:

- The geometry had to be easily obtainable by the general public, as one of the purposes of this experiment was to provide CFD validation data. Foil profile geometries are available in online foil databases, of which there are several.
- The geometry had to be “ship-like”, so that the physical phenomena that would occur in this experiment would be similar to the physical phenomena that would occur for an actual ship traveling with a drift angle. A 2D foil profile is different from a ship water line geometry, but not much.
- The geometry had to be simple enough so that depth changes, as well as changes in the bottom edge geometry could be done in a simple, systematic manner. This essentially required the sides of the geometry to be vertical, and that eliminates actual ship geometries, such as KVLCC2 or similar commonly available ship geometries.

The chosen foil profile is a slightly modified version of the foil “Eppler E836”. The original foil geometry can be downloaded from reference (Airfoil Tools). The foil was chosen based on the fact that it has a relatively sharp nose, and the point of maximum thickness located towards the middle, which are characteristics shared with ship water line profiles. The choice was made based on visual inspection of several publicly available symmetric foils. Modifications of the original foil geometry consists of making it slightly wider, as well as introducing a small, but finite trailing edge thickness. The trailing edge thickness was introduced for structural reasons, while the increase in thickness was to make it more similar to a normal ship with respect to width/length ratios. The original thickness of Eppler E836 is 12.6% of the length, while the new thickness is 16% of the length. The trailing edge thickness was set to 3.3 mm. This was expected to provide enough strength at the trailing edge, so that it would not break due to unfortunate events, but be small enough to not make a large difference in the results, compared to a perfectly thin trailing edge. The foil geometry in reference (Airfoil Tools) consists of discrete points with x and y coordinates. In order to introduce the finite trailing edge, the $y$ values of the trailing edge points were changed from zero to half the finite edge thickness. In order to scale the thickness, the $y$ values of the geometry was multiplied with $16/12.6 = 1.27$. In order to create a truly smooth geometry, rather than the discrete geometry in reference (Airfoil Tools), NURBS interpolation was used, with the commercial software “Rhinoceros” (Rhinoceros 3d Modeling Software). This was then used to create the two different 3D versions of the foil. For the sharp bottom edge version of the foil, the waterline geometry is simply extruded to make a 3D geometry with straight sides. The rounded bottom edge version of the foil was created by introducing a fillet radius at the bottom edge, which creates a circular arc instead of a sharp edge. The specific fillet radius used was constant for the entire foil, except close to the trailing edge. The fillet radius could not be larger than half the thickness of the foil profile, as there would be no room to make a circular arc if this was the case. The fillet radius of the rounded foil is therefore defined as the minimum of 0.1 m and half the thickness of the foil profile. This creates an almost linearly decreasing fillet radius towards the trailing edge. Fig. 2 shows both versions of the tested geometry, including dimensions.

The model was built by the MARINTEK workshop. A 5-axis milling machine, of the type Belotti MDL 12070, was used to carve out the geometry from divinycell foam, around an inner box structure of plywood. The sharp bottom edge version of the geometry was built and tested first, before the same model went in to the milling machine once more, to create the rounded bottom edge.

## 4. Experimental setup

The experiment was performed at the MARINTEK towing tank facilities (Marintek Towing Tank Facilities Description), located in Trondheim, Norway. The length and width of the towing tank is 260 m and 10.5 m respectively. The towing tank has two parts, the first part has a depth of 5.6 m, while the second part has a depth of 10 m. The model was mounted on a towing tank carriage, and the tests described in Section 4.1 was performed. Forces, moments, as well as movement of the model was measured, as described in Section 4.2. In order to move the model a hexapod system was used, which is described in Section 4.3. Finally, the results were post-processed, as described in Section 4.4. A picture of the model mounted in the towing tank with all the used equipment can be seen in Fig. 3.

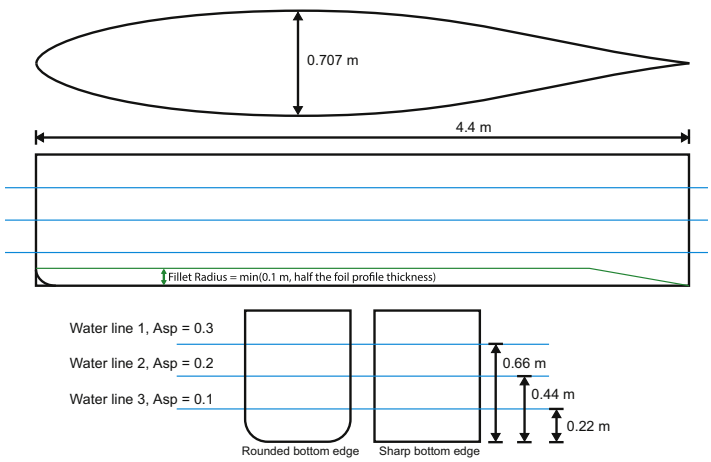


**Fig. 2.** Dimensions and shape of the tested model geometry.

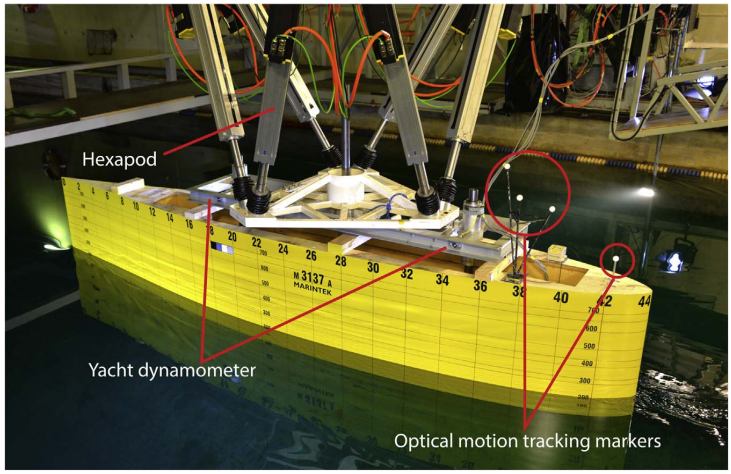


**Fig. 3.** Model with measurement equipment, mounted in the towing tank.

### 4.1. Performed tests

The sharp bottom edge version of the foil was tested first, and then the rounded bottom edge version. In addition, the sharp bottom edge version of the foil was used for uncertainty analysis (see Section 5). The following tests were performed:

- Each version of the foil was tested with 3 aspect ratios: 0.1, 0.2 and 0.3. The corresponding depth was 0.22 m, 0.44 m and 0.66 m. The depth of the model was changed by adding or removing weights. The largest depth was tested first.
- For each version of the foil, and each aspect ratio, 7 angles were tested: −5, −2.5, 0, 2.5, 5, 7–5 and 10 degrees. The reason for testing negative angles was so that it would be possible to correct the results for possible misalignment of the model in the post-processing (see Section 4.4 for more).
- Each towing tank run consisted of two speeds: $Fr=0.1$ and $Fr=0.2$, which gives carriage speeds equal to 0.657 m/s and 1.314 m/s respectively. Roughly half the tank was used for Froude number equal to 0.1, before the towing tank carriage was accelerated up to Froude number equal to 0.2.
- The uncertainty analysis was performed by testing the angles 2.5° and 7.5°, 9 times each. Both Froude numbers were used for both angles. The aspect ratio of the foil was 0.2.

The sharp bottom edge version of the foil was tested once for each angle. The rounded bottom edge version of the foil was tested twice for each angle, in order to decrease the uncertainty of the results. In total, neglecting test runs, 81 towing tank runs were performed, where each run consists of two speeds.

### 4.2. Measurement equipment

The force and moment measurements were done using a yacht dynamometer from the company Wolfson Unit (Wolfson Unit Towing Tank Dynamometers). The dynamometer contains two transducers for measurements of forces in the transverse direction, and one for measurements in the longitudinal direction. The yaw moment on the model is calculated by multiplying the value from each force transducer in the transverse direction with the correct arm. As the dynamometer is fixed to the model, the measurements happens in a ship fixed coordinate system. However, the results presented in this paper is transformed to a global coordinate system (see Section 4.4). The position of the model, represented by heave, roll, pitch and yaw, was measured using an optical motion capture system called “Oqus”, from the company Qualisys. Several infrared cameras, along with a computer system, was used to track the position of special markers attached to the model. The minimum requirement for the number of markers is three, however, four markers was used for increased accuracy. The position of the markers can be seen in Fig. 3. The measured data was then transmitted to computer system on board the towing tank carriage. The force measurements were collected with a frequency of 200 Hz, while the position measurements were collected with a frequency of 25 Hz. The low-pass filter frequency on the measurement system was 20 Hz. Speed and position of the towing tank carriage was also measured. In addition to the force and position measurements, cameras were used to take pictures of the model from both sides, for all the test runs. This was to provide information on the wave pattern around the model, mainly used for qualitative discussion (see Section 7).

### 4.3. Movement of model

The model was fixed to the towing tank carriage through the yacht dynamometer which again was fixed to a hexapod system. All types of movements were fixed, except for heave and pitch. The drift angle was altered using the hexapod system, consisting of 6 electrically actuated arms that could move the model based on user input. The control system allowed the user to specify the drift angle, and the hexapod system was supposed to take care of the movement automatically. However, the movement was experienced to not be very exact. Using the optical position measurement system as a reference, it was clear that going back and forth between two specific drift angles several times could lead to slight variations in the actual position of the model. Due to this, the position of the foil was always adjusted based on the measured position from the Qualisys optical measurements system. Tests were performed in order to see if rotation of the model caused any unwanted motion. The foil was moved to several drift angles, and sinkage, heel and trim was measured. The goal was that sinkage, heel and trim should be as small as possible. The result of this static motion test can be seen in Fig. 4. The motion detected in sinkage and trim was most likely due to friction in the bearings that keeps the model fixed in surge, sway, roll and yaw, but allows movement in heave and pitch. That is, the model was free to heave

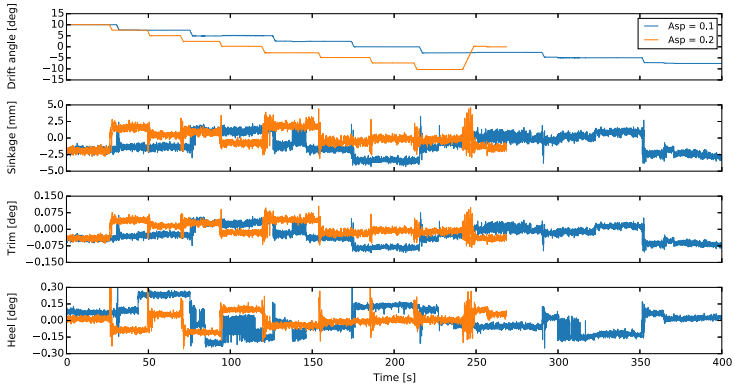


**Fig. 4.** Movement of model due to hexapod movement.

and pitch, but not necessarily perfectly free. The foil with the sharp bottom edge was tested, with two of the aspect ratios. As can be seen in the figure, only small unwanted motion did occur. This is expected to have a negligible effect on the overall results. The sinkage varied between $\pm 2.5$ mm, trim varied between roughly $\pm 0.075°$ while heel varied between $\pm 0.3°$.

### 4.4. Post-processing

The measured data was time dependent signals, of which only mean values were of interest. For a given run, two speeds were tested. In order to reach the target speed, the model was accelerated, which introduces time dependent variations in the forces. The average values of the measurements were taken over sections of constant speed, where time dependent variations in the forces had died out. The averaging was done in order to filter out the noise in the signals. A custom Python script was written to do this automatically, with manual visual control to ensure that the script did what it was supposed to do. The carriage speed measurements were analyzed in order to find sections of constant speed. This was done by first filtering out the noise from the measurements, before the derivative of the carriage speed was calculated numerically. Sections where the derivative was zero was defined as a constant speed section. In order to ensure that variations in the forces due to acceleration had died out, a buffer region on each side of the constant speed segment was used. Based on visual control of the raw data, a 2 s buffer region was considered sufficient. Fig. 5 shows the output from the post processing script, showing the segments of which average values were calculated, plotted on top of the raw data. This plot was also used when performing the visual control of the data.

There is high frequency noise in the signal. Based on spectral analysis of a few of the runs, it seems that the frequency of the noise is roughly 2 Hz. The frequency seems to be independent of the speed of the towing tank carriage, which suggests that this is most likely the resonant frequency of the model when connected to the carriage. The average values are taken over more than 50 s, which means that more than 100 oscillations are included, and this noise is therefore considered not to be a problem. After average values were taken from the raw data, the force measurements were transformed from a body fixed coordinate system, to a global coordinate system. The yacht dynamometer was fixed to the model, so that a rotation of the model meant a rotation of the force transducers as well. Lift and drag are defined as forces normal, and opposite to, the direction of travel, so that a transformation of the measurements was necessary. Fig. 6 shows the coordinate system used to present the results in this paper from a top view. The drift angle is defined such that a positive drift angle gives a positive force in the $y$-direction.

Each average force measurement represents a drift angle. As described in Section 4.1, drift angles equal to $-5°$, $-2.5°$, $0°$, $2.5°$, $5°$, $7.5°$ and $10°$ was tested for each speed and aspect ratio combination. However, these angles should be considered as the "target angles". The actual angle used as the representative drift angle in the presented results in this paper is the *measured drift angle* from the optical motion tracking system, with a slight correction.

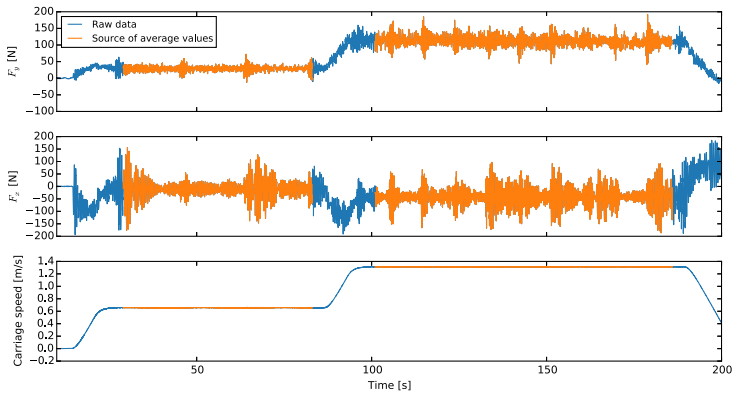


**Fig. 5.** Visualization of how the average values are calculated from the raw measured data.

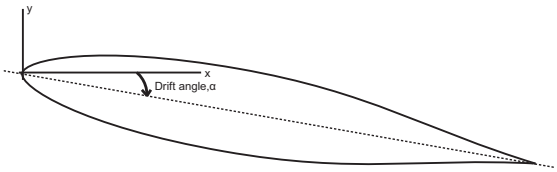


**Fig. 6.** Coordinate system used to present the result.

The model was positioned such that a zero-degree measured drift angle should correspond to a zero-degree actual drift angle. However, a perfect alignment of the model was difficult. In order to correct the measured drift angle, a zero-degree drift angle was defined as the position where the model had zero force in the y direction. The force measurements for all the measured drift angles was fitted to a second order equation, using least square curve fitting, from the Sci-Py library (Sci-Py Curve Fit). The equations used for the curve fitting was as follows:

$$F_y = a_0 + a_1\alpha + a_2\alpha|\alpha| \tag{6}$$

This is a second order equation, which was found to work well for the measured lift data in this experiment, as is can be seen in Section 6. The drift angle correction was then calculated as the drift angle which gives zero drift angle in Eq. (9). The drift angle correction was subtracted from all the measured drift angles. The value of the drift angle correction varied with the depth of the model, as well as bottom edge shape, but the largest correction was 0.44 degrees, which was used for the foil with the rounded bottom edge, at the largest depth. The mean of the absolute value of the drift angle correction for all the depths and both foils was 0.2°. The reason for the change in drift angle correction with both depth and bottom edge shape is probably due to the fact that the model was completely detached from the towing tank carriage during the removal of weights. This may have caused small changes in the exact position of the model. The drift angle correction should adjust the results so that this is not a problem. After extracting mean values of the measured forces, transforming the measurements to a global coordinate system, and correcting the measured drift angle, the final step was to calculate force coefficients and the center of pressure, which is the presented results in Section 6. The coefficients consist of lift ($C_L$), drag ($C_D$) and yaw moment ($C_M$). They are defined in the equations below. $F_x$ and $F_y$ are the forces in x and y direction and $M_z$ is the moment about the z-axis, in the global coordinate system defined in Fig. 6. $F'_y$ is the force in the y-direction in the body fixed coordinate system. $A$ equals the planform area of the foil, which is equal to the depth, $D$, multiplied by the length, $L$. $U$ is the speed, and $\rho$ is the density of the water. The value of $\rho$ used in the calculations of the coefficients was 1000 kg/m$^3$.

$$C_D = \frac{F_x}{0.5\rho AU^2} \tag{7}$$

$$C_L = \frac{F_y}{0.5\rho AU^2} \tag{8}$$

$$C_M = \frac{M_z}{0.5\rho ALU^2} \tag{9}$$

$$x_{cp} = \frac{M_z}{F'_y} \tag{10}$$

## 5. Experimental uncertainty

The error due to the random scattering in the measured values was quantified by calculating the precision limit of the measurements, following the method described in reference (Longo and Stern, 2005). 9 repeated tests were performed for the foil with the sharp bottom edge, with aspect ratio equal to 0.1, for two drift angles (2.5 and 7.5 degrees) and two Froude numbers (0.1 and 0.2). For each drift angle and speed combination, the model was first positioned at the right drift angle using the hexapod system. Then all the repeated tests were performed without moving the model. This was based on the assumption that the model and hexapod would not move during the repeated tests. Although the hexapod movement itself was considered to be inaccurate, the hexapod seemed to be very rigid, once positioned. All measured values were post-processed in the same way as described in Section 4.4. Then the precision limit where calculated as follows:

With N repeated test (for this case, $N=9$), the mean value of the measured variable $X$ is calculated:

$$\bar{X} = \frac{1}{N}\sum_{i=1}^{N} X_i \tag{11}$$

The standard deviation, $S_X$, is then estimated:

$$S_X = \sqrt{\frac{1}{N-1}\sum_{i=1}^{N}\left(X_i - \bar{X}\right)^2} \tag{12}$$

Assuming that the measured variable will have errors that follow a normal distribution, the precision limit for a single measurement ($P_X$), as well as the precision limit for the average value ($P_{\bar{X}}$), can be estimated with the Students t-distribution (Student, 1908) as follows:

$$P_X = tS_X \tag{13}$$

$$P_{\bar{X}} = \frac{P_X}{\sqrt{N}} \tag{14}$$

The precision limit represents a confidence interval. If the precision limit is calculated based on a 95% confidence interval there will be a 95% chance that the true value, excluding bias limits, will be within the interval $X \pm P_X$. $t$ is the coverage factor, which can be calculated based on the inverse cumulative density function ($F^{-1}$) of the Students t-distribution:

$$t = F^{-1}\left(\frac{1}{2}\left(1+\gamma\right), N-1\right) \tag{15}$$

The software library SciPy (Scipy Student's T-distribution) was used to calculate the value of $t$. With $N=9$ and $\gamma = 0.95$, $t=2.3$. The result of the uncertainty analysis, for all the variables of interest can be seen in Tables 1 and 2. For each variable, the mean value, the absolute value of the precision limit, as well as the relative value of the precision limit in percentage of the mean value is reported.

The relative precision limits vary, depending on both speed and drift angle. However, the difference in the absolute values of the precision limits are considered to be small. The results presented in Section 6 are plotted with error-bars, in order to visualize the uncertainty of the data. The chosen value for the uncertainty is then the largest absolute value for each variable in Tables 1 and 2 for the foil with the sharp bottom edge, while the uncertainty for the foil with the round bottom edge is corrected due to the fact that it is based on an average value of two measurements. That is, the precision limit for the foil with the round bottom edge is calculated to be the precision limit for the foil with the sharp bottom edge, divided by the square root of two, as is fitting with

**Table 1**
Precision limits, drift angle 2.5 deg.

| Variable | $Fr=0.1$ | | | $Fr=0.2$ | | |
|---|---|---|---|---|---|---|
| | $\bar{X}$ | $P_X$ | $100{\cdot}P_X/\bar{X}$ | $\bar{X}$ | $P_X$ | $100{\cdot}P_X/\bar{X}$ |
| $U$ | 6.574e−01 | 9.766e−05 | 0.015 | 1.314e+00 | 7.021e−05 | 0.005 |
| $C_D$ | 2.502e−02 | 1.023e−03 | 4.090 | 2.607e−02 | 3.066e−04 | 1.176 |
| $C_L$ | 3.269e−02 | 4.316e−03 | 13.203 | 3.258e−02 | 1.926e−03 | 5.910 |
| $C_M$ | 7.403e−03 | 1.021e−03 | 13.794 | 6.486e−03 | 2.808e−04 | 4.330 |
| Sinkage | −2.410e−03 | 1.217e−03 | −50.491 | 3.563e−04 | 2.767e−03 | 776.422 |
| Drift angle | 2.542e+00 | 4.566e−02 | 1.796 | 2.621e+00 | 1.121e−01 | 4.275 |
| Trim | −1.683e−01 | 3.251e−02 | −19.315 | −4.908e−01 | 7.336e−02 | −14.948 |
| $x_{cp}$ | 9.646e−01 | 1.612e−02 | 1.671 | 8.459e−01 | 2.724e−02 | 3.220 |

**Table 2**
Precision limits, drift angle 7.5 deg.

| Variable | $Fr=0.1$ | | | $Fr=0.2$ | | |
|---|---|---|---|---|---|---|
| | $\bar{X}$ | $P_X$ | $100{\cdot}P_X/\bar{X}$ | $\bar{X}$ | $P_X$ | $100{\cdot}P_X/\bar{X}$ |
| $U$ | 6.574e−01 | 2.378e−05 | 0.004 | 1.314e+00 | 2.248e−05 | 0.002 |
| $C_D$ | 3.618e−02 | 7.475e−04 | 2.066 | 3.756e−02 | 3.748e−04 | 0.998 |
| $C_L$ | 9.859e−02 | 5.412e−03 | 5.489 | 9.805e−02 | 2.083e−03 | 2.124 |
| $C_M$ | 2.367e−02 | 1.535e−03 | 6.485 | 1.944e−02 | 5.375e−04 | 2.765 |
| Sinkage | −2.906e−04 | 4.865e−04 | −167.372 | 1.520e−03 | 6.153e−04 | 40.486 |
| Drift angle | 7.569e+00 | 2.449e−02 | 0.324 | 7.680e+00 | 9.508e−03 | 0.124 |
| Trim | −1.344e−01 | 1.394e−02 | −10.367 | −5.611e−01 | 1.877e−02 | −3.346 |
| $x_{cp}$ | 1.016e+00 | 1.541e−02 | 1.517 | 8.369e−01 | 8.354e−03 | 0.998 |

Eq. (14). In addition to precision limits, there are always risk of bias errors, due to systematic errors in the experiment. This can for instance be due to wrong calibration of sensors or errors in the construction of the model. A complete estimation of the potential bias limit for this experiment is not done, due to lack of necessary information. However, the uncertainty of the motion variables presented in Section 6 has been calculated with additional considerations. The measurements of sinkage and trim was considered to have uncertainties due to the unwanted motion caused by the hexapod system. The combined uncertainty ($E$) of both precision limits and unwanted hexapod motion ($E_{\text{hexapod}}$) is calculated with "root sum square" as described in reference (Longo and Stern, 2005):

$$E = \sqrt{P_X^2 + E_{\text{hexapod}}^2} \tag{16}$$

As shown in Section 4.3, the hexapod caused unwanted sinkage that could be as large as ±2.5 mm and unwanted trim that could be as large as $\pm 0.075°$. Combining these values with the largest precision limits in Tables 1 and 2 predicts the uncertainty in the sinkage to be 3.7 mm and the uncertainty in the trim to be 0.17°.

In addition, the values for the center of pressure is believed to be more uncertain than what Tables 1 and 2 suggest. The largest calculated uncertainty is 2.7 cm, or 3.22%. However, by looking at Fig. 12 in Section 6, this seems to be a too optimistic estimate. The center of pressure is varying quite a bit more than 2.7 cm between positive and negative drift angles with the same magnitude. The exact reason why this happens is unclear, but one hypothesis is that this has something to do with the turbulence level in the towing tank. The exact location of the center of pressure might be very dependent on the turbulence level, as this can affect exactly how the flow separates around the model. The negative drift angles were always tested before the positive drift angles, and it was usually after a long break, such as an entire night. The time between towing tank runs in general was roughly 20 min. The exact time was chosen so that any disturbances on the free surface had time to die out. However, the fact that the free surface is calm does not necessarily mean that there is no background turbulence in the water. Perhaps the first runs in the towing tank had considerably lower levels of turbulence than the later runs, and this had an effect on the center of pressure. Arguments for this hypothesis is that the biggest variation is seen for lowest speed and the foil with the rounded bottom edge, which should be most affected by any background turbulence. If this is the case, the variation in the results shown in Fig. 12 is not due to uncertainty in the measurements, but rather due to the uncertainty in the turbulence level in the towing tank, which is unknown. The uncertainty in the center of pressure is off-course really an uncertainty in the moment measurements and/or in the side force measurements. However, the result of the uncertainty is much more visible for the center of pressure than for the lift and moment coefficients.

## 6. Experimental results

In this section the experimental results are presented. Coefficients for lift, drag and yaw moment are plotted. The actual measurements are plotted as dots with error-bars. The error-bars correspond to the estimated uncertainty described in Section 5. In addition to the actual measurements, least-square curve fitting is used to fit the data to a polynomial function. The curve fitting is done with Python and the SciPy library (Sci-Py Curve Fit). The polynomial function is plotted along with the measurements, and the polynomial coefficients are given in tables, so that numerical values for arbitrary drift angles can be extracted. The exact shape of the polynomial function is chosen based on trial and error, with some assumptions based on the simplified models in Section 2. Both positive and negative drift angles are used. In order to quantify how well the polynomial functions fit the measured data, the difference between the measured data and the polynomial function are calculated for all the measured drift angles. The average value of the difference between them is presented with the variable $\epsilon_{average}$ in the tables. For the lift and drag coefficients,

**Table 3**
Coefficients for the lift polynomial function defined in Eq. (17), based on the experimental data.

| Edge shape | Asp | $a_1$ | | $a_2$ | | $100 \cdot \frac{\epsilon_{average}}{C_L(\alpha=5)}$ | |
|---|---|---|---|---|---|---|---|
| | | $Fr=0.1$ | $Fr=0.2$ | Fr=0.1 | $Fr=0.2$ | $Fr=0.1$ | $Fr=0.2$ |
| Sharp | 0.1 | 7.675e−03 | 7.769e−03 | 1.578e−04 | 1.905e−04 | 2.584 | 3.357 |
| Sharp | 0.2 | 1.184e−02 | 1.165e−02 | 1.600e−04 | 1.895e−04 | 2.390 | 1.855 |
| Sharp | 0.3 | 1.355e−02 | 1.357e−02 | 2.625e−04 | 2.860e−04 | 6.103 | 1.442 |
| Round | 0.1 | 3.637e−03 | 3.747e−03 | 8.985e−05 | 8.089e−05 | 1.918 | 1.498 |
| Round | 0.2 | 5.188e−03 | 5.411e−03 | 2.158e−04 | 2.631e−04 | 5.755 | 2.656 |
| Round | 0.3 | 7.700e−03 | 7.461e−03 | 2.961e−04 | 3.581e−04 | 4.710 | 2.134 |

comparisons with theoretical models have been plotted in separate figures. The center of pressure is calculated based on the measured yaw moment, in order to compare it with the quarter chord linear foil theory. Motion measurements are also presented, although it must be noted that the relative uncertainty for these measurements are quite high. This is in part due to the relatively small values of the measurements. Lastly, a series of pictures of the wave field around the model is presented. This is used for qualitative discussion.

### 6.1. Lift

The polynomial function for lift as a function of drift angle is chosen as follows:

$$C_L(\alpha) = a_1 \cdot \alpha + a_2 \cdot \alpha|\alpha| \tag{17}$$

The values of the coefficients in this function can be seen in Table 3. Fig. 7 shows a plot of the result. The solid lines are the polynomial function. The uncertainty for a single measurement for the lift coefficient is 5.3e−3, while the error for the drift angle is 1.12e−1.

Eqs. (3) and (4) have been used to calculate the lift for the model based on large aspect ratio elliptic wing theory and low aspect ratio slender body theory. For each aspect ratio, the lift for the sharp foil, rounded foil, large aspect ratio theory and low aspect ratio theory is plotted. The result can be seen in Fig. 8. Only experimental values for Fr=0.1 is plotted, as Fig. 7 shows that there is very small difference between $Fr=0.1$ and $Fr=0.2$. The theories predict linear lift as a function of drift angle. As can be seen in the figure, the low aspect ratio theory only seems to fit the data for the rounded foil with aspect ratio equal to 0.3 and 0.2, for small drift angles. For the two smallest aspect ratios, the sharp bottom edge version of the foil have a larger lift than what elliptic wing theory predicts, even for small drift angles. The difference between the sharp bottom edge version of the foil, and the rounded bottom edge version of the foil is significant. The sharp bottom edge version of the foil has much larger lift. The linear coefficient, $a_1$, for the sharp bottom edge version of the foil, for aspect ratios 0.1, 0.2 and 0.3 is 110.8%, 111.2% and 76.1% higher compared to the rounded bottom edge version of the foil. The second order coefficient, $a_2$, is 75.5%, −15.2% and −11.5% higher. That is, the non-linear lift for the sharp bottom edge version of the foil is actually smaller for two of the aspect ratios, but the linear lift is much larger for all the aspect ratios.

### 6.2. Drag

The polynomial function for drag as a function of drift angle is chosen as follows:

$$C_D(\alpha) = a_0 + a_2 \cdot \alpha^2 \tag{18}$$

The values of the coefficients in this function can be seen in Table 4. Fig. 9 shows a plot of the results. The solid lines are the polynomial function. The uncertainty for a single measurement for

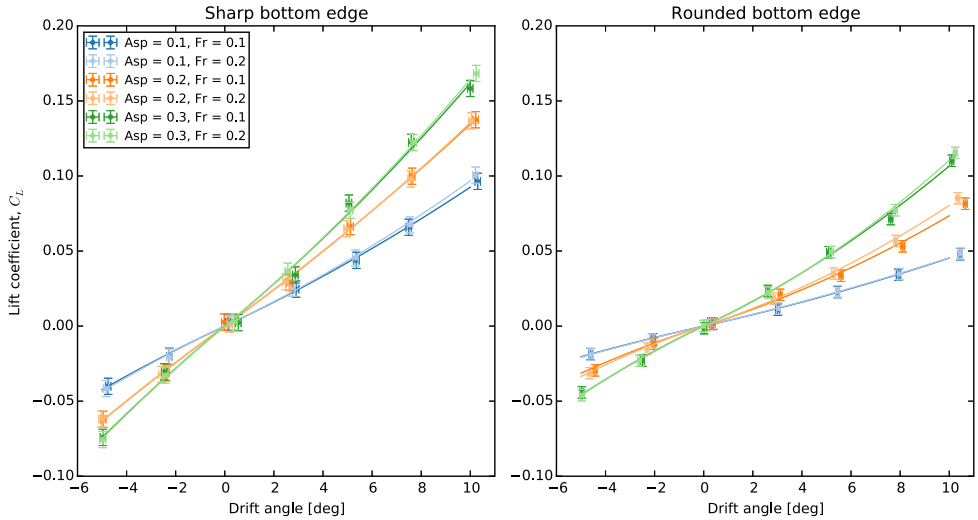


**Fig. 7.** Lift coefficient, $C_L$, defined in Eq. (8), as a function of drift angle. Measurements are shown as dots, with estimated uncertainty as error bars. The lines show the polynomial function defined in Eq. (17).

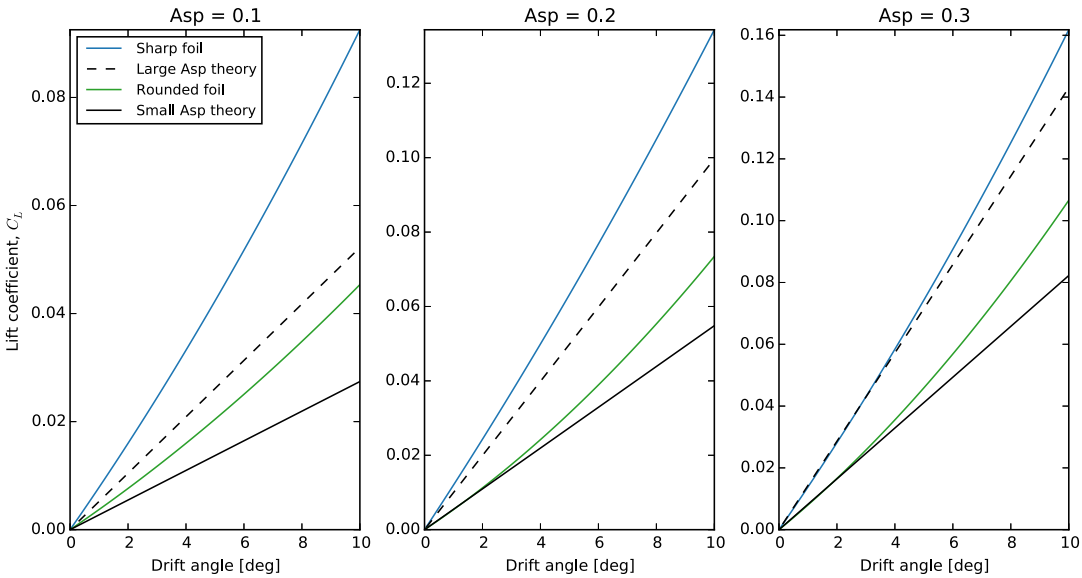


**Fig. 8.** Measured lift compared to theoretical lift. The large and small aspect ratio theories are defined in Eqs. (3) and (4) respectively. The Froude number for the experimental values is 0.1.

the drag coefficient is 7.48e−3, while the error for the drift angle is 1.12e−1.

For the smallest aspect ratio, there is a bigger difference between Froude number 0.1 and 0.2 than it is for the larger aspect ratios. The explanation is probably that the importance of the wave resistance is smaller for the larger aspect ratios, and that the friction resistance coefficient becomes smaller at larger speeds. For the larger aspect ratios, much more of the foil is far beneath the free surface. This suggest that the friction resistance is much more important for the larger aspect ratios compared to the smallest aspect ratio. When the Froude number increases, the wave resistance goes up, but the friction resistance coefficient goes down. That is, for the largest aspect ratio, the increase in the wave resistance coefficient seems to be almost perfectly canceled by the decrease in the friction resistance coefficient.

Eq. (5) has been used to calculate the lift induced drag theoretically. The experimental lift induced drag is calculated with the polynomial function as the drag at a the wanted drift angle, minus the drag when the drift angle is zero. Lift-induced drag as a function of lift coefficient is plotted in Fig. 10. The experimental lift induced drag for the foil with the sharp bottom edge is lower than the theoretical lift induced drag for an elliptic large aspect ratio wing. The lift induced drag as a function of lift coefficient is lower for the sharp bottom edge version of the foil, than it is for the rounded bottom edge version of the foil. There is only a small difference between the lift induced drag for $Fr=0.1$ and $Fr=0.2$.

### 6.3. Yaw moment

The polynomial function for yaw moment as a function of drift angle is chosen as follows:

$$C_M(\alpha) = a_1 \cdot \alpha + a_2 \cdot \alpha|\alpha| \tag{19}$$

The values of the coefficients in this function can be seen in Table 5. Fig. 11 shows a plot of the result. The solid lines are the polynomial function. The uncertainty for a single measurement for the yaw moment coefficient is 1.54e−3, while the error for the drift angle is 1.12e−1.

When looking at the results in Fig. 11 one should note that the polynomial model does not fit the experimental results very well for $\alpha = 2.5$ for the rounded bottom edge version of the foil. Higher order polynomials were tried, without great success, and since this problem is mainly for the smallest drift angle, with the rest of the values captured well, the second order polynomial model was kept. In order to compare the yaw moment to linear foil theory, the center of pressure is plotted in Fig. 12. The center of pressure is

**Table 4**
Coefficients for the drag polynomial function defined in Eq. (18), based on the experimental data.

| Shape | Asp | $a_0$ | | $a_2$ | | $100 \cdot \frac{c_{average}}{C_D(\alpha=5)}$ | |
|---|---|---|---|---|---|---|---|
| | | $Fr=0.1$ | $Fr=0.2$ | $Fr=0.1$ | $Fr=0.2$ | $Fr=0.1$ | $Fr=0.2$ |
| Sharp | 0.1 | 3.181e−02 | 3.536e−02 | 1.690e−04 | 1.883e−04 | 0.648 | 0.289 |
| Sharp | 0.2 | 2.398e−02 | 2.434e−02 | 2.206e−04 | 2.325e−04 | 1.252 | 0.731 |
| Sharp | 0.3 | 1.922e−02 | 1.928e−02 | 2.359e−04 | 2.587e−04 | 2.398 | 0.318 |
| Round | 0.1 | 1.679e−02 | 1.917e−02 | 8.584e−05 | 9.576e−05 | 0.759 | 0.651 |
| Round | 0.2 | 1.240e−02 | 1.290e−02 | 1.335e−04 | 1.483e−04 | 3.206 | 1.722 |
| Round | 0.3 | 1.098e−02 | 1.080e−02 | 1.624e−04 | 1.777e−04 | 2.710 | 2.794 |

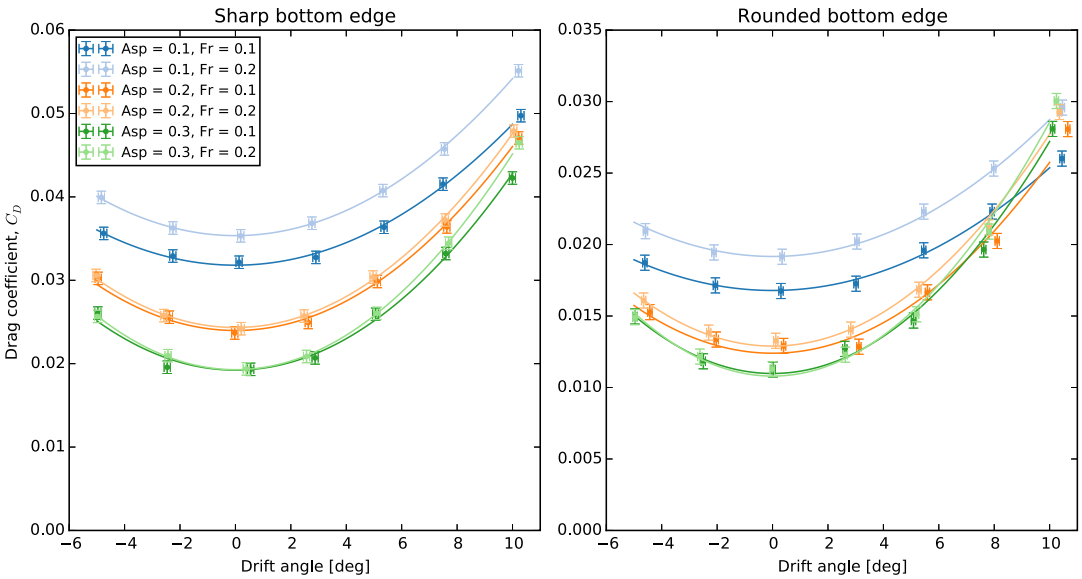


**Fig. 9.** Drag coefficient, $C_D$, defined in Eq. (7), as a function of drift angle. Measurements are shown as dots, with estimated uncertainty as error bars. The lines show the polynomial function defined in Eq. (18).

generally in front of quarter chord. The rounded bottom edge version of the foil shows much more variation in the location of the center of pressure compared to the sharp bottom edge version of the foil. Both Froude number and drift angle affects the exact location. The yaw moment itself also shows a difference between the two Forude numbers. As the lift force is almost identical for the two Froude numbers, the difference in the yaw moments must be explained by a shift in the center of pressure alone. As discussed in Section 5, the predicted uncertainty for $x_{cp}$ are not that high, but the fact that there is a large difference in the result for positive and negative drift angles suggest that the actual uncertainty is higher than what is predicted. This is important to consider when comparing values from for instance (CFD) simulations.

### 6.4. Motion measurements

The measured sinkage and trim of the model is presented in this section. No polynomial model of sinkage and trim as a function of drift angle is made. The reason is, as can be seen in Figs. 13 and 14, that the relative uncertainty of the data is much larger

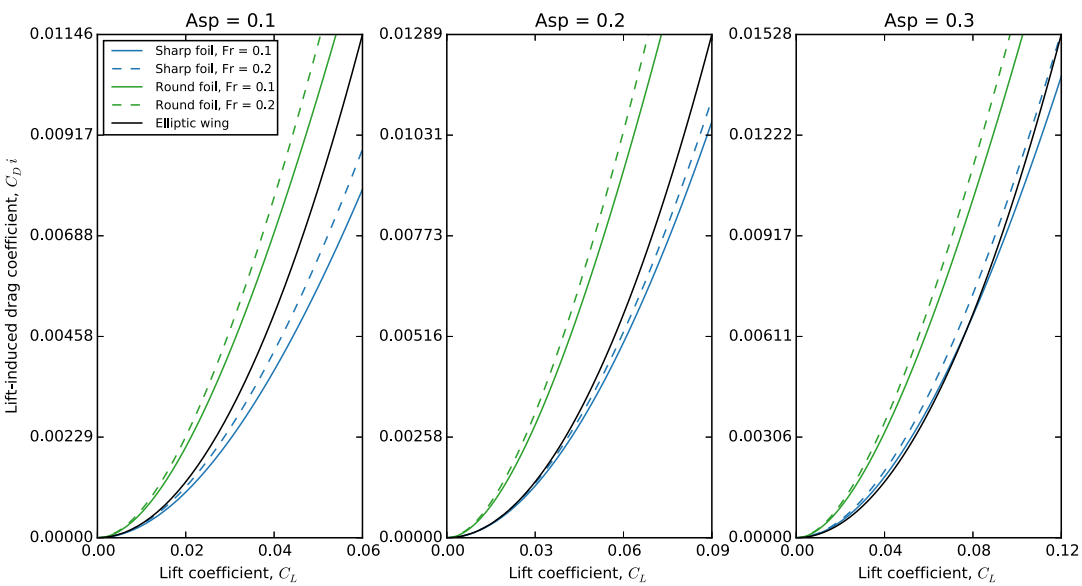


**Fig. 10.** Measured lift induced drag compared to theoretical lift induced drag calculated by Eq. (5), as a function of lift coefficient. The measured lift induced drag is calculated by subtracting the drag at zero drift angle from the total drag.

**Table 5**
Coefficients for the yaw moment polynomial function defined in Eq. (19), based on the experimental data.

| Edge shape | Asp | $a_1$ | | $a_2$ | | $100 \cdot \frac{\epsilon_{average}}{C_{M,Z}(\alpha = 5)}$ | |
|---|---|---|---|---|---|---|---|
| | | $Fr = 0.1$ | $Fr = 0.2$ | $Fr = 0.1$ | $Fr = 0.2$ | $Fr = 0.1$ | $Fr = 0.2$ |
| Sharp | 0.1 | 1.379e−03 | 1.031e−03 | 1.010e−04 | 1.095e−04 | 6.637 | 10.122 |
| Sharp | 0.2 | 2.079e−03 | 1.784e−03 | 1.439e−04 | 1.198e−04 | 2.958 | 4.525 |
| Sharp | 0.3 | 2.254e−03 | 1.878e−03 | 1.589e−04 | 1.662e−04 | 5.148 | 0.745 |
| Round | 0.1 | 4.800e−04 | 4.976e−04 | 8.263e−05 | 6.566e−05 | 7.399 | 7.210 |
| Round | 0.2 | 1.309e−05 | −2.512e−04 | 1.758e−04 | 2.000e−04 | 17.526 | 14.963 |
| Round | 0.3 | −6.689e−05 | −4.034e−04 | 2.334e−04 | 2.476e−04 | 12.925 | 9.654 |

than the relative uncertainty for the forces, and it is difficult to see a clear pattern in the results. The combined uncertainty of precision limits and hexapod motion for sinkage is estimated to be 3.7 mm and for trim it is estimated to 0.17°. Many of the runs have measured sinkage and trim which is at the same order of magnitude as the uncertainty. The data in Figs. 13 and 14 must therefore be used with care. The measured values of sinkage and trim is in general larger for Froude number equal to 0.2 than it is for Froude number equal to 0.1. The maximum magnitude of the trim is around 0.5°, while most of the measured sinkage values are below 1 cm, with a few exceptions that goes as high as 2.5 cm.

### 6.5. Wave observations

Cameras located on both sides of the model were used to take pictures from both sides at the same time, during the experiment. The intention was to see how the waves along the model changed as a function of drift angle. The pictures for the foil with the sharp bottom edge and both aspect ratio and Froude number equal to 0.2 can be seen in Fig. 15. The general tendency is that the waves on the suction side of the foil becomes larger with increasing drift angle, while the waves on the pressure side gets smaller. For the largest drift angle, there is almost no waves at the pressure side of the foil, but large waves at the suction side. The result was very similar for all the other aspect ratios as well. For Froude number equal to 0.1, there was almost no waves at all, even with drift angles. There was no observed separation from the leading edge. The free surface seemed to remain smooth around the leading edge, even at the largest drift angle, and there were no ventilation or other visible violent disturbances in the flow.

## 7. Discussion

The results show that the aspect ratio of the foil is an important parameter for the drift-induced forces. Slender body theory predicts the lift to be linearly dependent on the aspect ratio of the ship, but by looking at Fig. 8, it is clear that slender body theory does not work as a general equation for estimating the lift on the geometries tested in this experiment. The equation compares well with the rounded bottom edge version of the foil, at least for the two largest aspect ratios, but for the sharp bottom edge version of the foil, the lift predicted by slender body theory is too small. However, the importance of the aspect ratio is clearly visible in the results, as seen in Fig. 7. It is interesting to note that elliptic wing theory for lift seems to accurately predict the lift for the foil with the largest aspect ratio and sharp bottom edge. However, as the equation only fits one version of the foil, it is not enough to make any definitive statement of the validity of elliptic wing theory for aspect ratios around 0.3. Elliptic wing theory does not fit any of the other foils, which, due to its assumptions of large aspect ratio, is not very surprising.

At least for the smallest Froude number, the free surface should have a negligible effect on the lift. At Froude number equal to 0.1,

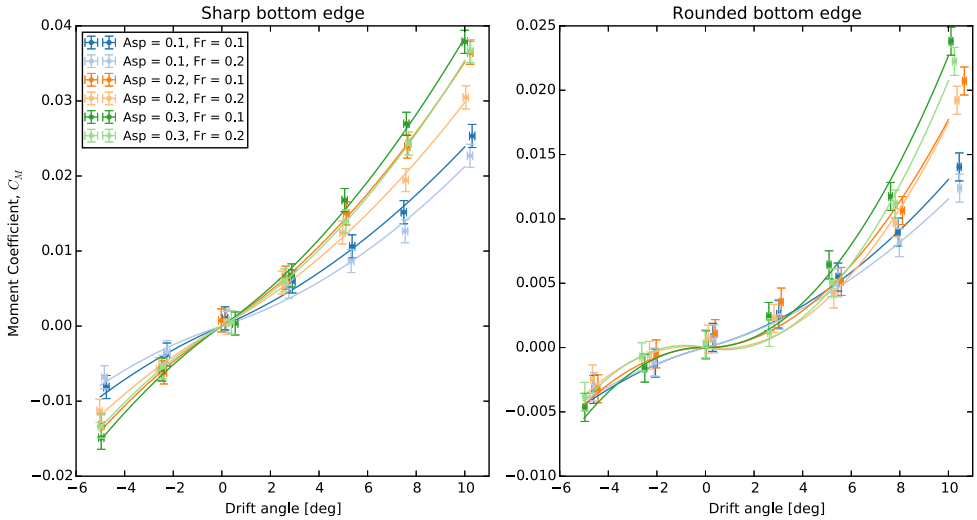


**Fig. 11.** Yaw moment coefficient, $C_M$, defined in Eq. (9), as a function of drift angle. Measurements are shown as dots, with estimated uncertainty as error bars. The lines show the polynomial function defined in Eq. (19).

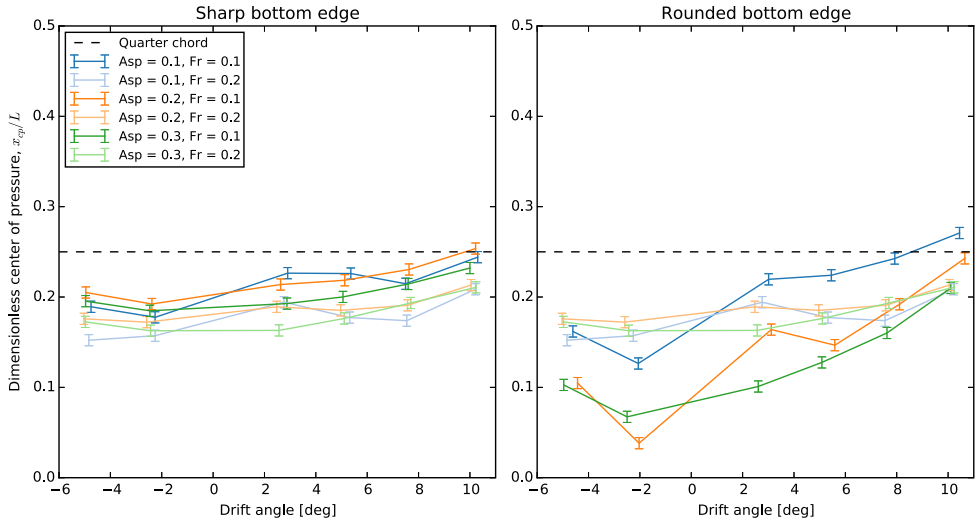


**Fig. 12.** Center of pressure calculated with Eq. (10). The predicted result from linear foil theory, which is the quarter chord, is shown for comparison.

the free surface was almost completely flat around the model. The fact that the lift on the sharp bottom edge version of the foil differs so much from slender body theory therefore seems to have only two possible explanations: either there is more lift created due to the separation at the trailing edge than what slender body theory predicts, or there are significant cross-flow effects, even at drift angles as small as 2.5°. When the cross-flow velocity is large, simple theory predicts that cross-flow lift is proportional to the drift angle squared. This suggests that slender body theory should work for very small drift angles, and that cross-flow only becomes important for larger drift angles. However, as discussed in Section 2, for small cross-flow velocities, which is the case for small drift angles, the physics becomes much more complicated, and it is harder to make general conclusions of the importance of cross-flow. The sharp bottom edge might force separation at the bottom edge, and therefor cross-flow, even at very small drift angles, which would explain the large difference in the measured lift between the two bottom edge shapes. Reference (Tian et al., 2014) shows numerical results for the flow normal to a flat plate. The importance of the curvature of the edges of the flat plate is studied, and it is clear that a smaller radius creates flow separation more easily. A completely sharp edge, as used in this experiment, should cause separation very easily. The other option is that the very thick foil tested in this experiment have a span efficiency factor larger than one. The reduction in lift due to 3D effects in potential flow can be explained by non-separating flow around the wing tip, or bottom edge, of the lifting surface. The sharp bottom edge, in combination with the very large thickness of the foil might make it harder for the flow to move around the bottom edge. Although, separating the cross-flow effect from the potential tip vortices, are a bit artificial. The large amount of lift observed for the sharp bottom edge version of the foil could be due to a combination. The separation at the bottom edge of the ship could cause a reduction in the strength of the tip vortex.

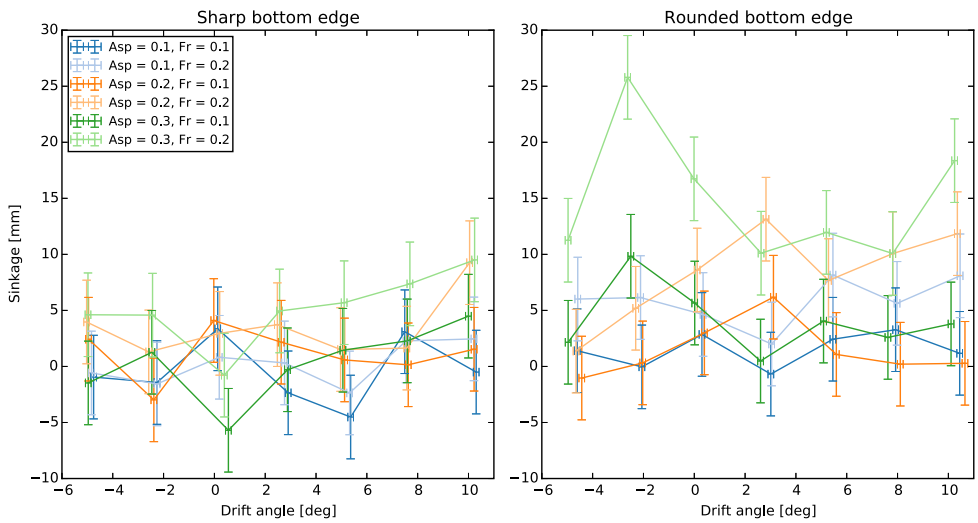


**Fig. 13.** Measured sinkage.

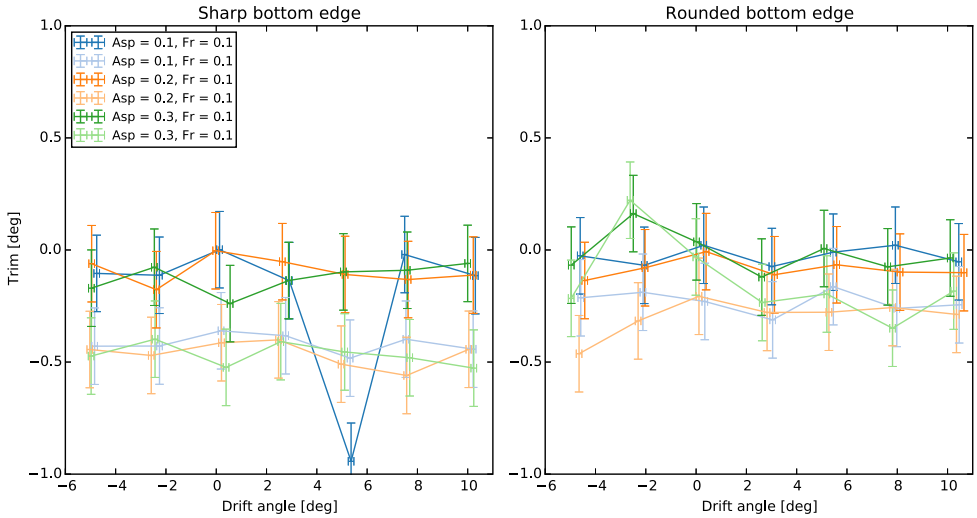


**Fig. 14.** Measured trim.

Nonetheless, the large difference between the sharp bottom edge version of the foil and the rounded bottom edge version of the foil was somewhat surprising. Although it was expected that there would be a difference at the larger drift angles, it was also expected that the result for the sharp and rounded bottom edge should be about the same for the smaller drift angles. By just rounding the bottom edge of the foil with a fillet radius of 0.1 m, roughly half of the lift is lost, even at drift angles as small as 2.5°. Another way of looking at this could be that one can double the lift produced from a ship hull by introducing a sharp bottom edge.

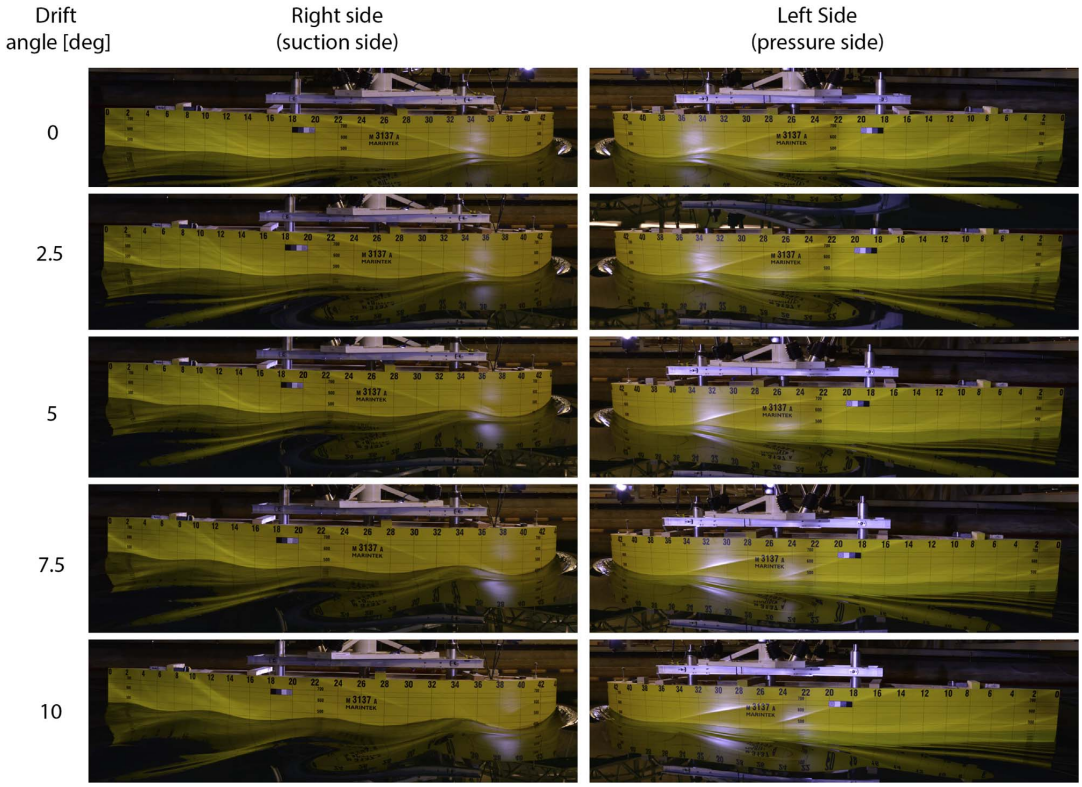


**Fig. 15.** Wave pattern on both sides of the model for different drift angles. The Froude number is 0.2 and the aspect ratio is 0.2.

This suggests that for instance bilge keels will be very important to consider if one is interested in the lift forces on a ship. However, there might be significant Reynolds number effects which are not visible in the experimental data presented in this paper. Since the boundary layer will be very different in full scale, the way the flow separates could also be different. Separation around the bottom edge could happen for smaller drift angles for a full scale ship, so that the difference between a sharp and round bottom edge could be smaller. While there is uncertainty regarding the importance of cross-flow for the smaller drift angles, it is clear that cross-flow is present for the larger drift angles, based on the fact that the lift coefficient as a function of drift angle is non-linear. For instance, the lift for the rounded bottom edge version of the foil fits well with slender body theory for the two largest aspect ratios when the drift angles are small, but as the drift angle increases, the difference between experimental results and theory becomes larger. This must be cross-flow effects.

The shape of the bottom edge also affects the drag. The sharp bottom edge version of the foil has much higher drag at zero drift angle. However, if the lift-induced drag is plotted as a function of lift coefficient, as is done in Fig. 10, it is seen that the sharp bottom edge version of the foil creates less lift-induced drag for the same amount of lift. In a sense, both the increase in lift and the decrease in lift-induced drag means that the foil with the sharp bottom edge acts like a foil with higher effective aspect ratio than the foil with the rounded bottom edge. It is interesting to note that the potential elliptic wing theory predicts higher lift-induced drag than what is actually measured for the sharp bottom edge version of the foil, for the two smallest aspect ratios. An elliptic wing is considered the optimal planform for a planar wing, in terms of minimizing the lift-induced drag, and it is also known that the potential lift-induced drag is only one part of the total lift-induced drag. Viscous effects could be very important too. The fact that it is possible to have less lift-induced drag for a planar lifting surface than the elliptic wing theory predicts is therefore surprising. Although the comparison with elliptic wing theory is interesting, it is again artificial. The separation of lift-induced drag and cross-flow is not necessarily valid, and as already mentioned, it seems reasonable to assume that tip vortices will be affected by cross-flow. One possible way of studying this topic further would be to simulate the same case with different strategies. By modeling a pure potential flow, with separation at the trailing edge only, for instance with a BEM code, it would be possible to check if the separation at the bottom edge has anything to do with the result. If a full viscous simulation method is necessary to reproduce the results, it would suggest that the separation at the bottom edge is an important factor.

Two Froude numbers were tested in order to see how this would affect the results. For Froude number equal to 0.2, surface waves were produced by the foil and the resistance was increased due to wave resistance. However, lift and lift-induced drag was not very much affected by the change in Froude number. During the experiment it was observed that the waves on the suction side of the foil would increase as the drift angle increased, while the waves at the pressure side would decrease. As the lift-induced drag was roughly the same for the two Froude numbers, the energy in the waves produced by the foil should be roughly the same for all drift angles. This suggest that the waves on the suction side should increase roughly as much as the waves on the pressure side decreases. More Froude numbers and more ship geometries should be tested in order to see if this is a general phenomenon. The yaw moment on the foil differs much more between the two Froude numbers tested. If one assumes that the yaw moment is primarily due to the lift force, the conclusion is that the center of pressure moves when the Froude number changes. That is, even if the free surface deformation does not change the amount of lift on the foil, it changes the distribution of lift on the foil significantly. The center of pressure is located ahead of the quarter chord for almost all the measurements, but is seen to vary as function of both speed and drift angle. The foil with the sharp bottom edge has much less variation in center of pressure than the foil with the rounded bottom edge, as can be seen in Fig. 12. The center of pressure is also, in general, located closer to the quarter chord. However, the variation in center of pressure for positive and negative drift angles are puzzling. The estimated uncertainty in the measurements does not explain the large difference. As discussed in Section 5, the explanation could have something to do with the turbulence level in the towing tank, which implies that the center of pressure is very sensitive to background turbulence when the speed is low, the drift angles are small, and the foil has a round bottom edge.

## 8. Conclusion

In this paper, the drag and lift forces, as well as yaw moment, for a ship-like foil is presented for three aspect ratios, two Froude numbers and two different bottom edge shapes. The results from the experiments are fitted to polynomials and compared to simplified models of lift and lift induced drag. The polynomial coefficients are presented in tables, so that the results from this experiment can be used to validate simulations. Estimation of the precision limit of the results are calculated based on repeated tests. Simplified models does not predict the forces on the foil very accurately. Slender body theory does not predict the lift correctly, and the lift-induced drag is seen to be smaller than the equation for an elliptic wing in some of the cases. Both the aspect ratio and the shape of the bottom edge are very important parameters for the magnitude of the forces acting on the foil. The difference in lift and lift-induced drag between Froude numbers 0.1 and 0.2 is very small, while the yaw moment is much more different for the two Froude numbers. The latter is explained by a shift in the center of pressure, caused by the free surface deformation.

## Acknowledgments

We would like to thank the Research Council of Norway, DNV GL and Rolls-Royce Marine AS for funding this research through the research program called “Low Energy and Emission Design of Ships” (LEEDS) (Grant no. 216432/O70) at the Department of Marine Technology, NTNU.

## References

Airfoil tools – Eppler e836 Hydrofoil Airfoil (e836-il), ⟨http://airfoiltools.com/airfoil/details?airfoil=e836-il⟩.
Anderson, J.D. Jr, 1985. Fundamentals of Aerodynamics, Tata McGraw-Hill Education, Singapore.
Faltinsen, O., 1993. Sea Loads on Ships and Offshore Structures Vol. 1. Cambridge University Press, Melbourne, Australia.
Faltinsen, O.M., 2005. Hydrodynamics of High-Speed Marine Vehicles. Cambridge University Press, New York, USA.
IHS, Ihs, Sea-web Ship Database, ⟨http://www.sea-web.com⟩.
Kroo, I. Nonplanar wing concepts for increased aircraft efficiency, VKI Lecture Series on Innovative Configurations and advanced Concepts For Future Civil Aircraft.
Kume, K., Hasegawa, J., Tsukada, Y., Fujisawa, J., Fukasawa, R., Hinatsu, M., 2006. Measurements of hydrodynamic forces, surface pressure, and wake for obliquely towed tanker model and uncertainty analysis for cfd validation. J. Mar. Sci. Technol. 11 (2), 65–75.
Longo, J., Stern, F., 2005. Uncertainty assessment for towing tank tests with example for surface combatant dtmb model 5415. J. Ship Res. 49 (1), 55–68.
Marintek Homepage, ⟨http://www.sintef.com/home/marintek/⟩.
Marintek towing tank facilities description, ⟨http://www.sintef.com/home/MARINTEK/Laboratories/The-Ship-Model-Tank/⟩.

Newman, J.N., 1977. Marine Hydrodynamics. MIT Press, London, England.
Ommani, B., Faltinsen, O.M., 2014. Viscous and potential forces on an advancing surface-piercing flat plate with a fixed drift angle. J. Mar. Sci. Technol., 1–14.
Prandtl, L. Applications of modern hydrodynamics to aeronautics, Classical Aerodynamic Theory 1050.
Rhinoceros 3d Modelling Software, ⟨http://www.rhino3d.com⟩.
Sci-Py Curve Fit, ⟨http://docs.scipy.org/doc/scipy/reference/generated/scipy.optimize.curve_fit.html⟩.
Scipy Student's T-distribution, ⟨http://docs.scipy.org/doc/scipy-0.14.0/reference/generated/scipy.stats.t.html⟩.
Stern, F., Agdrup, K., Kim, S., Hochbaum, A., Rhee, K., Quadvlieg, F., Perdon, P., Hino, T., Broglia, R., Gorski, J., 2011. Experience from simman 2008 the first workshop on verification and validation of ship maneuvering simulation methods. J. Ship Res. 55 (2), 135–147.
Student, 1908. The probable error of a mean. Biometrika, 1–25.
Tian, X., Ong, M.C., Yang, J., Myrhaug, D., 2014. Large-eddy simulation of the flow normal to a flat plate including corner effects at a high reynolds number. J. Fluids Struct. 49, 149–169.
Van Den Brug, J., Beukelman, W., Prins, G., 1971. Hydrodynamic Forces on a Surface Piercing Flat Plate. Delft University of Technology, Delft, Netherlands.
Wolfson Unit Towing Tank Dynamometers, ⟨http://www.wumtia.soton.ac.uk/products/dynamometry⟩.

## Paper 2: Drift Forces – Wingsails vs Flettner rotors

Written by Jarle Vinje Kramer, Sverre Steen, and Luca Savio
Published and presented on the High-Performance Marine Vehicles Conference in October 2016

# Drift Forces – Wingsails vs Flettner Rotors

**Jarle A. Kramer**, NTNU, Trondheim/Norway, jarle.a.kramer@ntnu.no
**Sverre Steen**, NTNU, Trondheim/Norway, sverre.steen@ntnu.no
**Luca Savio**, Marintek, Trondheim/Norway, luca.Savio@marintek.sintef.no

**Abstract**

*When sails produce thrust, they also produce side force, which makes the ship move with a drift angle. The drift angle increases the resistance of the ship, which cancels some of the positive effect from the sails. This paper explores the importance of drift for two different types of sail technologies. A general cargo ship is analyzed, using historical wind data on an example route from Rotterdam to Trondheim, using wingsails and Flettner rotors. The analysis uses CFD and a custom route simulation software.*

## 1. Introduction

Using sails on modern cargo ships, as a way to reduce the fuel consumption, has been suggested many times by both researchers and commercial companies. Recent examples include the "Wind challenger" project from the university of Tokyo, *Ouchi et al. (2013),* and the work presented in *Traut et al. (2014)* where a Flettner rotor is compared to a kite. There are also many older, but more famous projects such as the Walker Wingsail, *Walker (1985)*, the "turbo sail" developed by the Cousteau foundation, *Charrier et al. (1985)* and the original Flettner rotor ship. Although many solutions exist, the two most popular wind propulsion technologies seem to be wingsails and Flettner rotors. Both of these technologies, create thrust mainly by using "lift", i.e. the force normal to the incoming wind velocity. A single element symmetric wingsail creates this lift by having an angle of attack relative to the wind, while Flettner rotors are spinning cylinders that create lift by utilizing the Magnus effect. One of the consequences of creating thrust in this way is an unavoidable side force. That is, as long as the thrust from the sails is created by lift, there is no way of pushing the ship forward, without also pushing it sideways. How much the ship is pushed sideways is dependent on the apparent wind direction. If the wind is coming directly from the side of the ship, the only contribution to the side force is from the drag on the sails. However, if the apparent wind is from any other direction, the lift will also contribute to the side force. The result is that in typical conditions, the side force is often many times larger than the thrust. This side force has an effect on the flow around the ship hull. Since the hull is pushed sideways, it starts moving with an increasing drift angle, until the drift induced side force on the hull is equally strong, but with opposite direction to the side force from the sails. The drift angle makes the ship hull into a lifting surface. The problem is, as is the case with all lifting surfaces: with lift, there is also lift induced drag. That is, due to the drift angle, the resistance on the ship hull is increased, which cancels some of the positive effect from the sails. How big of a problem this is, is dependent on several factors, such as the hydrodynamics of the ship hull, the side force to thrust ratio of the sails and the amount of thrust that is generated from the wind. An interesting aspect of modern sails, which are not much studied previously, is the difference in side force to thrust ratio. For instance, Flettner rotors generate very large forces, relative to the sail area. Dependent on the speed of the ship, and the wind direction, the result is often that a Flettner rotor can generate much more thrust than a wingsail, with equal sail area. However, the side force to thrust ratio is also larger, which means that for the same amount of thrust, the ship is also pushed sideways with a much stronger force.

This paper explores two main questions: how big of a problem is the drift-induced resistance for a normal cargo ship with modern sails, and how much difference is there between wingsails and Flettner rotors?

The case study chosen in for these questions is a 120 m long general cargo ship, with 40 m tall sails, on an example route from Rotterdam, Netherlands to Trondheim, Norway. Historical wind data,

Computational Fluid Dynamics (CFD) analysis of both the sails and the ship hull, and a route analysis code, is used to calculate the importance of drift induced effects. The Flettner rotor in this analysis is a simple spinning cylinder, without any end plates or flaps, while the wingsail is a two-element wing, where both elements are of equal length. We limit the study to one aspect ratio for the sails, which is equal to 5. However, the number of sails is varied between 1 and 8, in order to change the amount of thrust produced from the wind. Two different control strategies for the sail are tested: maximum power delivered from the sails, or maximum effective power delivered. The effective power is the power from the sails, minus the added required power due to the sails. In this analysis, the sails generate added resistance due to two main components: the added resistance on the hull, and the added resistance on the rudder. These two are considered to be different effects, as the rudder might be necessary in order to balance the ship hull at the right drift angle. A keel model will also be used to assess the effect of installing a simple keel on a normal cargo ship, with regard to drift-induced resistance. We will also run the analysis with two different assumptions regarding the sail mechanism: one where the sails cannot be retracted, or stowed away when they are not in use, and one where they can. Since the main focus of this study is to evaluate the importance of drift, some simplifications regarding other effects have been made. For instance, we have not calculated added resistance due to waves, interaction effects between sails, or used any form of engine model. The energy savings presented in this paper should therefore be evaluated critically, and the focus should rather be on how including drift changes the results predicted by the simplified model.

All the code used for creating the results in this paper is published on Jarle Kramer's GitHub page, *Kramer (2016)*. This includes a library and scripts used to set up CFD simulations, a ship analysis library, a geometry handling class, a route simulation code, a particle swarm optimization algorithm, a non-linear lifting line code, and weather data analysis code. Everything is written in Python or Cython. Most of the code is written in an object oriented way, with classes that sometimes inherits from each other. Due to page limitations, not everything in this paper is explained in detail, but references will be made to the GitHub page, where the specific code is available for further study, if this is of interest.

## 2. CFD simulations

CFD is used to analyze both the hull and the sails with the open source software library OpenFOAM, version 3.0+, http://www.openfoam.com. A custom python library written specifically for Open-FOAM simulation setup is used. This library can be found on GitHub, *Kramer (2016)*, along with example scripts that show how it is used. There is one general library, called "myPyFoam", in addition to three specialized classes, called "TowingTank", "WingSimulation" and "FoilSimulation" which is used to set up simulations of ship hulls, 3D wings, and 2D foil geometries respectively. This approach to CFD simulation setup is based on the idea that, for a specific type of simulation, such as foil simulations, there is a general strategy for setup, that are not very much dependent on details in the geometry. That is, a simulation strategy that works for one foil should also work for another foil, if the Reynolds number and main dimensions are the same. Based on experience developed while running CFD simulations in the past, as well as recommended best practices from different sources, the setup library manages both the meshing process and solver settings automatically, with main dimensions and velocity as input. This scripting approach to CFD ensures that we set up the simulations in a consistent matter, every time.

Three different types of OpenFOAM solvers are used for this case study:

- simpleFoam, which is a steady state incompressible solver that uses the SIMPLE algorithm, *Patankar and Spalding (1972)*. This solver is used for the wing and foil simulations.
- pimpleFoam, which is an unsteady, incompressible solver that uses a mix between the SIMPLE algorithm and PISO algorithm, *Issa et al. (1986),* to deal with large time steps. The time loop is driven forward with the PISO algorithm, with the option of doing several "inner iterations" using the SIMPLE algorithm. This solver is used for all the simulation classes.

- interFoam, which is an unsteady, incompressible solver, similar to pimpleFoam, but with support for two fluids, such as air and water. The interface between the two fluids are tracked using the Volume of Fluid (VoF) method, *Hirt and Nichols (1981)*. This solver is used to find the wave resistance for the ship hull.

All the simulations in this case study use Reynolds Average Navier-Stokes (RANS) turbulence modelling. The setup library supports several turbulence models, but the k-ω SST, *Menter (1994),* is the default, and has been used for all the simulations for this paper. A continuous wall function is used, which is an implementation of the equation presented in *Spalding (1961)*. The initial conditions for the variables in the turbulence model follows standard practices, with 1% inlet turbulence, http://www.esi-cfd.com/esi-users/turb_parameters/. The meshing is done with the OpenFOAM meshing tool "snappyHexMesh". SnappyHexMesh generates hexahedra and split-hexahedra mesh cells, by iteratively refining and moving a background mesh. The process is controlled by specifying refinement levels, and wall-layers, at the geometry present in the simulation, as well as in optional refinement regions. The size of the cells closest to a geometry is adjusted based on a target y+ value and a case specific maximum size. The length of the cells corresponding to a certain y+ value is calculated with a friction line, and the Reynolds number for each simulation. The background mesh is adjusted based on a target size alone. The CFD simulations for ships and 3D wings use wall functions, and general guidelines for wall functions often suggest y+ values between 30 and 100, which is in the range of the logarithmic law of the wall. Both too small and too large y+ values can be problematic, as is for instance shown in *Hympendahl and Ciortan (2015)*. The y+ values chosen by default by the setup library is 60, if wall functions are used, otherwise it is 1. However, depending on the Reynolds number and mesh settings, this can sometimes lead to a too coarse mesh, which in our experience are worse than "wrong" y+ values. Each case class therefore uses a custom maximum size, for the mesh cells right outside the wall layers. If the target y+ value suggest that the mesh will be too coarse, the library will first try to alter some mesh settings, such as layer expansion. The maximum layer expansion factor is 1.5, but this is generally reduced to about 1.1-1.3 automatically by the library. If this does not work, a smaller y+ value will be used. If the y+ value drops below 30, a warning is generated, so that we can decide if we need to resolve the boundary layer instead. Some important simulation parameters are presented in Table 1. "L" and "U" is reference to the characteristic length dimension (ship length and chord length) and inlet velocity in the simulation respectively. The "max feature cell" size is a reference to the smallest cell size used in the simulation outside the wall layers, which are generated at "features", or sharp edges in the geometry. All the other cells close to a geometry will be one refinement level less, or twice the size. The number of refinement levels varies, depending on the ratio between the background mesh and the feature cells, but are never larger than 8. The time step in the simulation is adjusted so that the Courant number is never above a maximum limit, which is adjusted automatically by OpenFOAM, in addition to a maximum absolute limit that is proportional to the characteristic length dimension divided by the inlet velocity.

Table 1: Simulation parameters

| | Foils | Wings | Ships |
|---|---|---|---|
| Max feature cell size/L | 0.001 | 0.005 | 0.001 |
| Max background cell size/L | 0.1 | 0.5 | 0.1 |
| Number cells per refinement level | 10 | 5 | 5 |
| Number of wall layers | 15 | 5 | 5 |
| Target y+ value | 1 | 60 | 60 |
| Approximate number of cells | 100 000 | 10 million | 1-5 million |
| Max Courant number | 10 | 10 | 10 |
| Max time step · U/L | 0.005 | 0.005 | 0.0025 |
| Simulation time · U/L | 15 | 35 | 14 |
| Max steady state iterations | 10000 | 6000 | Not used |

In addition to different maximum sizes, different case classes have different refinement regions, which primarily is made to capture the wake in the simulations. This includes refinement in the kelvin wake for ship simulations, tip wake for 3D wings, and a wake that starts at the trailing edge for 2D foil profiles. The ship simulations also use anisotropic refinements only in the vertical direction, in the region where the free surface is located. This is necessary to keep the boundary between water and air relatively sharp. The different meshes used in this analysis can be seen in Fig.1.

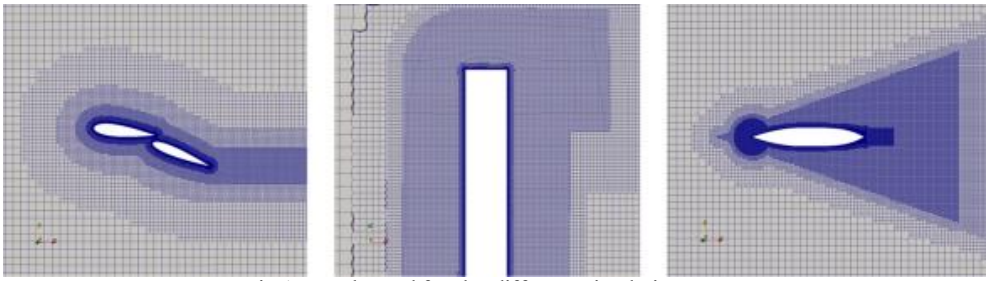

Fig.1: Mesh used for the different simulation cases

The parameters shown in Table 1 are the default settings for each simulation class, corresponding to a "medium" mesh. However, each class also have the option of creating "very coarse", "coarse", "fine" and "very fine" meshes. When these settings are activated the length dimensions in the mesh is either multiplied or divided by a factor. A "very coarse" and "coarse" mesh corresponds to a mesh where the maximum length dimension is multiplied with two or the square root of two respectively. For a "very fine" and "fine" mesh, the length dimension is divided by two or the square root of two respectively. This is used to do mesh convergence studies, and the result of such a mesh study for the ship hull can be seen in section 3. The setup library has also been used to perform validation simulations. Some of these validation experiments will be presented along with the numbers for this case study.

## 3. Description of the case study

### 3.1 Ship

The ship chosen for this case study is a 120 m long general cargo ship. The main dimensions, as well as the service speed, are chosen so that it is similar to a real general cargo ship, and can be seen in Table 2. Both the full-scale values, and the model scale values used in the CFD simulations are shown. A small, relatively slow, cargo ship is considered to be an interesting case study, simply due to the size; we are mostly interested in ships were a significant portion of the total thrust comes from the sails. A very large ship would also need very large sails in order to generate significant amounts of thrust. Very large sails can be problematic, both from a structural point of view, and from practical point of view, due to bridges and cranes in harbors. A smaller ship might need larger sails relative to its own size, as larger ships are more efficient, but the absolute size can still be reduced. It therefore seems more realistic that a small cargo ship can get a large portion of the total thrust from sails, at least in the near future.

Table 2: Ship main particulars

| | Full scale ship | CFD model ship |
|---|---|---|
| Lwl [m] | 120 | 7 |
| Bwl [m] | 20 | 1.167 |
| D [m] | 12.5 | 0.729 |
| T[m] | 5.5 | 0.321 |
| Volume displacement [$m^3$] | 7990 | 1.586 |
| Wetted surface, w.o. rudder [$m^2$] | 2591 | 8.817 |
| Rudder planform area [$m^2$] | 11.25 | 0.0383 |
| Keel planform area [$m^2$] | 22.5 | 0.0766 |

| | | |
|---|---|---|
| Service speed [m/s] | 7 | 1.69 |
| Service Froude number | 0.204 | 0.204 |
| Resistance coefficient, $C_T \cdot 10^3$ | 3.149 | 4.256 |
| Friction resistance coefficient, $C_F \cdot 10^3$ | 1.723 | 3.041 |
| Roughness resistance coefficient $\Delta C_F \cdot 10^3$ | 0.211 | 0 |
| Pressure resistance coefficient $C_P \cdot 10^3$ | 1.215 | 1.215 |
| Propeller diameter, D [m] | 4 | 0.233 |
| Propeller pitch P/D | 0.997 | 0.997 |
| Propeller number of blades | 4 | 4 |

The hull geometry is a custom design. The reason for designing a new geometry, rather than using an already existing design, is that most open ship geometries are either very large tankers or very larger container ships. The hull design was created with the goal making a realistic, but simple ship. It does not have a bulb, but instead a straight slender bow. It was made using a Catmull-Clark subdivision surface, *Catmull and Clark (1978)*, in the open source geometry modeling software Blender, https://www.blender.org. The subdivision surface representation of the geometry was chosen due to its flexibility with regards to topology. Unlike for instance NURBS based geometry, a subdivision surface can have arbitrary topology, i.e. the entire ship hull can be created as one surface, rather than several individual NURBS patches. Fig.2 shows the hull lines; the 3D model can be downloaded from GitHub.

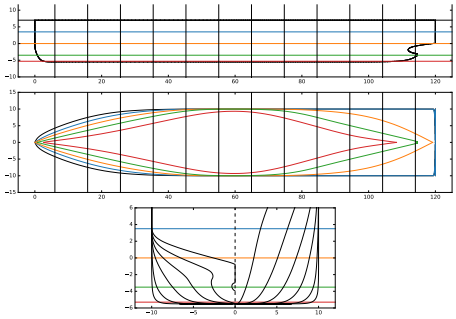

Fig.2: Line drawings of the ship hull

The hydrodynamic forces on the ship are modeled with the "Hull" class in the "Ship" library that can be found on GitHub. This class is initialized with the main dimensions of the ship. Based on the main dimensions, the class estimates the forces that act on the ship hull as function of Froude number, Reynolds number and drift angle, either using simplified theories and empirical models or results from CFD simulation and experiments. For this analysis, CFD is used to compute all the necessary values. When using CFD to estimate the calm-water resistance, the pressure resistance and friction resistance from the simulations are extracted individually. The CFD simulations are performed in model scale, for several Froude numbers. When calculating the full-scale resistance, the pressure resistance is assumed to be independent of Reynolds number, but dependent on Froude number, while the friction resistance is dependent on both. In order to scale the friction resistance to full scale, for a given Froude number, a friction line is used, along with an empirical roughness factor. The scaling factor is the value of the friction line at full scale, divided by the value of the friction line in model scale. The friction line used is a numerical friction line, based on the k-ω SST turbulence model, which can be found in *Eca and Hoekstra (2008)*. The reason for choosing a numerical friction line, rather than the more standard ITTC-57 friction line, is based on the work published in *Raven et al. (2006)*. The paper suggests that using the ITTC-57 friction line might not be the best scaling strategy, and that for instance a numerical friction line is a better choice. The CFD values and scaled values for the resistance coefficients in calm water at service speed can be seen in Table 2.

In order to calculate the side force and added resistance due to drift, CFD simulations of the ship hull

with a drift angle, but without free surface modeling is used. The free surface has previously been found to not be very important for estimating the drift-induced forces, and neglecting the free surface simplifies the simulations, *Kramer and Steen (2015)*. The hull is simulated with five drift angles. The data from the simulations are then fitted to second-order polynomials by the "Hull" class, as this is a model that have been found to work well for drift induced forces. The induced drag coefficient is defined as the drag at a specific drift angle, minus the drag at zero drift angle. That is, it is the added resistance due to drift. The computed lift, lift-induced drag, and yaw moment, as a function of drift angle can be seen in Fig.3. The coordinate system is located in the bow of the ship, with the x-axis pointing towards the stern, when the drift angle is zero, and the z-axis pointing up. $F_x$ is the force in the x-direction, $F_y$ is the force in the y-direction, while $M_z$ is the moment around the z-axis. The coefficients are defined as follows, where L is the ship length, T is the ship draft, U is the ship velocity, $\rho$ is the water density and $\alpha$ is the drift angle:

$$C_L = \frac{F_y}{0.5\rho\, L\, T\, U^2}$$

$$C_{Di} = \frac{F_x(\alpha) - F_x(0)}{0.5\rho\, L\, T\, U^2}$$

$$C_M = \frac{M_z}{0.5\rho\, L^2\, T\, U^2}$$

The CFD values are plotted for three different meshes: coarse, medium and fine. This is to show that the result is not very dependent on the mesh resolution. The result for the fine mesh is used in this analysis. The polynomial curve fit is shown as solid lines. In order to validate the CFD simulations, the setup scripts have also been used to generate simulations that reproduce the experiments published in *Kramer et al. (2016)*. In this experiment, a foil-like ship is towed in a towing tank for three aspect ratios, two bottom edge shapes and two Froude numbers. The experimental data shown in Fig.3 is for the lowest aspect ratio, with the rounded bottom edge, and Froude number 0.1.

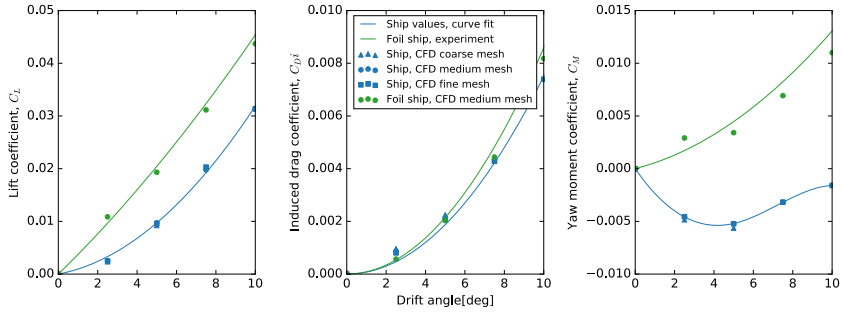


Fig.3: Lift, lift-induced drag and yaw moment coefficients for cargo ship and validation experiment

We are also interested in the effect of rudder and a keel. The rudder was present in all the CFD simulations performed for the ship hull, but only with zero rudder angle. The effect of setting the rudder angle to something other than zero is modeled with the "Rudder" class in the ship library. This is a simple model of a lifting surface, based on a simplified rudder model suggested in *Bertram (2012)*. The exact flow around a rudder is a complicated phenomenon, with very high Reynolds number, presence of a propeller slip stream and interaction from the ship hull. The details of this flow has been neglected. Rather, steady state CFD simulations of the rudder geometry is performed, where the rudder is standing on a symmetry plane in order model the presence of the ship hull. The CFD simulations are performed for a Reynolds number equal to 2E6, but the since the rudder will actually be experiencing a Reynolds number more close to 15E6, the friction resistance on the rudder is scaled in the same way as for the ship hull. Only rudder angles well below stall is simulated. Rudder stall is not directly modeled in the route simulation, but the magnitude of the rudder angle is evaluated to assess whether stall is a likely problem or not. The values for lift and drag from the CFD simulations

are then used to construct polynomial models. The lift is assumed to be linearly dependent on the rudder angle, while the lift-induced drag is assumed be a second order polynomial. The rudder geometry is a spade rudder, with NACA 0018 foil profile, aspect ratio of 2.22 and taper ratio of 0.83. Fig.4 shows the computed lift and drag coefficients.

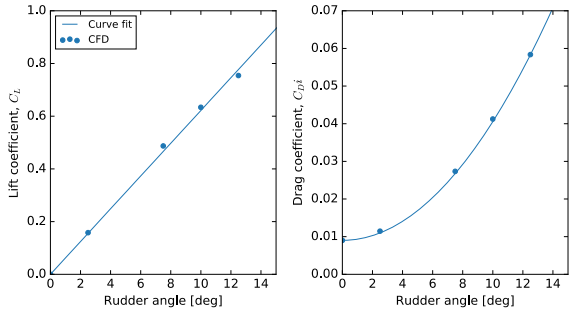


Fig.4: Lift and drag coefficients for the rudder and the keel

The area of the rudder, $A_R$, is calculated from a recommended formula in *Bertram (2012)*, as follows:

$$\frac{A_R}{L \cdot T} \geq 0.01\left(1 + 25\left(\frac{B}{L}\right)^2\right)$$

The effect of the propeller slip stream is treated by adding lift, ΔL, and drag, ΔD, as a function of thrust, T, to the lift and drag calculated by the coefficients from CFD. The formulas are taken from *Söding (1998)*. $C_{Th}$ is the thrust coefficient for the propeller, and $\alpha$ is the rudder angle.

$$\Delta L = T\left(1 + \frac{1}{\sqrt{1 + C_{Th}}}\right)\sin\alpha$$

$$\Delta D = T\left(1 + \frac{1}{\sqrt{1 + C_{Th}}}\right)(1 - \cos\alpha)$$

The incoming velocity to the rudder is assumed to be following the ships center line, as the rudder is located in the ship and propeller wake. That is, the lift and drag from the rudder is in a ship fixed coordinate system, and must be rotated when they are added to the global forces. The keel is modeled in the same way as the rudder, only with twice the area, and with the assumed incoming velocity to be in the ship traveling direction. The yaw moment from both the rudder and the keel is calculated by multiplying the force normal to the ship centerline with the distance from the bow to the rudder/keel. The rudder is located at the stern of the ship, so the distance is 0.95·L, while the keel is located in the middle of the ship, or 0.5·L, which is also the assumed mean center of pressure for the sail. Global forces and yaw moment on the ship hull as function of drift and rudder angle, with and without keel, at service speed can be seen in Fig.5.

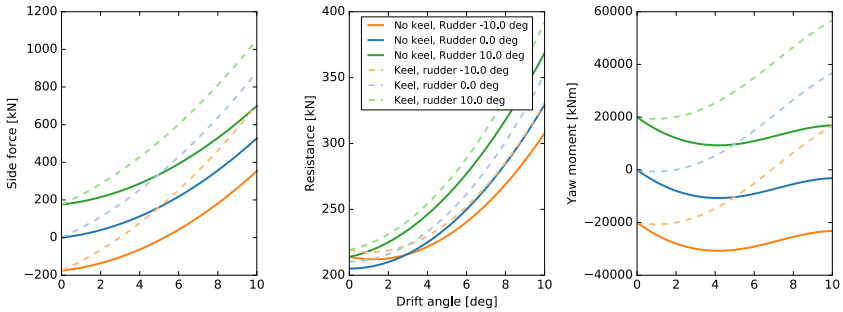


Fig.5: Forces on the ship as a function of drift and rudder angle, with and without keel

### 3.2 Sails

Two different types of sails are modeled in this paper: a two-element wingsail and a Flettner rotor. Both sails have a geometric aspect ratio of 5 but they are assumed to stand on a large deck structure, so that the effective aspect ratio is 10. That is, we assume that the deck acts as a symmetry plane. The Flettner rotor analyzed is a spinning cylinder, with a constant diameter along the span of the rotor. The wingsail is assumed to have a taper ratio of 0.4. The leading element of the wingsail is based on the NACA 0020 profile, while the trailing element is based on NACA 0015. Both elements are of equal length. The maximum flap angle is 15 degrees. The hinge point of the flap is at the quarter chord of the foil as a whole, or halfway into the first element. The sails are modeled with the "Sail" class in the "Ship" library published on *Kramer (2016)*. This class consists of methods for calculating lift, drag, thrust and side force, as well as a method that can optimize the sail control parameters based on an arbitrary input objective function. The forces are determined from force coefficients. More specifically, the input parameters used to initialize the sail class are the area of a single sail, the height of the sail, the number of sails in total, the lift and drag coefficients for a single sail, along with the corresponding control parameters. For the Flettner rotor, the power coefficient is also needed, which tells us how much input power is required in order to spin the Flettner rotor at a given speed. The control parameter can be either the spin ratio (Flettner rotor) or the angle of attack and flap angle (wingsail). The coefficients are defined as follows, where A is the sail planform area and U is the wind velocity:

$$C_{L/D/x/y} = \frac{\text{Lift/Drag/Thrust/Side force}}{\frac{1}{2}\rho A U^2}$$

$$C_P = \frac{\text{Sail input power}}{\frac{1}{2}\rho A U^3}$$

The optimization of the sail control parameters can be done with several methods: brute force, built in optimization methods from the SciPy library, http://scipy.org, or a custom written optimization method, based on the particle swarm method, *Eberhart and Kennedy (1995)*. For the wingsail in this analysis, the particle swarm method is used, while the Flettner rotor is optimized with brute force.

The force coefficients for the wingsail are analyzed using a combination of 2D CFD and a non-linear numerical lifting line. The non-linear numerical lifting line uses the basic principle of the traditional lifting line, *Prandtl and Tietjens (1934)*, but with linear foil theory exchanged with a non-linear viscous 2D lift coefficient, as well as an iterative method to solve the equations. This approach for analyzing 3D wings in general is for instance described in textbooks such as *Anderson (2005)*, but has also been used specifically for modelling two-element wingsails in the scientific literature, *Graf et al. (2014)*. Details of the algorithm can be found in *Anderson (2005)* chapter 5, while the implementation used specifically for this analysis can be viewed in the "LiftingLine" code on *Kramer (2016)*. The work presented in *Graf et al. (2014)* shows that the method works well for predicting the lift and drag on the sail while the flow is attached. The method can also work for stalled wings, which is shown both in *Anderson (2005)* and *Graf et al. (2014)*. However, *Graf et al. (2014)* show that the maximum lift coefficient can be over predicted compared to 3D CFD, and when the maximum lift coefficient is very large, there is sometimes problems with convergence for the iterative solver. The wing used in this analysis has a large maximum lift coefficient. From the 2D analysis, the maximum lift coefficient is 2.26, which happens with an angle of attack of 12.5°, and a flap angle of 15°. In order to avoid the convergence problems with the method, we have used the lifting line method for angles of attack almost up to stall for the largest flap angle, but not above. A stalled wing is in general of little interest, as this will only be useful when there is a tail wind, with a speed that is higher than the ship speed. The maximum angle of attack used with the lifting line method is 13.5°, which gives a lift coefficient of 2.04 for a flap angle of 15°. Larger angles of attack caused convergence problems for the largest flap angle, and based on the lift coefficient, this is fairly close to stall. The benefit of the method is calculation time. Since the wingsail is a two element wing, the forces depend on both the angle of

attack and the flap angle. The number of simulations that must be performed in order to get a complete picture of the forces on a wingsail can quickly become large. For instance, in this case, 4 flap angles have been simulated with at least 18 angles of attack each, giving more than 72 CFD simulations. 2D CFD allows for simulations with a higher resolution relative to the chord length, at a much shorter time, compared to the 3D case. The resulting lift and drag coefficients used in this analysis for the wingsail can be seen in Fig.6.

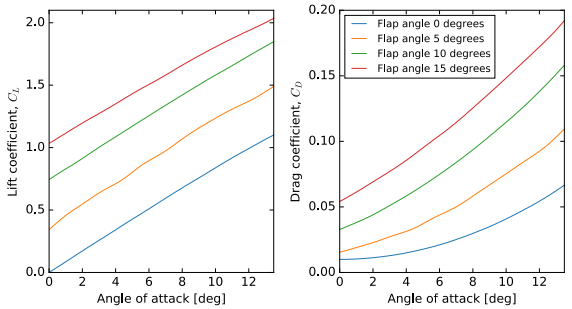


Fig.6: Lift and drag coefficients for the wingsail as function of angle of attack and flap angle

In order to get values for the lift and drag for the Flettner rotor, 3D CFD simulations have been used. The non-dimensional value for the spin velocity is called the spin-ratio ($\alpha$), and is calculated as the velocity of the outer surface of the cylinder, divided by the incoming wind velocity. The flow around a Flettner rotor can be both steady and unsteady, depending on the spin-ratio, and both aspect ratio and Reynolds number have an effect on the resulting forces. The little experimental data that is available is only for very small Reynolds numbers, well below realistic conditions for a Flettner rotor on a cargo ship. It is therefore hard to say much about the uncertainty of the forces we have calculated. Many study this phenomenon using very high fidelity simulations, with many cells, small time steps and LES turbulence models. However, this is very time consuming, and only practical for smaller Reynolds numbers. The work presented in *Zhang et al. (2013)* show fairly good agreement between experimental values and steady state CFD values for both lift and drag, with meshes with less than 10 million cells, and a Reynolds number of 40000. The difference between simulation and experiments are between 1-15% depending on spin ratio, number of cells and turbulence model. The same approach was used to analyze the Flettner rotor in this paper, as it is both practical and relatively accurate. We have also simulated the case presented in *Zhang et al. (2013)*, with the same setup script as used for our case. The "WingSimulation" class applies slightly different settings due to the low Reynolds number, for instance for the wall functions, but the overall rules for setting up the mesh are the same. The difference between simulations and experiment for the low Reynolds number case, as well as the values for the lift, drag and power coefficients for our high Reynolds number case can be seen in Fig.7.

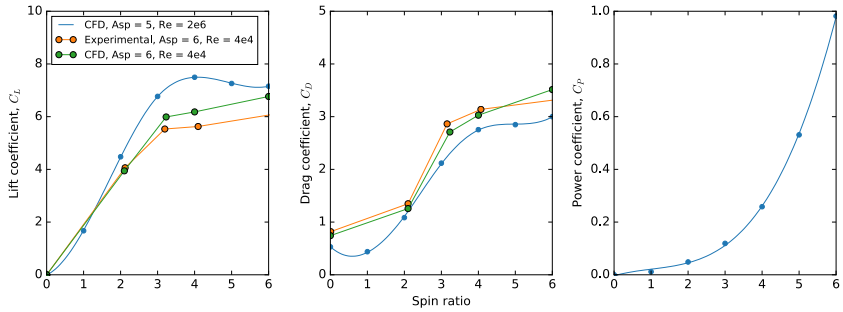


Fig.7: Lift, drag and power coefficient for the Flettner rotor

The lift and drag coefficients is used to calculate thrust and side force. Fig.8 shows the calculated thrust coefficient and side force to thrust ratio for the two different sails, with different ship speed to wind speed ratios, as a function of true wind direction. 0° are head wind, 90° are wind directly from the side and 180° are tail wind. The thrust coefficient is made non-dimensional with the wind velocity, so an increase in ship speed can actually increase the thrust coefficient for the wingsail. This is not the case for the Flettner rotor, which has a lower lift to drag ratio. The figure also shows the difference between the wingsail and the Flettner rotor when it comes to the amount of side force relative to the thrust. In general, the Flettner rotor has significantly higher side force, for the same amount of thrust.

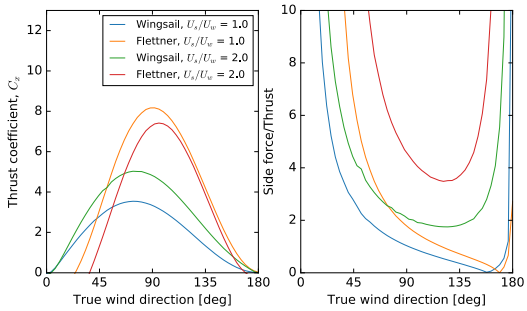


Fig.8: Thrust coefficient and side force to thrust ratio for the sails, at different ship speed to wind speed ratios

### 3.3 Route and wind

The wind data used in this analysis is taken from the European Centre for Medium-Range Weather Forecasts (ECMWF) ERA-interim reanalysis dataset *Berrisford et al. (2011)*. This dataset includes the wind velocity 10 m above the surface, covering the entire globe with a spatial resolution of 0.75°, and four time instances per day. Data from the beginning of the year 2000 until the end of 2015 is used in this analysis. The discrete points making up the route traveled by the ship is created by manually mapping out rough waypoints, and then calculating the great circle lines between the waypoints with the "Route" class located on *Kramer (2016)*. The distance between each discrete point is set to be 50 km. The route is plotted on top of the world in Fig.9, with the average wind velocity for the used dataset as a color map in the background. In order to find the wind velocity on a specific point and a specific time, cubic spline interpolation is used, with the help of the SciPy library. Details can be found in the "Wind" class on GitHub.

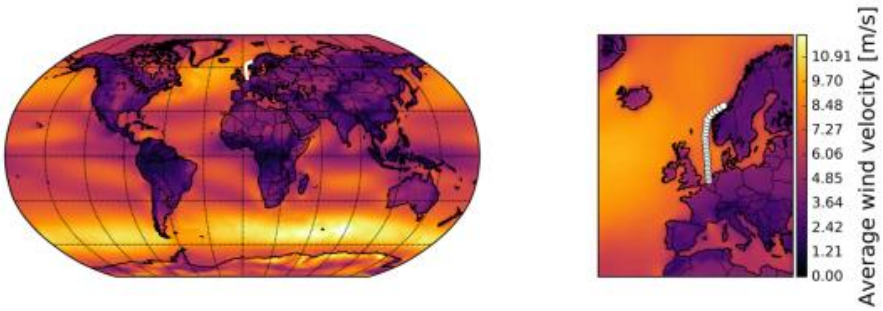


Fig.9: Example route plotted on maps with average wind speed color-mapped to the background

A histogram plot of the wind direction and velocity for this specific route can be seen in Fig.10. The wind direction is relative to the ships center line, where 0° is head wind, 90° side wind, and 180° tail wind. The wind data is only shown for 0-180° due to symmetry. In total, the number of individual discrete points with wind data for this route is 1,262,304. In order to decrease the computational time,

the dataset used in the simulation is reduced by randomly picking 10 000 points from the overall dataset. This reduction is not expected to alter the overall statistics. Both the reduced dataset and the full dataset is shown in Fig.10.

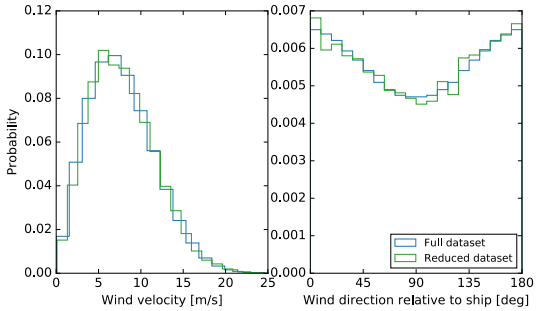


Fig.10: Wind statistics

## 4. Route simulation

The route simulation is based on steady state evaluation of the ship at each discrete point in the route and weather data. The resulting statistics will therefore tell us how the ship will perform if it is located at a random place on the route, at a random time. Details on how exactly the ship is moving, i.e. when it is located at a specific point, is neglected, as it is considered to not be relevant for this study. Using the data presented in section 3, the following steps are performed in order to evaluate the ship and sails:

- The performance of the ship without sails is evaluated for the given ship speed. This includes wave resistance, friction resistance, with roughness, and propeller characteristics, such as efficiency.
- For a given wind speed, direction and sail loading, the forces on the sails are computed. That is, both thrust, side force and yaw moment.
- The necessary drift angle is found numerically using Newton's method, from the SciPy library. The input function to the numerical solver is a function that returns the side force from the sails, minus the side force from the hull, keel and rudder, with a drift angle as input. For a given drift angle, the rudder angle is calculated such that it balances the yaw moment. However, for an arbitrary sail loading, it is not guaranteed that there is a drift angle that provide balance both in terms of side force and yaw moment. In addition, the function that gives side force as function of drift, with the rudder always balanced might have local maxima/minima, which can be problematic for the numerical solver. In order to handle this problem, several initial values for the drift angle can be used. First, 5° are tried as default. If this does not lead to a solution, random values between 0° and 30° are tried, either until the maximum number of tries are reached, or a solution is found. The maximum number of tries is set to be 10. If the algorithm cannot find a solution, the hull drift angle is set to a very large value (90°), which causes the added resistance due to drift to become so large that the sail control algorithm will avoid the specific sail loading.
- When the necessary drift and rudder angle is found, the forces on the ship is recalculated, and the effective thrust is found by subtracting all the added resistance that is caused due to drift and rudder angles. The necessary power to the propeller is found by multiplying the total resistance on the ship hull, keel and rudder with the ship velocity, and dividing it with an estimated propeller efficiency.

In order to decide the sail control parameters for each discrete point in the route simulation, the built in sail optimization method is used, as described in section 3.2. The objective function in the sail optimization will be delivered power to the propeller, calculated with and without drift-induced

effects. When drift-induced effects are not considered, the wingsail will deliver maximum thrust, independent of what the consequences of this strategy will be, while the Flettner rotor will deliver maximum power. The power from the Flettner rotor is calculated as the thrust multiplied with the ship velocity, minus the required input power. When drift-induced effects are included, the sail loading might decrease in order to reduce added resistance due to drift and rudder angles. Even when drift-induced effects are not included in the optimization of the sail, there will always be an explicit check of how the performance of the ship would be without the sails "turned on". That is, either how the ship would be without sails altogether, if the sails are retractable, or how it would be with the control parameters set to zero, if the sails are not retractable. If the control parameters from the sail optimization gives worse performance than a sail in "off position", the sail control algorithm will choose to turn it off. This is to model a situation where the captain on board the ship will decide to turn of the sails, if he detects that the sail control program increases the fuel consumption.

## 5. Results

Fig. 11 and Fig. 12 show the predicted reduction in delivered power to the propeller, due to the sails, as a percentage of the necessary power in calm water without sails. Fig. 11 is the data for the non-retractable sails, while Fig. 12 is the data for the retractable sails. The power reduction is shown as a function of number of sails, as well as with and without drift-induced effects, with and without rudder and keel, and with and without hydrodynamics in the sail control.

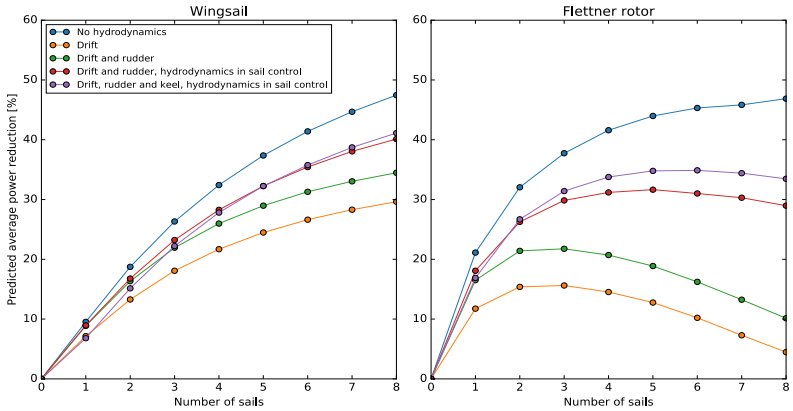


Fig. 11: Average power reduction, with non-retractable sails

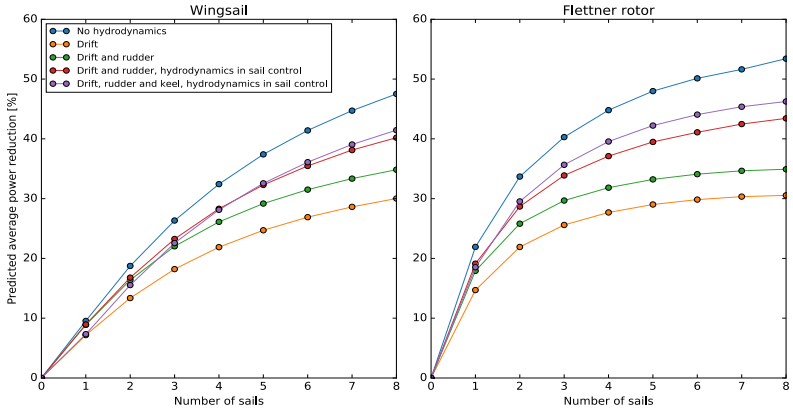


Fig. 12: Average power reduction, with retractable sails

A lot of data is generated in the route simulation, regarding the details of the ship as a system. Fig. 13 is used to represent some of this data. It shows histogram plots, and mean values of the drift and rudder angle, for the case with 6 non-retractable sails. Similar patterns can be generated for all the other cases as well, only with smaller/larger values, depending on how many sails there are. This figure is included, as it shows an important result, which is discussed in section 6.

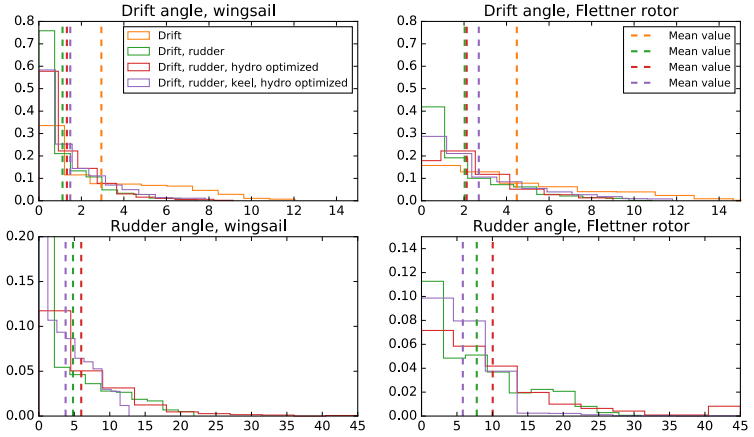


Fig. 13: Drift and rudder angle statistics, for 6 non-retractable sails

## 6. Conclusion and discussion

Whether drift is an important effect or not is dependent on the sail type, the amount of thrust generated from the sails, the sail control strategy, the sails ability to be stowed away, and of course the hydrodynamics of the ship hull. When just one sail is used, there is only a small reduction in the energy savings due to drift. When more sails are used, and the amount of thrust from the wind increases, the hydrodynamic effects get more and more important, which is not very surprising. What is interesting is the effectiveness of including the hydrodynamics into the control algorithm of the sails. For instance, with the most extreme example, which is the case with 8 non-retractable Flettner rotors, the energy savings due to sails are increased from roughly 10% to almost 30%, by just including the information about the hydrodynamics in the sail control. When the hydrodynamics of the ship hull is considered, the loading of the sail, or amount of thrust produced, is sometimes reduced. That is, sometimes it is better to produce less thrust from the sails, in exchange for less added resistance. Another consequence of considering hydrodynamics is that the sails can be used more often. In the route simulation, there is a very basic "captain model", that will always turn off the sails, if having the sails on is worse than having them off. When we look at the mean values for drift angles in Fig. 13, we can see that it is slightly larger for the case with hydrodynamics in the sail control, than it is for the case without. Considering that drift causes added resistance, this might seem strange. If drift is the problem, how can a larger mean drift angle cause more power reduction for the ship? The reason for this is simply that the captain will allow the sails to be turned on more often when the hydrodynamics are included in the control algorithm. That is, without hydrodynamics in the control algorithm, the sails will sometimes produce so much side force that all the thrust, and more, is lost to drift-induced resistance. This will cause the captain to turn off the sails, which results in no thrust from the sails at all, but also smaller drift angles. By including hydrodynamics in the control algorithm, the sails will operate at a lower loading, ensuring that they actual produce positive effective thrust, but also a larger drift angle compared to the sails in off position. There is a clear difference in the importance of drift between wingsails and Flettner rotors. Flettner rotors, which have larger side force to thrust ratios in general, have more added resistance due to drift, for the same amount of thrust. This is true both for the retractable sails and the non-retractable sails, although the pattern is more clear for the non-retractable sails. For the Flettner rotor, the difference between retractable and non-retractable sails is large. This is explained by the relatively large drag coefficient in off-position.

Not only can a non-retractable sail generate drag by itself, it can also push the ship sideways, whenever the wind is coming from the side. It seems that a Flettner rotor in off position is a large source of added drift-induced resistance. The performance of the wingsail is much less affected by the ability to retract when not in use, as the drag coefficient in off-position is very small. It is interesting to see how the rudder is greatly increasing the performance. At first, one might think that the only purpose of a rudder is to balance the yaw moment from the sails. However, in doing so, the side force on the ship as a whole is greatly increased. As the rudder is an effective lifting surface, it is much better to produce side force with the rudder than it is to produce it with the ship hull. The fact that the keel has a very small effect on the overall performance of the ship can also be explained by this. Since the keel is increasing the stabilizing yaw moment on the ship hull, there is less need for the rudder. However, the rudder was not actually the problem. Since the rudder is less needed for balancing the yaw moment, it produces less side force, which must instead be balanced by the ship hull and keel. This is part of the reason why the mean drift angle is increased when the keel is added. Another reason is that the sail control algorithm allows larger drift angles, as the keel improves the drift characteristics of the ship hull. The influence of the rudder could change significantly if the balance of the hull was different. For instance, if the yaw restoring moment from the hull was larger than the yaw moment from the sails, the rudder would have to be turned in the opposite direction, in order to balance the ship. This would produce a side force in the same direction as the sails, which would increase the drift angle. Since the yaw moment from the keel affects how the rudder is used, the position of the keel can probably be optimized to give better results. From a purely steady state perspective, where rudder stall is not an issue, the more optimal position would be further forward, so that it generates less stabilizing yaw moment. However, this could be problematic from a maneuvering perspective, as the necessary rudder angle for turning might increase. Maneuvering and hull balance is in fact already an issue. The necessary rudder angle calculated by the route simulation code is sometimes larger than 30 degrees, which would probably cause the rudder to stall in reality. That is, some of the events that happened in the simulation is not realistic, and in reality, the sail loading would need to be reduced in order to avoid rudder stall. This would further reduce the predicted energy savings due to the sails. The rudder angle is in general larger when Flettner rotors are used, than it is when wingsails are used, which means that this problem is more severe for the Flettner rotor. Moving the keel further back should help the rudder stall problem. Even if the rudder is not stalling in steady state condition, it might stall if a turning maneuver is necessary, which is an argument for putting the keel further back.

**Acknowledgements**

We would like to thank the Research Council of Norway, DNV GL and Rolls-Royce Marine AS for funding this research through the research program called "Low Energy and Emission Design of Ships" (LEEDS) (Grant no. 216432/O70) at the Department of Marine Technology, NTNU.

**References**

ANDERSON, J.D. (2005), Fundamentals of Aerodynamics, McGraw-Hill

BERRISFORD, P. et al. (2011), *The ERA-Interim archive Version 2.0*, ERA Report Series 1, ECMWF, Shinfield Park, Reading

BERTRAM, V., 2012. Practical ship hydrodynamics. Oxford: Elsevier.

CATMULL, E.; CLARK, J. (1978), *Recursively generated B-spline surfaces on arbitrary topological meshes*, Computer-Aided Design 10(6), pp.350-355

CHARRIER, B. et al. (1985), *Foundation Cousteau and windship propulsion,* J. Wind Eng. and Industrial Aerodynamics 20, pp.39-60

EBERHART, R.C.; KENNEDY, J. (1995), *A new optimizer using particle swarm theory*, 6th Symp.

Micro Machine and Human Science, New York, pp.39-43

ECA, J.; HOEKSTRA, M. (2008), *The numerical friction line*, J. Marine Science and Technology 13(4), pp. 328-345

GRAF, K.; HOEVE, A.; WATIN, S. (2014), *Comparison of full 3D-RANS simulations with 2D-RANS/lifting line method calculations for the flow analysis of rigid wings for high performance multihulls*, Ocean Engineering 90, pp.49-61

HIRT, C.W.; NICHOLS, B.D. (1981), *Volume of fluid (VOF) method for the dynamics of free boundaries*, J. Computational Physics 39(1), pp.201-225

HYMPENDAHL, O.; CIORTAN, C. (2015), *Systematic assessment of model errors in CFD ship resistance simulations*, NuTTS, Cortona

ISSA, R.I.; GOSMAN, A.; WATKINS, A. (1986), *The computation of compressible and incompressible recirculating flows by a non-iterative implicit scheme*, J. Comp. Physics 62(1), pp. 66-82

KRAMER, J. (2016), GitHub profile, https://github.com/jarlekramer

KRAMER, J.; STEEN, S. (2015), *Importance of the free surface for the drift-induced forces on a ship-like foil*, NuTTS, Cortona

KRAMER, J.A.; STEEN, S.; SAVIO, L. (2016), *Experimental study of the effect of drift angle on a ship-like foil with varying aspect ratio and bottom edge shape*, Ocean Eng. 121, pp.530-545

MENTER, F.R. (1994), *Two-equation eddy-viscosity turbulence models for engineering applications*, AIAA J. 32(8), pp.1598-1605

OUCHI, K.; UZAWA, K.; KANAI, A.; KATORI, M. (2013), *"Wind Challenger" the Next Generation Hybrid Sailing Vessel*, 3rd SMP, Launceston, pp.562-567

PATANKAR, S.V.; SPALDING, D.B. (1972), *A calculation procedure for heat, mass and momentum transfer in three-dimensional parabolic flows*, Int. J. Heat and Mass Transfer 15(10), pp.1787-1806

PRANDTL, L.; TIETJENS, O.G. (1934), Fundamentals of Hydro- and Aeromechanics, Dover Publ.

RAVEN, H.C.; PLOEG, A.v.d.; ECA, L. (2006), *Extending the benefit of CFD tools in ship design and performance prediction*, 7th Int. Conf. Hydrodyn., Ischia, pp.573-580

SÖDING, H. (1998), *Limits of potential theory in rudder flow predictions,* Ship Technology Research 45(3)

SPALDING, D. (1961), *A single formula for the "law of the wall"*, J. Applied Mech. 23(3), pp.455-458

TRAUT, M. et al. (2014), *Propulsive power contribution of a kite and a Flettner rotor on selected shipping routes*, Applied Energy 113, pp.362-372

WALKER, J.G. (1985), *A high performance automatic wingsail auxiliary propulsion system for commercial ships*, J. Wind Eng. and Industrial Aerodynamics 20, pp.83-96

ZHANG, W.; BENSOW, R.; GOLUBEV, M.; CHERNORAY, V. (2013), *Flow past a rotating finite length cylinder: numerical and experimental study*, AIAA, Texas

## Paper 3: Hydrofoil simulations – non-linear lifting line vs CFD

Written by Jarle Vinje Kramer, John Martin Kleven Godø, and Sverre Steen

Published and presented on the Numerical Towing Tank Symposium in October 2018

# Hydrofoil simulations – non-linear lifting line vs CFD

**Jarle V. Kramer, John Martin K. Godø, Sverre Steen**
Norwegian University of Science and Technology, Trondheim/Norway
jarle.a.kramer@ntnu.no

## 1 Introduction

In this article we present results from two different simulation methods. One is a relatively simple and computational fast lifting line method, with significant extensions from the classical lifting line theory in order to handle non-linear lift, non-planar geometry, interaction effects between several wings in close proximity, and model free surface effects at high speed. The other is three-dimensional RANS CFD using OpenFOAM. We present comparisons of the integrated forces as well as the lift distribution over the span of the wing from the two methods for some test cases. The validity of the lifting line method is discussed relative to the free surface modelling and the capability of modelling non-planar geometry

Our motivation for developing the lifting line method is to create a computational tool for design of hydrofoils. In order to optimize a hydrofoil design, one needs to perform many simulations of different wing geometries. The problem with three-dimensional CFD simulations for this task is the computational time. The required mesh size for a hydrofoil CFD simulation will typically be 10-20 million cells – even with a relatively coarse resolution – and this can take days to complete on a relatively fast desktop workstation. A solution is to first use a simpler and faster simulation method in an optimization loop with all necessary design variables in order to create an initial design. The practical limitation on the range and number of design variables are dependent on the computational speed of the simulation method. Based on the initial design one can further *fine tune* the geometry based on CFD simulations– or other advanced simulation methods – by for instance using fewer design variables in the final optimization process.

The lifting line method is an interesting candidate for a simplified simulation tool due to its ability to handle viscous effects. This can be important to take into account, as the lift can easily vary with 5-10% for a given wing geometry as a function of Reynolds number. Neglecting viscous effect on the lift can therefore introduce relatively large errors in the results. The lifting line method finds the circulation along the span of the wing by matching Kutta-Juokowski's law with the lift calculated from sectional lift coefficients that is dependent on the local two-dimensional foil geometry. Viscous effects on both drag and lift can be included in the model, for instance by using two-dimensional CFD simulations to calculate the force coefficients. This is an advantage relative to other potential theory methods such as panel methods and vortex lattice methods. Although it is possible to include viscous effects in panel methods as well, it is significantly more complex, and it relies on simplified models of boundary layer theory.

That being said, the lifting line method introduces large simplifications as well and will only be valid for a limited set of hydrofoil designs. The purpose of this work is to investigate when the lifting line method is accurate, and when the fundamental simplifications are too large.

## 2 Non-linear lifting line method

Our non-linear lifting line method builds on the same basic principle as Prandtl's classical lifting line theory but is extended to include more physics and to be more flexible in terms of geometry. Specifically, the following features are included in our method:

- Non-linear lift model which can take into account viscous effects, including stall
- Free surface effects based on the simplified *high-speed* version of the linear free surface condition

- Arbitrary span shape, which for instance can include features such as winglets, wing-sweep and dihedral.
- Interaction effects between several wings in close proximity – e.g. a main wing and a tail wing
- Unsteady simulations, which is explained more in detail in reference [1]. In this paper, only the steady state version of the lifting line method is used

Similar modern extensions of Prandtl's lifting line theory have been made before. Examples can be found in reference [2], [3] and [4]. However, we have not found any examples that include a model of free surface effects. The free surface can have a large effect on the lift distribution and is therefore important to consider when analyzing and designing hydrofoils.

**The lifting line algorithm works as follows:**
The lifting line model collapses the three-dimensional wing geometry into a several horseshoe vortices with constant vortex strength. There are *bound vortices* that makes up the span geometry of the wing, and *free vortices* that extends from the wing in the direction of the incoming velocity. The bound vortex represents the circulation created by the wing, while the free vortices represents the circulation that is shed into the wake while the wing is moving.

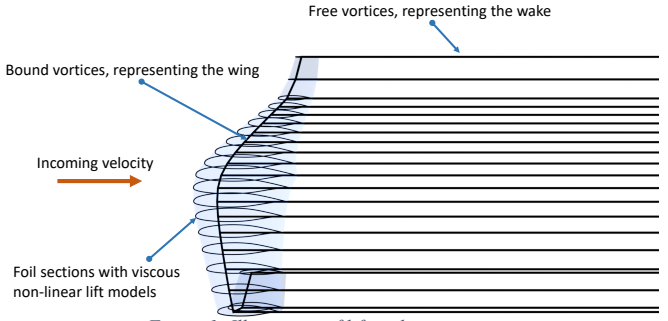

*Figure 1: Illustration of lifting line geometry*

Each line segment making up the horseshoe vortices induces velocity at every point in space. This velocity is calculated based on the line geometry and the strength of the horseshoe vortex. The induced velocity at any point in space will be linearly dependent on the strength of each horseshoe vortex. In order model a wing we need to calculate the induced velocity at several control points which is defined to be in the middle of each bound vortex. The induced velocity at every control point can be expressed as a matrix, $\boldsymbol{A}$, that is only dependent on the geometry of the lifting line multiplied with a vector representing the strength of each vortex, $\boldsymbol{\Gamma}$, so that the induced velocity, $\boldsymbol{u}_i = \boldsymbol{A\Gamma}$. The strength of each horseshoe vortex is the unknown quantity in the simulation. The basic principle behind the equation system to be solved is to require that lift calculated from Kutta-Juokowski's law matches the lift calculated from the sectional lift coefficient at each control point along the wing. The sectional lift from Kutta-Juokowski's law can be calculated from the following equation, where $U$ is the incoming velocity and $\rho$ is the density:

$$L = \rho \Gamma U$$

The lift from the sectional lift coefficient is dependent on the foil geometry and the angle of attack. In order to calculate the lift coefficients for a section of the wing, one can use two-dimensional CFD, panel methods such as XFoil or use experimental data if available. The lift function can be linear for small angles of attack but will have non-linear behavior for angles of attacks close to stall. The angle of attack on each control point along the wing is dependent on the geometric angle of attack and the induced angle of attack – and therefore the strength of each horseshoe vortex. The following equation ca be used to calculate the lift, where $c$ is the chord length, $C_L$ is the sectional lift coefficient, which is dependent on the effective angle of attack $\alpha_{eff}$:

$$L = \frac{1}{2}\rho C_L(\alpha_{eff}) c U^2$$

These two equations can be combined to solve for the strength of each horseshoe vortex which gives the following relation at every control point.

$$\frac{2\Gamma}{cU} = C_L(\alpha_{eff})$$

This gives a non-linear equation system, where $\alpha_{eff}$ is dependent on both the geometrical and the induced angle of attack. Using the expression for the induced velocity, we get the following equation for the effective angle of attack, where $\boldsymbol{n}$ is a vector on each horseshoe vortex that is normal to both the incoming velocity and the bound vortex line, while $\boldsymbol{t}$ is a vector that is parallel to the incoming velocity:

$$\alpha_{eff} = \alpha + \alpha_i = \alpha + \tan^{-1}\left(\frac{\boldsymbol{u_i} \cdot \boldsymbol{n}}{\boldsymbol{U} + \boldsymbol{u_i} \cdot \boldsymbol{t}}\right) = \alpha + \tan^{-1}\left(\frac{\boldsymbol{A_i}\,\boldsymbol{\Gamma} \cdot \boldsymbol{n}}{\boldsymbol{U} + \boldsymbol{A_i}\,\boldsymbol{\Gamma} \cdot \boldsymbol{t}}\right)$$

In order to linearize this equations system, we can assume the lift is linearly dependent on the effective angle of attack such that $C_L = C_{L0} + \frac{\partial C_L}{\partial \alpha}\alpha_{eff}$, that $\tan^{-1} x \approx x$, and that $u_i \cdot t \approx 0$. In order to solve the complete non-linear system, we perform several iterations, where we construct a new local linear version of the system that is always based on the last estimate of the effective angle of attack. That is, the linear lift model is updated to match the complete non-linear model in the vicinity of the last effective angle of attack and the tangential velocity is updated to include the induced velocity from the last iteration. The iteration loop stops when the estimated circulation distribution converges.

In order to capture the effect of the free surface, we use a simplified model. Under the assumption of high speed, linear free surface condition and potential theory, the velocity potential due to the wing at the free surface should be constant. See for instance reference [5] for an in-depth explanation. This can be achieved by mirroring the lifting line geometry about the free surface and reversing the vortex strength. That is, the line geometry is mirrored, but the direction of the lift is the kept the same for the mirrored geometry. This is different from a *normal* mirroring that could be used to model a ground plane, as in that case, the direction of the lift would also be reversed. The induced velocity from the mirrored vortex lines is evaluated at the three-quarter chord, or half a chord length behind the bound vortex. This was deemed necessary in order to model the vertical induced velocity from the mirrored line, and greatly improves the results relative to evaluating the induced velocity at the bound vortex. This was inspired by the Weissinger approximation [6], which suggest that the three-quarter chord is good location to evaluate the induced velocity.

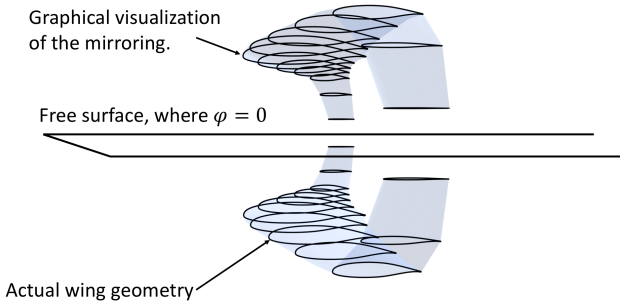


*Figure 2: Illustration of the free surface. Notice the direction of the foils in the mirrored wing geometry*

## 3 CFD setup

OpenFOAM version 1712+ is used to do the CFD simulations. Simulations with free surface modelling is done with the *interFoam* solver which is based on the unsteady PISO algorithm and the *Volume of* Fluid (VoF) model to capture the free surface. Simulations without free surface effects are done with *simpleFoam* which is a steady state solver based on the SIMPLE algorithm. The turbulence model is k-omega SST. We use a custom Python library that we develop to set up the CFD simulations in a consistent and automated manner. The library uses the dimensions of the geometry, the Reynolds

number and best practices based on our own past experience to create the case folders and setup files for OpenFOAM. The mesh is created using SnappyHexMesh. Right outside the wing geometry there are inflation layers. The friction on the wing surface is first estimated using a friction line, and the thickness of the first layer is then calculated based on the estimated friction coefficient and a target y+ value. The cell length right outside the inflation layers is set according to a maximum cell length value that ensures the geometry is captured. An illustration of the mesh can be seen in the figure below, also showing refinement regions in the wake and around the free surface. Table 1 shows the most important settings in the CFD simulation as created by the Python library for this specific case. There are two columns; one for the three-dimensional simulations and one for the two-dimensional simulations that are used to generate data to be used together with the lifting line model. The three-dimensional simulations are performed with lower resolution than the two-dimensional simulations in order to keep the simulation time down to a practical level.

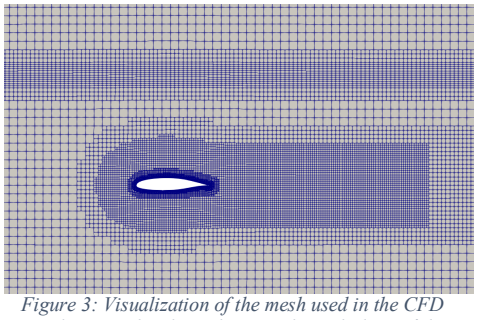

*Figure 3: Visualization of the mesh used in the CFD simulations. The plane shown is the mid-plane of the wing. There are refinement zones in the wake of the wing and in the area close to the free surface.*

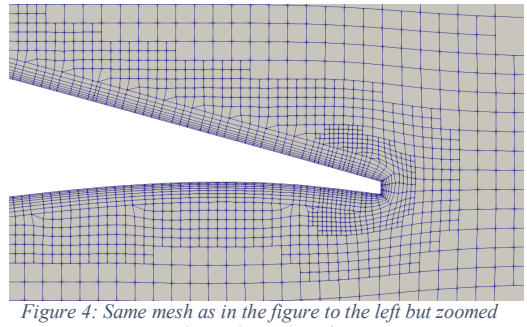

*Figure 4: Same mesh as in the figure to the left but zoomed into the trailing edge of wing.*

*Table 1: Simulation parameters*

| Parameter name | 3D wing simulations | 2D foil simulations |
|---|---|---|
| Max feature cell size / chord length | 0.0021 | 0.001 |
| Max background cell size / chord length | 0.14 | 0.1 |
| Wake refinement cell size / chord length | 0.35 | 0.01 |
| Number cells between layers | 5 | 5 |
| Number of wall layers | 7-9 | 5-10 |
| Target y+ | 60 | 60 |
| Approximate number of cells | 15 Million | 100 000 |
| Max Courant number | 20 | 10 |

## 4 Results

The results of our validation study are shown below. The goal is to answer two fundamental questions: can the lifting line method model free surface effects at speeds that are realistic for hydrofoil vessels, and can it model non-linear wing geometries? First, we tested non-linear wing geometries using steady state CFD simulations, without free surface modelling. Then we tested a planar wing geometry at different speeds and different Froude submergence numbers, with free surface modelling. All wing geometries tested used the foil profile NASA LS417, which is a common foil geometry for low-speed airplanes. The sectional lift and drag for the foil profile as a function of Reynolds number and angle of attack was computed using two-dimensional CFD simulations. The results are presented as the lift distribution over the non-dimensional span of the wing, and as integrated forces in terms of coefficients. The difference in the lift distribution between the CFD and lifting line is also plotted. The non-dimensional span distance goes from 0.0 at the mid-section of the wing, to 1.0 at the wing tip.

**Non-linear wing geometry – sweep and winglet**

The non-linear wing geometries we tested consisted of a non-swept wing with a simple winglet design with varying *winglet radius* and a wing without any winglet, but with different sweep angles. The wings had an aspect ratio of 8 and a mean chord length of 0.5. The wings with the winglet had a taper ratio of 0.3, while the swept wings had a taper ratio of 0.5. The geometry and results from the simulations can be seen in the figures below

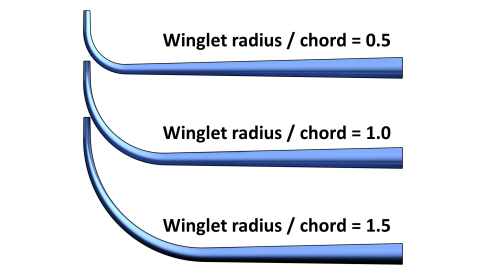


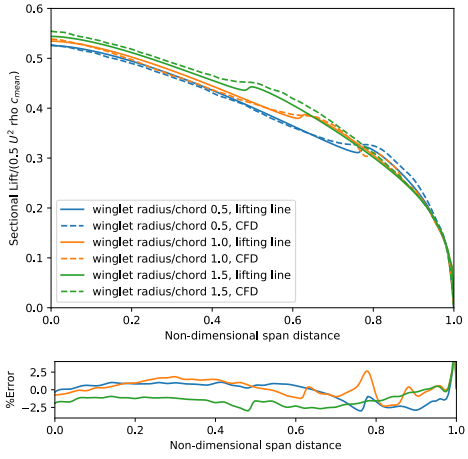


| Case | $C_L$ LL | $C_L$ CFD | E[%] | $C_D$ LL | $C_D$ CFD | E[%] |
|---|---|---|---|---|---|---|
| | 0.415 | 0.411 | 0.8 | 0.01732 | 0.01710 | 1.3 |
| | 0.434 | 0.423 | 2.6 | 0.01825 | 0.01945 | -6.2 |
| | 0.450 | 0.455 | -1.1 | 0.01915 | 0.01895 | 1.1 |

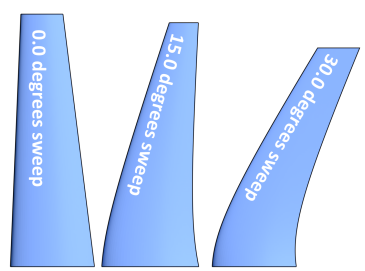


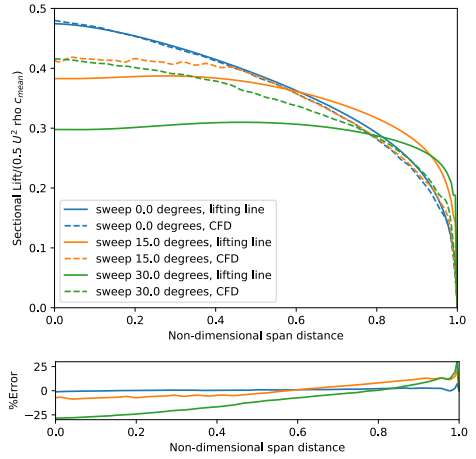


| Case | $C_L$ LL | $C_L$ CFD | E[%] | $C_D$ LL | $C_D$ CFD | E[%] |
|---|---|---|---|---|---|---|
| | 0.368 | 0.365 | 0.8 | 0.01523 | 0.01542 | -1.2 |
| | 0.346 | 0.353 | -2.1 | 0.01522 | 0.01468 | 3.6 |
| | 0.280 | 0.297 | -6.0 | 0.01483 | 0.01318 | 12.6 |

**Free surface effects**

In order to test the free surface model in the lifting line method we simulated a planar wing with aspect ratio of 8, taper ratio of 0.5 and a mean chord length equal to 0.5 m. The importance of the free surface is dependent on both the actual submergence – the less the foil is submerged, the more important is the free surface – and on the Froude submergence number defined as $Fr_h = U/\sqrt{gh}$, where $h$ is the submergence – the higher the Froude submergence number, the more valid should the high-speed version of the free surface condition be. There are many types of hydrofoils with different speeds and submergence, but a case we are currently working on is hydrofoils for high-speed passenger ferries. These hydrofoils will have a submergence between 1 – 2 chord lengths, and Froude submergence numbers between 4 and 6. These numbers are based on a design speed of 30-35 knots and mean chord length of roughly 1 m. We have chosen to use these numbers in our test case. The results are shown below

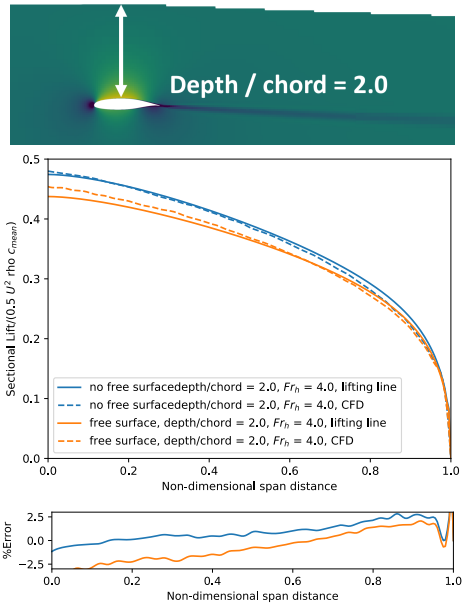


| Case | $C_L$ LL | $C_L$ CFD | E[%] | $C_D$ LL | $C_D$ CFD | E[%] |
|---|---|---|---|---|---|---|
| | 0.368 | 0.365 | 0.8 | 0.01523 | 0.01542 | -1.2 |
| | 0.344 | 0.349 | -1.3 | 0.01586 | 0.01574 | -0.7 |

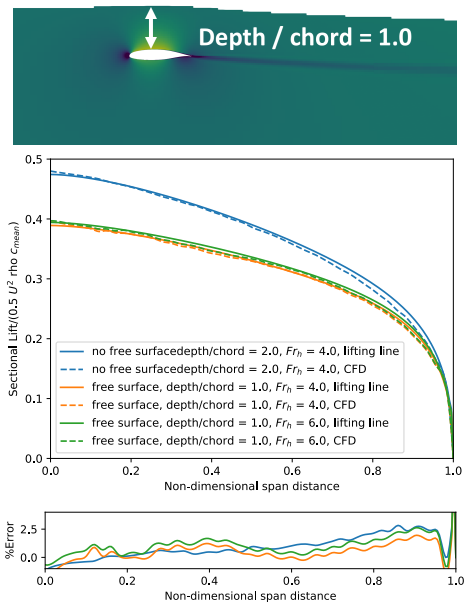


| Case | $C_L$ LL | $C_L$ CFD | E[%] | $C_D$ LL | $C_D$ CFD | E[%] |
|---|---|---|---|---|---|---|
| | 0.368 | 0.365 | 0.8 | 0.01523 | 0.01542 | -1.2 |
| | 0.312 | 0.311 | 0.3 | 0.01681 | 0.0157 | 7.0 |
| | 0.317 | 0.315 | 0.9 | 0.01634 | 0.01503 | 8.7 |

## 5 Conclusion

The lifting line method – including the high-speed version of the linear free surface condition - is both simple to implement and fast to execute on a computer. While a CFD simulation can take days, the lifting line method takes seconds. The test cases presented in this paper show a relatively good match between the lift distribution calculated with lifting line and CFD both with winglet and with free surface. However, the lifting line method shows relatively large differences in the lift distribution when sweep is introduced. This suggest that the lifting line method is limited to wing geometries that lies in the plane that is normal to the incoming velocity. Considering the simplicity of the method, we are particularly happy about the match between the CFD simulations with a non-linear free surface model (VoF) and the lifting line method with a high-speed version of the linear free surface condition.

## Bibliography


[1] J. M. K. Godø, J. V. Kramer, S. Steen and L. Savio, "Unsteady forces on hydrofoil vessels in waves - validation of a dynamic lifting line using CFD," in *Numerical Towing Tank Symposium*, Cortona, 2018.

[2] D. F. Hunsaker, "A Numerical Lifting-Line Method Using Horseshoe Vortex Sheets," Utah State Univeristy, 2011.

[3] W. F. Phillips and D. O. Snyder, "Modern Adaptation of Prandtl's Classic Lifting-Line Theory," *Journal of Aircraft,* vol. 37, no. 4, pp. 662-670, 2000.

[4] C. Duport, M. Deberque, J.-B. Leroux, K. Roncin and C. Jochum, "Local Results Verification of a 3D Non-Linear Lifting Line Method for Fluid-Structure Interactions Simulation on a Towing Kite for Vessels," in *High-Performance Marine Vehicles*, Zevenwacht, 2017.

[5] O. M. Faltinsen, Hydrodynamics of High-Speed Marine Vehicles, Cambridge University Press, 2005.

[6] J. Weissinger, "The Lift Distribution of Swept-Back Wings," NASA, 1947.

[7] J. D. Anderson, Fundamentals of aerodynamics, Tata McGraw-Hill, 2010.

[8] B. Maskew, "VSAERO Theory Document," NASA, 1987.

# Paper 4: Simplified Test Program for Hydrodynamic CFD Simulations of Wind-Powered Cargo Ships

Written by Jarle Vinje Kramer and Sverre Steen

Published in Journal of Ocean Engineering, December 2021

Ocean Engineering 244 (2022) 110297

Contents lists available at ScienceDirect

Ocean Engineering

journal homepage: www.elsevier.com/locate/oceaneng

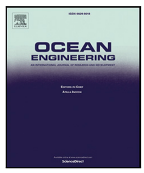

# Simplified test program for hydrodynamic CFD simulations of wind-powered cargo ships

Jarle Vinje Kramer *, Sverre Steen

*Department of Marine Technology, Norwegian University of Science and Technology, Otto Nielsens veg 10, 7052 Trondheim, Norway*

ARTICLE INFO

*Keywords:*
Computational Fluid Dynamics
Wind-power
Hydrodynamics
Simplifications
Rudder model

ABSTRACT

Four practical simplifications for modeling the hydrodynamic properties of a wind-powered cargo ship with CFD and a route simulation model is evaluated. We first test how much the drift-induced hull forces are dependent on Froude number, model scale, and heel angle. Then, we test the mathematical assumptions in the MMG maneuvering model, with particular focus on the rudder resistance as a function of drift angle, rudder angle and propeller thrust. The overall goal is to see if the hydrodynamics of the ship can be modeled with both a simplified CFD setup and a simplified route simulation model. For each tested simplification, we find that they can be used under specific conditions, but not always. We give specific recommendations based on our results. To improve the predicted rudder resistance from the MMG model, we suggest a slightly modified model based on classical lifting line theory. All the numerical experiments are performed using the open source CFD library OpenFOAM. The simulation setup is described, including details of the mesh design. The numerical uncertainty is quantified, and the simulations are compared against benchmark experiments.

## 1. Introduction

Modern sail technology, such as wing-sails, rotor sails, and kites, can significantly reduce a cargo ship's fuel consumption. Some examples of the benefit of wind power are shown in Ouchi et al. (2013), Tillig et al. (2020), Kramer et al. (2016a), and Väinämö (2017) where the estimated reduction in fuel consumption is between 8%–48%. However, the wind generated thrust is not without its challenges. For practical cargo ship velocities and wind conditions, there is usually a side force from the sails that is several times larger than the thrust (Kramer et al., 2016a). The aerodynamic side force and the resulting yaw moment must therefore be balanced by opposite hydrodynamic forces. Depending on the longitudinal placement of the sails, this is achieved by generating a lift force on both the hull and the rudder by moving with a steady drift and rudder angle. Additionally, the sails will often apply a significant heel moment, as the side force is effectively acting at a position far above the deck. When the hull rotates to balance the heel moment, the hydrodynamic properties of the ship might change. These hydrodynamic effects are important to consider for a wind powered vessel as they can significantly increase the calm water resistance. The fuel savings due to wind-power might be overestimated if the effect of the side force is neglected and the side force can have an influence on how the sails should be operated (Kramer et al., 2016a).

To quantify the benefit of wind-power for a given ship design, it is common to perform route simulations where a model of the ship and the sails are used together with weather data. The hydrodynamic model of the ship mus be able to calculate the resistance, side force, yaw moment and heel moment as a function of the aerodynamic forces if the added resistance due to the sails is included in the simulation. Although there is no standard way of modeling these things, it is common to use models from ship maneuvering theory, either directly or as inspiration. Two examples of this type of modeling can be found in Tillig et al. (2020) and Kramer et al. (2016a).

Depending on the mathematical form of the hydrodynamic model used in the route simulation, there are usually several design specific coefficients that needs to be estimated based on some method. In the earliest stages of a design phase, purely theoretical or empirical methods might be a good choice (Tillig, 2020; Tillig et al., 2020; Tillig and Ringsberg, 2020). At the end of the design phase, the ship can be thoroughly tested with either Computational Fluid Dynamics (CFD), towing tank experiments, or both. The data from experiments or simulations are then used to tune the coefficients in the model so that the forces and moments predicted by these models are as close to the tuning data as possible. CFD is also a potential tool for the middle of the design phase, where several different geometries of both the hull and the rudder need to be tested. However, during an iterative design loop, long simulation times quickly becomes impractical. To generate a complete hydrodynamic model of the ship, several variables must

* Corresponding author.
*E-mail address:* jarle.a.kramer@ntnu.no (J.V. Kramer).

https://doi.org/10.1016/j.oceaneng.2021.110297
Received 4 February 2021; Received in revised form 12 November 2021; Accepted 28 November 2021
Available online 21 December 2021

be accounted for and the required number of tests can easily become high. A quick and simplified approach is therefore beneficial, but it is also important to be aware of potential inaccuracies introduced by a simplified approach.

This paper explores four practical simplifications that can be used when generating a hydrodynamic route simulation model of a wind powered ship based on CFD results. We focused on simplifications that are already used in the scientific field, but where we believe there is a need for better documentation of the accuracy. The tested simplifications are listed below, with further explanation in the following paragraphs:

- Neglect the free surface for the computation of drift-induced forces.
- Compute drift-induced forces in model scale
- Neglect the effect of heel on the drift-induced forces
- Use an established maneuvering model – the MMG model – as basis for a route simulation model

All of these simplifications reduce the complexity and time for setting up a hydrodynamic model of a wind powered ship, but they also introduce potential errors in the estimated forces and moments. The main question in this paper is: how large is the error introduced by each simplification? We explore this question by using a case study of a 5000 DWT general cargo ship. The magnitude of the error is discussed in regards to predicting the hydrodynamic resistance of wind-powered ships under the influence of a side force from sails. We focus exclusively on the hydrodynamics, and the aerodynamics of the sails and other aspects of route simulations are therefore not addressed directly.

Neglecting the free surface allows for a considerable speed up of a CFD simulation due to several factors: the physical model becomes simpler without the free surface dynamics, the mesh size can be reduced when the geometry above the free surface is not part of the simulation, and it may allow for time-efficient steady-state solvers. Although it is well-known that the wave resistance of a ship is significant for practical cargo ship Froude numbers, it is less clear how maneuvering coefficients and drift-induced forces are affected by the free surface. It is common to neglect the free surface in maneuvering simulations when the Froude number is lower than approximately 0.15 (Ohashi et al., 2018) while the free surface is usually included for higher Froude numbers (Duman and Bal, 2019). Although it is natural that the waves generated by the ship will affect the drift-induced forces at some point, the exact limit on the Froude number is unclear in the existing work. We have previously studied drift-induced forces on a low aspect-ratio foil geometry, both experimentally (Kramer et al., 2016b) and with CFD (Kramer and Steen, 2015), and concluded that the free surface effects where small for Froude numbers up to approximately 0.25. Longo and Stern (2002) presents experimental data for the drift-induced forces on the ship geometry Series 60 for a wide range of Froude numbers. The results indicate that the side force and drift-induced drag only differ with up 11% for Froude numbers between 0.1 and 0.3. Due to the computational practicality of neglecting the free surface, we wanted to test this simplifications for our case study ship for Froude numbers between 0.15 and 0.3.

Small scale models are routinely used to test drift-induced forces on ships. This is done both in experiments (van der Kolk et al., 2019) – where the size of the model is limited by the size of the towing tank – and in simulations (van der Kolk et al., 2020) — where reduced model size is used to increase the relative cell size close to solid walls and therefore reduce the total mesh size and computational time. The drift-induced force coefficients are usually not scaled based on Reynolds number. However, there are also papers in the literature that indicate that this is not a very accurate approach for computing full-scale drift-induced forces and maneuvering coefficients. One example is Jin et al. (2016), which shows the result from numerical experiments of both static drift and pure sway for the ship geometry KVLCC2 at model scales 1:58, 1:100, 1:225, and 1:1. The results indicate that the yaw moment is not much affected by scale effects, but the sway force is overpredicted by as much as 21.3% in the static drift test and 27.4% in the pure yaw test. Another example can be found in Bhushan et al. (2009) which shows results from a 20/20 zig-zag test of the ship geometry DTMB 5415 in a model-scale of approximately 1:211 and full-scale. The results show that both the rudder checks and the overshoot on the heading angle is overpredicted in model scale, by 5% and 13% respectively. As such, these papers indicate that too low Reynolds number might be problematic for estimating full-scale drift-induced forces. At the same time, they both focus on model scales suitable for physical towing tanks while CFD simulations are not restricted by physical limitations. We therefore wanted to test how the drift-induced forces on a ship depend on the Reynolds number, and whether there exists a scale large enough to avoid scaling issues on the drift-induced force coefficients, yet small enough to speed up the CFD simulations considerably relative to full-scale simulations.

Neglecting heel when computing the drift-induced forces on a ship is practical as it removes an entire state variable from the model, and therefore the number of necessary CFD simulations. It is also a simplification that is common in existing maneuvering models (Yasukawa and Yoshimura, 2015; Abkowitz, 1964), even though a maneuvering ship can experience significant heel angles. For instance, Bhushan et al. (2009) show an example of a ship that experiences heel angles in the range of −18 degrees to +15 degrees during a standard 20/20 zig-zag test. Bertram (2000) states that the effect of heel on drift-induced forces is small for many practical maneuvering situations for cargo ships, but that it must be included for situations where the heel angle exceeds 25 degrees. This limit is well above what we expect will be the case for wind-powered merchant ships. Although the experienced heel angle might be large for conventional sailing vessels, such as regatta boats and pleasure crafts, there will probably be strict limits for wind-powered cargo ships that must be enforced by the control system of the sails. The recommended limit on the heel angle due to steady continuous wind loads is for instance 16 degrees in the DNV stability classification rules (DNV-GL, 2016). This is because continuous operation with large heel angles could be problematic for cargo storage, the comfort of the crew, and generally pose a safety risk. Neglecting the effect of heel on the drift-induced forces therefore seemed like a possible simplification for route simulations of wind-powered ships, but we also saw it as necessary to test this simplification further due to lack of existing validation in the literature.

The final simplification evaluated in this paper is to utilize the simplicity of the MMG model to reduce the number of CFD simulations for a given ship design to a minimum. This is a widely used maneuvering model that contains several practical simplifications for modeling the forces on a ship as a function of drift angle, yaw rate, rudder angle and propeller thrust. In particular, the interaction between the rudder, hull and propeller is treated with models containing relatively few variables. If the assumptions in the model are appropriate, the model can be tuned using the results from just a few CFD simulations, while still be accurate for state values not directly tested. The accuracy of several of the assumptions in the model regarding hull forces and rudder sway force has been tested before (Yasukawa and Yoshimura, 2015). Although not directly related to the MMG model, similar simplifications on the rudder forces are also explored in Molland and Turnock (1995, 2002) with good results. However, we have not seen any examples in the scientific literature that focus on the model's ability to predict rudder resistance. This might be because this force component is often not that important for maneuvering applications. It is, however, one of the most important variables for route simulations of wind-powered ships. We therefore test all aspects of this model relevant for wind-powered ships, and in particular the rudder resistance at varying propeller loading. We test both the standard version of the MMG model and a slightly modified version where the default rudder model is switched to a classical lifting line model. The reason for this switch was that

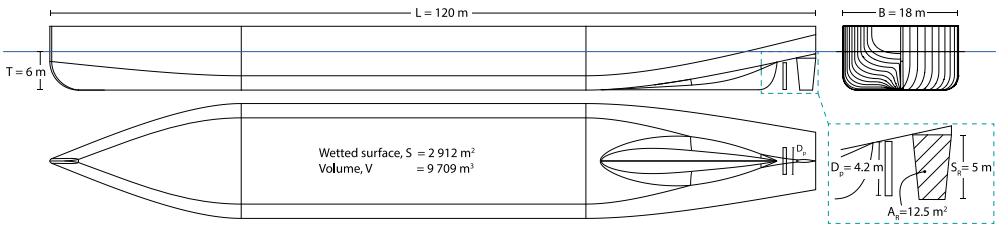


**Fig. 1.** Illustration of the case study ship geometry.

**Table 1**
Solver parameters.

| | Free surface | No free surface |
|---|---|---|
| OpenFoam solver | InterFoam | SimpleFoam |
| Simulation time | $7L/U$ | 6000 iterations |
| Max time step, physical | $0.01L/U$ | |
| Max Courant number | 40 | |
| Max alpha Courant number | 10 | |

the default model was found to not be very accurate for the rudder resistance, as will be shown later in this paper.

Section 2 introduces our case study ship along with an overview of the test program for the experiments performed for this paper. The setup of the CFD simulations, along with details of the mesh design is described in Section 3. Section 4 explains the tested route simulation model, including our modifications to the MMG model and the tuning procedure for adjusting the coefficients in the model based on CFD results. Section 5 shows results from convergence studies and validation experiments. Section 6 presents results from the numerical experiments for each simplification along with discussions. We end with our conclusion in Section 7.

## 2. Case study details

### 2.1. Ship geometry

The ship tested in this paper represents a 5000 DWT general cargo ship intended to operate at a design speed of 10 knots. The hull shape is a custom geometry with a flat bottom, no bulb, and a slender skeg. An overview of the design with main dimensions, can be seen in Fig. 1. The geometry is also available online at Kramer (2021). The propeller model used in this case study consist of an actuator disk which applies a constant thrust and torque independent of the inflow at the location of the propeller. The rudder is a spade rudder geometry with a taper ratio of 2/3. The foil profile is of the type NASA LS0013, where the thickness is increased from the original 13% to 15%.

### 2.2. Test performed for this case study

The hull without the rudder is first tested at varying drift and heel angles, at different model scales and Froude numbers. The drift angle is varied between 0 and 12 degrees, while the heel angle is varied between −20 and +20 degrees. The Froude number is varied between 0.15 and 0.3, which corresponds to full scale speeds of 10, 13.3, 16.7 and 20 knots. The model scale is varied between 1:20 and full scale. Most of the tests in this paper is done at the model scale 1:4, corresponding to a model length of 30 m and Reynolds number of approximately 68 million.

We then test the hull and rudder together at zero heel, without the free surface included in the simulation setup, at varying drift and rudder angles both with and without thrust from the propeller actuator disk. The thrust from the propeller corresponds to thrust coefficients equal to 0.5 and 0.25. The largest thrust coefficient is a rounded value that is approximately the necessary thrust for pushing the ship forward at the design speed without wind power. At 10 knots, the full scale ship resistance was estimated to be 75.1 kN. This is based on the results from the CFD simulations shown in Section 6 and conventional scaling methods for ship resistance. With a rough assumption of 10% thrust deduction, this actually corresponds to a thrust coefficient of 0.44 with the chosen propeller dimensions, but we rounded the value up to 0.5 to account for effects not analyzed in this paper, such as added resistance due to wind and waves. We chose to also test a thrust coefficient of 0.25 as a wind powered ship will operate with variable propeller thrust depending on the thrust from the sails. More details regarding our test program is also given along with each simplification in Section 6.

## 3. CFD setup

The simulations were all performed with the open-source CFD software OpenFOAM v2006+ (OpenCFD ltd, 2021). As part of an effort to ensure both consistency and efficiency when setting up CFD simulations, we use a rule-based scripting approach for setting up simulations implemented in an internally developed Python library. We present the settings used for the simulations in this paper, which matches the rules we apply to ship simulations in general. We have also published the OpenFOAM case folders, including the mesh setup and ship geometry files, for a few representative cases at an online repository found in Kramer (2021). The repository also contains all the custom extensions to the OpenFOAM library we use in this paper.

### 3.1. Solvers

We used two different OpenFOAM solvers called interFoam and simpleFoam. Both are solving the incompressible version of the Navier–Stokes equation. SimpleFoam is a steady-state solver for single phase fluids, while interFoam is an unsteady solver that allow for two different fluids in one simulation through the use of the Volume-of-Fluid (VoF) method (Hirt and Nichols, 1981). InterFoam use a combination of the PISO-algorithm (Issa et al., 1986) and the SIMPLE-algorithm (Patankar and Spalding, 1983) for solving the pressure–velocity coupling. For unsteady ship applications, we use only the PISO algorithm, with two pressure iterations per time step. SimpleFOAM only uses the SIMPLE-algorithm with relaxation factors for stabilizing the solution.

The time step in the unsteady simulation is adjusted based on two criteria; a physical limit based on ship length an velocity and a mesh limit based on the measured Courant number in the simulations. The physical limit is taken from the ITTC recommendations for practical CFD simulations of ships (International Towing Tank Conference, 2011). The Courant number limit adjusts the time step based on both the flow velocity and the velocity of the Volume of Fluid fraction. The latter is known as the alpha Courant number in OpenFOAM nomenclature. Parameters for the simulation time and time step can be seen in Table 1. In the equations listed, $L$ refers to the ship length and $U$ is the forward velocity of the ship. A convergence study of the time step can be found in Section 5.3.

### 3.2. Numerical schemes

For the most part we used a fairly standard setup for RANS simulations, with linear upwind schemes for the convection of turbulence variables, central difference for most other variables and a Euler scheme for the time integration in the unsteady simulations. A full overview of our scheme setup can be found in Kramer (2021). The only exception is the interpolation scheme used for the convective term in the velocity equations, where we use the LUST scheme rather than the more typical linear upwind scheme. The LUST scheme is a blend between linear upwind and central difference interpolation with a constant blending factor of 0.25 and 0.75 for the different schemes respectively. In our experimental validation simulations, found in Section 5.6, we have performed several of the tests using both the linear upwind scheme and the LUST scheme with the same mesh. In these tests, the LUST scheme provides slightly more accurate values for the lift and lift-induced drag at large drift angles, and comparable accuracy for the straight-ahead resistance.

### 3.3. Turbulence model

We used the turbulence model k-$\omega$ SST based on the implementation from Menter et al. (2003). The equations used to calculate the inlet values for the turbulence model is shown in Fig. 2. The value for the turbulent energy, $k$, is based on a target turbulent intensity, $I$, which is set to 1% for all the simulations in this paper. The equation for the turbulent dissipation rate, $\omega$, is the recommended value from Spalart and Rumsey (2007) which discuss different turbulent inlet values for external aerodynamic flows.

van der Kolk et al. (2020) argue that the simplifications introduced by an isotropic turbulence model could limit the accuracy of drift-induced forces on a ship due to the potentially complex flow structures arising from the separation around the hull. They therefore choose to use an Explicit Algebraic Stress Model (EASM) for their simulations. They also show results for one validation case where the error in the predicted side force with the k-$\omega$ SST model is 11.3% while the error with the EASM model is reduced to 4.7%. Although the results presented for the EASM model in van der Kolk et al. (2020) is interesting, OpenFOAM currently has a very limited selection of Reynolds Stress Models, none of which are explicit models. DES and LES alternatives are available, but both options increase the simulation time significantly due to requirements for small time steps. Our choice of the k-$\omega$ SST model was motivated by the fact that we get a relatively good match between simulation and experiment for our benchmark experiments using the k-$\omega$ SST model (see Section 5.6 for results on this) combined with a lack of good time-efficient alternatives in our chosen simulation software.

### 3.4. Boundary conditions and simulation domain

The boundaries of the computational domain consist of an inlet, outlet, a top boundary and the boundaries representing the ship geometry. An overview of the computational domain, with boundary conditions, dimensions, coordinate system and locations of the different boundaries can be seen in Fig. 2. The variables listed in the figure refer to the fields included in the simulation. $U$ and $p$ is the velocity and pressure, $k$ and $\omega$ is the turbulent kinetic energy and the specific rate of dissipation, and $\alpha$ is the volume fraction of the water. The boundaries of the hull and rudder geometry are specified as no-slip walls with continuous wall functions. When the free surface is not modeled directly, we use a symmetry plane as a boundary condition on the top of the domain, referred to as double body simulations.

There are wave damping zones close to the inlet and outlet in the simulations with free surface modeling. These zones contain body force sources that opposes the ship generated waves. We have made a custom version of wave damping for OpenFOAM simulations that are a direct implementation of the methods presented in Perić and Abdel-Maksoud (2016). The implementation can be found along with the rest of the simulation case files in Kramer (2021). The custom code is automatically complied by OpenFOAM at run time when a simulation is executed.

### 3.5. Propeller model

The propeller is modeled as an actuator disk where both the thrust and the torque is specified as body forces that varies depending on the radial distance from the propeller center. The purpose of this study was not to test a specific propeller but investigate the effect of propellers in general. As such, we chose the generic theoretical distribution known as the Goldstein optimal distribution (Goldstein, 1929). This distribution represents an ideal propeller with an optimal lift distribution according to simplified lifting line theory. The distribution is adjusted for the presence of a propeller hub, that we assume to have a diameter of 20% of the propeller diameter. The expressions for the radially varying axial force, $f_x$, and the tangential force, $f_\theta$, are shown in Eqs. (1)–(3). In the same equations, $r$ refers to the non-dimensional radial distance, and $r_h$ to the non-dimensional radial propeller hub location. Both are made non-dimensional by dividing the absolute value by the propeller radius, $R_p$. $T$ refers to the applied thrust and $Q$ to the applied torque. $\Delta$ refers to the total volume of the actuator disk and $R_h$ to the radius of the propeller hub:

$$f_x = r^* \sqrt{1 - r^*} \left( \frac{105}{8} \frac{T}{\pi \Delta \left(3R_H + 4R_p\right)\left(R_p - R_H\right)} \right) \tag{1}$$

$$f_\theta = \frac{r^* \sqrt{1 - r^*}}{r^* \left(1 - r_h\right) + r_h} \left( \frac{105}{8} \frac{Q}{\pi \Delta R_p \left(3R_H + 4R_p\right)\left(R_p - R_H\right)} \right) \tag{2}$$

$$r^* = \frac{r - r_h}{1 - r_h} \tag{3}$$

The propeller body forces are applied to all cells within a disk zone in the mesh with the same diameter and location as the propeller. The thickness of the disk is specified to be 25% of the diameter of the propeller. The mesh resolution inside the propeller disk is set to be one level higher than the resolution at the ship hull in general, which is specified in the next section. The OpenFOAM implementation of the actuator disk can be found in Kramer (2021). The relationship between thrust and torque is taken to be the same as for a four bladed Wageningen B-series propeller (Oosterveld and Oossanen, 1975) with pitch ratio of 1.2 and expanded blade area ratio of 0.8. This corresponds to a propeller that operate with advance ratio of 0.92 and 1.04 and efficiency of 69.6% and 71% for the thrust coefficients of 0.5 and 0.25 respectively.

### 3.6. Mesh

The mesh was made with the software snappyHexMesh (OpenCFD ltd, 2021), which generates primarily hexadra cells with the possibility of wall layers close to solid objects. The mesh resolution is based on two general rules. The first rule specifies the cell length normal to solid walls. The first layer thickness close to a wall is set to have a length corresponding to a target y+ value, which further depends on the friction on the walls. To estimate the frictional forces ahead of each simulation, an empirical friction line is used. We have chosen a friction line that is specifically tuned to the k-$\omega$ SST turbulence model, presented in Eça and Hoekstra (2008) and also shown in Section 3.8. The equations for calculating the thickness of the first layer are presented in Table 2, where $L$ is the ship length, $U$ the ship velocity, $\nu$ the kinematic viscosity and $C_F$ the estimated frictional coefficient. The table also show the layer expansion which dictates the increase in thickness for each new layer added, and the ratio between the final layer and the cells outside the wall layers. We use the same layer thickness close to the wall for the hull, skeg and rudder as both the skeg and the rudder are placed in the

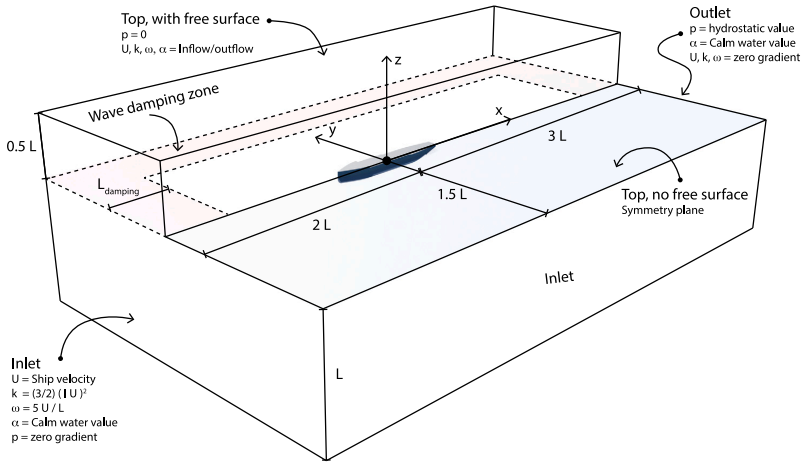


**Fig. 2.** CFD domain with boundaries and inlet values.

**Table 2**
Rules for calculating number of wall layers.

| Variable | Equation/value |
|---|---|
| Frictional velocity, $u_\tau$ | $\sqrt{0.5 C_F U^2}$ |
| Distance to wall center, $h_{\text{center}}$ | $y^+_{\text{target}} \nu / u_\tau$ |
| Thickness of first cell, $h_{\text{cell}}$ | $2h_{\text{center}}$ |
| Target y + value, $y^+_{\text{target}}$ | 60 |
| Ratio between last wall layer and first outer cell | 0.5 |
| Layer expansion | 1.3 |
| Maximum number of layers | 15 |

wake of the ship hull and therefore highly influenced by the boundary layer of the ship. We verified that this assumption was appropriate by checking the achieved y+ values on the different patches for a few representative cases. As an example, for a case with zero drift angle and rudder angle at model scale 1:4, the achieved average y+ value for the hull, skeg and rudder was 67, 75 and 44 respectively.

The second rule changes the resolution in the rest of the mesh based on target cell lengths that are assumed to be independent of the Reynolds number. These target cell lengths are related to patches on the ship geometry and in refinement zones in the wake. Fig. 3 shows the mesh generated for our case study ship from a few different angles at a model scale equal to 1:4. The figure also contains the target cell length at important places relative to the ship length, $L$. The mesh is shown both for simulations with the free surface present and for simulations without the free surface. The differences are mainly related to refinements areas that are necessary for capturing the ship generated waves and the geometry above the free surface.

To bridge the resolution calculated from the two rules, the number of wall layers are adjusted for each simulation. As we manually fix the wall layer settings, except for the number of layers, it is impossible to always reach a cell length that matches the target cell length in each zone perfectly. As such, we choose the number of layers that most closely match the target cell lengths for each patch. As a result, the actual cell length in the mesh can vary up to 15% in both directions relative to the target cell length when the wall expansion ratio is 1.3. As the mesh resolution outside the wall layers are different on the main hull, skeg and rudder, the number of layers is also different. As an example, for the model scale 1:4, the number of layers on the hull, skeg and rudder is 10, 8 and 3 respectively.

We also limit the number of layers to a maximum as we have experienced problems with the layer generation process in snappyHexMesh when the number of layers gets too high. In these cases, we let the mesh be generated with a higher y+ value than the target value, as this mostly will happen for high Reynolds number flow. The increase in the target y+ values did only occur for model scales larger than 1:4, and the largest target y+ value for the experiments in this paper was 120. We show the effect of different y+ values on a few example cases in 5.4, which indicate that this is an acceptable simplification.

### 3.7. Forces from simulations

The rudder and the hull geometry is represented as different patches in the mesh, and we can therefore measure the forces on these patches separately. For most of cases without a free surface, the forces appeared completely steady, and we use the value from the last iteration in further post-processing. A few of the cases showed small oscillation on the rudder forces. This indicates a small amount of unsteady behavior, but we then used the average value of the last 1000 iterations as the final value. For simulations with the free surface included, the force on the hull is usually oscillating due to waves bouncing off the boundaries in the simulation domain. Although these waves will die out eventually, due to the wave damping zones, it usually takes an impractically long time. We have found that the mean value of the oscillating signal after the flow has moved 3–5 ship lengths is close to the final mean value when the waves are dampened out.

In order to evaluate the mean value, we fit a harmonic model function with exponentially decaying amplitude to the measured force values by using the values from a time window representing half the simulation length. An example of such a study is shown in Fig. 4. The values from our tuned force model are shown in green, while the dashed green line show the mean value if the model is tuned to every time step in the simulation. The purpose of the latter is to show how the mean value changes over time. We use the same procedure for the side force and the yaw moment, which in general show smaller relative oscillation than the resistance. All force coefficients are made non-dimensional by dividing them by the dynamic pressure, $0.5\rho U^2$, multiplied with a representative area. For the ship hull, the representative area is taken as the length multiplied with the depth, as this is the common area in maneuvering applications. For the rudder, we use the projected rudder area, which are equal to the rudder span multiplied with the mean chord.

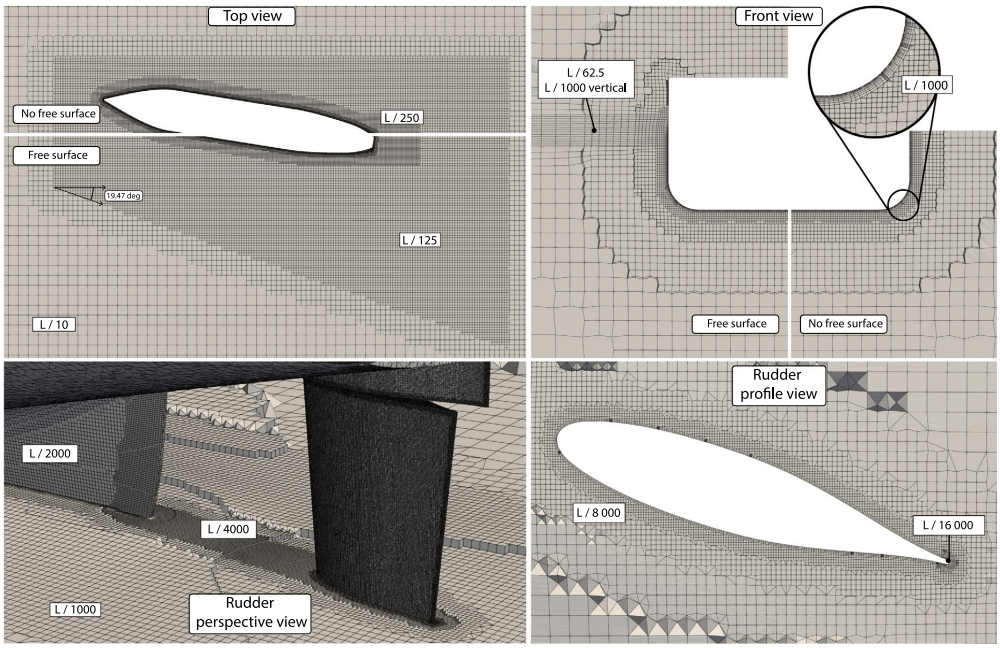


**Fig. 3.** Mesh illustration.

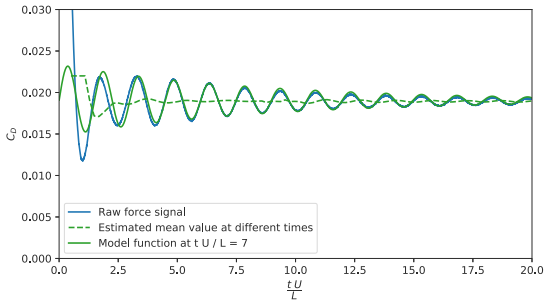


**Fig. 4.** Post-processing of force signal from simulations with free surface modeling for a case with drift angle equal to 9 degrees. (For interpretation of the references to color in this figure legend, the reader is referred to the web version of this article.)

### 3.8. Scaling from model scale to full-scale

Only the straight-ahead resistance is adjusted from model scale to full-scale, while drift-induced forces are assumed to be independent of Reynolds number (validity of this assumption is shown in Section 6.2). We assume that the resistance from a simulation without the free surface present can be scaled with a friction line and the wave resistance is calculated as the additional resistance in a simulation with the free surface present. There are many empirical friction lines available, and the most common one in the marine community is the ITT57 friction line. However, as for instance shown in Raven et al. (2008), this default friction line is not always the best choice for scaling ship resistance. As we are scaling results from CFD simulations with the turbulence model k-$\omega$ SST, we use a friction line from Eça and Hoekstra (2008), which is tuned based CFD results using the same turbulence model. Equations for this friction line is given below along with the scaling method for the drag coefficient, $C_D$, from a simulation without the free surface, performed at a Reynolds number $Re_0$:

$$C_F(Re) = 0.089\,Re^{-0.283+4.73\cdot10^{-3}\log Re+2.43\cdot10^{-5}(\log Re)^2} \tag{4}$$

$$C_D(Re) = C_D(Re_0)\frac{C_F(Re)}{C_F(Re_0)} \tag{5}$$

## 4. Route simulation model

This section presents our current route simulation model, which is a slightly modified version of the MMG model, Yasukawa and Yoshimura (2015). We only show the parts of the model that is relevant for a steady state route simulation of a ship and neglect the terms for modeling inertia forces, added mass effects and forces due to yaw rate of the ship.

### 4.1. Mathematical formulation

Two different coordinate systems are necessary for this discussion. The MMG model is expressed in a body fixed coordinate system where the $x$-axis is always aligned with the ships centerline independent of drift angle. However, when discussing the energy consumption of a wind-powered ship, we are mainly interested in the resistance and the side force of the vessel, also known as drag and lift. These forces act parallel and normal to the forward velocity respectively. We call this coordinate system a course fixed coordinate system. An overview of the two different coordinate systems is shown in Fig. 5.

The MMG model is modular and can be divided into three different parts when it is applied as a steady state route simulation model for wind powered ships. The different parts are listed below:

- A model for computing the forces acting on the hull as a function of drift angle and rudder forces
- A model for computing a representative velocity vector for the rudder which includes interaction effects from both the hull and the propeller

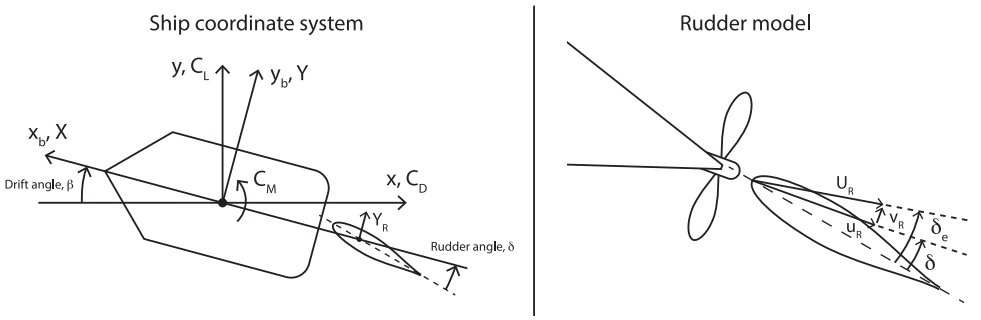


**Fig. 5.** Coordinate systems used in this paper and an overview of variables in the rudder velocity model.

- A model for computing the forces on the rudder as a function of the single representative velocity vector at the rudder position

The hull surge force, $X_H$, sway force, $Y_H$, and yaw moment, $N_H$, are assumed to be dependent on the sway velocity, $v$, and the forces on the rudder, $X_R$, and $Y_R$. The variable $\Delta X_R$ represents the increase in the surge force on the rudder at rudder and drift angles different than zero. The surge force consists of calm water, straight-ahead resistance, $R$, and otherwise drift- and rudder-induced forces. The model coefficients for the drift-induced forces are given as $X_{vv}$, $X_{vvvv}$, $Y_v$, $Y_{vvv}$, $N_v$, and $N_{vvv}$, while the model coefficients for the rudder-induced forces are given as $t_R$, $a_H$ and $x_H$. The complete equations for the hull forces are listed in the equations below:

$$X_H = -R + X_{vv}v^2 + X_{vvvv}v^4 - t_R\Delta X_R \tag{6}$$

$$Y_H = Y_v v + Y_{vvv}v^3 + a_H Y_R \tag{7}$$

$$N_H = N_v v + N_{vvv}v^3 + a_H x_H Y_R \tag{8}$$

The forces on the rudder are assumed to depend on a single representative velocity vector in the body fixed coordinate system represented with the symbols $u_R$ and $v_R$ for the surge and sway velocity. The vector gives both the velocity magnitude and the effective angle of attack on the rudder. The surge velocity is assumed to depend on both the drift angle and the propeller thrust, while the sway velocity is assumed to only depend on the drift angle. The complete model for the rudder velocity vector is listed below:

$$u_R = U(1-w)u_p \tag{9}$$

$$\frac{1-w}{1-w_0} = \left(1 + \left(1 - e^{-C_1|\beta|}\right)\right)\left(C_2 - 1\right) \tag{10}$$

$$u_p = \sqrt{\eta\left(1 + \kappa\left[\sqrt{1+C_T} - 1\right]\right)^2 + (1-\eta)} \tag{11}$$

$$C_T = \frac{T}{0.5\rho A_p U^2} \tag{12}$$

$$v_R = U\gamma\beta \tag{13}$$

$$U_R = \sqrt{u_R^2 + v_R^2} \tag{14}$$

$$\delta_e = \delta + \tan^{-1} v_R/u_R \tag{15}$$

The model contains a single wake factor, $w_0$, when the drift angle and propeller loading is zero. There are two coefficients that adjust for the effect of drift angle for the surge velocity, $C_1$ and $C_2$, while there is just one coefficient, $\gamma$, for adjusting the sway velocity. The effect of the propeller thrust is calculated according to classic actuator disk theory. The increase in the surge velocity is dependent on the thrust coefficient of the propeller, $C_T$, which is calculated as the thrust of the propeller, $T$, divided by the dynamic pressure multiplied by the propeller disk area, $A_p$. The variable $\eta$ is the rudder span divided by the propeller diameter, which adjusts the model for different propeller sizes. There is a single empirical coefficient that needs to be tuned to each case represented by the symbol $\kappa$.

The forces on the rudder are calculated based on the representative rudder velocity and a model that represents a general lifting surface. In the standard MMG model, the rudder force is assumed to act normal to the rudder chord for all rudder angles, and the rudder tangential force is completely neglected. The rudder normal force is further assumed to be linearly dependent on the effective rudder angle, which is calculated from the rudder velocity model. The equations for the model are listed below, where $f_a$ is a model coefficient that must be tuned:

$$F_N = 0.5\rho A_R U_R^2 f_a \sin\delta_e \tag{16}$$

$$X_R = -F_N \sin\delta \tag{17}$$

$$Y_R = -F_N \cos\delta \tag{18}$$

$$N_R = -x_R F_N \cos\delta \tag{19}$$

This is a typical model for ship maneuvering applications, but it is also a model that greatly simplifies the relationship between lift and lift-induced drag. For route simulation applications, resistance is an important variable, and we therefore decided to switch to a different rudder model based on classical lifting line theory. However, we kept the rudder velocity model from the standard MMG model. Although this introduce slightly more coefficients to the model, we found this to be necessary in order to accurately model the rudder resistance. A comparison between the original MMG model and the classical lifting line model is shown in Section 6.4.

We assume that the rudder experiences a lift force, $L_R$, that acts normal to the representative rudder velocity vector and a drag force, $D_R$, that act parallel to the representative rudder velocity vector. Both the lift and the drag are corrected for the geometrical aspect ratio of the rudder, $\lambda$, according to classical lifting line theory, but with empirical correction factors, $e_D$ and $e_L$, that corrects for the presence of the ship hull, and that can be tuned based on simulation data. The drag model also includes a polynomial for calculating the viscous drag. The equations for our modified rudder model are listed below:

$$C_{L,2D} = 2\pi\delta_e \tag{20}$$

$$C_{L,R} = \frac{C_{L,2D}}{1 + 2/(\lambda e_L)} \tag{21}$$

$$C_{D,R} = a_0 + \frac{C_{L,R}^2}{\pi\lambda e_D} + a_4\delta_e^4 \tag{22}$$

$$L_R = 0.5\rho A_R C_{L,R} U_R^2 \tag{23}$$

$$D_R = 0.5\rho A_R C_{D,R} U_R^2 \tag{24}$$

### 4.2. Adjusting model coefficients based on CFD results

The coefficients in the model equations are adjusted so that the values predicted by the model is as close to the CFD results as possible. We do this by using a line search optimization algorithm from the SciPy library (Virtanen et al., 2020) to minimize the squared difference between the model predictions and the simulations results, also known as least square regression.

The components in the hull and rudder force model are adjusted separately for each degree of freedom. For instance, the coefficients for the hull surge force are adjusted independently from the coefficients from the hull sway force and the coefficients for the rudder lift is tuned independently from the coefficients for the rudder drag. This is possible as the different models predict the forces in independent directions. For the rudder wake model, the coefficients affects both the rudder lift and drag at the same time. In this case, we minimize the errors from the estimated lift and drag by adding them in the same objective function. We also scale the error measurement so that both values are given approximately equal weight. For this particular case, the rudder lift coefficient is around 10 times larger than the drag coefficient, so the error in the drag is therefore weighted by 10. When we tune the original MMG rudder model, there is only one coefficient that is used to calculate both the lift and the drag at the same time. In this case, we only adjust the model based on the estimated lift. Adding the drag to the tuning procedure could in theory improve the drag accuracy, but not without reducing the lift accuracy. The results from an arbitrary number of CFD simulations can be given to the tuning procedures. We specify which CFD simulations that have been used for the tuning of the models along with the results presented in Section 6.

### 4.3. Balancing the model

The drift angle and rudder angle in the model can be automatically adjusted to produce a target amount of side force and yaw moment. This functionality is implemented so that the hydrodynamic model can balance externally applied forces and moments from sails. The variables are adjusted with a non-linear numerical solver from the SciPy library, based on the Newton algorithm. There are in total three balancing functions; adjust the rudder angle to reach a target yaw moment, adjust the drift angle to reach a target side force, and a combination function that adjust the drift angle and the rudder angle at the same time. The combination function has two levels. The first level balances the yaw moment for each drift angle, which gives the rudder angle as a function of the drift angle. The second level tunes the drift angle by using the first level. As the rudder angle is adjusted for each drift angle, this balances both the yaw moment and side force at the same time.

## 5. CFD verification and validation

To estimate the errors and the uncertainty in the simulations we have performed convergence studies and compared our simulation results against experiments. The results from these tests are shown in this section.

### 5.1. Generalized uncertainty estimate

We follow the general procedure for convergence studies recommended by the ITTC in International Towing Tank Conference (2017), which is to a large degree based on the work presented in Eça et al. (2010). The recommendations presents different methods for estimating the numerical uncertainty based on a parameter convergence test. All methods are based on the concept of Richardson extrapolation (Richardson, 1911). As we use an unstructured mesh, we have chosen to estimate the uncertainty using the least square approach. In this method, the relationship between a simulation value, $S_i$, at a given parameter value, $h_i$, and the converged simulation result, $S_0$, is estimated according to different model functions:

$$S_i = S_0 + ah_i^p \tag{25}$$

$$S_i = S_0 + ah_i^2 \tag{26}$$

$$S_i = S_0 + a_1 h_i + a_2 h_i^2 \tag{27}$$

The coefficients in the equations ($S_0$, $a$, $p$, $a_1$ and $a_2$) is found using a least square approach. This requires a set of CFD simulations with different parameter values. A curve fitting algorithm is then used to estimate the coefficients in the equations by minimizing the squared difference between the model prediction and the actual values. We use a line search optimization algorithm from the SciPy library (Virtanen et al., 2020) for this task.

Eq. (25) is first used to make an initial estimate. If the predicted order of accuracy – the value of $p$ – is between 0.5 and 2, the equation is kept as the model function for the parameter variation. If the predicted order of accuracy is larger than 2, the model equation is switched to Eq. (26). If the predicted order of accuracy is less than 0.5, the best fit of Eqs. (26) and (27) is used.

The estimated relative error in the simulation result as a function of the tested parameter is then calculated as $\delta_i = (S_i - S_0)/S_0$. However, there is an exception if the simulation data is seen to oscillate above and below the estimated converged simulation result, $S_0$. In that case, the simulation error is instead estimated according to the equations below, based on a set of $n$ simulation results with parameter values $h_i$ and simulation results $S_i$:

$$S_0 = \text{Mean}(S_i) \tag{28}$$

$$\delta = \left( \frac{\text{Max}(S_i) - \text{Min}(S_i)}{h_n/h_1 - 1} \right) / S_0 \tag{29}$$

Finally, the uncertainty, $U_i$, due to the parameter in question is estimated with a safety factor, $F_s$, as $U_i = F_s|\delta_i|$. The value of $F_s$ is somewhat ambiguous, but recommended by the ITTC to be 1.25 for situations where there is a good fit between the data and the model equations, and 3.0 for situations where the data is seen to oscillate.

This generalized approach is used both for the mesh convergence and the time step study. At least four different parameter values are used for each Richards extrapolation study. For a more in depth explanation of this method, we recommend either International Towing Tank Conference (2017) or Eça and Hoekstra (2014).

### 5.2. Mesh convergence

When varying the mesh resolution, we multiply all length factors in the mesh set-up software by the same value so that the cell length at each level in the mesh is changed by the same factor. However, we keep the target y+ value constant for our convergence study and check the y+ dependency in a separate study in Section 5.4. To change the mesh such that the wall layer part remain as constant as possible, we change the mesh with a factor that matches the wall layer expansion ratio. As such, for each variation of the mesh resolution in the convergence studies, the cell lengths in the mesh varies with a factor of 1.3 to some power. This is slightly less than the more typical approach of using the square root of two as a mesh refinement factor but has the benefit that each refinement of the mesh removes exactly one wall layer and replaces it with a finer outer mesh.

The uncertainty related to the grid size for the hull is estimated by performing 5 different mesh convergence studies for different cases. All of them contain the ship hull at a drift angle of 9 degrees. The result of this study can be seen in Figs. 6 and 7. Fig. 6 show the results for the cases with free surface modeling and Fig. 7 show the results without the free surface. We also test the hull and rudder together both with and without the propeller present in the simulation. The drift angle was still 9 degrees, and the rudder angle was 6 degrees. The result of

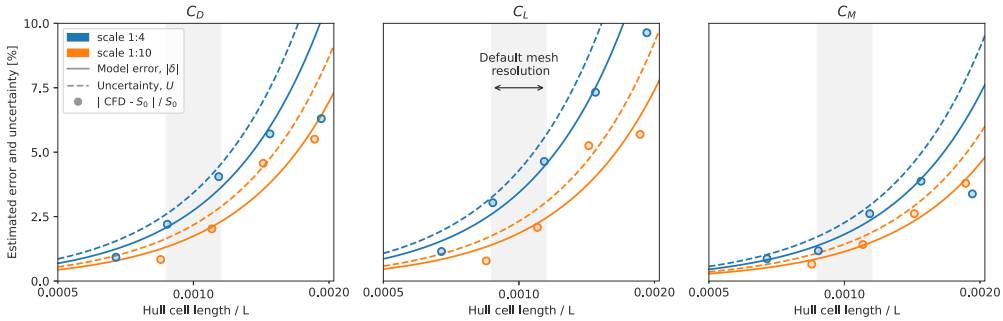


**Fig. 6.** Convergence study for the hull, without the rudder, with free surface modeling. Drift angle = 9 degrees and Fr = 0.25.

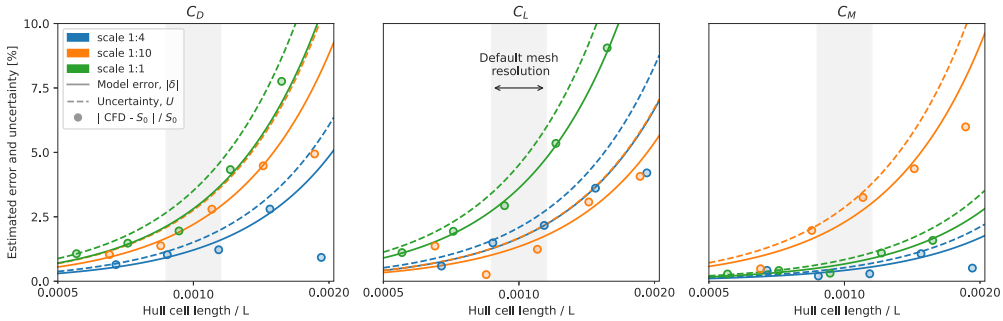


**Fig. 7.** Convergence study for the hull, without the rudder, without the free surface. Drift angle = 9 degrees.

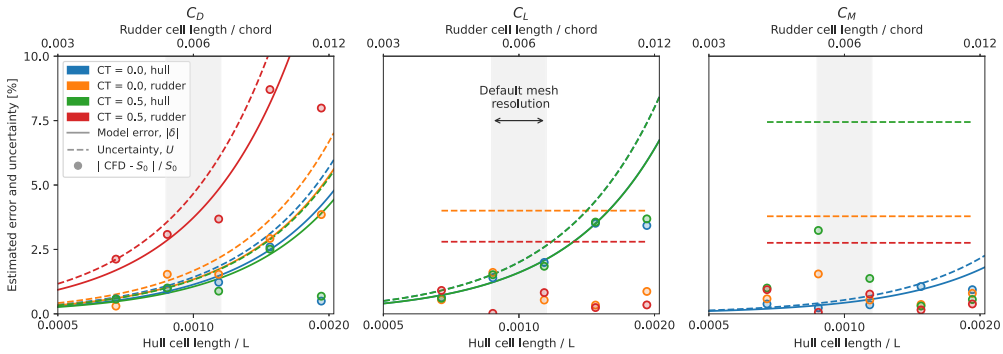


**Fig. 8.** Convergence study for the hull and rudder together, with and without the propeller actuator disk at a model scale of 1:4. Without the free surface.

this study can be seen in Fig. 8. The plots show the estimated values for the simulation error due to the mesh and the corresponding mesh uncertainty. Both model equation values and CFD values are shown in order to show the fitness of the uncertainty estimate. Most of the cases have an estimated mesh uncertainty well below 5% for the default cell length, and many cases are below 2.5%.

When the estimate for the uncertainty is shown to be a flat line, it is due to oscillating convergence, and the uncertainty is therefore estimated with Eqs. (28) and (29). In these cases, there is a large difference between the CFD values and the estimated uncertainty, due to the large safety factor for oscillating data. However, all of the oscillating cases have result values that are very close together over all the tested mesh resolutions. The largest uncertainty is estimated to be close to 7.5% for the yaw moment on the hull in the case with the hull and rudder together and a thrust coefficient of 0.5. However, the difference between the default cell length and the finest mesh is only 1.7%. We therefore conclude that the mesh resolution is adequate even in the cases where the general Richardson extrapolation has failed to find a good fit of the CFD data.

As mentioned in Section 3.6, the default cell length are allowed to vary within a narrow range to match the outer cell length with the wall layers. The cell length corresponding to our default values (as shown in Fig. 3) is therefore marked with a light gray background that show the range of possible values from our case setup procedure.

### 5.3. Time step convergence

The effect of changing the time step was tested by simulating the hull alone in the model scale 1:4, Froude number equal to 0.25, and 9 degrees drift angle. Both the physical time step limit and the Courant

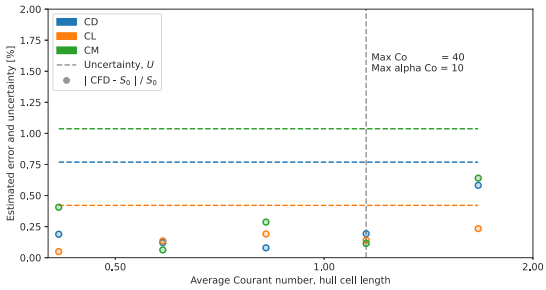


**Fig. 9.** Time step convergence study, testing a bare hull in model scale 1:4, with free surface modeling, and drift angle equal to 9 degrees.

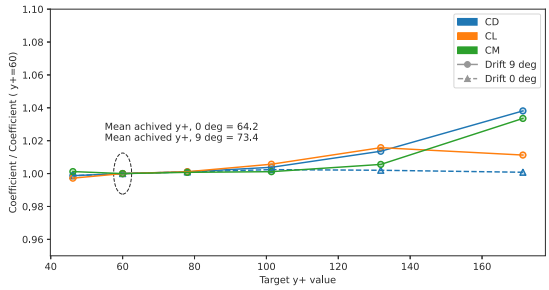


**Fig. 10.** Effect of target y+ value on the simulated forces at mode scale 1:4.

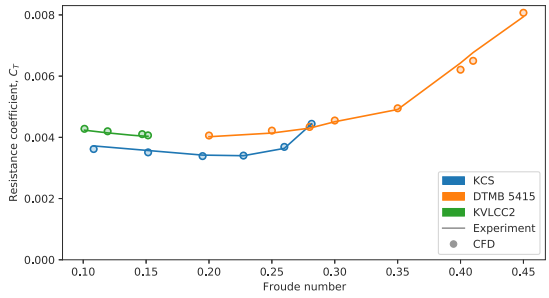


**Fig. 11.** Calm water straight ahead resistance, from CFD simulations and experiments.

number limits were changed at the same time, although the Courant number limits was the dominating factor in this case. The results from the study can be seen in Fig. 9. The time step change factor was set to the square root of two. The Courant number limits adjust the time step based on the largest measured Courant numbers in the mesh. The time step will therefore vary along with the velocity field over the course of the simulation. In addition, the time step might not change with the same factor as the target Courant number, as the velocity field are altered when the time step is altered. We have therefore plotted the simulated resistance, side force and yaw moment as a function of the average time step in the simulation, made non-dimensional by calculating the average Courant number based on the ship length, ship velocity and the outer cell length at the hull.

Although the convergence study show that the results oscillate over the tested time-steps, the estimated uncertainty is only around 1% or less. This indicate that fairly large maximum Courant numbers are acceptable. However, we have experienced a few cases where the time step must be reduced from the default values due to stability problems with the simulation. This was not a problem for any of the case-study ship simulations in this paper, but it did happen for a few of the validation experiments we show in Sections 5.5 and 5.6. In those cases, we reduced the time step to a maximum Courant number of 20 and maximum interface Courant number of 5.

### 5.4. Y+ variation

The effect of y+ values was checked separately from the rest of the mesh variation. This was done at the model scale 1:4 for drift angles 0 degrees and 9 degrees, with steady state simulations without the free surface present. The target y+ value was changed by multiplying it with the layer expansion ratio, to different powers. As such, for a change in the target y+ value, only the number of wall layers were changed while all the other mesh parameters where kept constant. The result of this study can be seen in Fig. 10.

Unlike other simulation parameters, it is not necessarily given that a small y+ value provides more accurate results than a large y+ value when wall functions are applied. The achieved y+ values around the hull geometry will vary based on local velocity and friction. Although we use continuous wall functions, the error can still be larger for cells where the local y+ are falling into the transition zone between the logarithmic region and the linear region in the law of the wall. This is for instance shown in Hympendahl and Ciortan (2018), where both continuous and logarithmic wall functions are tested for ship resistance with various simulations codes. Although the continuous wall functions are in general better than purely logarithmic models, the simulation error for both types is shown to increase as the y+ values approach 30. As such, we do not use the generalized Richardson extrapolation model to estimate the uncertainty due to the target y+ value. We do however conclude that the change in force values around our chosen target y+ value of 60 is small, both for larger and smaller values, which suggest that our target value is appropriate. This is also confirmed with the experimental validation in the next two sections.

### 5.5. Straight ahead resistance

In order to validate our general simulation setup, we have reproduced several experiments published in the scientific literature. For the calm water, straight ahead, resistance, we have chosen the three open ship geometries KCS – a large and fast container ship – KVLCC2 – a large and slow tanker – and DTMB 5415 — a fast naval combatant ship with a sonar dome in the bow. Articles with experimental data and geometry specifications are found the Gothenburg 2010 proceedings, which are summarized in Larsson and Stern (2014). The results from our validation cases are plotted in Fig. 11. The simulation setup for every case is mostly based on the same rules as the one presented for the case study in this paper, including the same mesh resolution. The ship model in the experiments and the simulations where free to move in both heave and pitch. More details of the simulation setup for the validation experiments can be found online in Kramer (2021). The mean error in the predicted resistance from the CFD simulations are 1.21% for all the ship geometries and Froude numbers, while the maximum error is 4.07%. The largest error occurs for the DTMB 5414 at Froude number equal to 0.41.

### 5.6. Drift-induced forces

In order to validate the drift-induced forces on the hull we used two different validation experiments, with three different ship geometries in total. The first experiment is published in Kramer et al. (2016b), and tests the drift induced forces on different foil shapes, with varying depths at two different Froude numbers. The depths were chosen such that depth to length ratio of the foils where close to typical values for cargo ships, and the geometries were therefore called foil-ships.

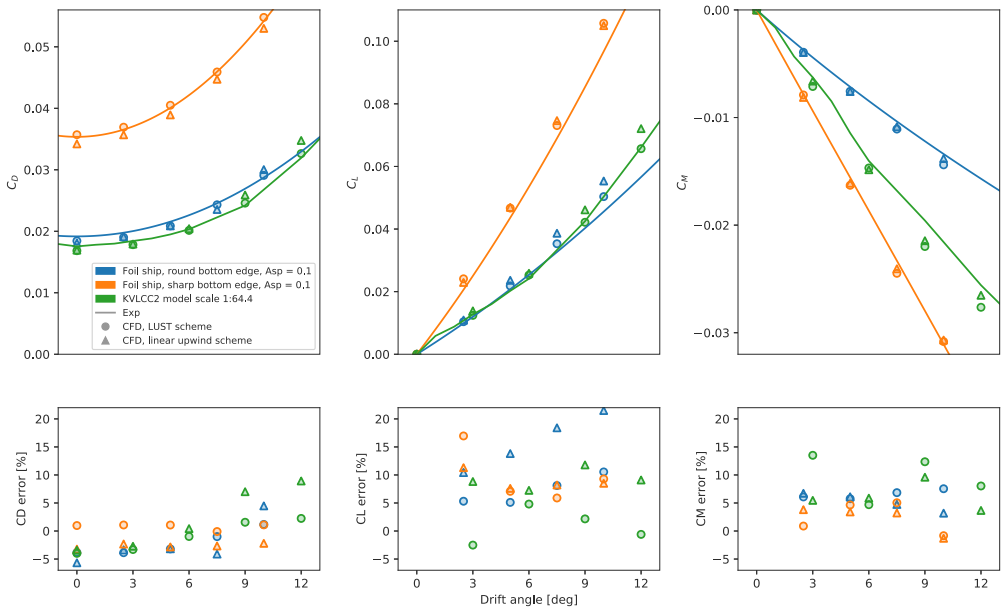


**Fig. 12.** Experimental validation of drift-induced forces on ship geometries.

For each depth, two different versions of the bottom edge shape were tested; one perfectly sharp and one with a rounded edge. The second experiment can be found in Kume et al. (2006). It consists of experimental data for the forces and moments acting on the tanker ship KVLCC2 at different drift angles at model scale of 1:64.4.

The comparison between experimental data and our CFD data can be seen in Fig. 12 which also show the simulation error defined as the difference between the simulated value and the experimental value, divided by the experimental value. We have performed all the validation experiments with the both the LUST scheme for the convective term, and with the more conventional linear upwind scheme. For large drift angles, the linear upwind simulations tend to overestimate both the lift and the lift-induced drag. This is seen to be less of a problem with the LUST scheme, which is why we have used this scheme for the rest of the simulations in this paper. The tested mesh resolution is the same as for the straight-ahead resistance validation cases described in Section 5.5.

The average absolute value of the error for the LUST scheme is 1.96%, 5.23% and 5.08% for the drag, lift and yaw moment respectively. The same values for the linear upwind scheme are 4.11%, 9.28% and 3.52%. The largest errors are observed for lift at the larger angles of attack. For the round foil ship, the error in the lift is 10.5% with the LUST scheme and 21.5% with the linear upwind scheme. For the KVLCC2 at drift angle equal to 12 degrees, the error is −0.6% with the LUST scheme and 9.1% with the linear upwind scheme. For the sharp foil geometry, the error is comparable with the LUST scheme and the linear upwind. At 10 degrees drift, the error is 10.5% and 9.3% for the LUST scheme and the linear upwind scheme. We suspect this is because the flow separation around the bottom edge is easier to predict with a sharp bottom edge than with a rounded one.

The difference in the error for the yaw moment and the error for the side force illustrates the uncertainty in the predicted center of effort for the side force. For the sharp bottom edge foil ship, the side force is predicted to act too far towards the stern. For instance, at 10 degrees drift, the error in the yaw moment is close to zero, but the side force is overestimated with approximately 10%. This indicates that the yaw moment arm is around 10% too small. For the two other geometries, the side force is predicted to act too far towards the front. For instance, for the KVLCC2 at 9 degrees drift, the error in the side force is small, while the magnitude of the yaw moment is overestimated with close to 12%, indicating that the yaw moment arm is overestimated with approximately the same amount.

## 6. Results

The results from the numerical experiments are presented according to each simplification in the following subsections. At the end of the result section, we also discuss the relative importance between the rudder and the hull forces and the global consequence of each simplification with route simulation models tuned based on different data.

### 6.1. Neglect the free surface

The effect of the free surface was tested by simulating the ship hull at different drift angles and Froude numbers, both with and without free surface modeling. The Reynolds number was kept constant to separate out potential model scale effects from the effect of the free surface alone. This was achieved by keeping a constant velocity and viscosity in the CFD simulations, while changing the acceleration of gravity to correspond to the target Froude number. As such, for each tested drift angle, there is one simulation per Froude number with VoF free surface modeling, and one double body simulation where the free surface is neglected. The simulations were done without rudder and propeller as the hull forces are believed to be most influenced by the free surface.

Non dimensional coefficients for resistance, $C_D$, drift-induced resistance, $C_{D,i}$, side force, $C_L$, and yaw moment, $C_M$, for drift angles 0, 6 and 9 degrees and Froude numbers 0.15, 0.2, 0.25, and 0.3 are plotted in Fig. 14. The figure also contains plots with a simplified modeling approach for the total forces shown as dashed lines. In this model, the straight-ahead resistance is taken from the simulations with the free surface present, while the drift-induced forces are added from the simulations without the free surface. Fig. 13 shows the waves generated by the ship while moving with 9 degrees drift angle, to give

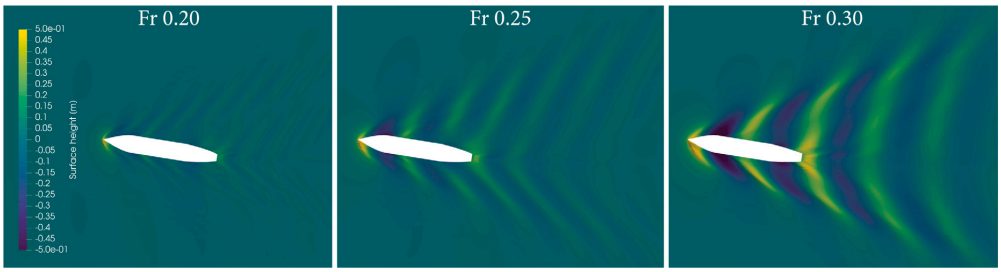


**Fig. 13.** Waves generated by the ship while moving with 9 degrees drift, for different Froude numbers. Model scale 1:4.

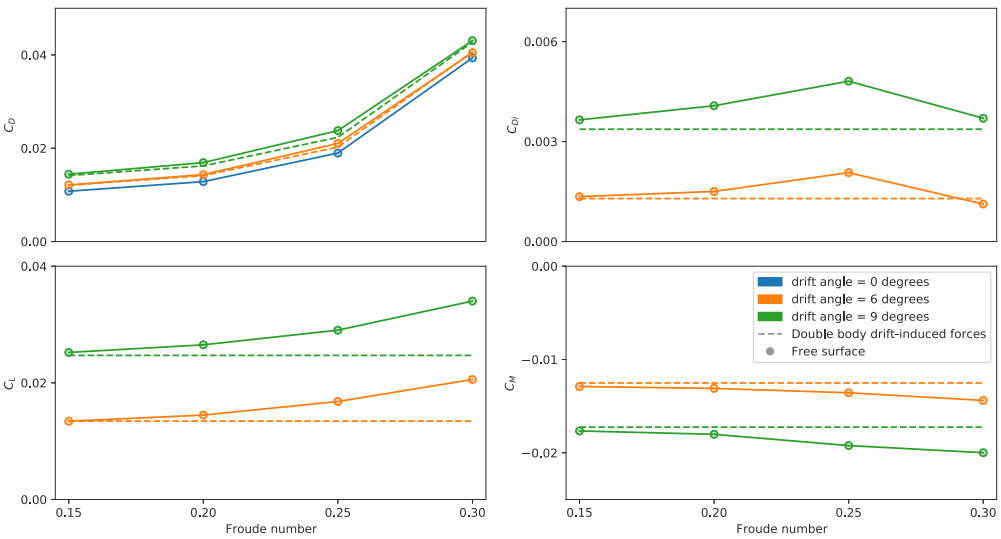


**Fig. 14.** Effect of Froude number on drift-induced forces. Tested at model scale 1:4 corresponding to Reynolds number of 67.8 million.

an indication of the disturbance on the free surface for the different Froude numbers.

The results show that the drift-induced forces are affected by the waves generated at the free surface, and the error is in general increasing with Froude number. This is natural as the waves generated by the ship is increasing in size with increasing Froude number as shown in Fig. 13. However, the effect is small for Froude numbers up to 0.2 and the drift-induced forces are seen to be much less affected than the straight-ahead resistance. When the Froude number is changed from 0.15 to 0.3, the straight-ahead resistance is increased with almost 300%. As a comparison, the drift-induced resistance, side force and yaw moment at 9 degrees drift is only changed by 8.9%, 27.4% and -13% respectively. We also see that the importance of the drift-induced resistance is decreasing with increasing Froude numbers. At 9 degrees, the drift-induced resistance is 33.8% of the total resistance when the Froude number is 0.15, while it is only 9.0% of the total resistance when the Froude number is 0.3. As such, if the free surface effects are only included on the straight-ahead resistance, while the drift-induced resistance is calculated with a double body simulation, the error in the total resistance is only 0.8% for Froude number 0.3 and 9 degrees drift angle.

### 6.2. Test in model scale

The effect of model scale was tested by simulating the ship hull at different Reynolds numbers corresponding to model scales 1:20, 1:10, 1:4, 1:2 and 1:1.33, without the free surface included in the simulation. The result is shown in Fig. 15. The resistance is shown both as the direct value from the CFD simulations and full-scale values calculated with the scaling method described in Section 3.8. The predicted full-scale straight-ahead resistance only differ by 0.56% between the actual full-scale values and those from scaled values from CFD simulations in model scale 1:20 when the friction line based on the k-$\omega$ SST model is used. This shows that the chosen scaling approach is accurate for our case study ship. For the sake of comparison, we also calculated values using the standard ITTC-57 friction line, which gave a difference of more than 7%. The drift-induced values are not scaled in any way. We observe that both the side force and the drift-induced resistance is gradually decreasing with increasing Reynolds number, while the yaw moment is less affected. The difference between full-scale and the model scale 1:20 is 51.6%, 15.5% and 3.25% for drift-induced drag, side force and yaw moment respectively, at 9 degrees drift angle. However, if the model scale is increased to 1:4, the difference from full scale is reduced to 10%, 3.7% and −0.55%. The full-scale total resistance is overpredicted by 15% when scaled values from model scale 1:20 is used, while it is overpredicted by 2.36% when the model scale 1:4 is used.

The difference in the values for the drift-induced forces are likely explained by larger cross-flow drag in model scale than in full-scale. This is natural as flow separation will happen more easily at low Reynolds numbers. An example of this is shown in Fig. 16, which show the cross-flow velocity component - i.e., the velocity in the $y$-direction

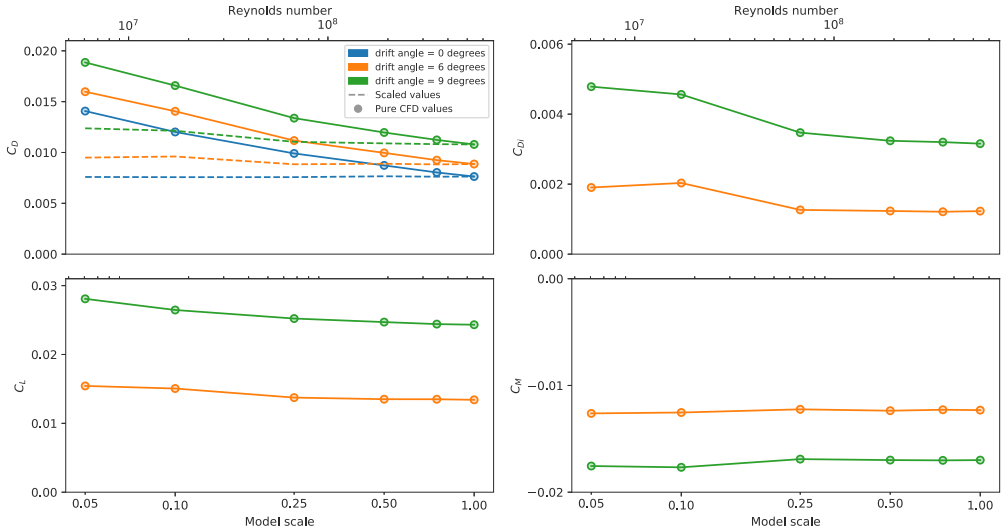


**Fig. 15.** Effect of model scale on the drift-induced forces.

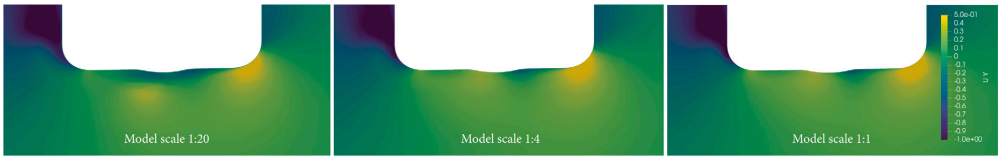


**Fig. 16.** Contour plot of the cross-flow velocity component at a cutting plane located 30 m from the stern, for different model scales. Both the geometry and the velocity is scaled to full-scale.

- at the same cutting plane, but different model scales. While the flow field is similar for model scale 1:4 and 1:1, there is a clear difference for model scale 1:20. The flow is clearly separating around the bottom of the ship for smallest model scale, while less so for the two other scales.

### 6.3. Neglect heel

The effect of heel was tested by simulating the ship hull at different heel angles and drift angles without free surface modeling in the simulation. The model scale was set to 1:4 in this test. The results can be seen in Fig. 17. The negative heel angles are in reality the most interesting tests for wind-powered cargo ships. The experienced heel angle is mostly due to the side force from the sails, which will act a large distance above the deck, in the opposite direction of the side force from the hull. This means that the ship will mostly heel to the opposite side of the hydrodynamic side force, which is the negative heel angles in the plot. The results show that the side force and resistance are not very much affected by the heel angle in the test with drift angle equal to 6 degrees. The side force at −20 degrees heel is 7% lower than the side force at 0 degrees heel, while the resistance is 2.8% higher. However, the effect of heel increases rapidly with increasing drift angle. At 9 degrees drift, the side force is reduced with almost 20% at −20 degrees heel, while the resistance is increased with 3.9%. The yaw moment is affected at both the tested drift angles. The absolute value of the yaw moment at −20 degrees heel is 45% and 48% higher than at zero degrees heel at drift angles equal to 6 and 9 degrees respectively.

The effect of heel can be modeled with simplified models based on classical linear lifting surface theory, as shown in Ross (2008). However, the fact that the effect of heel is so much larger for 9 degrees drift than 6 degrees drift suggest that non-linear cross-flow drag effects are strongly affected by the heel angle, while linear effects are less affected. As such, simplified modeling approaches are not sufficient in this case. Fig. 18 shows the cross-flow velocity component at drift angles equal to 6 and 9 degrees, and heel angles equal to 0 and -15 degrees at a cutting plane located mid-ship. The figure shows that the flow separates around the bottom edge of the ship at both drift angles when the heel angle is −15 degrees, while no separation is observed for zero heel. This illustrates that a heel angle can induce cross-flow drag on the hull-sections, which again affects the drift-induced forces and moments. If the stability of the ship is such that large heel angles are possible, they are likely to occur at the same time as large drift angles as they are the consequence of the same aerodynamic side force. Whether or not to include heel as part of the test matrix for a wind powered cargo ship design is therefore mostly a question of whether or not large heel angles are likely for the specific ship. This is dependent on the stability of the ship, and could therefore vary a great deal between different ships.

### 6.4. Assumption in the modified MMG model

To test the assumption in the MMG model, we used the results from CFD simulations without the free surface, at model scale 1:4, where the drift angle, rudder angle and propeller thrust coefficient is changed. There are mainly three questions we wanted to answer:

1. Is the order of the polynomial model for the hull appropriate?
2. Is the interaction model between the hull and the rudder accurate?
3. Is the interaction model between the propeller and rudder accurate?

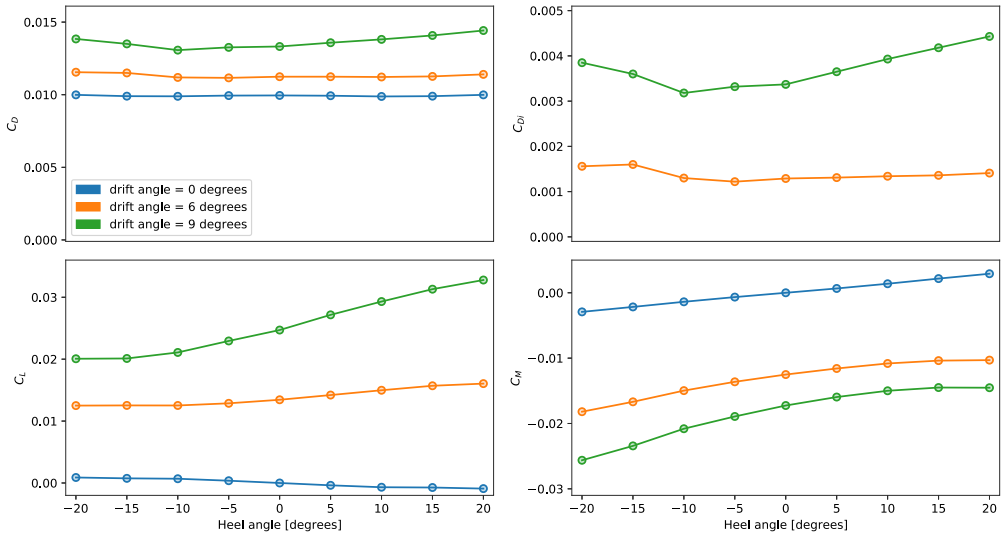


**Fig. 17.** Effect of heel on the drift-induced forces.

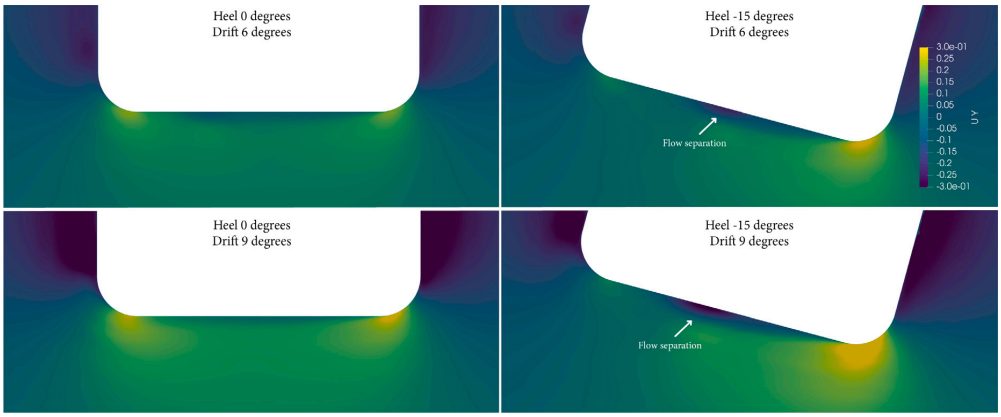


**Fig. 18.** Contour plot of the cross-flow velocity component for different drift and heel angles.

We explored the first question by tuning the MMG hull polynomial model using results from simulations that tested the hull alone at different drift angles. The complete data set consists of drift angles between 0 and 12 degrees, with 1 degree step size. Both the drift-induced forces and the drift-induced yaw moment are modeled using polynomials with two coefficients. The minimum number of data points necessary to tune the model is therefore two. We have plotted the results from the CFD simulations, as well as the estimated values for resistance, side force and yaw moment based on tuned model results in Fig. 19. The solid line shows the results from the polynomial hull model that is tuned based on the CFD data from drift angles 6 and 9 degrees. The lighter blue area in the figure shows the range of values between the minimum estimated value and maximum estimated value if two random data points are chosen as tuning data from the data set where the drift angle is larger than 3 degrees. This area illustrates the sensitivity of the model accuracy to the chosen tuning data. The smaller drift angles were excluded as we found this to greatly improve the results.

The rudder-induced forces on the hull are assumed to be linearly dependent on the rudder forces in the MMG model, when the body fixed coordinate system is used. In order to separate rudder-induced forces from drift induced forces, we tuned a route simulation model based on the CFD data including both the rudder and the hull. We then estimated the rudder induced forces in a CFD simulation as the direct values from the simulation minus the drift-induced values in the tuned model. The results are shown in Fig. 20 where both the CFD data and the estimated values form a tuned model is shown. Unlike most of the other plots in this paper, the body fixed coordinate system is used to show the linearity in the model. We also tried to estimate the rudder induced hull forces by comparing simulations with and without the rudder present, but this gave slightly worse results than the tuning approach. This indicates that the presence of the rudder slightly affects the drift-induced forces on the hull.

The linear model of the rudder-induced forces appears to be appropriate for both the side force and the yaw moment. The rudder induced forces along the ship's centerline does not show a clear linear

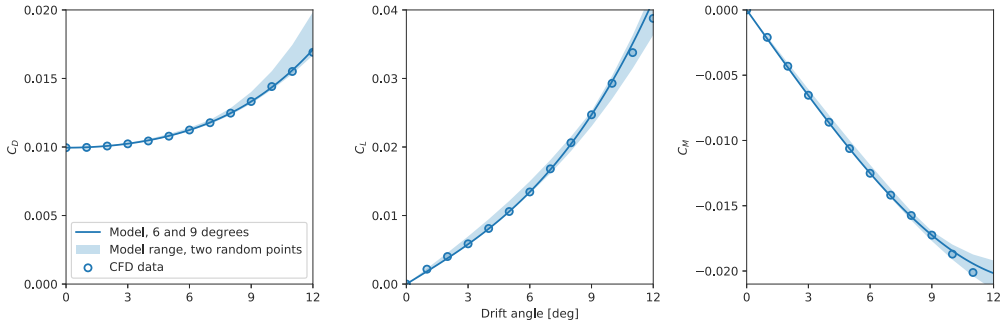


**Fig. 19.** Hull model in the MMG-model.

pattern, but is also seen to be very small for our case study ship. The rudder-induced hull forces in this direction are presented relative to the total hull force in the same direction in order to show the relative importance of this force. At different rudder angles, drift angles, and propeller loadings, the rudder induces a force on the hull that is around 2% of the total hull resistance at the maximum and less than 1% for most of the cases.

The final part of the verification of the MMG-based route simulation model is the rudder force model. This model was tested by comparing values directly from CFD simulations against values from tuned route simulation models. The result can be seen in Fig. 21. Both the default MMG model and our modified rudder model based on classical lifting line theory are shown. We limit the plot for the MMG model to the case with zero propeller loading in order to avoid clutter as the general trend is the same of all thrust coefficients. We also do not show plots of the yaw moment from the rudder, as both the shape and accuracy of the yaw moment is comparable to the side force plot. However, we do report the accuracy of the yaw moment model later in the text.

Only some of the data points in Fig. 21 was used to tune the models. The models for the rudder lift and drag as a function of effective rudder angle was tuned based on a static rudder test where both the drift angle and the propeller loading were zero. The total data set for the tuning procedure consisted of rudder angles equal to 0, 3, 6 and 9 degrees. The wake factor used in the model was taken as the average wake factor at the location of the rudder from a CFD simulation without the rudder present, where both the drift angle and thrust coefficient was set to zero. It is hard to separate out the effect of velocity from the effect of force coefficients in the model, and we therefore found it necessary to estimate the wake factor from the velocity field in a CFD simulation. The model for the change in rudder inflow as a function of drift angle was tuned based on a static drift test, with varying rudder angles and zero propeller loading. The included drift angles where 6, and 9 degrees, and the included rudder angle was −6 and +6 degrees.

The final tuning procedure adjusts the flow acceleration factor, $\kappa$, in the propeller model. We tuned the model by minimizing the error in the predicted lift and drag from the rudder at a propeller thrust coefficient of 0.5, rudder angles of −6 and +6 degrees, and a drift angle of 6 degrees.

The average error for the lift and yaw moment is approximately 7% for both the default MMG model and our modified rudder model for cases with lift coefficient larger than 0.1. The error in the estimated drag coefficient from the standard MMG model is essentially large for all cases with an average value of 95%. The same statistics for our modified rudder model is 25%. The main issue with the modified rudder model seems to be for cases when both the thrust coefficient and drift angle is large at the same time. For cases with zero thrust coefficient or zero drift angle, the error in the drag coefficient is 10%. Including more data in the tuning procedure did not improve the results notably.

Fig. 22 shows a contour plot of the velocity over the rudder when the propeller thrust coefficient is equal to 0.5. This illustrates some of the complexity in the flow field around the rudder. The jet stream from the propeller actuator disk is clearly visible, with flow structures that vary as a function of both drift and rudder angle. The MMG model assumes that the entire effect of the propeller jet stream can be modeled with a single correction to the axial velocity. Based on the flow structures visible in Fig. 22, it does not seem strange that this simplified modeling approach is not perfect. However, the accuracy of the MMG simplification might still be acceptable for early design iterations and simplified case studies. A wind-powered ship will experience smaller thrust coefficients when the force from the sails is large. In other words, when large drift angles and rudder angles are necessary, the thrust coefficient is likely to be small. As such, the most important case for a rudder model for a wind-powered ship is the accuracy for small thrust coefficients, which was also the cases with the highest model accuracy.

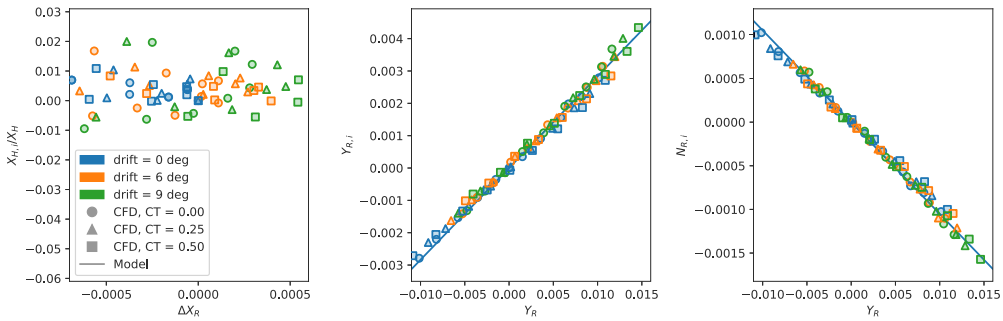


**Fig. 20.** Hull and rudder interaction.

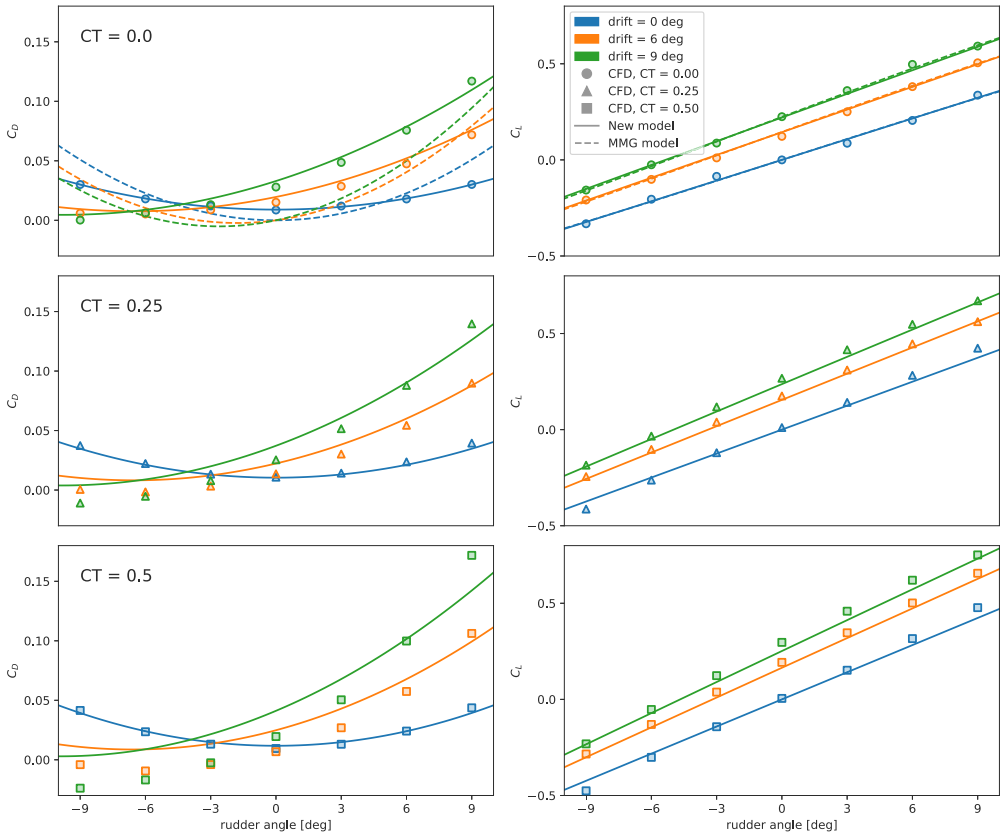


**Fig. 21.** Rudder forces as function of drift angle, rudder angle, and propeller loading.

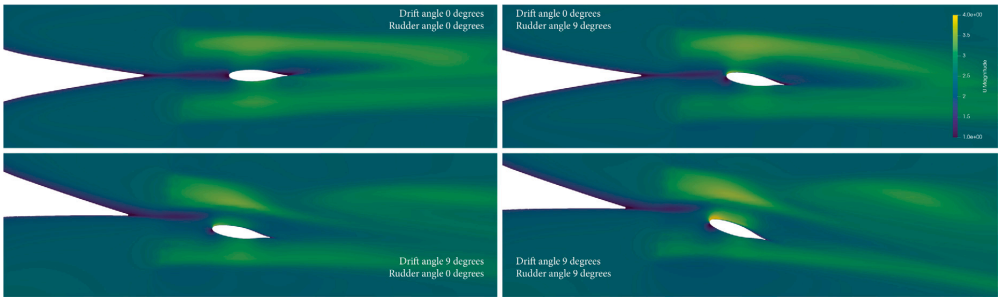


**Fig. 22.** Contour plot of the velocity magnitude at a cutting plane located at the same depth as the propeller center. The thrust coefficient in these simulations were 0.5.

### 6.5. Comparison of simulation time and global errors

The main goal of a route simulation model is to predict the resistance on the vessel at different operating conditions. The importance of the different parts of the model can therefore be evaluated by how much they contribute to the total resistance. The sources of resistance in the route simulation model can be divided into the straight-ahead resistance, drift-induced resistance, rudder resistance and rudder-induced resistance on the hull. With the exception of the straight-ahead resistance, each of the resistance components is highly dependent on the aerodynamic forces from the sail. The increase in resistance due to both drift and rudder angle is a consequence of balancing the side force and yaw moment generated from the sails. For the sake of this discussion, we have chosen to use a simplified aerodynamic model consisting of a side force vector acting at a fixed point in space where the yaw moment is dependent on the longitudinal location of the force. An overview of the simplified aerodynamic model can be seen in Fig. 23.

The amount of side force from the sails will vary depending on wind direction, sail type, and ship speed. As for instance shown in Kramer et al. (2016a), the side force produced by both a wing sail and a rotor sail can be more than 10 times as large as the thrust even at wind directions that produce significant amount of thrust. The same reference also shows that if the ship is moving two times faster than

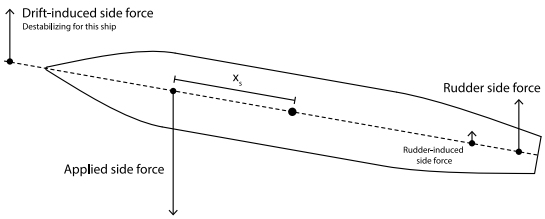


**Fig. 23.** Illustration of simplified aerodynamic model with resulting hydrodynamic forces.

the wind, the side force from a rotor sail can be almost 4 times as large as the thrust even at the most optimal wind direction. We have varied the side force from the sails between 0 and 3 times the straight-ahead resistance of the ship at the design speed and used the route simulation model to calculate the increase in resistance as a function of side force. The result for three different placements of the sail force vector is shown in Fig. 24. The model is tuned based on the CFD data for model scale 1:4 and the assumed thrust coefficient in the model is 0.25. The figure shows that the source of the increase in resistance varies depending on the placement of the side force. When the side force are placed towards the bow of the ship, the drift-induced resistance on the hull is the largest part of the added resistance. The rudder becomes more and more important as the placement of the side force is shifted backwards.

Both the rudder and the drift-induced resistance is a large part of the increase in resistance and both therefore deserve accurate modeling. Somewhat surprisingly, the increase in resistance due to the side force is fairly constant for different sail placements for our case study ship. The sail-induced increase in resistance on the ship is around 6%, 18% and 35% for side force ratios of 1, 2 and 3. We consider both the main dimensions and the rudder aspect ratio and size to be fairly typical for this type of ships. The fact that the low-aspect ratio hull is capable of balancing the side force approximately as efficiently as the rudder is therefore interesting. The explanation is likely that the hull is producing the lift with a very low loading relative to the representative area. As lift-induced drag is typically assumed to be proportional to the lift coefficient squared, it seems reasonable that the resistance increase is small, even with the low aspect-ratio. The drift and rudder angles experienced by the ship also varies depending on the placement of the sails. The drift angle is less than 8 degrees for all the test cases in the figure, while rudder angle is as large as 16 degrees for the sail placement at the middle of the ship. We also tested sail-placements further towards the stern, but this quickly resulted in rudder angles approaching a likely stall limit. This indicates that the rudder is probably too small for balancing large sails placed towards the stern, and that the placement of the sails should either be towards the front, or the size of the rudder should increase.

To evaluate the global consequence of each simplification, we tuned the route simulation model based on different CFD simulations and computed the resistance as a function of side force. The left plot shown in Fig. 25 show the consequence of different simplifications for the drift induced hull forces. The route simulation model is balanced using only the drift angle. Although this is technically not possible for our case study ship, since some amount of rudder force is necessary to achieve yaw moment balance, the purpose is to show the worst possible consequence of each simplification for the drift-induced forces. We then did the same exercise, with the rudder included, and both rudder models. The result is shown in the right plot in Fig. 25. Both the yaw moment and the side force are balanced. The drift induced forces are simulated at a model scale of 1:4, without the free surface resent, and the thrust coefficient is assumed to be 0.25. We also tested the ship with CFD with the same values for the drift and rudder angle as the tuned model for side force ratios of 1, 2 and 3.

When the side force ratio is 3, the double body model underestimates the resistance with 1.4% relative to the CFD simulations with free surface modeling. The difference between model scale 1:10 and model scale 1:4 is 5.2%. The difference between the model tuned from the data with 10 degrees heel and the same data at zero degrees heel is 9.6%. The difference between the standard MMG rudder model and our modified rudder model is 39% for the largest side force ratio. We also see that our new model fits well with the data directly from the CFD simulations.

These errors must be evaluated against simulation time. We measured the clock-time for each simulation in this paper, executed on the same computer. Neglecting the free surface reduced the simulation time from almost 8 h to just above 1, when the model scale was 1:4. This is therefore a simplification with a large reduction in simulation time, but with just a small error in the resistance model. A full-scale simulation without the rudder took around 2.3 h, compared to around 0.8 h in model scale 1:10. This shows that model scale 1:4 is comparable to model scale 1:10 in simulation time, while the simulation results is comparable to full-scale values. Neglecting heel mainly has the consequence that we can run fewer simulations. As such, including heel in the test matrix will increase the total simulation time with a factor of 2–3 depending on the number of heel angles one decides to test. However, the error in the added resistance can be quite large, and this might be necessary for ships where the stability is not sufficient to avoid larger heel angles.

## 7. Conclusion

Although there was a clear effect of the free surface on the drift induced forces for our case study ship, the effect was much smaller than on the straight-ahead resistance. The importance of the drift-induced forces is also reduced for increasing Froude number, as the importance of the wave resistance is increasing. Considering the large decrease in computational time achieved by neglecting the free surface, this is a simplification that is worth considering for design studies of wind powered cargo ships. For Froude numbers around 0.2 or less, the free surface seems to be safely neglected, both based on the experiments done in this paper and the other references from the literature. Slightly higher Froude numbers could also be considered, although the error due to this simplification was shown to increase along with the Froude number.

We found that the error due to too low Reynolds number is fairly large for model scales in the range typically used in towing tanks, shown both in our experiments and in other papers in the literature. The explanation is likely that the flow around the bottom of the hull separates more easily at lower Reynolds numbers, which leads to larger cross-flow drag. However, the error is reduced to a minimum for model scales larger than 1:4 for our case study ship. This represents a Reynolds number of 67.7 million and model length of 30 m. Although this would be a very large model for a towing tank experiment, it is still small enough to be a time efficient scale for CFD simulations. As such, it seems that drift-induced forces can accurately be predicted at practical model scales for CFD simulations, but scales typical for towing tanks should be avoided if possible.

The effect of heel turned out to be large when large heel angles were combined with large drift angles. This is expected to be due to changes in the cross-flow drag on the ship as a function of heel. Whether or not heel should be part of the test program for a wind-powered ship is therefore primarily a question about ship stability. If the expected heel angles due to wind power approaches 10 or 15 degrees, a more comprehensive test program and route simulation model are probably necessary.

The hull forces due to both drift and rudder angle was predicted well with the polynomials in the MMG model. The default rudder model was, however, not very accurate for computing the rudder resistance. This was not surprising considering the simplicity of the model. The

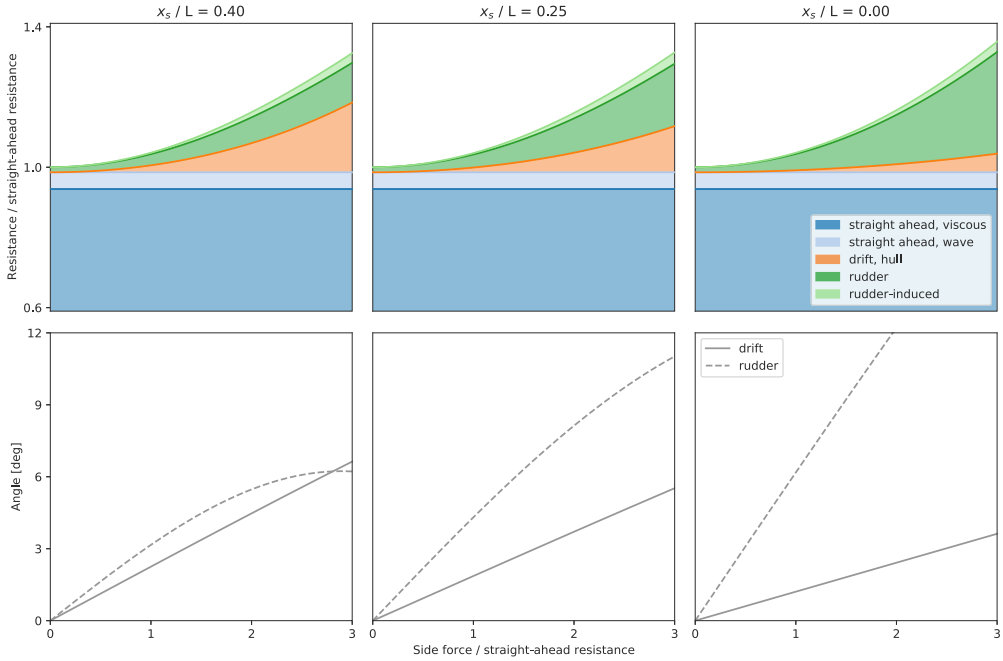


**Fig. 24.** Importance of different resistance components.

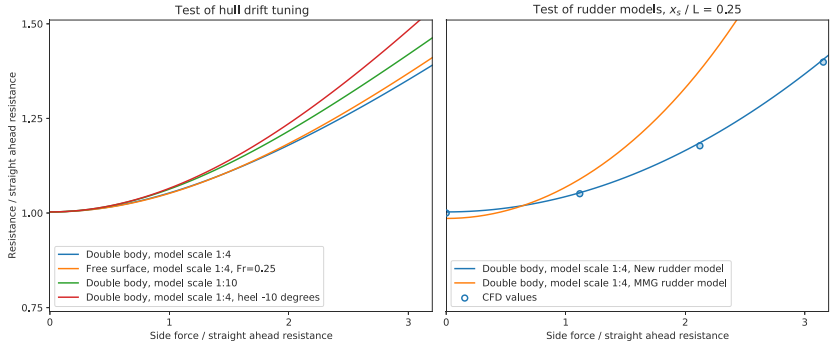


**Fig. 25.** Comparison of models.

accuracy was greatly improved by switching to a more conventional model for lifting surfaces based on classical lifting line theory. With the new model, the rudder forces could be estimated accurately as a function of drift angle and rudder angle using just a few CFD simulations as tuning data. Although it was not perfect, the main problem with the model was predicting the forces when both the drift angle was large, and the propeller thrust coefficient was high at the same time. This is expected to be due to a complex flow field in the jet from the propeller, that are affected by both propeller thrust, drift angle and rudder angle at the same time. However, the purpose of a sail is to reduce the required thrust from the propeller and the main problem with the model will therefore reduce as the amount of thrust from the sails increase. Although it is likely possible to find more advanced models that better capture the dynamics between the rudder and the propeller, this would probably entail more variables that needs to be tuned based on either CFD or experimental data. We therefore conclude that the modified MMG model is a good compromise for quick design iterations and simplified case studies.

As an interesting note, the rudder resistance was found to be as large or larger than the drift-induced hull resistance for our case study ship, depending on the placement of the sails. This was somewhat surprising, and indicate that both sources of resistance deserve equal amount of attention during a design loop.

## CRediT authorship contribution statement

**Jarle Vinje Kramer:** Conceptualization of this study, Methodology, Software, Writing. **Sverre Steen:** Assistance in conceptualization of this study, Guidance, Text revision.

## Declaration of competing interest

The authors declare that they have no known competing financial interests or personal relationships that could have appeared to influence the work reported in this paper.

## Acknowledgment

This work was carried out at SFI Smart Maritime (WP2) supported by the Research Council of Norway through the Center for Research-based Innovation (SFI) scheme (Grant number 237917).

## References

Abkowitz, M.A., 1964. Lectures on Ship Hydrodynamics Steering and Manoeuvrability. Technical Report, Technical Univeristy of Denmark, Lyngby, Denmark.

Bertram, V., 2000. Practical Ship Hydrodynamics. Butterworth Heinemann.

Bhushan, S., Xing, T., Carrica, P., Stern, F., 2009. Model- and full-scale URANS simulations of athena resistance, powering, seakeeping, and 5415 maneuvering. J. Ship Res. 54 (4), 179–198.

DNV-GL, 2016. Rules For Classification, Part 3 Hull, Chapter 15 Stability. Technical Report, DNV-GL.

Duman, S., Bal, S., 2019. A quick-responding technique for parameters of turning maneuver. Ocean Eng. 179, 189–201.

Eça, L., Hoekstra, M., 2008. The numerical friction line. J. Mar. Sci. Technol. 13, 328–345.

Eça, L., Hoekstra, M., 2014. A procedure for the estimation of the numerical uncertainty of CFD calculations based on grid refinement studies. J. Comput. Phys. 262, 104–130.

Eça, L., Vaz, G., Hoekstra, M., 2010. Code verification, solution verification and validation in RANS solvers.

Goldstein, S., 1929. On the vortex theory of screw propellers. Proc. R. Soc. A 123 (792), 440–465.

Hirt, C.W., Nichols, B.D., 1981. Volume of fluid (VOF) method for the dynamics of free boundaries. J. Comput. Phys. 39 (1), 201–225. http://dx.doi.org/10.1016/0021-9991(81)90145-5.

Hympendahl, O., Ciortan, C., 2018. Systematic assessment of model errors in CFD ship resistance simulations. In: Proceedings of Numerical Towing Tank Symposium. Cortona Italy.

International Towing Tank Conference, 2011. Practical Guidlines for Ship CFD Applications. Technical Report, International Towing Tank Conference.

International Towing Tank Conference, 2017. Uncertainty Analysis in CFD Verification and Validation Methodology and Procedures. Technical Report, International Towing Tank Conference.

Issa, R.I., Gosman, A.D., Watkins, A.P., 1986. The computation of compressible and incompressible recirculating flows by a non-iterative implicit scheme. J. Comput. Phys. 62 (1), 66–82. http://dx.doi.org/10.1016/0021-9991(86)90100-2.

Jin, Y., Duffy, J., Chai, S., Chin, C., Bose, N., 2016. URANS study of scale effects on hydrodynamic manoeuvringcoefficients of KVLCC2. Ocean Eng. 118, 93–106.

van der Kolk, N.J.V.D., Akkerman, I., Keuning, J.A., Huijsmans, R.H.M., 2020. Part 2: Simulation methodology and numerical uncertainty for RANS-CFD for the hydrodynamics of wind-assisted ships operating at leeway angles. Ocean Eng. 201.

van der Kolk, N.J.V., Keuning, J.A., Huijsmans, R.H.M., 2019. Part 1: Experimental validation of a RANS-CFD methodology for the hydrodynamics of wind-assisted ships operating at leeway angles. Ocean Eng. 178, 375–387.

Kramer, J.V., 2021. GitHub page for the article "Simplified test program for hydrodynamic CFD simulations of wind-powered cargo ships". https://github.com/jarlekramer/Hydrodynamic-test-program-for-wind-power.

Kramer, J., Steen, S., 2015. Importance of the free surface for the drift-induced forces on a ship-like foil. In: Numerical Towing Tank Symposium. Cortona, Italy.

Kramer, J., Steen, Savio, L.S., 2016a. Drift forces–wingsails vs flettner rotors. In: High-Performance Marine Vehicles. Cortona.

Kramer, J., Steen, S., Savio, L., 2016b. Experimental study of the effect of drift angle on a ship-like foil with varying aspect ratio and bottom edge shape. Ocean Eng. 121, 530–545.

Kume, K., Hasegawa, J., Tsukada, Y., Fujisawa, J., Fukasawa, R., Hinatsu, M., 2006. Measurements of hydrodynamic forces, surface pressure, and wake for obliquely towed tanker model and uncertainty analysis for CFD validation. J. Mar. Sci. Technol. 11, 65–75.

Larsson, L., Stern, F., 2014. Numerical Ship Hydrodynamics - An Assessment of the Gothenburg 2010 Workshop. Springer.

Longo, J., Stern, F., 2002. Effects of drift angle on model ship flow. Exp. Fluids 32 (5), 558–596.

Menter, F.R., Kuntz, M., Langtry, R., 2003. Ten years of industrial experience with the SST turbulence mode. In: Proceedings of the Fourth International Symposium on Turbulence, Heat and Mass Transfer. Antalya, Turkey.

Molland, A.F., Turnock, S.R., 1995. Wind Tunnel Tests on the Effect of a Ship Hull on Rudder-Propeller Performance at Different Angles of Drift. Technical Report, University of Southampton, Southampton, England.

Molland, A.F., Turnock, S.R., 2002. Flow straithtening effects in a ship rudder due to upstream propeller and hull. Int. Shipbuild. Prog. 49, 195–214.

Ohashi, K., Kobayashi, H., Hino, T., 2018. Numerical simulation of the free-running of a ship using the propeller model and dynamic overset grid method. Ship Technol. Res. 65, 153–162.

Oosterveld, M.W.C., Oossanen, P.V., 1975. Further computer-analyzed data of the wageningen B-screw series. Int. Shipbuild. Prog. 22.

OpenCFD ltd, 2021. OpenFOAM homepage. https://www.openfoam.com/.

Ouchi, K., Uzawa, K., Kanai, A., Katori, M., 2013. "Wind Challenger" the next generation hybrid sailing vessel. In: Proceedings of the Third International Symposium on Marine Propulsors.

Patankar, S.V., Spalding, D.B., 1983. A calculation procedure for heat, mass and momentum transfer in three-dimensional parabolic flows. Int. J. Heat Mass Transfer 15 (10), 1787–1806. http://dx.doi.org/10.1016/0017-9310(72)90054-3.

Perić, R., Abdel-Maksoud, M., 2016. Reliable damping of free-surface waves in numerical simulations. Ship Technol. Res. 63, 1–13.

Raven, H.C., van der Ploeg, A., Starke, A.R., Eca, L., 2008. Towards a CFD-based prediction of ship performance—progress in predicting full-scale resistance and scale effects. Int. J. Marit. Eng. 150.

Richardson, L.F., 1911. The approximate arithmetical solution by finite differences of physical problems involving differential equations, with an application to the stresses in a masonry dam. Phil. Trans. R. Soc. A 210 (459-470), 307–357.

Ross, A., 2008. Nonlinear Manoeuvring Models for Ships: A Lagrangian Approach. Technical Report, Norwegian University of Science and Technology, Trondheim, Norway.

Spalart, P.R., Rumsey, C.L., 2007. Effective inflow conditions for turbulence models in aerodynamic calculations. AIAA J. 45, 2544–2553.

Tillig, F., 2020. Simulation Model of a Ship's Energy Performance and Transportation Costs. Technical Report, Chalmers Univeristy of Technology, Gothenburg, Sweden.

Tillig, F., Ringsberg, J.W., 2020. Design, operation and analysis of wind-assisted cargo ships. Ocean Eng. 211.

Tillig, F., Ringsberg, J.W., Psaraftis, H.N., Zis, T., 2020. Reduced environmental impact of marine transport through speed reduction and wind assisted propulsion. Transp. Res. D 83.

Väinämö, J., 2017. Operational experience and results from the first reference installation from Nov-2014, roro-ship estraden (9700 DWT). In: 24th International HISWA Symposium on Yacht Design and Yacht Construction. Amsterdam, Netherlands.

Virtanen, P., Gommers, R., Oliphant, T.E., Haberland, M., Reddy, T., Cournapeau, D., Burovski, E., Peterson, P., Weckesser, W., Bright, J., van der Walt, S.J., Brett, M., Wilson, J., Millman, K.J., Mayorov, N., Nelson, A.R.J., Jones, E., Kern, R., Larson, E., Carey, C.J., Polat, I., Feng, Y., Moore, E.W., VanderPlas, J., Laxalde, D., Perktold, J., Cimrman, R., Henriksen, I., Quintero, E.A., Harris, C.R., Archibald, A.M., Ribeiro, A.H., Pedregosa, F., van Mulbregt, P., SciPy 1.0 Contributors, 2020. SciPy 1.0: Fundamental algorithms for scientific computing in python. Nature Methods 17, 261–272. http://dx.doi.org/10.1038/s41592-019-0686-2, URL: https://rdcu.be/b08Wh.

Yasukawa, H., Yoshimura, Y., 2015. Introduction of MMG standard method for ship maneuvering predictions. J. Mar. Sci. Technol. 20, 37–52.

# Paper 5: Sail-induced resistance on a wind-powered cargo ship

Written by Jarle Vinje Kramer and Sverre Steen

Submitted to Journal of Ocean Engineering in January 2022. The first round of reviews was completed in April 2022 and the preprint with the changes due to the feedback from the reviewers is presented in this document.

# Sail-induced resistance on a wind-powered cargo ship

Jarle Vinje Kramer* and Sverre Steen

Pre-print, written during the autumn of 2021, and last updated in April 2022
* Corresponding author: jarle.a.kramer@ntnu.no
Department of Marine Technology, Norwegian University of Science and Technology, Otto Nielsens veg 10, 7052 Trondheim, Norway

**Abstract**
This article explores the added resistance due to side forces from wingsails, called the sail-induced resistance. A cargo ship is tested with varying speed, appendages, number of sails, and control algorithms for the sails. The appendages consist of bilge keels, a high aspect-ratio fixed keel, and a dynamically controlled keel. The sails were controlled both to maximize the thrust and to iteratively optimize the angle of attack including hydrodynamic effects. The physical modelling was done with a combination of CFD, maneuvering theory, discrete lifting line, and empirical models. The magnitude of the sail-induced resistance without any keels was found to be comparable to the added resistance in waves. The main source of the resistance was the rudder, which was forced to operate at large angles in steady state conditions. Adding the appendages reduced the sail-induced resistance, but the fixed appendages also increased the friction. The dynamic keel was therefore the only appendage that significantly improved the fuel savings. The side force from the sails could be significantly reduced with limits in the control algorithm. Although this limit also reduced the thrust from the sails, the fuel savings remained high due to a roughly equal reduction in the sail-induced resistance.

**Keywords:** Wind-power – CFD – Discrete lifting line – Route simulation – Hydrodynamic design

## 1 Introduction

Modern sail technologies have the potential to significantly reduce the energy consumption of cargo vessels. The popularity of the technology is therefore increasing, both in the scientific literature and in the maritime industry. Several ships have recently installed wind-power devices, and more projects are planned for the near future. Examples include the general cargo ship SC Connector that recently installed two 35 m tall rotor sails (Ship Technology, 2021), the general cargo ship MV Ankie that have installed two 10 m tall suction sails (Econowind, 2020), and the planned car carrier Ocean Bird that is designed with four 80 m tall wingsails (Wallenius Marien and Alfa Laval, 2021). Although there are clear benefits with sails, they also come with new challenges for the design and operation of the ships that use them. A well-known problem is the direction of the force that is created from the wind: depending on the apparent wind angle relative to the ship direction, there is often a side force component from the sails that is several times larger than the thrust. If the ship is to move with a steady direction and heading, this aerodynamic side force must be balanced with opposing hydrodynamic forces from the hull and the rudder. To achieve this, the ship must be operated with a steady drift angle – also known as leeway angle - and rudder angle. As a result, the resistance of the vessel is increased. This increase in resistance can in some cases reduce the benefit from the sails considerably. We refer to this added resistance as the *sail-induced* resistance, defined as the resistance on the ship with sails minus the resistance without sails at the same velocity. This article explores three questions related to this resistance component:

- How large is the sail-induced resistance on a wind-powered cargo ship?
- What is the main source of the resistance?
- How can the sail-induced resistance be reduced?

To answer these questions, we performed a case study of a cargo ship equipped with several large wingsails on a coastal route in northern Europe. The hydrodynamic forces as a function of drift angle, rudder angle, propeller loading, and ship speed was analyzed with Computational Fluid Dynamics (CFD). The results from these simulations were used to generate a hydrodynamic route simulation model based on maneuvering theory. The sails were analyzed with a discrete lifting line method that includes interaction effects between multiple wings. The propeller and the added resistance in waves were analyzed using empirical methods. All models were combined with weather data using a route simulation framework. Numerical solvers ensured balance between the aerodynamic and the hydrodynamic forces and moments in 4 degrees of freedom: surge, sway, roll and yaw. Table 1 shows a list of physical effects that are included or neglected in the simulation, with more details described throughout the article.

The importance of the sail-induced resistance is dependent on several factors. In this paper, we vary the hydrodynamic design of the ship, the operational speed, the total sail area, and the control policy of the sails. The number of sails is varied between 1 to 5 and the design speed is varied between 8 to 16 knots. The number of sails vary the magnitude of both the thrust and the side force from the sails. The variation in the ship velocity varies both the ship resistance and the apparent wind angle.

The variation due to the physical design was evaluated by testing four different ship configurations. A bare hull with a spade rudder was the base-line design. We then tested the effect of three different keel-designs, all intended to increase the side-force-to-drag ratio of the ship: low aspect-ratio bilge keels, a static high aspect-ratio keel, and a dynamic keel that is both retractable and where the angle of attack can be adjusted. The main purpose of adding the bilge keels was to move the center of lateral resistance – also known as the hydrodynamic center of effort – backwards on the hull. For the bare hull, the rudder was generally forced to operate

with large angles to keep the ship balanced in yaw. This created a large increase in the resistance on the rudder. Adding the bilge keels was an attempt to reduce the required rudder angle, and therefore the rudder resistance. The high aspect-ratio keels were tested as the lift-induced resistance generally decrease rapidly with an increasing aspect-ratio of the lifting surface. They were therefore expected to improve the side-force-to-drag-ratio relative to the low aspect-ratio hull. The dynamic keel was introduced to decouple the side force on the keel from the drift angle of the vessel, and thereby allow more of the side force to be balanced by the high aspect-ratio keel.

Two different control policies were tested. The first policy always maximizes the thrust from the sails. The second policy iteratively optimizes the angle of attack to maximize the thrust minus the sail-induced resistance. The full hydrodynamic route simulation model is used in the optimization procedure for the second policy. The purpose was to quantify how much the sail-induced resistance is dependent on the control algorithm of the sails. For both algorithms, explicit limits on the side force, rudder angle, and heel angle are used to ensure safe and realistic operation of the ship. To explore a simple way to manage the sail-induced resistance, we also investigated the effect of varying the value of side force limit for both control algorithms.

When analyzing wind-powered ships, the primary goal is usually to quantify the fuel savings due to the sails. This involves some form of route simulation which combines models of the ship with weather data. There is currently a large variation in model complexity and assumptions between different papers on this topic. Although the concept of the sail-induced resistance is text-book knowledge for sailboats (Larsson, et al., 2000), it has been common to neglect this effect when analyzing merchant ships. Examples of scientific papers from the last decade using this simplification can for instance be found in (Ouchi, et al., 2011), (Traut, et al., 2014), (Bøckmann, et al., 2014), (Yuankui, et al., 2014), (Bentin, et al., 2016), (Talluri, et al., 2016) and (Talluri, et al., 2018). The papers investigate the fuel savings due to rotor sails, wingsails, wind turbines and kites using different route simulation frameworks. Most of these examples only include the calm water straight-ahead resistance in the hydrodynamic model, while one also includes the added resistance in waves. Whether the sail-induced resistance is neglected due to the added complexity or because it is assumed to be a negligible resistance component is not explicitly stated by the authors. The interest in the sail-induced resistance for merchant ships has, however, increased recently. Examples of route simulations where the sail-induced resistance is included can be found in (Tillig & Ringsberg, 2020), (Lu & Ringsberg, 2020) and (van der Kolk, et al., 2019). The papers analyze different ships with rotor sails and the hydrodynamic models are based on either empirical expressions or CFD simulations of the ship. A dedicated paper about hydrodynamic CFD-simulations of wind-powered ships can be found in (van der Kolk, et al., 2020). The focus is on efficient meshing strategies and turbulence models, to facilitate efficient hydrodynamic testing of wind-powered ships.

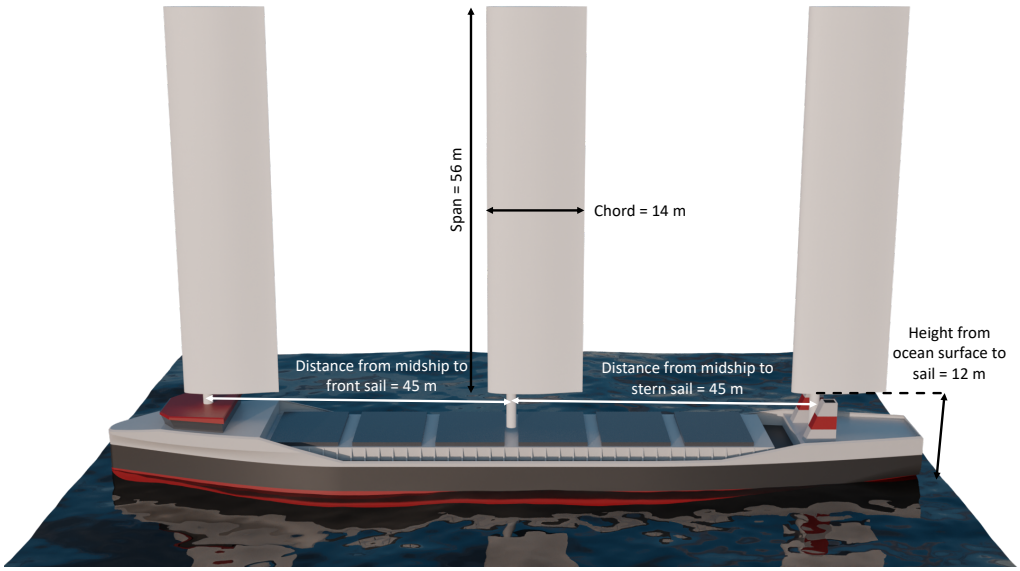


*Figure 1: Illustration of the superstructure and sail geometry used for this case study.*

Although these references fully acknowledge the negative hydrodynamic effects related to wind-power, they do not focus directly on the importance of the sail-induced resistance. Rather, it is either only a part of a larger resistance model used to explore the benefit of wind-power, or the focus is on the technical requirements for the hydrodynamic modelling. Although this resistance is clearly important for sailboats – especially for vessels intended for high speed – there are some differences for merchant ships. On one hand, merchant ships are generally hybrid ships, where only part of the propulsion comes from the wind. This suggest that the sail-induced resistance may not be that large in many cases. On the other hand, merchant ships are not designed for balancing large side forces. This could mean that even relatively small side forces could lead to problems. The magnitude of the sail-induced resistance is a good indicator for whether changes should be made to the hydrodynamic design. If it is large, ship designers working

on wind-powered ships should update the hull and appendage design to balance the side force more efficiently. If it is small, they can largely continue with the same designs as today.

There have been some hydrodynamic design investigations of wind-powered merchant ships in the literature previously. An example is (van der Kolk, et al., 2021), which present results from a large experimental study of low-aspect-ratio bilge keels. The goal was to see how much the keels could improve the ship's ability to balance the side forces from sails. The paper presents results for the hydrodynamic side force, resistance, and center of lateral resistance, as a function of drift angle. However, it does not include any analysis of aerodynamic forces or route simulations to quantify the actual improvements during operation. An example of a design exploration that do include route simulations is presented in (Minami, et al., 2003). The paper explores the effect of adding different shallow keels to a wind-powered merchant ship. The main goal was to reduce the rudder angle to maintain steerability in unfavorable weather conditions. The authors stated that they were initially worried that adding the keels would increase the fuel consumption due to the added friction. The results show that the fuel savings from the sails are not much affected by the keels, but that the rudder angle was reduced. The keels are therefore seen to reduce the average sail-induced resistance roughly as much as they increase the frictional resistance.

Variations in the control algorithm for sails have also been studied previously. The work presented in (Sacher, et al., 2015) and (Aubin, et al., 2016) explores how the shape of soft sails can be optimized including a simple method for accounting for the negative hydrodynamic effects due to the sails. A penalty that is proportional to the side force from the sails is added in the objective function in the optimization. However, the focus of the papers is on the aerodynamic testing and the optimal value of the linear penalty is therefore not evaluated directly.

We have previously done a smaller but similar study as the one presented in this paper, found in (Kramer & Steen, 2016). The conclusion then was that the sail-induced resistance had a large impact on the fuel savings for a wind-powered merchant ship, and that the control strategy for the sails should be optimized with hydrodynamic effects included in the objective function. However, the previous study was based on a simplified model of the ship, the sails, and the control algorithm. The current paper can in some ways be seen as a significantly updated version of (Kramer & Steen, 2016), which resulted in somewhat different conclusions.

The structure of the article is as follows: details of the case study are given in Section 2, the CFD setup is explained in Section 3, the hydrodynamic modelling framework in Section 4, the aerodynamic modelling framework in Section 5, and the route simulation framework in Section 6. The results and conclusion are then presented in Section 7 and 8. We show how the hydrodynamic resistance of the different design variants depends on an externally applied side force and which part of the ship – the hull, the rudder, or the keel – experiences the largest resistance. Results from route simulations are used to measure how much the fuel savings due to wind-power are reduced due to the negative hydrodynamic effects and we compare the sail-induced resistance against all the other resistance components on the ship. Finally, we compare the difference between the two control algorithms and the effect of varying the side force limit on the sails.

*Table 1: Physical effects in this case study*

| Domain | Effects included | Effects neglected |
|---|---|---|
| **Hydrodynamics** | - Calm water resistance<br>- Drift forces<br>- Rudder forces<br>- Drift and rudder coupling effects<br>- Heel angle<br>- Propeller efficiency<br>- Interaction between rudder, hull, and propeller<br>- Added resistance due to ocean waves | - Dynamic sinkage and trim<br>- Heel and drift coupling effects<br>- Drift effects on the propeller<br>- Side force and yaw moment from ocean waves |
| **Aerodynamics** | - Viscous effects on lift and drag on the wingsails<br>- Lift-induced effects on lift and drag<br>- Interaction effects between multiple sails<br>- Optimized operation policy | - Interaction between sails and ship superstructure<br>- Aerodynamic forces on the superstructure<br>- Height variation in wind direction<br>- Aerodynamic damping of ship motion in waves<br>- Dynamic effects such as gusts and sudden weather changes |
| **Ship operation** | - Coastal route with hindcast weather data<br>- Limits on the sail control to avoid capsizing<br>- Limits on the sail control to avoid loss of steering | - Details in the logistics of the route, such as variation in cargo and time schedule<br>- Maneuvering in harbors<br>- Short term dynamics from control systems, such as the sails influence on the autopilot |

# 2 Case study details

The ship design used in this case study was intended to represent a simple yet typical cargo ship with roughly 5 000 tons dead weight capacity (DWT). The exact cargo type is not considered directly, but we imagine either a coastal general cargo ship or a dry bulker. The features of the ship that are kept constant throughout the case study are presented in Section 2.1 before the different appendages are explained in section 2.2. An illustration of the hydrodynamic design features along with main dimensions of the ship is shown in Figure 2. This figure also includes the coordinate system used when evaluating the hydrodynamic forces and moments. The sails and super structure of the ship are illustrated in Figure 1.

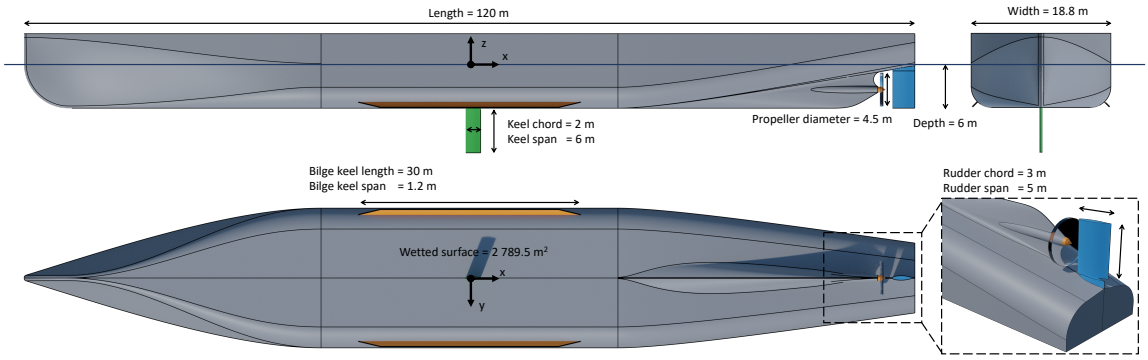


*Figure 2: Hydrodynamic design overview. The ship is shown with all appendages installed.*

## 2.1 Fixed features

### 2.1.1 Main dimensions

The values for the length, width, depth, and displacement of the ship are based on similar reference ships with significant rounding on all values. The fully loaded mass of the ship is 9 000 tones. The ratio between deadweight and loaded displacement for a cargo ship will vary based both on type and size of the ship. Schneekluth & Bertram (1998) state that this ratio is often between 60-80% for general cargo ships with 5 000 – 15 000 DWT. We chose a slightly lower ratio of roughly 55%, based on numbers from a previous commercial project at our department. The rudder planform area is right above 2% of the underwater hull lateral area, calculated as the ship's length multiplied by depth. As a comparison, Bertram (2012) states that this variable is typically around 1.5% for cargo ships.

### 2.1.2 Speed and power

The design speed of the ship was varied between 8 to 16 knots, with a step size of 2 knots. Each design speed is assumed to represent a different ship where the engine size is adjusted to the required power. The maximum engine power is a variable that is used to determine involuntary speed loss. The engine size is adjusted based on the calm water resistance, the propulsion efficiency of the propeller, an assumed sea margin of 30%, and an engine design load of 80%. The resulting power is 530, 1 100, 2 100, 3 400 and 5 700 kW for the ship speeds 8, 10, 12, 14 and 16 knots respectively. Data for the hull resistance and propeller efficiency will be presented later in the text. The propeller diameter was the same for all speeds and design configurations. The size corresponds to a thrust loading coefficient in calm water between 0.4 and 0.53 depending on the design variant and speed. The thrust loading coefficient is defined as $C_{T,p} = T \,/\, \left(0.5\, \rho\, A_p\, U_s^2\right)$, where $T$ is the propeller thrust, $\rho$ the water density, $A_p$ the propeller disk area and $U_s$ the ship speed.

### 2.1.3 Stability

The ship was assumed to have a relatively high stability as the primary interest in this study was the lift and lift-induced drag due to drift and rudder angles. Limiting the heel angle allows for practical simplifications on the hydrodynamic model, which are addressed later in the text. According to (Schneekluth & Bertram, 1998), recommended values for the minimum initial metacentric height (GM) in fully loaded conditions varies between 0.8 m and 1.0 m for general cargo ships. Dry bulkers can have significantly higher values due to heavy cargo placed low in the hull. Based on data from commercial projects at our department, we know of general cargo ships of similar size as our case study ship that typically operate with a GM between 1.0 m and 2.0 m, depending on the cargo. We have therefore assumed a GM value of 1.5 m for this case study. The heel angles during the route simulation are calculated based on this value and an initial linear stability model for the hull: the restoring heel moment is defined as $M_x = GM\ \phi\ g\ \Delta$, where $\phi$ is the heel angle, $g$ the acceleration of gravity, and $\Delta$ the mass displacement of the ship. In addition, the hydrodynamic heel moment from the rudder and the keel is calculated based on the side force they produce at a given weather condition and a fixed center of effort at the midspan of each appendage. The heel moment from the appendages is generally destabilizing since the vertical center of effort is below the center of gravity of the ship. However, the importance of the appendages for the heel angle was small in this case study due to the relative magnitude of the hydrostatic moment on the hull.

Details on how the side force from the appendages is calculated will be given in Section 4 and values for the heel angle during route simulations will be presented in Section 7.

#### 2.1.4 Sails and superstructure

The sails in the case study were solid single element symmetric wingsails with a NACA 0015 foil profile. The dimensions of the sails were manually adjusted to achieve well above 50% reduction in fuel consumption on average for the lowest test speeds on a case study route between Trondheim and Rotterdam. More information regarding the route and weather data will be given in Section 6.2. The placement was such that the average location of the quarter chord is always midship. The sails are assumed to be retractable, for instance by using a telescopic mechanism. When the sails are retracted, the area is reduced to a quarter of the full size in the aerodynamic model, to minimize the drag force. When to retract is governed by the control algorithm for the sails, which will be presented in Section 6.1.2. Retractability can be a challenging design feature that is not necessarily used on vessels with small sails. However, both existing and planned vessels with larger sails seem to value this feature enough to include the added complexity. Examples of modern retractable sails include the telescopic wingsails in the Ocean Bird project (Wallenius Marien and Alfa Laval, 2021), the foldable wingsails from Ayro and VPLP (Ayro, 2022), the tiltable rotor sails from Norsepower on the ship SC connector (Ship Technology, 2021), and the inflatable wingsails from Michelin (2021).

## 2.2 Appendages

#### 2.2.1 Bilge keels

A solution for improving the ship's ability to balance side forces is bilge keels. This is also a design feature that is already installed on many merchant ships for seakeeping purposes. As mentioned in the introduction, this design feature is explored experimentally for wind-powered ships in (van der Kolk, et al., 2021). Although the paper clearly showed that bilge keels would increase the side force and move the hydrodynamic center of lateral resistance backwards for a given drift angle, it was unclear exactly how much the fuel savings for a wind-powered ship would change. We therefore decided to explore this further in this study. Inspired by the results in (van der Kolk, et al., 2021), we used relatively short bilge keels. The difference in the center of lateral resistance for long and short bilge keels was shown to not be very dependent on the length and shorter bilge keels will add less frictional resistance when moving straight-ahead. The intended functionality of bilge keels is to ensure separation around the bottom edge of the ship. To have this effect, it is important that the edge of the bilge keels extend outside the boundary layer. The height of the bilge keels is dimensioned based on an empirical estimation of the boundary layer thickness, $\delta$, and a safety factor. The Schlichting equation (Schlichting, 1979) was used, which states that the turbulent boundary layer thickness depends on the Reynolds number, $Re_x$, calculated based on the length from the bow to the location where the thickness is evaluated, $x$. The expression is given as $\delta = 0.37\, x\, / Re_x^{1/5}$ . The CFD simulations in this paper were done in model scale 1:4. The reduced scale was chosen as a practical compromise between scaling accuracy and computational speed based on previous work (Kramer & Steen, 2022). The boundary layer thickness furthest back at the bilge keels in model scale 1:4 was estimated to be 0.2 m, which corresponds to 0.8 m with simple geometrical scaling to full-scale. We then assumed a safety factor 1.5 and set the height of the full-scale bilge keels to 1.2 m.

#### 2.2.2 High aspect-ratio keel

With inspiration from conventional sailboats, high aspect-ratio keels are a natural design feature to consider for wind-powered cargo ships. However, the increased depth due to a keel can in some cases be problematic. For instance, in our hometown of Trondheim, there are several cargo ports that have a maximum depth of 8 m. The case study ship tested in this paper would therefore not be able to enter these ports with the static keel shown in Figure 2. In addition, we also discovered that the fixed high aspect-ratio keel only had a limited impact on the sail-induced resistance – which is further addressed in Section 7.1. We therefore decided to also test a keel that could be dynamically controlled, using two mechanisms. First, the angle of the keel relative to the ship's centerline can be adjusted, like a rudder. Second, it can be retracted into the hull when it is not needed, similar to many types of roll stabilizing fins. It is controlled by an algorithm – further outlined in Section 6.1.3 – that both determines when to deploy the keel and how large the operating angle should be for a given weather condition.

# 3 CFD simulations

CFD simulations were used for two tasks. First, it was used to simulate the hull, rudder, and keel together at various speeds, drift angles, rudder angles, and propeller loadings. This generated data that were further used to tune the hydrodynamic models in the route simulation framework presented in Section 4. Second, it was used to validate the lifting line model that was used to simulate the sails, presented in Section 5.

## 3.1 Overview of setup

The simulations were performed with the open-source software OpenFOAM, version 2006+ (ESI-Group, 2020). We used an internally developed software framework written in Python to automate and script all the details in the simulation setup. More details of the setup-procedure are presented in a recently published article found in (Kramer & Steen, 2022). The simulations for this study follow the same rules, and the explanation is therefore kept brief.

#### 3.1.2 Solvers and turbulence model

Two different OpenFOAM solvers are used. First, the solver simpleFoam is used for steady state single phase simulations. This includes hydrodynamic simulations for estimating forces that are assumed to not be dependent on free surface effects – such as

forces due to drift and rudder angles – as well as aerodynamic simulations of the wingsails. Second, the solver interFoam is used to calculate the wave resistance on the ship. This solver uses the Volume of Fluid method (Hirt & Nichols, 1981) to capture the interaction between water and air. All simulations are performed with the turbulence model k-omega SST (Menter, et al., 2003).

### 3.2.3 Simulation domain and boundary conditions

An overview of the simulation domains is shown in Figure 3. The size of the hydrodynamic domain is given relative to the ship length, L, while the size of the aerodynamic domain is given relative to the wingspan, S. The domain for the hydrodynamic simulations is shown in two different versions; one where the free surface is included in the simulation and one where it is simplified with the symmetry plane approximation. The symmetry plane approximation is referred to as double body simulations later in the text. When the free surface is included, wave damping zones based on the expressions in (Perić & Abdel-Maksoud, 2016) are used near the outer boundaries. The inlet values for the turbulent variables are based on recommended values from (Spalart & Rumsey, 2007) and an assumed turbulent intensity of 1%. Solid walls are modeled with continuous wall functions that blend between the logarithmic model and the viscous model using an exponential transition (Popovac & Hanjalic, 2007).

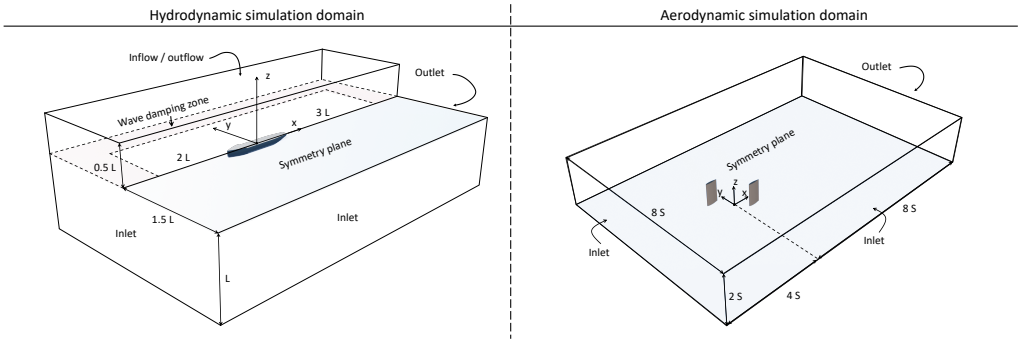


*Figure 3: Illustration of the simulation domain for both hydrodynamic and aerodynamic simulations.*

### 3.1.3 Propeller model

The ship propeller is modeled as an actuator disk. The distribution of both thrust and torque is based on a theoretical Goldstein optimum distribution originally found in (Goldstein, 1929). Equations can also be found in (Kramer & Steen, 2022). The specific implementation of the actuator disk is based on a custom code for the OpenFOAM library, available in the online repository found in (Kramer, 2021). The relationship between thrust and torque is further based on the open water propeller data we assume for our analysis, further presented in Section 4.

## 3.2 Mesh

The mesh for the simulations is generated with snappyHexMesh – a meshing tool that is part of the OpenFOAM library. The resolution at different parts of the simulation domain is adjusted based on two main principles. The first principle adjusts the number of inflation layers close to solid walls so that the y+ value reaches a target value of 60. The height of the first inflation layer is calculated based on a theoretical friction line and the Reynolds number of the tested geometry. The second principle adjusts the resolution in different parts of the domain relative to the representative length of the simulation. The chosen resolution is based on mesh convergence studies. More details of our mesh generation procedure can be found in (Kramer & Steen, 2022).

### 3.2.2 Hydrodynamic mesh

An example of a mesh for the hydrodynamic simulations is shown in Figure 4. All cell lengths are given relative to the ship length, L. The resolution at rudder was increased relative to the rest of the hull to better capture geometrical features. The resolution at the high aspect-ratio keel matches that of the rudder, while the bilge keels were refined to one level above the rest of the hull. The figure also shows the wake refinement zones, which vary slightly for cases with and without free surface. The difference is related to the need to capture waves generated by the ship. For cases with the free surface included, there is anisotropic vertical refinement in the region around the free surface to reduce the smearing of the volume fraction. The number of cells was approximately 9 and 12 million for double body cases without and with the high aspect-ratio keel respectively. The number of cells for the cases with the free surface included in the simulation was approximately 4.6 million. These simulations where only used to predict the straight-ahead resistance of the hull and therefore assumed symmetry across the centerline of the ship – i.e., with half the mesh size relative to cases where the side force is of interest.

Kramer & Steen (2022) contains an analysis of the uncertainty for the hydrodynamic simulations using an identical simulation setup as the one used in this paper. This included convergence studies of both the mesh resolution and the time step, as well as comparisons against benchmark experiments. The mesh uncertainty for the hull forces at a drift angle equal to 9 degrees was generally less than 2.5% for various model scales both with and without free surface modeling. The mesh uncertainty for the rudder-forces at a drift angle equal to 9 degrees and rudder angle equal to 6 degrees was generally less than 5%. The time step uncertainty was less than 1% for a ship hull moving with a drift angle equal to 9 degrees. The calm-water, straight-ahead resistance was compared against three open ship geometries – KCS, KVLCC2 and DTMB 5415 – at Froude numbers varying from 0.1 to 0.45.

The average error for the resistance was 1.2% and the maximum error was 4.1%. The resistance, side force, and yaw moment as a function of drift angle were compared against experimental values for the tanker ship KVLCC2, and two simplified ship geometries. The difference in the forces and moments between experiments and CFD was in general around or below 10%, with an average value around 5%.

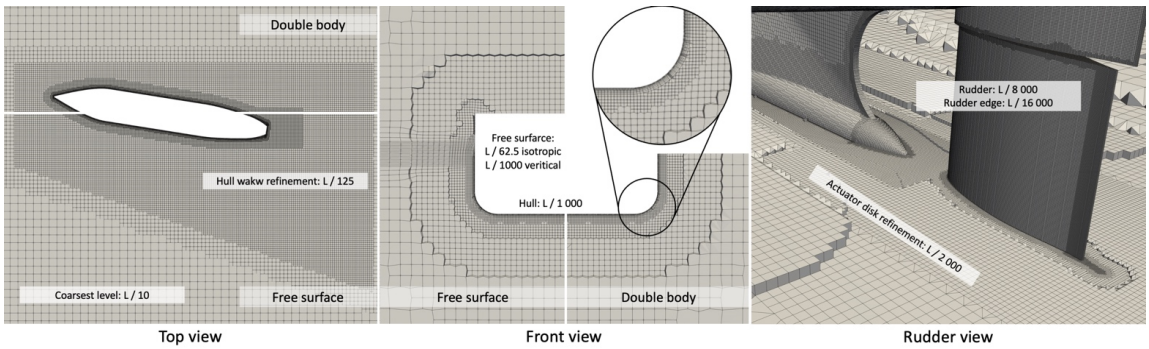


*Figure 4: Illustration of the hydrodynamic mesh with values for the cell lengths at different regions.*

### 3.2.3 Aerodynamic mesh

An overview of the aerodynamic mesh is shown in Figure 5. The wake downstream of the wings are refined within a box shape that covers the entire span length in the vertical direction. The wing tips and the trailing edge is refined one and two levels above the rest of the wing to better capture the geometry. All CFD simulations of the wingsails are done with a symmetry plane at the midspan to reduce the mesh size. The resolution shown in Figure 5 corresponds to roughly 7 million cells for a single sail and 13 - 14 million cells for two sails.

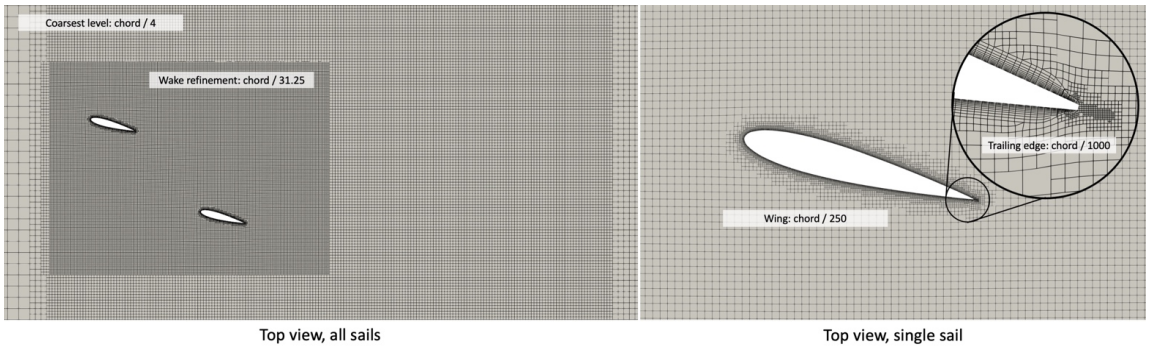


*Figure 5: Illustration of the aerodynamic mesh with values for the cell lengths at different regions.*

The mesh resolution for the aerodynamic simulations was determined based on a convergence study with a single wing, at an angle of attack of 15 degrees and a Reynolds number of 10 million. The smallest and largest mesh had 1.7 and 38 million cells respectively. The recommended practice from the ITTC (2017) was used to estimate the error and uncertainty related to mesh resolution for both lift and drag. In short, least square regression was used to fit polynomial models that estimated the error in the result as a function of mesh resolution. However, since the data showed some oscillatory behavior in the tested range for both the lift and drag, the final uncertainty was estimated based on the data range parameter. See (International Towing Tank Conference, 2017) or (Kramer & Steen, 2022) for further explanation of the method. The mesh uncertainty at our chosen resolution was estimated to roughly 5.5% and 2.7% for the drag and lift coefficient respectively. This was for an angle of attack that is well below stall, but with a relatively high lift coefficient close to 1.0. The drag force on the wing is therefore dominated by lift-induced effects. The values of the drag coefficient, $C_D$, and lift coefficient, $C_L$, as a function of mesh resolution are shown in Figure 6. Both coefficients are defined as the force on the sail divided by the dynamic pressure – equal to $0.5\ \rho\ U^2$, where $\rho$ is the density and $U$ the free stream velocity – and the planform area of the wing – equal to the chord multiplied by the span.

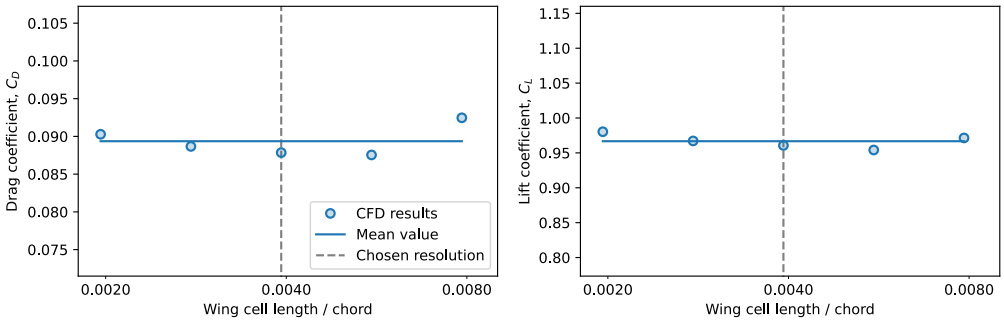


*Figure 6: Drag and lift coefficient for single wing as a function of mesh resolution.*

# 4 Hydrodynamic model

The resistance, side force, and yaw moment on the ship are first estimated with CFD simulations as a function of velocity, drift angle, rudder angle, and propeller thrust. The results are then used to tune route simulation models of the forces on the hull and rudder in calm water. Empirical models are used for the added resistance in waves and the propeller characteristics. The CFD based modeling of the ship is explained in Section 4.1 while the empirical models are outlined in section 4.2

## 4.1 CFD-based models

### 4.1.1 Coupling of CFD data and models

The models presented in this section are used to generalize the results from the CFD simulations to arbitrary ship states. The choice of modelling equations is based on two main goals: to reduce the number of CFD simulations to a level that is practical and to get models that are well behaved in numerical solvers, which are heavily used in the route simulations. The equations are therefore chosen based on a compromise between simplicity and accuracy. Each model is based on either existing ship maneuvering theory or theoretical lifting surface equations. In each equation, there are coefficients that are adjusted such that the model values and the CFD results matches as closely as possible. This is achieved with a least square regression method. The models are implemented in the programming language Python, and we therefore use the curve fitting function from the optimization library in Scipy for this task (Virtanen & Al, 2020). The only difference between the tuning process of the different models is the objective function and input data that is given to the least square regression method.

### 4.1.2 Resistance on the hull in calm water and straight-ahead conditions

The calm water resistance on the hull, $R$, when no aerodynamic side force is applied to the ship is calculated from Equation 1 and 2. The frictional resistance coefficient, $C_F$, is found from the empirical friction line presented in (Eca & Hoekstra, 2008). The added friction due to surface roughness, $\Delta C_F$, is calculated with the empirical model in the "Performance Prediction Method" from ITTC (2017). The hull roughness, $k_s$, is set to 150 micrometers. The thrust-induced resistance is assumed to be linearly dependent on the propeller thrust, $T$, calculated with a thrust deduction factor, $t$. The other symbols in the equations are the wave resistance coefficient, $C_R$, the shape factor, $k$, the ship speed, $U_s$, and the wetted surface of the ship, $S$.

$$C_{T,S} = C_R(F_r) + (1+k)C_F(Re) + \Delta C_F(Re, k_s) \quad (1)$$

$$R(Fr, Re, T) = 0.5\,\rho\,S\,U_s^2\,C_{T,S} + t\,T \quad (2)$$

The shape factor is adjusted so that the corrected friction matches the total resistance on the hull from double body simulations without any thrust from the propeller. The thrust deduction factor is adjusted based on two double body simulations with propeller thrust different than zero and assumed independent of ship speed. Two CFD simulations are executed for every design speed: one with free surface modeling and one without. The wave resistance is calculated as the difference in the resistance between the two. Spline interpolation is used to generalize the wave resistance model to Froude numbers not directly tested. The results from both CFD simulations and the tuned models can be seen in Figure 7. The wave resistance is assumed to not be affected by the keel geometry and is therefore only calculated for the bare hull form. The shape factor for the bare hull and the hull with bilge keels is estimated to 0.100 and 0.142 respectively. The thrust deduction factor is almost identical between the two design configurations with a value of approximately 0.10. The effect of the high aspect-ratio keel is not shown in the plots below, as this component is treated with a separate model explained in Section 4.1.4.

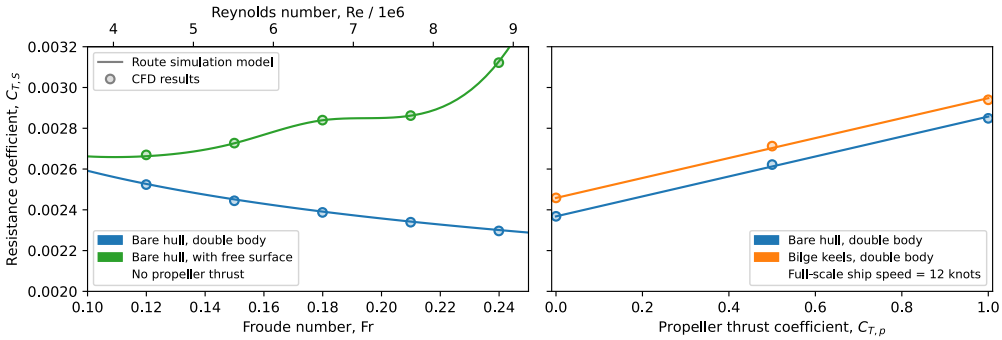


*Figure 7: Calm water straight ahead resistance of the hull in model scale 1:4. The plot to the left shows the wave resistance and the viscous resistance without bilge keels. The plot to the right shows how the resistance varies as a function of propeller thrust. The values on the y-axis are the same for both plots.*

### 4.1.3 Hull and rudder under the influence of sail forces

The forces and moments on the ship as a function of drift angle, rudder angle, and propeller thrust are estimated based on a slightly modified version of the MMG maneuvering model (Yasukawa & Yoshimura, 2015). This modelling approach was one of the main topics in our recently published article (Kramer & Steen, 2022), where we explored both the tuning processes and the accuracy. The explanation in this article is therefore kept brief. Most of the original formulations from the standard MMG model is kept. For route simulations, all terms related to unsteady effects are neglected, such as the yaw rate and inertia. The model includes interaction effects between the rudder and the hull through a polynomial model for the flow straightening in the wake and the induced lift on the hull from the rudder. The effect of the propeller is modeled with a simple expression based on actuator disk theory. Different from the standard MMG model, we calculate the lift and drag force on the rudder based on classical lifting line equations, rather than the "normal force" approximation. This change was done to improve the accuracy of the rudder resistance, based on results presented in (Kramer & Steen, 2022). The lift and drag act normal and parallel to the effective rudder velocity vector estimated from the MMG model. The rudder drag is scaled to different Reynolds numbers based on the same empirical friction line used for the hull resistance multiplied with a rudder shape factor, $k_r$. The expressions are shown in equation 3 and 4, where $C_L$ and $C_D$ are the lift- and drag-coefficient respectively. The symbol $\delta_e$ is used for the angle of attack of the rudder which is corrected for flow straightening effects according to the MMG model. The symbol $\lambda$ is used for the geometrical aspect-ratio, while $e_L$ and $e_D$ are correction factors used to tune the model to CFD results.

$$C_L = \frac{2\pi\delta_e}{1+\frac{2}{\lambda\, e_L}} \tag{3}$$

$$C_D = 2(1+\ k_r)\, C_F(Re) + \frac{C_L^2}{\pi\, \lambda\, e_D} \tag{4}$$

The coefficients in the model are adjusted based on CFD results from double body simulations with both the rudder and the hull together. The simulations are done in model scale 1:4, and only for a single velocity – corresponding to 12 knots full scale. The CFD results used in the tuning procedure consist of a static drift test with zero propeller loading, and three static rudder tests with propeller thrust loading coefficients equal to 0.0, 0.5 and 1.0. The thrust loading coefficient in the route simulations was between these values most of the time. The rudder model, including the rudder-induced forces on the hull, was found to be almost independent of the keels. We therefore limit the presentation of the rudder forces to one ship geometry to reduce clutter in the plots.

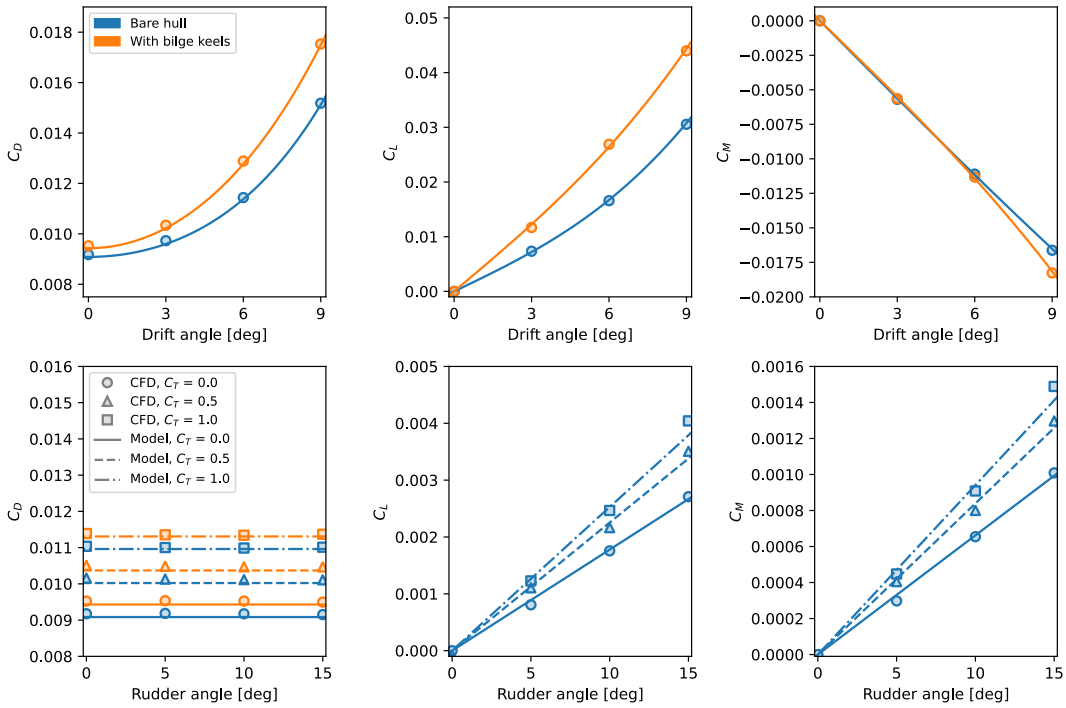


*Figure 8: CFD results and tuned models for the hull. The coefficients for drag, $C_D$, lift, $C_L$, and yaw moment, $C_M$, are made non-dimensional by the dynamic pressure based on the ship speed and the underwater hull lateral area calculated as the ship length multiplied by the depth. The yaw moment is measured relative to the midship location, and the coefficient is divided by the ship length in addition to the area.*

Two differences in the tuning procedure were implemented for this paper relative to (Kramer & Steen, 2022). First, the process for finding the wake factor in the MMG model is somewhat ambiguous. We have previously used the average velocity field at the rudder location from a CFD simulation without the rudder present. In this study, the wake factor is adjusted so that the difference in the effective aspect-ratio for the lift and drag is minimized. This is a slightly more practical approach. Second, the standard MMG model assume that all model coefficients are independent of the propeller thrust. This was also found to work well for the case study in (Kramer & Steen, 2022). However, for the ship in this paper, both the rudder shape factor in equation 4 and the coefficients for the rudder-induced hull forces varied somewhat as a function of the thrust loading coefficient. We therefore used linear interpolation on the coefficient data to calculate the values for arbitrary thrust loading coefficients. Although this illustrates an inaccuracy in the assumptions in the MMG model, it is a relatively minor issue. Both the rudder drag at zero rudder angle and the rudder-induced hull forces are small relative to the other parts of the force model.

The effect of heel on the drift induced forces are neglected which is also a common simplification for maneuvering simulations. This choice was based on our previous work (Kramer & Steen, 2022) where we investigated the effect of heel on the drift-induced forces on a ship similar to the one in this study. In short, we found that heel angles mainly affect the drift-induced forces in cases with large cross-flow drag – as a consequence of large drift angles – while the effect was found to be small for the circulatory lift on the hull. The coupling effects between heel angles and drift angles could be important for many sailing ships, but we allowed for this simplification in this case study as both the drift angles and the heel angles are relatively small. This will be shown in the data from the route simulations in Section 7.2. We also used a slightly simplified approach for the relationship between the rudder and propeller. Due to the rotational motion of the propeller jet, there can be differences in the rudder model for positive and negative drift angles (Yasukawa & Yoshimura, 2015). This effect was neglected for the current study to reduce the number of required CFD simulations.

Figure 8 shows the match between the CFD results and the tuned model for the hull forces as a function of drift angle, rudder angle and propeller thrust. It shows that the bilge keels increase both the lift and lift-induced resistance relative to the bare hull, while the yaw moment is not much affected. The rudder-induced hull force was found to be 27%, 22% and 18% of the rudder sway force for thrust loading coefficients 0.0, 0.5 and 1.0 respectively. Figure 9 shows the match between CFD and the tuned models for the rudder forces. The data used for tuning the rudder model for different drift angles were limited to 3 and 6 degrees, as this gave a better match between the model and the CFD results at low drift angles. As will be shown in Section 7.1.1, the drift angle during the route simulations was generally below 6 degrees. The effective aspect-ratio for the rudder was found to be 0.93 times the geometrical aspect-ratio. The value of the rudder shape factor was 1.5, 1.8 and 0.6 for increasing thrust loading coefficients. The wake factor at the rudder was estimated to approximately 0.19 for both hull forms. The flow straightening from the hull with bilge keels is seen to be larger than for the bare hull. At a given drift angle, the effective rudder angle with bilge keels is estimated

to be around half the value of the bare hull. The consequence of these differences for the overall resistance of wind-powered vessel will be explored further in Section 7.

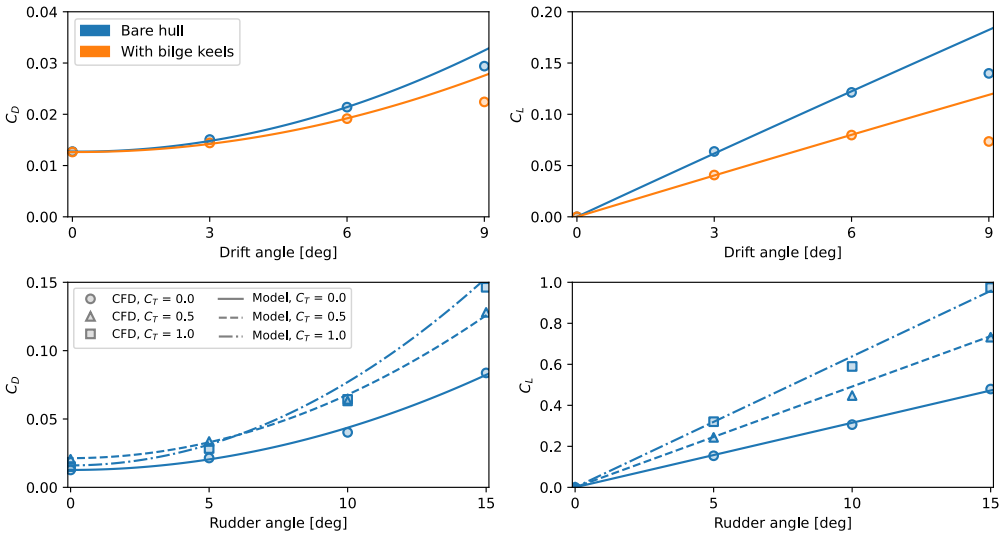


*Figure 9: CFD results and tuned models for the rudder as a function of drift angle and rudder angle. The coefficients for the rudder drag, $C_D$, and lift, $C_L$, are made non-dimensional by the dynamic pressure based on the ship speed and the rudder planform area.*

### 4.1.4 High aspect-ratio keel model

The high aspect-ratio keel is modeled with the same general expressions as the rudder. However, as the keel is placed underneath the hull, the model for the effective velocity is simplified. The effective angle of attack is set equal to the drift angle for a static keel and by adding the drift angle with the imposed keel angle in the case of a dynamic keel. The ships forward velocity without any correction for a wake is used to compute forces from the lift and drag coefficients. The correction factors for the aspect-ratio and the shape factor for the keel is estimated from CFD simulations of the keel, hull, and rudder together, where both the drift angle and the dynamic keel angle are varied. A comparison between the forces predicted by the tuned model and the raw CFD results are shown in Figure 10. The effective aspect-ratio of the keel was estimated to be 1.5 times the geometrical aspect-ratio for both the lift and drag. The expressions from the MMG maneuvering model computes an additional sway force and yaw moment on the hull as a function of the rudder force. A similar behavior was observed for the interaction between the keel and the hull. At a drift angle equal to zero degrees there was a sway force on the hull that was roughly 25% of the sway force on the keel. The induced yaw moment and surge force on the hull was negligible. The rudder also experienced a small lift force when the keel angle was varied, corresponding to approximately 10% of the lift on the keel. This indicates that the rudder experiences some lift-induced velocities due to the keel. However, we neglected this effect for simplicity.

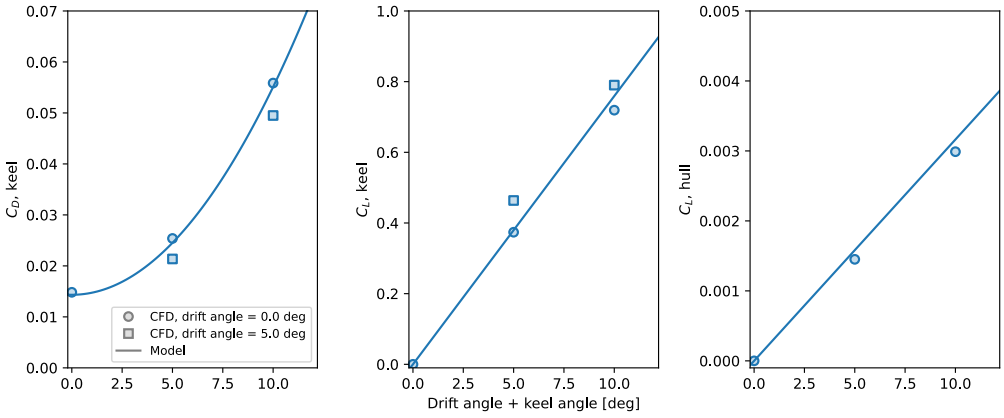


*Figure 10: Keel forces as a function of drift and keel angle. The force coefficients for the keel are made non-dimensional by the dynamic pressure and the keel planform area. The hull lift coefficient is calculated based on the underwater lateral area.*

## 4.2 Empirical models

### 4.2.1 Added resistance in waves

The added resistance in waves is calculated using the empirical model known as SNNM (Liu & Papanikolao, 2020). The side force and yaw moment from the waves are neglected for simplicity. As an example of the output from the model, the calculated response amplitude operator (RAO) of the added resistance in waves for our case study ship is shown in Figure 11. The data is shown for different wave directions and wave lengths, labeled $\lambda_{wave}$. The RAO can be combined with wave spectrum data to compute the mean added resistance, $\bar{R}_{AW}$, in short crested irregular waves according to equation 5. In this equation, $S$ is the wave spectrum as a function of wave direction, $\alpha$, and wave frequency, $\omega$. The wave resistance for a single harmonic wave is labeled $R_{AW}$, computed using the SNNM method. The ship speed is labeled $U_s$, and the wave amplitude $\zeta_A$.

$$\bar{R}_{AW} = 2\int_0^{2\pi}\int_0^{\infty} \frac{R_{AW}(\zeta_A, \omega, \alpha, U_s)}{\zeta_A^2} S(\omega, \alpha)\, d\omega\, d\alpha \tag{5}$$

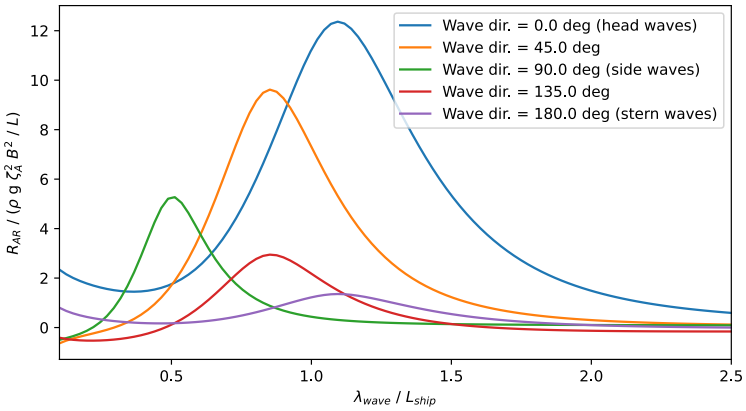


*Figure 11: RAO for the added resistance in waves from the empirical model as a function of wavelength and wave direction. The ship speed used in the generation of the plot was 12 knots.*

The integration of equation 5 is done numerically using the trapezoidal method. The wave frequencies are limited to wavelengths between 0.1 and 3 times the ship length, with 21 discrete steps. The integration of wave directions has a step size of 5 degrees. A two-dimensional wave spectrum is created from the wave data used in the route simulation, which is further presented in Section 6.2. The input variables are the significant wave height, $H_s$, the peak frequency, $\omega_p$, the mean direction, $\theta_0$, and the directional spreading, $\sigma$. A Pierson-Moskowitz spectrum (DNV, 2014) is used in the frequency domain and a Gaussian spectrum (International Towing Tank Conference, 2017) in the directional domain. The expressions are shown in equation 6-8.

$$S(\omega, \theta) = F(\omega) \cdot D(\theta) \tag{6}$$

$$F(\omega) = \frac{5\, H_s^2 \omega_p^4}{16\, \omega^5} Exp\left(-\frac{5\, \omega_p^4}{4\, \omega^4}\right) \tag{7}$$

$$D(\theta) = \frac{1}{\sqrt{2\pi}\sigma} Exp\left(-\frac{(\theta - \theta_0)^2}{2\sigma^2}\right) \tag{8}$$

### 4.2.2 Propeller model

The empirical polynomials for the Wageningen B-series are used as a model for the propeller open water characteristics (Oosterveld & Oossanen, 1975). The pitch ratio was set to 1.2, the expanded blade area ratio to 0.8, and number of blades to 4. The open water characteristics can be seen in Figure 31 in Section 7.2 together with statistics of the simulated advance ratios for the case study ship. Originally, we considered introducing a variable pitch propeller in the modelling framework. However, this plan was dropped when we discovered that the required power to the propeller at zero thrust is small, even with fixed pitch. As an example, at 12 knots speed and zero thrust, the propeller only requires around 3% of the necessary power without sails. The thrust is assumed to always point in the axial direction of the ship and sway forces are neglected. The required revolutions for given thrust and speed is found by using a numerical solver based on Newton's method. The velocity experienced by the propeller, $U_p$, was calculated from the ship speed with a constant wake factor, $w_p$, and a simplified correction for the drift angle based on the suggested expression from (Amini, et al., 2012). The expression is shown in equation 9.

$$U_p = U_s\left(1 - w_p\right)\cos\beta \tag{9}$$

The wake factor at the propeller location is found from the velocity field from a CFD simulation of the hull alone, shown in Figure 12. The relative wake factor is assumed constant for different ship velocities.

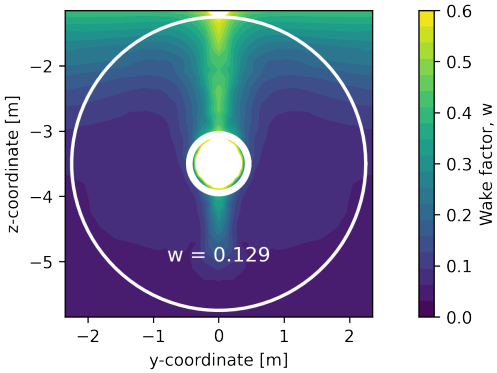


*Figure 12: Wake field at the propeller location in CFD simulations at model scale 1:4.*

# 5 Aerodynamic model

The sails are simulated with a discrete lifting line method which also include simplified expression for the forces on the sails for angles of attack above stall. The ship deck is assumed to be relatively flat and without significant obstacles. All effects related to the superstructure is therefore neglected for simplicity. First, an overview of our implementation of the aerodynamic model is given in section 5.1. Then, the lifting line is compared with CFD simulations in section 5.2. Finally, the forces from the aerodynamic model as a function of apparent wind direction is presented in Section 5.3.

## 5.1 Implementation

### 5.1.1 Lifting line

The discrete lifting model is built on the same fundamental principle as the classical lifting line method developed independently by Prandtl (1918) and Lanchester (1907). However, it is extended to handle non-planar wings, several wings in the same simulation, and non-linear relationship between lift and angle of attack. We have previously explored the accuracy of this method when modeling non-planar wing shapes in (Kramer, et al., 2018). The current paper shows some further validation results for the interaction effects between two wings. Other papers with similar discrete lifting line methods can be found in (Hunsaker, 2011), (Phillips & Snyder, 2000) and (Duport, et al., 2017). An overview of the geometry of the lifting line method is shown in Figure 13. Each sail in the simulation is built up by 10 horseshoe vortices with different vortex strength along the span of the wing. The resolution was determined based on a compromise between computational time and accuracy. The lift and drag with 10 horseshoe vortices on a single wing at an angle of attack of 10 degrees only differed from a test with 100 horseshoe vortices by roughly 4%. The bound vortices are placed at the quarter chord, while the free vortices are oriented such that they point in the direction of the free stream velocity. At the middle of each bound vortex, there is a control point where induced velocities are computed. The ocean surface is modeled as a symmetry plane. The induced velocity from a vortex segment is linearly dependent on the line geometry and the strength. The full set of equations for calculating the induced velocities from vortex lines are presented in both (Katz & Plotkin, 2001) and (Maskew, 1987).

The lift force on each segment is defined as the force component acting normal to both the incoming velocity and the vortex line. It can be calculated in two ways. First, Kutta-Juokowski's law states that the lift on the bound vortex is proportional to the vortex strength and the velocity magnitude. Second, the lift can be calculated from the two-dimensional lift-coefficient of the foil profile as a function of the effective angle of attack, which is further explained in Section 5.1.2. The vortex strength can be found by requiring that both expressions give the same value. There are several ways to solve this system. For angles of attack below stall, it is possible to use local linearization to solve the system very rapidly, as we outline in (Kramer, et al., 2018). Although the method can handle some non-linear effects, it tends to become unstable for angles of attack close to stall. A slower but more robust method is therefore used in this case study. This solver is a direct implementation of the method described in (Anderson, 1991), chapter 5. It starts by setting the strength of each vortex segment based on the geometric angle of attack and the foil profile model. Then, the induced velocities with the current vortex strength are calculated, which gives a new estimation of the effective angle of attack at each control point. The vortex strength is updated based on the new estimation, but with significant numerical damping to make the solver stable. This loop continues until the vortex strength converges. See (Anderson, 1991) for more.

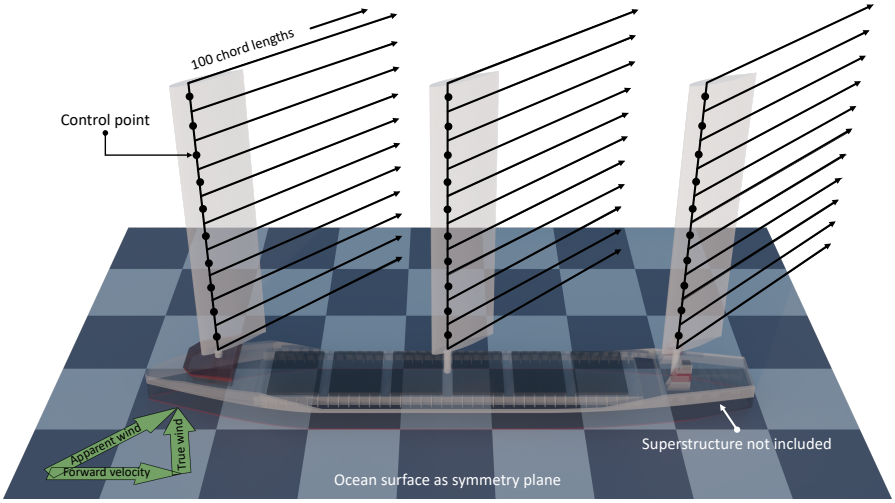


*Figure 13: Lifting line geometry.*

### 5.1.2 Foil profile model

A requirement for the method is a function that calculates the two-dimensional lift and drag on each control point as a function of the effective angle of attack. From the perspective of the lifting line, the source of this data can be from both simulations and experiments. However, the optimal angle of attack for the wingsails is very close to stall for most wind directions. As for instance shown in (Rumsey, et al., 2019) and (Blount & Protell, 2021), this is a region where RANS CFD simulations often contain large uncertainties. We therefore used the experimental data from (Sheldahl & Klimas, 1981) for the current case study. The report presents lift and drag coefficients for several symmetrical foil sections for a range of angles of attack between 0 and 180 degrees. The data for the foil profile NACA 0015 and Reynolds number equal to 10 million is used, which corresponds to an apparent wind speed of roughly 9 m/s for the dimensions of the sails in this study. The exact stall angle will depend on both Reynolds number and other environmental factors, such as the turbulence level in the atmosphere. For simplicity, we assume that the foil profile model is independent of the weather conditions. Spline interpolation is used to generalize the model to arbitrary angles of attack.

### 5.1.3 Three-dimensional corrections to the post-stall drag coefficient

The three-dimensional effects on the forces acting on the sail can be divided in two: the effects of lift-induced velocities and the reduction to the viscous drag due to finite span effects on the separated flow. The first effect is directly captured by the lifting line method. To capture the second effect, the drag from the two-dimensional foil profile model is multiplied with a correction factor for large angles of attack. The correction is based on values found in (DNV, 2014). For a rectangular surface with aspect-ratio of 4 – the value for the sails in this case study – the three-dimensional drag coefficient is reduced to roughly 65% of the two-dimensional value. The reduction should only be applied to the drag coefficient when the flow is separated, and not when the sails are operated as lifting surfaces. The correction is therefore gradually introduced by linearly decreasing it from 1 to 0.65 for effective angles of attack between 20 to 30 degrees. An overview of both two-dimensional and three-dimensional force coefficients are presented in Figure 14, which shows the effect of both lift-induced velocities and the simplified model for finite span effects on the drag.

### 5.1.4 Viscous wake

In addition to the lift-induced velocities from the horseshoe vortices, there are also viscous interaction effects between the sails in the simulation. A sail downwind of another sail will experience a reduction in the incoming velocity due to the viscous wake from the upwind sail. This is mainly an issue when the sails are operated with angles of attack above stall, which causes highly separated flow. To model this effect, we use the same procedure as outlined in (Bordogna, 2020). The reduction in velocity behind a sail is calculated according to a simplified wake model, shown in equation 10 and 11. The input to the method is the free stream velocity, $U_\infty$, the integrated viscous drag coefficient on the sails, $C_{D,v}$, and the projected width of the sail relative to the incoming velocity, $d_w$. This velocity reduction is calculated iteratively in the lifting line method, along with solving the vortex strength. For each iteration, the viscous wake is estimated from the drag coefficients and the average velocity in the last iteration. The reduction in the velocity only happens directly downwind from each sail. The coordinates in the equation, $x$ and $y$, refers to downwind direction – positive x – and normal to the downwind direction respectively. The effect of this model can be seen Figure 14. The thrust is significantly reduced in downwind conditions when several sails are simulated together. However, for most wind directions, the viscous wake model has little to no effect on the forces. The report in (Bordogna, 2020) contains further discussion and experimental validation of this model for both rigid sails and rotor sails.

$$U_{viscous} = U_\infty \left(1 - 0.98 \left[\frac{x}{C_D\, d_w}\right]^{-0.5} \left[1 - \left(\frac{2y}{b}\right)^{1.5}\right]^2\right) \tag{10}$$

$$b = 1.14\left(C_{D,v}\, d_w\, x\right)^{0.5} \tag{11}$$

### 5.1.5 Atmospheric boundary layer

The free stream velocity in the aerodynamic model is a combination of the ships forward velocity and the wind velocity. For a real ship, the wind speed and direction will vary as a function of the height above the sea due to the atmospheric boundary layer. Although the lifting line model can handle this variation, we chose to neglect it to simplify the control policy of the sails – explained further in Section 5.3.1. A simplified expression for the vertical variation in the wind speed due to the atmospheric boundary layer effects is shown in equation 12. The variable $U_{10}$ is the wind speed at 10 m height, $z$ is the distance above the ocean surface, and $z_0$ is a parameter representing the effective surface roughness. The report in (DNV, 2014) states that the value of the surface roughness will typically vary between 0.0001 for calm water conditions to 0.01 for weather conditions with significant waves. We have used a constant value of 0.0002. The input to the lifting model is the height averaged value of the wind speed, based on equation 12.

$$U_W(z) = U_{10}\frac{\log\left(\frac{z}{z_0}\right)}{\log\left(\frac{10}{z_0}\right)} \tag{12}$$

## 5.2 Comparison between Lifting Line and CFD

### 5.2.1 Single sail

Figure 14 shows the lift and drag coefficient for a single sail and on the 2D foil profile model for different angles of attack. The foil profile data is the experimental data from (Sheldahl & Klimas, 1981), while the three-dimensional values are computed both with the lifting line model and with CFD simulations. The purpose of the comparison is primarily to validate the lift-induced effects on the forces calculated by the lifting line method. We have therefore only tested angles of attack below stall. The grey dashed line in the figure shows the maximum angle of attack that is used when a single sail operates in "lift-mode", explained further in Section 5.3.1. In short, the sails are mostly operated below this limit in the route simulations. The sails were simulated with a symmetry at the midspan to reduce the mesh size in the validation test. This is equivalent to removing the ocean symmetry plane shown in Figure 13. The effective aspect-ratio is therefore slightly lower in the validation test than in the sail model in the route simulations. This will increase the lift-induced velocities and is therefore considered a more challenging validation case for the lifting line model.

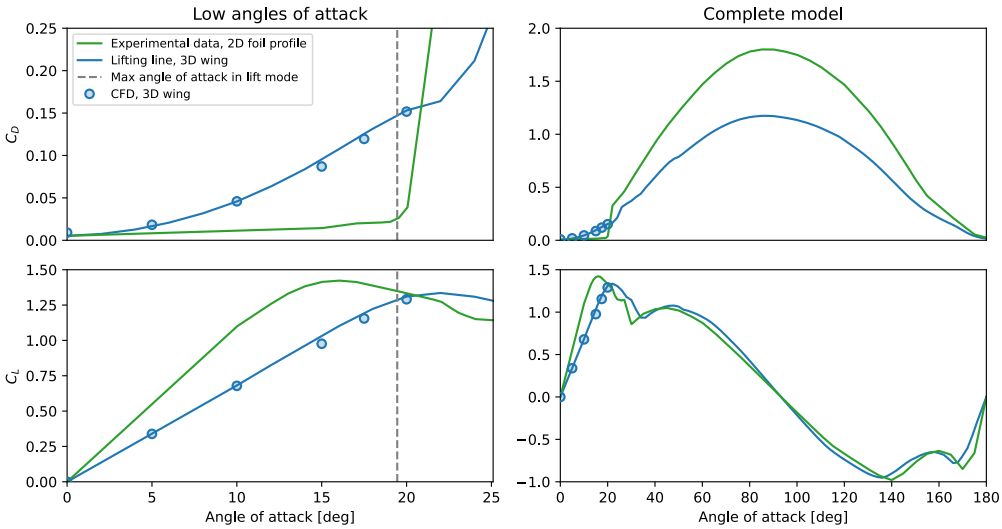


*Figure 14: Comparison between the experimental two-dimensional foil profile model, the lifting line method based on the foil profile model and CFD simulations for a single three-dimensional sail. The Reynolds number is 10 million, both for the experimental data and the CFD simulations.*

### 5.2.2 Interaction effects

Figure 15 shows a comparison of the interaction effects predicted by the lifting line model and CFD simulations. Running CFD simulations of multiple wings together can lead to large meshes. This validation test was therefore adjusted somewhat relative to the sail model used in the route simulation to reduce the computational time. First, although the test is done with two sails, the space between the sails was adjusted to match the configuration with three sails. That is, the space between the sails is set to 45 m, and not 90 m as would be the case for two sails in the route simulations. This was done to increase the interaction effects in the validation test – to roughly correspond to a case with three sails – without having to include more sail geometry in the CFD simulations. Second, the sails were simulated with a symmetry plane at the midspan – in the same way as for the single sail validation test in Section 5.2.1. The angle of attack of the sails where set to 15 degrees, while the apparent wind angle was varied. We then measured the forces acting on each individual sail. Thrust is defined as the force pushing along the ship's center line,

while the side force is the force normal to the thrust. The forces are made non-dimensional by dividing them by the dynamic pressure and the planform sail area. Both the CFD simulations and the lifting line model show clear interaction effects, as both the thrust and the side force vary between the two sails. The max difference between the lifting line model and the CFD simulations is approximately 5.9% for the side force on the stern sail at an apparent wind direction of 20 degrees. The error in the total side force on both sails for the same case is only 2.0%.

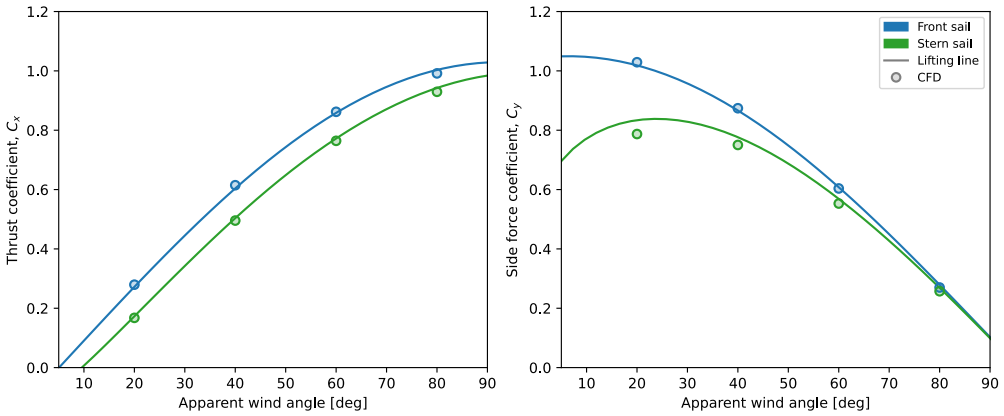


*Figure 15: Comparison of the interaction effects between two wing sails calculated by the lifting line method and with CFD. The geometric angle of attack on the sails where set to 15 degrees, and the space between the sails was 45 m.*

## 5.3 Aerodynamic forces

### 5.3.1 Maximizing thrust

The angle of attack as a function of weather conditions in the route simulations is set based on a control policy. The full policy also depends on the hydrodynamic response of the ship – which will be further explained in Section 6.1 – but the starting point is the angle of attack that maximize the thrust from the sails. Due to the simplifications introduced in the aerodynamic modelling, the optimal angle is only dependent on the apparent wind direction and independent of the apparent speed. We first assume that there are two distinct modes of operation for the sail: "lift-mode" – where the angle of attack is below stall – and "drag-mode" – with angles of attack above stall.

The optimal angle of attack in lift mode is found using a line search method from the SciPy library (Virtanen & Al, 2020). To make sure the optimization results stay within the pre-stalled part of the model, the effective angle of attack halfway up the sails is limited to 16 degrees. This is achieved by adding quadratic penalty to the objective function if the limit is exceeded. The reason for this limit was to stabilize the optimization and avoid spikes in the results when lift-mode and drag-mode provide similar values of thrust. The effective angle of attack is measured by adding the induced angles of attack from the lifting line simulation to the geometrical angle of attack. In drag mode, the sails are set to an orientation normal to the ship center line. The limit for when the policy should switch from lift-mode to drag-mode is set manually. For apparent wind directions larger than approximately 130 degrees, drag-mode was found to give the best results. The resulting control policy for three sails is shown in Figure 16, as an example. The figure also illustrates the interaction effects in the control policy for multiple sails; when one sail is placed close to the wake from another, the angle of attack is increased on the downstream sail to adjust for the induced angle of attack from the upstream sail.

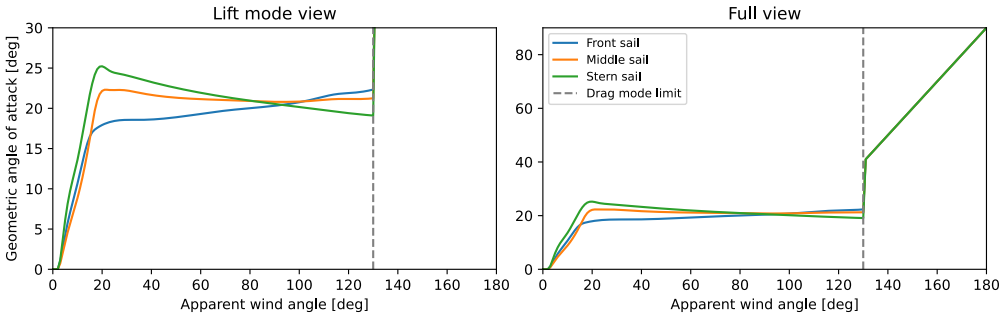


*Figure 16: Control policy for three sails showing the geometric angle of attack that gives the maximum thrust as a function of apparent wind angle.*

### 5.3.2 Resulting forces

The resulting thrust and side force when using this operational policy is shown in Figure 17 for varying number of sails. The forces are made non-dimensional by the total sail area and the dynamic pressure based on the apparent wind speed. As the sails are optimized including interaction effects, the non-dimensional values for the forces are not very dependent on the number of sails. A notable exception is for downwind sailing, where the viscous wake has a large effect. Large side forces from the sails are mainly an issue for apparent wind angles less than 60 degrees. However, the smaller apparent wind directions are more likely than the larger values due to the forward velocity of the ship, as will be shown in Section 6.2.

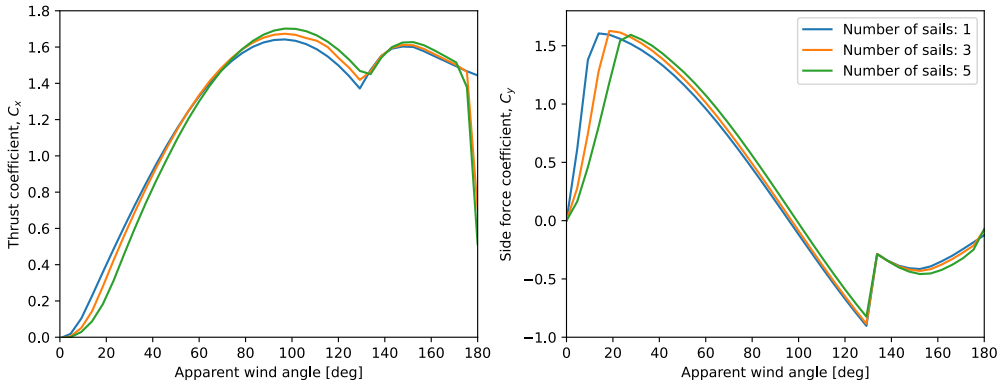


*Figure 17. Sail forces predicted by the lifting line model and the max thrust policy. The forces are made non-dimensional by the dynamic pressure of the apparent wind and the total sail area.*

# 6 Route simulation

The route simulation calculates statistics for all variables in the complete ship model for the weather conditions on the route. The most important results are the estimated fuel savings for the ship due to wind-power, the magnitude of the different resistance components in the model, and the magnitude of the ship response due to the sail forces – i.e., drift angle, rudder angle, heel angle and thrust from the propeller. Two major simplifications are made when running the route simulation. First, we only calculate the steady-state conditions of the ship and neglect all time varying dynamics. This includes maneuvering conditions, short variations in wind speed such as wind gusts, and wave-induced ship motions. Second, the logistics of the ship is not analyzed. Every geographical point and time instance on the route is therefore assumed to be equally likely. Using both simplifications means that we can represent the case study route as a dataset with independent weather conditions. The aerodynamic forces and moments are computed from wind data, and the hydrodynamic forces are computed from the sail-forces and wave data on the route. Figure 18 gives an overview of how the input data is used together with the different models.

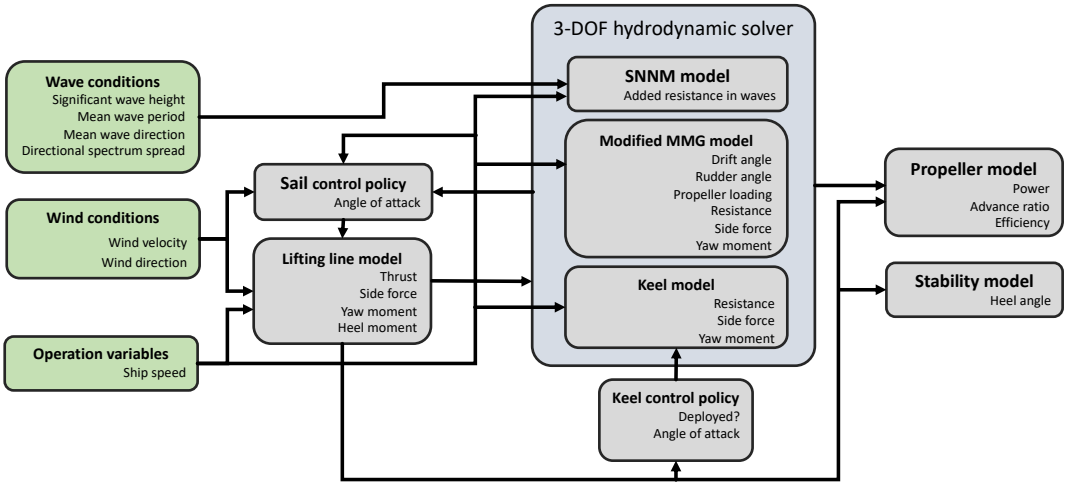


*Figure 18: Overview of the route simulation algorithm for a given weather condition and ship speed.*

## 6.1 Control algorithms and solvers

### 6.1.1 Hydrodynamic solver

The variables in the hydrodynamic model must be adjusted to balance the aerodynamic forces and moments from the sails. The drift angle, rudder angle, and thrust from the propeller is found in a coupled analysis with the sail thrust, side force and yaw moment as input. This is done with a numerical non-linear solver from the Scipy library (Virtanen & Al, 2020), which is an implementation of the Newton method. The required heel angle of the ship is solved separately from the other ship states based on the hydrostatic model of the hull and the dynamic heel moment from the appendages. Most of the time, the ship was operating at the design speed. However, in a few cases with particularly high added resistance in waves, the speed was reduced so that the required power never exceeded the maximum power installed in the ship. This was done using an outer loop that iteratively reduces the velocity with 0.5 knots step size until the required power is less than the max power for the ship.

### 6.1.2 Sail control algorithm

Two control algorithms for the sails were evaluated in this project. The first algorithm maximizes the thrust for any given weather condition – as explained in Section 5.3.1 – but with limits based on the forces on the sails and response of the ship. If any limit is exceeded, the angle of attack of the sails is reduced. The limits are as follows:

- The heel angle is limited to a maximum value of 10 degrees to ensure sufficient ship stability. There are some ambiguities in exactly what this limit should be for a wind-powered cargo ship, but one possible guideline is class rules for stability. For instance, the rules in (DNV-GL, 2016) recommends that the maximum heel angle due to steady wind loads should be maximum 16 degrees or 80% of the angle of deck immersion. As another comparison, the route simulations presented in (Tillig & Ringsberg, 2020) use 8 degrees as a maximum heel limit.
- The rudder lift-coefficient is limited to a maximum value of 1.0. This is a convenient way to set a suitable limit for rudders with different effective aspect-ratios. A high aspect-ratio rudder will stall at a lower geometrical angle than a low aspect-ratio rudder, but the magnitude of the lift-coefficient is likely to be similar. The lift-coefficient is calculated based on the effective rudder velocity from the MMG model, which includes interaction from both the hull and the propeller. As a comparison, (Tillig & Ringsberg, 2020) uses 10 degrees as a limit on the geometrical rudder angle in their route simulations. This would correspond to a limit on the lift-coefficient of approximately 0.5 for our case study.
- The side force on the sails is limited independently of the ship response. The purpose is to be able to adjust the operation of the sails independently of the ship configuration. We set the limit using a side force coefficient made non-dimensional by the dynamic pressure based on the ship speed and underwater planform area. The allowable side force from the sails is therefore higher for higher ship speeds. The largest value for this side force coefficient is set to 0.04, which corresponds a side force that is between 2.9 – 3.0 times the calm water straight ahead resistance, depending on the ship speed. We also explore the effect of varying the value of this limit in Section 7.2.4
- The thrust from the sails is limited to the total resistance at the target speed.

These limits are implemented in the route simulation framework by multiplying the angle of attack from the sail policy presented in Section 5.3.1 with a reduction factor whenever the limit is exceeded. The same reduction factor is used for all sails in cases with multiple sails. The necessary value of the reduction factor is found by using the same type of numerical solver as outlined in Section 6.1.1. The objective function for the solver is the actual value for the variable that exceeds a limit minus the maximum value. Each limit is checked and enforced one by one, starting with the side force limit, then the heel limit, the rudder limit and finally the thrust limit.

The second control algorithm includes hydrodynamic effects on the resistance and power delivered to the propeller when adjusting the sails. The algorithm starts by testing the performance of the ship with an angle of attack identical to the first control algorithm. Then, it starts iteratively lowering the angle of attack in steps of 10% of the maximum angle and measures the resulting change in power delivered to the propeller. If the power is reduced by lowering the angle of attack, the search continues, and the effective angle of attack is reduced further. If the power is increased, the search stops and the previous value with the lowest power is used. This algorithm will therefore reduce the angle of attack in cases where the sail-induced resistance is larger than the thrust. The angle of attack is reduced with the same relative amount for all sails for simplicity. This means that the aerodynamic center of effort is mostly kept close to the midship location. The background for this simplification was an analysis of the hydrodynamic models which suggested that the sail-induced resistance is not very sensitive to the exact location of the aerodynamic center of effort. A plot showing this analysis will be given in Section 7.1.1. However, improvements could potentially be achieved by introducing individual reduction factors for each sail. This is a potential topic for future work.

For both control algorithms, the sails are retracted in some weather condition. However, the exact criteria for retracting the sails differ between the algorithms. For the first algorithm, the sails are only retracted if they produce negative thrust. For a control algorithm that does not include hydrodynamic effects, this is the only way to detect when the sails are not useful. For the second algorithm, the sails are retracted whenever they do not decrease the fuel consumption for any of the tested angles. This is measured by comparing the power delivered to the propeller with the sails up against the power with the sails retracted. In cases where the sails are retracted, the effective sail area in the model is reduced to a quarter of the size, and the angle of attack is set to zero. The forces on the sails in these conditions is therefore only the drag estimated from the model at zero angle of attack, which act parallel to the apparent wind.

### 6.1.3 Dynamic keel control algorithm

The dynamic keel is adjusted based on two rules. The first rule determined when the keel should be deployed. This only happens when the side force from the sails exceeds a minimum value to avoid unnecessary drag. The second rule determines the angle of attack for the keel when it is deployed. This is based on a simple open loop controller that adjusts the angle proportional to the side force from the sails. However, the maximum angle of the keel relative to the ship is also limited to 14 degrees, which corresponds to a lift-coefficient of approximately 1.0 in cases with no drift.

The numerical values of the settings in the control policies are adjusted based on the hydrodynamic model of the hull, rudder, and keel. The proportionality controller was adjusted based on an optimization process where the resistance from the hydrodynamic model was minimized, under the influence of an applied side force. We tested different values for the applied side force that corresponded to 0.5, 1.0, and 2.0 times the straight-ahead resistance of the ship. The values are around the typical values from the sails on the case study route, as will be shown in Section 7.2. We also varied the velocity between 8 to 16 knots. The results from the optimization showed that the sail-induced resistance was lowest when the keel balanced between 50% – 51% of the applied side force for the tested conditions. In other words, the optimal relative side force from the keel was not very sensitive to ship speed or the value of the applied side force. The final value in the route simulations was rounded off to 50% for all ship speeds. We also manually verified that balancing 50% of the applied side force was more efficient than a 100%. The former resulted in 25-40% lower sail-induced resistance than the latter, depending on the tested conditions.

The limit for when to deploy the keel was set to the minimum value where there is a positive effect on the total ship resistance. This was found to correspond roughly to 16.7% of the max side force limit for the sails, which was explained in Section 6.1.2. Plots showing the effect on the forces using this control algorithm, as well as the keel angles as a function of the applied side force, are presented in Section 7.1

## 6.2 Route and weather data

Weather data for the year 2020 was downloaded from the ERA-5 hindcast model from the European Center of Medium range Weather Forecast (ECMWF) (Hersbach, et al., 2020). The data consist of wind velocity components 10 m above the sea surface as well as wave data for both wind- and swell-driven waves. The global data is presented on a Gaussian grid. The data for the route is found by first discretizing the path into equally spaced line segments and then using nearest neighbor interpolation on the global grid for each discrete control point. Figure 19 shows a map of the route where global grid points are shown together with the discrete grid points making up the route. We downloaded data for the hours 0, 6, 12, and 18 for each day during the year. Since the ship is traveling both to and from Trondheim, each scalar variable – wave height, wave period, directional width, and wind velocity – is added twice to the complete dataset, while directional variables – wind and wave direction – are computed individually for both directions. This resulted in approximately 79 thousand individual weather conditions.

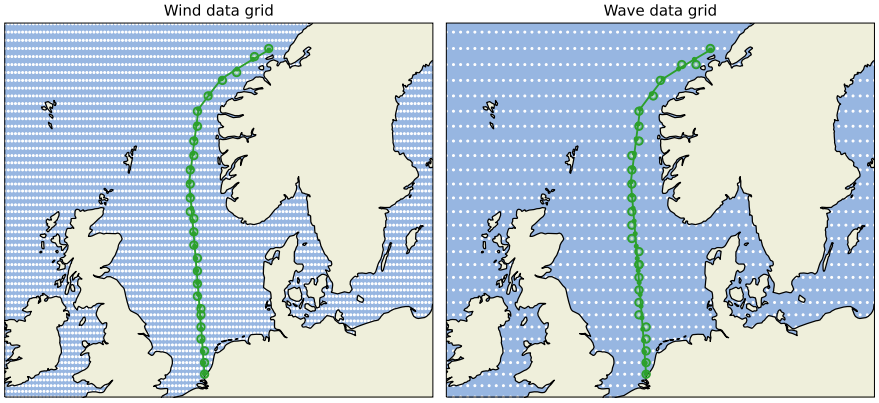


*Figure 19: Map of the route on top of the global grid. Each grid point on the global grid is shown as white dots. The green line and smaller dots represent the discretized route. The larger green circles show the nearest neighbors to the route points on the grid.*

Two operations are used to reduce the complete dataset. First, the worst weather conditions are filtered out as they could represent cases where it is unlikely that a small cargo ship would operate. The exact limit for such cases is somewhat ambiguous. As an estimate, the model for the added resistance in waves is used to calculate when the ship speed is reduced to such a degree that steerability may become an issue. The ship was required to reach at least 7 knots speed with the smallest engine size and without sails in all weather conditions used in the route simulation. This requirement removed around 4% of the worst conditions from the raw data. Second, we randomly picked 10 000 data points from the filtered data to reduce the execution time for each route simulation. The resulting weather statistic are shown Figure 20 and Figure 21. The wind data is shown for various ship velocities to illustrate the effect of forward speed on the variables.

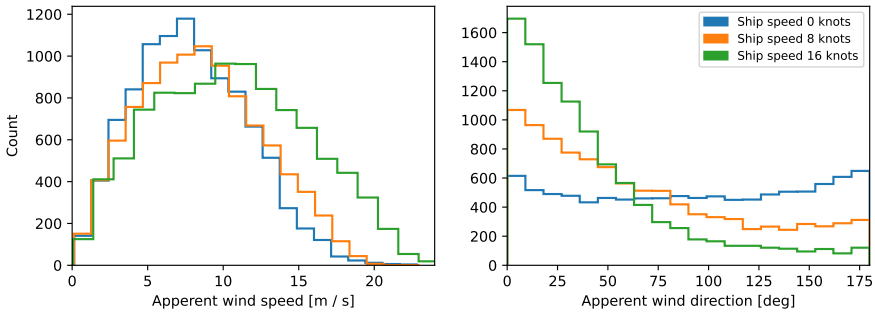


*Figure 20: Apparent wind statistics as a function of ship speed.*

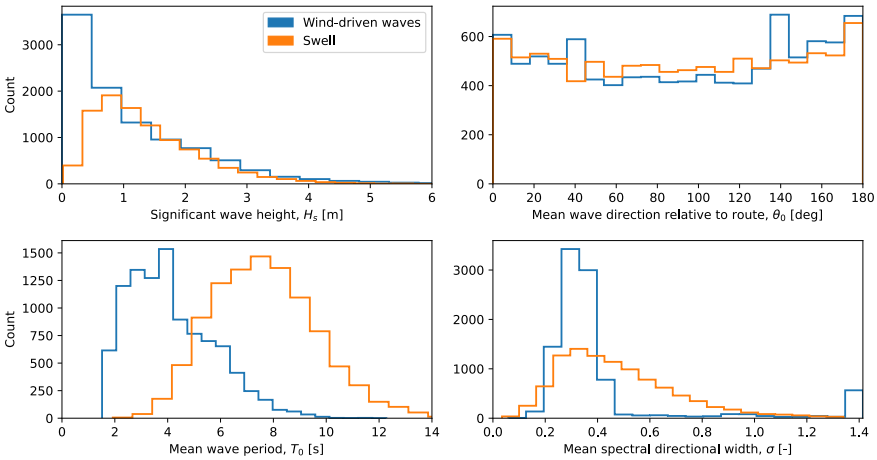


*Figure 21: Wave statistics from the dataset used in the route simulations.*

# 7 Results

The results are presented in two main subsections. We start with an initial analysis of the hydrodynamic models generated for the various design configurations in Section 7.1. The results quantify how the resistance of the ship depends on the amount of side force from the sails that must be balanced, and whether the added resistance is mainly caused by forces acting on the hull, the rudder, or the keel. The results from the route simulations are then presented in Section 7.2. These results show how much the estimated fuel savings are reduced due to the sail-induced resistance and how large the sail-induced resistance is relative to the other resistance components in the analysis. We also present statistical values for the sail forces and the resulting ship state. Finally, the effect of varying the control strategy is quantified in Section 7.2.4.

## 7.1 Hydrodynamic models

### 7.1.1 Externally applied side force

The hydrodynamic models of the different design variants are tuned based on a static drift test and static rudder tests with varying propeller loading, as shown in Section 4.1. However, a wind-powered ship needs to balance both the side force and the yaw moment from the sails and will therefore always travel with combination of drift and rudder angles during steady state operation. To give an initial overview of the sail-induced resistance, we have calculated how the ship will respond to an externally applied side force at a ship speed of 12 knots, using the hydrodynamic models. Two different tests are performed. The first test varies the magnitude of the externally applied side force but keep the center of effort fixed at the midship location. This is roughly the location of the aerodynamic center of effort for the forces from the sails with the sail location and control algorithm used in this case study. The second test use a fixed side force equal to two times the straight-ahead resistance of the bare hull and vary the center of effort. The results from both tests are shown in Figure 22. The y-axis in the figure is the resistance of the ship divided by the calm water straight-ahead resistance of the bare hull as a reference value. The plot to the left show how the resistance varies with the magnitude of the applied side force while the plot to the right show how the resistance is dependent on the center of effort of the applied side force. The lines are only plotted up to the point where the rudder model experiences a lift-coefficient equal to the limit in the sail-control algorithm, presented in Section 6.1.2. The actual operational limit during a route simulation also depends on the propeller thrust, but the results in Figure 22 give an indication of the maximum side force that is possible to be balanced by the ship when the sails are the main source of thrust..

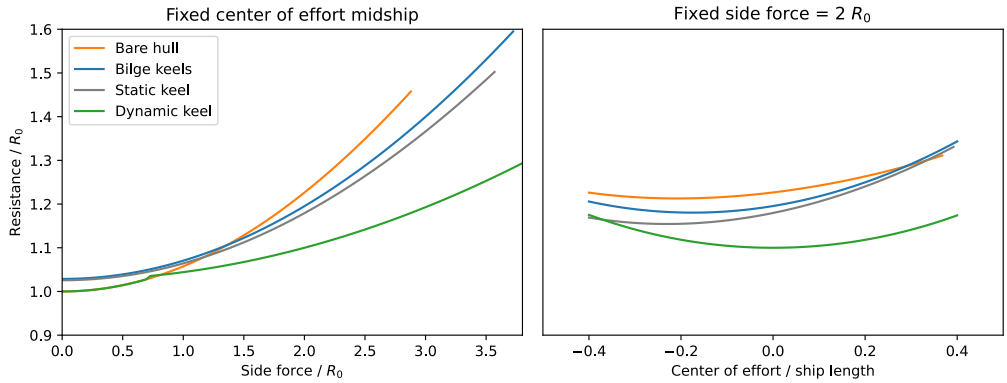


*Figure 22: Sail-induced resistance as a function of an externally applied side force. Assumed operational speed is 12 knots and there is no propeller thrust. $R_0$ refers to the straight-ahead resistance of the bare hull, which corresponds to approximately 130 kN.*

The results show that the sail-induced resistance can reach values as high as 46% of the straight-ahead resistance for the bare hull before the rudder limit is exceeded. The max side force ratio is estimated to roughly 2.9. Adding the bilge keels or the static high aspect-ratio keel is shown to both increase the max side force and reduce the sail-induced resistance. At a side force ratio of 2.9, the sail-induced resistance is reduced to approximately 37% and 34% of the straight-ahead resistance for the bilge keels and the high aspect-ratio static keel respectively. This constitutes a reduction in the sail-induced resistance of 20% and 26% relative to the sail-induced resistance of the bare hull at the same side force ratio. The fact that the low aspect-ratio bilge keels are roughly as efficient as the high aspect-ratio static keel is interesting. More on that later. Both keel types also increase the straight-ahead resistance with roughly 2.5% due to the increased wetted surface. The dynamic keel has a much larger impact on the sail-induced resistance. At a side force ratio of 2.9, the sail-induced resistance is reduced to roughly 18% of the straight-ahead resistance, which constitutes an improvement of 61% relative to the bare hull. As the dynamic keel is retractable, the resistance in straight ahead conditions is identical to the bare hull. Although the center of effort of the applied side force does influence the sail-induced resistance, the variation is relatively small. The optimal location is ahead of the midship location for all design variants except the one with the dynamic keel. However, the difference in the resistance between a center of effort midship and the optimal center of effort is only around 1-2%. As mentioned in Section 6.1.2, the sails are not optimized to vary the center of effort during the route simulations, and the aerodynamic center of effort is generally midship for all weather conditions. This simplification was motivated by the results presented in Figure 22.

The computed values for the drift, rudder, and keel angle as a function of the applied side force with a center of effort midship are shown in Figure 23. The values are shown both relative to the flow and relative to the ship's center line. In the case of the rudder, the flow angle is estimated from the rudder velocity expressions in the MMG model. For the keel, the angle relative to the flow is the dynamic keel angle plus the drift angle. The plot shows that the drift angle is small relative to the rudder and keel angle, even for large side force ratios. As expected, the keels – static or dynamic – reduce both the drift and rudder angle.

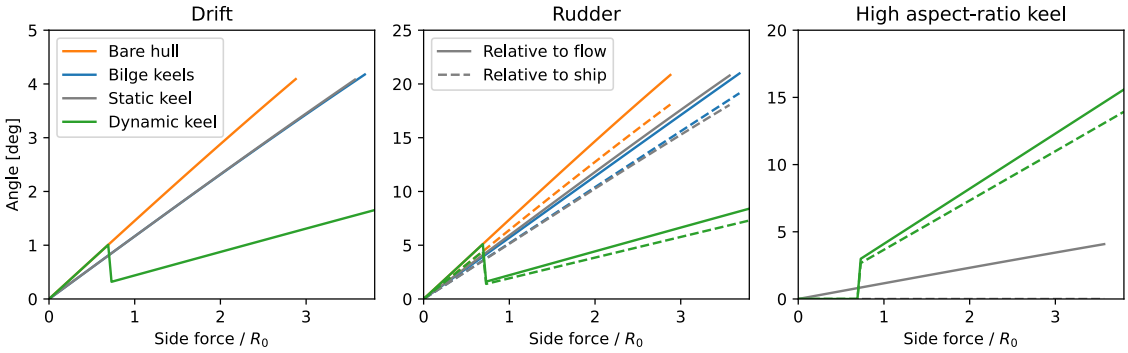


*Figure 23: Drift, rudder, and keel angles as a function of an externally applied side force acting midship. Assumed operational speed is 12 knots and there is no propeller thrust. $R_0$ refers to the straight-ahead resistance of the bare hull, which corresponds to approximately 130 kN.*

To investigate the source of the resistance, we have divided the hydrodynamic side force and the sail-induced resistance into separate components for the hull, rudder, and keel. The result of this analysis is shown in Figure 24. The figure shows the magnitude of the forces at a ship speed of 12 knots and a side force ratio of 2.0. This is a case representing a relatively large side force from the sails – as will be shown later Section 7.2.3 and 7.2.4. For both the bare hull and the hull with static keels – low or high aspect-ratio – the rudder is the main source of the added resistance. Despite this, the hull is balancing as much of the hydrodynamic side force as the rudder or more. When the dynamic keel is added, it becomes the main source of both the side

force and the sail-induced resistance. The lift-induced drag on the dynamic keel is significantly lower than for the rudder. This is explained by a higher geometrical aspect-ratio than the rudder, but also by the placement of the keel. The rudder is placed in the wake of the hull and close to the skeg which cause significant interaction effects, while the keel is placed at the flat midship section. Consequently, the effective aspect-ratio for the keel model is higher and there is no wake that reduces the lift force. The value of the estimated effective aspect-ratio for the rudder is roughly 1.57, while the same value for the keel is 5.4.

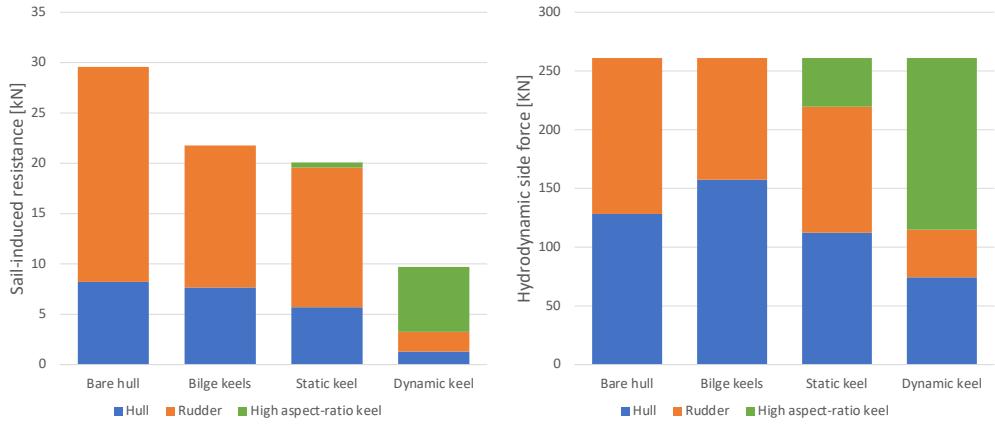


*Figure 24: Division of the sail-induced resistance and the hydrodynamic side force into different components for the hull, rudder, and keel. The values in the figure are for a ship speed of 12 knots and a side force ratio of 2.*

Initially it may seem strange that the hull, which is a lifting surface with a small aspect-ratio, can produce a side force more efficiently than the rudder. However, this is not so strange if the lift coefficients of the two different surfaces are compared. This is done in Figure 25. For each lifting surface, the lift coefficient is calculated based on the individual representative area and the local velocity, including the wake. As shown in the expressions in Section 4.1.3, lifting line theory predicts that the lift-induced drag is roughly proportional to the lift coefficient squared and the representative area while inversely proportional to the aspect-ratio. The rudder has a geometrical aspect-ratio that is more than 30 times higher than the hull and a planform area that is only 2% of the representative area of the hull. However, at a side force ratio of 2.9, the lift coefficient on the bare hull is only 0.013, while the lift-coefficient on the rudder is close to 1.0. Based on the simplified theory, the lift-induced drag on the rudder should be roughly 3.7 times as high as the lift-induced drag on the hull. For comparison, the hydrodynamic models tuned based on CFD data suggest that the hull is around 3 times as efficient as the rudder. This also explains the effect of the bilge keels and the limited effect of the static high aspect-ratio keel. When the bilge keels are added, more of the side force is shifted from the rudder to the hull. As the hull is a more efficient surface, the total drag is reduced. The static high aspect-ratio keel is shown to have a relatively low lift-coefficient for all side force ratios. This is because the angle of attack of the static keel is dependent on the drift angle of the hull. As a result, to achieve large lift coefficients on a static keel, there must also be large lift on the hull. This problem is solved by the dynamic keel, where the lift on the hull and the keel is separated. The lift coefficient for the dynamic keel is therefore roughly 4 times as high as for the static keel.

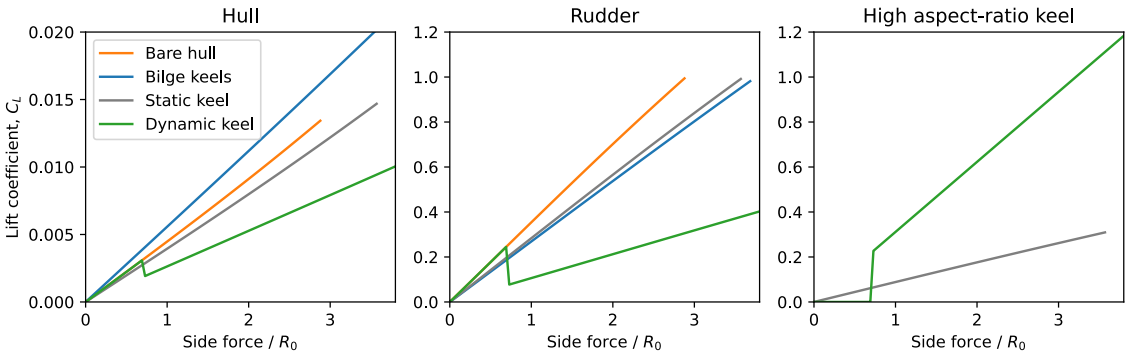


*Figure 25: Lift coefficient of the different lifting surfaces making up the ship.*

### 7.1.2 Center of lateral resistance

The reason the static keels can reduce the lift from the rudder is explained by a shift in the center of lateral resistance as a function of drift angle. The variable determines how much the rudder must be actively used to balance the hydrodynamic yaw moment on the ship for a given side force. Theoretically, it is possible to place the sails such that they apply a side force at the location of the center of lateral resistance. In that case, the aerodynamic side force can be balanced by drift-induced forces alone. However, this

is often impractical, especially when using several sails. The center of lateral resistance is usually far ahead of the midship location. As an example, the tanker KVLCC2 has a center of lateral resistance that varies between 0.44 and 0.54 ship lengths ahead of the midship location, for drift angle between 3 to 6 degrees (Kume, et al., 2006). The work presented in (van der Kolk, et al., 2021) shows experimental values for a ship with varying configurations of bilge keels. The main dimensions and shape of the ship are similar to the one in this study. The exact value for the center of lateral resistance varies as a function of the bilge keel configuration but is mostly seen to be ahead of the bow. For the most extreme cases it is seen to be an entire ship length ahead of the midship location. Adding the bilge keels generally moved the center of lateral resistance close to, but not always behind, the bow. The center of lateral resistance for the ship in this study is plotted in Figure 26 for the static design variants. The location is calculated by dividing the hydrodynamic yaw moment acting on the hull and the rudder by the sway force. The location is then made non-dimensional by the ship length. The bare hull in this case study is seen to have a center of lateral resistance ahead of the bow. Both the bilge keels and the high aspect-ratio keel is seen to shift the center of lateral resistance backwards with similar magnitude. However, the location is relatively close to the bow for all versions.

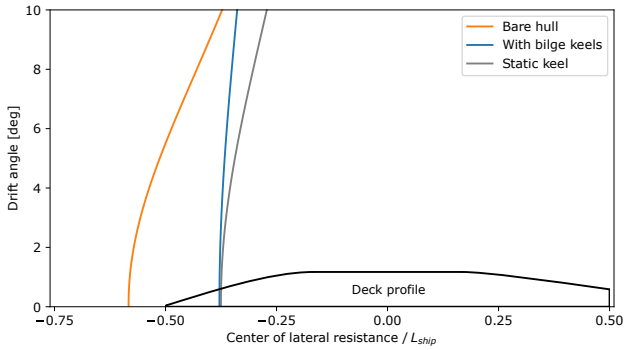


*Figure 26: Center of lateral resistance for the hydrodynamic side force as a function of drift angle.*

## 7.2 Route simulations

Three different route simulations are used for each combination of design configuration, number of sails, and velocity. First, the ship is tested without sails to generate reference data on the resistance and propulsion power. The route simulation is necessary in this case to quantify the effect of the added resistance in waves. The ship is then tested with a modified sail model where the side force and yaw moment are neglected which also removes the sail-induced resistance. The sails are still affected by the side force limit, but not the limits on the rudder and heel angle. The propeller efficiency is calculated as a function of the required thrust. This gives a theoretical maximum value for the fuel savings if the side force could be balanced without any added resistance. Finally, the ship is tested with all hydrodynamic effects included. The thrust, side force, yaw moment, and heel moment from the sails are balanced by opposing hydrodynamic forces and moments on the hull. The sail control algorithm is affected by the response of the ship. We present the results from these route simulations in the following sections. The first sections show results with the max thrust control algorithm as outlined in Section 6.2.1. We then show the consequence of including hydrodynamic effects in the algorithm and altering the side force limit in Section 7.2.4. The presentation of design configurations is limited to the bare hull, the hull with bilge keels, and the dynamic keel. This is because the results for the high aspect-ratio static keel are almost identical to the results for bilge keels.

### 7.2.1 Fuel savings

The fuel saving on the route for a given test condition is defined as the reduction in the average propeller power when sails are used, relative to a simulation with the bare hull, but without sails. Figure 27 shows the values both with all hydrodynamic effects included in the simulation and with the side force and yaw moment neglected. The fuel savings due to sails are estimated to be between 21 – 70% without hydrodynamic effects, depending on the number of sails, ship speed and design configuration. With hydrodynamic effects included, the numbers are reduced to 17 – 63%. The reduction in the fuel savings due to hydrodynamic effects are seen to be between 4.3 and 10.3 percentage points. The reduction is largest for the bare hull, at either low ship speed or many sails, but is also clearly visible for the other configurations. Adding the bilge keels is not seen to improve the fuel savings relative to the bare hull configuration. The sail-induced resistance is reduced – as shown in Section 7.1 and 7.2.3 – but the added frictional resistance in straight ahead conditions is just large enough to cancel out the positive effect. The dynamic keel is seen to increase the fuel savings with 4.0 percentage points for the lowest speed. The reduction in fuel savings due to hydrodynamic effects is thereby only 6.3 percentage points.

When the number of sails is fixed to three, the fuel savings are reduced with increasing ship speed due to the increase in hydrodynamic resistance. When the velocity is fixed, the fuel savings increase with the number of sails. However, there is a clear effect of diminishing returns when adding more sails. This happens both with and without sail-induced resistance included in the model. The explanation is that some wind directions offer significantly more thrust than others, as shown in Figure 17. When the total sail area is small, the energy extracted from all wind directions can be increased by increasing the number of sails. At some point, the most favorable wind directions are completely utilized, and adding more sail area only increases the fuel savings during

the less favorable wind conditions. These wind conditions offer less fuel savings per sail area, and the effect of increasing the number of sails is therefore smaller.

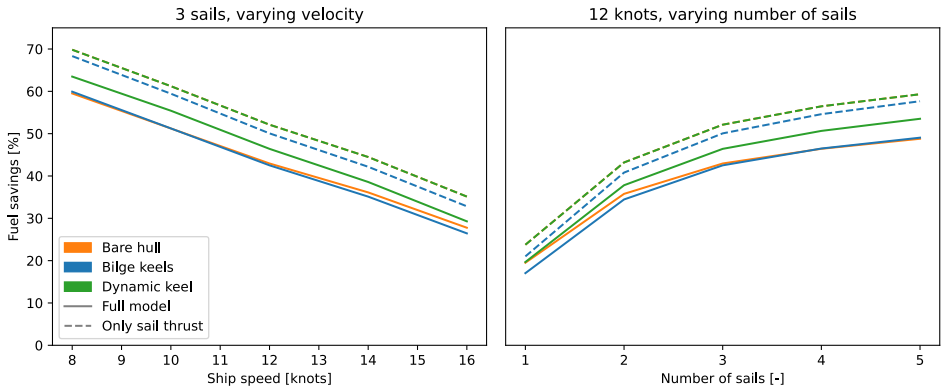


*Figure 27: Fuel savings on the ship as a function of velocity and number of sails.*

### 7.2.2 Resistance components

The average values for all resistance components in the route simulation are shown in Figure 28. The sail-induced resistance is seen to be between 4.8% to 14.5% of the total resistance depending on the ship speed. As a comparison, the magnitude is around the same value as the estimated added resistance due to waves for the bare hull. Although the calm water resistance is still the largest source of resistance for all the tested speeds, the lowest speeds are particularly affected by weather induced resistance components. The added resistance in waves and the sail-induced resistance accounts for 32.1% of the total resistance at 8 knots while only 15.3% at 16 knots. This is partly because the case with lowest speed experiences the largest sail forces relative to the ship resistance, but also because the added resistance due to waves does not change much with ship speed. Similar conclusions regarding the added resistance in waves are made in (Taskar & Andersen, 2020). The relative reduction in fuel savings and the relative importance of the sail-induced resistance is similar in magnitude. This suggests that the increase in resistance is the main reason for the reduction in fuel savings, and not changes in the operational angle of attack on the sails – for instance due to the rudder limit. For the lowest speed, the sail induced resistance for the bare hull, the hull with bilge keels and the dynamic keel is 14.5%, 12.4% and 9.7% respectively. This shows that the bilge keels and the dynamic keel reduce the average sail-induced resistance with almost 14% and 33%.

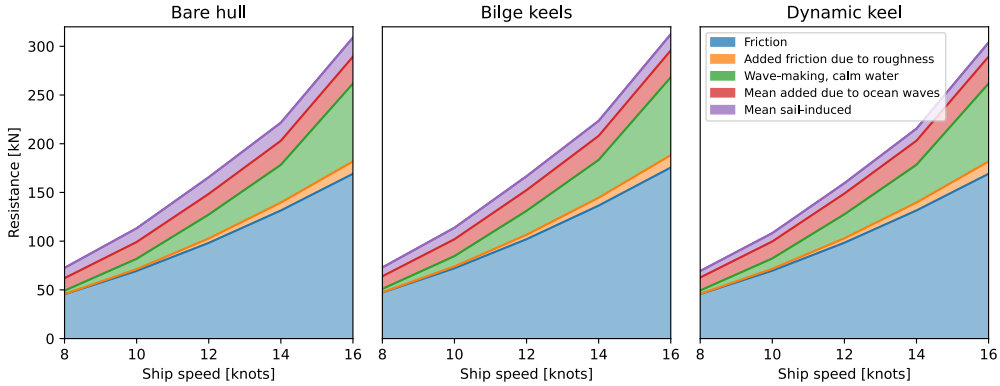


*Figure 28: Resistance components for the ship with three sails.*

### 7.2.3 Model state overview

Average statistical values for sail forces, propeller thrust, drift, rudder and heel angle are plotted in Figure 29. The force values are shown relative to the straight-ahead resistance of the ship as a function of velocity – which is equal to the sum of the frictional resistance, the added friction due to roughness and wave-making resistance in Figure 28. The results show that both the thrust and the side force from the sails are slightly increased when sail-induced effects are included in the route simulation. This is because the resistance of the ship increases, which makes the sails operate with larger angles of attack in cases where the max angle is not already reached. The average values of the side force vary between 0.6 and 1.4 times the straight-ahead resistance. This is in many ways a relatively moderate value if we compare this value to the results in Figure 22. The lift-coefficient on both the rudder and the hull is low and the ship is operating far from the limits in the control algorithm for the sails. However, these are only average values, and there are several situations where the limits come into play. This will be further explored later. The

drift and rudder angles are decreasing with increasing ship speed. This is because the hydrodynamic forces are proportional to the ship velocity squared, and the ship is therefore capable of balancing larger aerodynamic side forces at higher velocity. Both the drift and the rudder angle are reduced when the keels are added. The hydrostatic moment on the hull is not affected by hydrodynamic effects and the heel angle is therefore increasing with the velocity. As mentioned in Section 2.1.3, the rudder and the keel generate a hydrodynamic heel moment that is proportional to the side force they produce and a fixed vertical center of effort. However, the added heel angle due to the appendices is small for this case study as the hydrostatic moment on the hull is dominating the restoring moment. As an example, the average increase in heel angle due to the dynamic keel was less than 0.3 degrees at 16 knots. With increasing speed, the sail forces are reduced relative to the ship resistance, but they are increased in absolute value. As an example, the average side force from the sails at 16 knots is around 3.9 times larger than the value at 8 knots. The reason is that the increase in ship velocity also increases the apparent wind velocity and decreases the apparent wind angle, as shown in Figure 20.

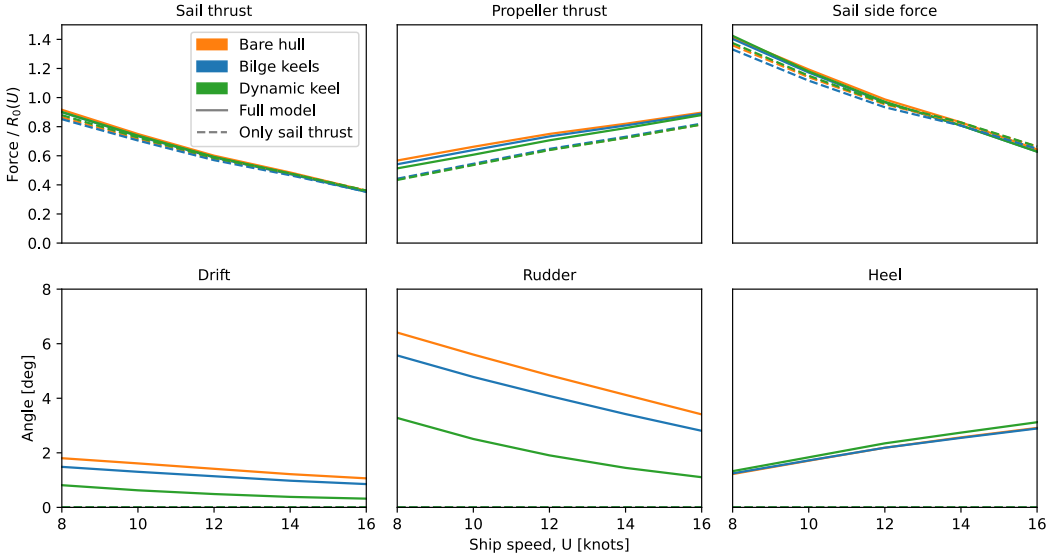


*Figure 29: Average ship state with three sails and variable ship speed.*

An overview of the heel angle and the propeller operating conditions for the bare hull configuration is presented in Figure 30 and Figure 31. The results are very similar for all configurations since both the hydrostatic hull model and the propeller model are identical between the design configurations. The only ship speed where the heel angle is affecting the sail control algorithm is 16 knots. For 8 knots, the maximum heel angle is only 4 degrees. Although this is data for a ship with a relatively high stability, it shows that large fuel savings can be possible for merchant ships without significant heel angles. The propeller is seen to mostly operate around the design point, although there are a few cases where the efficiency is reduced considerably due to a high advance ratio. However, this only happens for cases with very small amount of thrust from the propeller and the effect of this is therefore small. As a sidenote, such high advance ratios might lead to risk of damaging pressure-side cavitation on the propeller and might be a reason to use a variable pitch propeller. However, this is outside the scope of the present study.

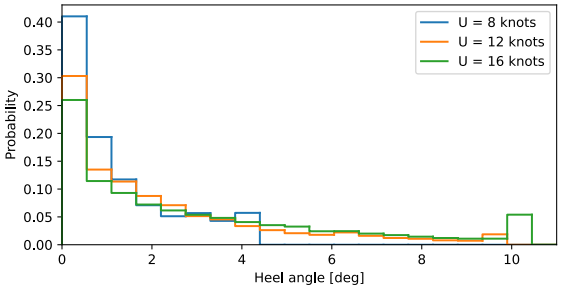


*Figure 30: Statistics for the heel angle during the route simulation. The results are shown for the bare hull.*

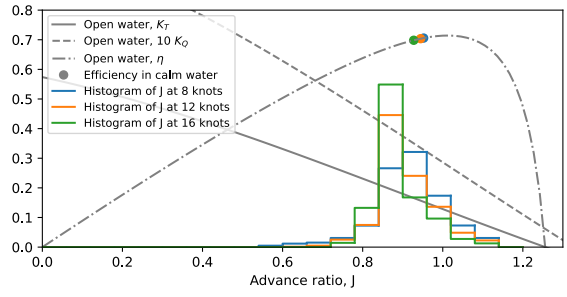


*Figure 31: Statistics for the propeller advance ratio plotted on top of the open water characteristics for the propeller.*

### 7.2.4 Adjustments to the control algorithm

The route simulation results presented in the previous sections were computed with the control strategy that maximized the thrust from the sails, and with the largest side force limit, as explained in Section 6.1.2. In this section, we also include the control

algorithm that iteratively optimize the angle of attack by evaluating the hydrodynamic performance of the ship. Both control strategies are tested with varying values for the side force limit. The variation in the side force limit serves two purposes. First, it is a simple way to modify the max thrust control algorithm to avoid situations with large sail-induced resistance. We wanted to test if a reduction in the side force limit could lead to better fuel savings without any other changes to the control algorithm. Second, even if the fuel savings are not improved by reducing the side force limit, it could still be beneficial to ensure low side forces from the sails. This could for instance be a way to achieve better steerability of the ship or to avoid large heel angles. In this case, it is useful to quantify any loss in the fuel savings due to more strict limits on the sail forces.

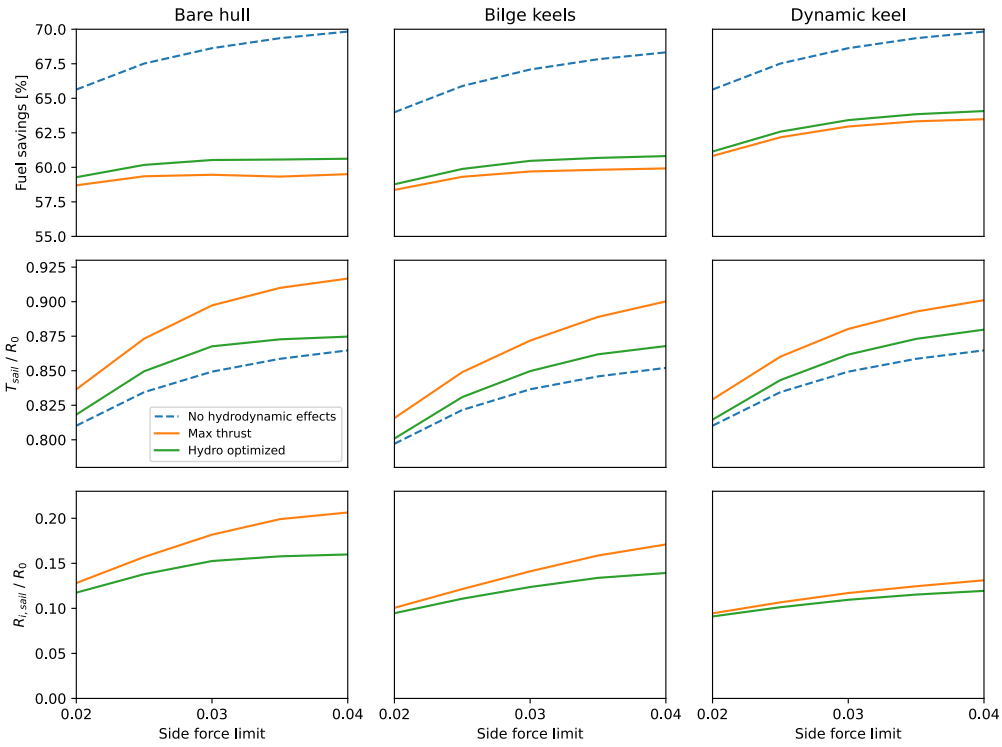


*Figure 32: Fuel savings, sail thrust, labeled $T_{sail}$, and sail-induced resistance, labeled $R_{i,sail}$, as a function of the side force limit in the control algorithm. The data is from cases with 8 knots ship speed and 3 sails.*

Figure 32 shows the averaged statistical values for the fuel savings, the thrust from the sails, and the sail-induced resistance as a function of different values for the side force limit in the control algorithm. For the control strategy study, we limit the presentation to the case with 8 knots ship speed and three sails. This was the case with both the largest fuel savings and the largest reduction due to hydrodynamic effects. It is a case where the rudder is operating with angles close to the rudder limit relatively often – as will be shown later - while the max heel limit is never reached. The max thrust control algorithm with an optimal side force limit results in an estimated fuel saving that is only 1% less than the hydro optimized control algorithm for the bare hull. This result is slightly different than our previous study found in (Kramer & Steen, 2016). In the previous paper, a control algorithm optimized with hydrodynamic effects included in the objective function showed improvements to the fuel savings that approached 5%, for a case with close to 50% fuel savings. However, an important difference between the previous study and this one is the limits on the rudder lift coefficient and the side force. The previous study simulated a ship that in some situations operated with a much larger side force than the current case, and the benefit of including hydrodynamic effects in the control algorithm was therefore larger. As seen in this study, the difference between the two control algorithms increases with increasing side force limit. This indicate that a simple max thrust control algorithm combined with a correct side force limit can be almost as good as a hydrodynamically optimized control algorithm. Another interesting observation is that the fuel savings are not very sensitive to the side force limit within the tested range. Even though the thrust from the sails is reduced with roughly 8% with the changing side force limit, the fuel savings are changed with roughly 1% for the bare hull. The explanation is found in the change in the sail-induced resistance; it is shown to be reduced almost as much as the sail thrust. The drawback with strict limits on the side force is therefore seen to be small for this case. The effect is different for the configuration with the dynamic keel, which shows larger reduction in the estimated fuel savings along with the side force limit. This is because the keel is capable of balancing larger side forces without too much sail-induced resistance.

Figure 33 shows a scatter plot of both the rudder angle and sail thrust as a function of the side force from the sails. This figure shows the spread in the variables during the route simulations and illustrate the consequence of the different control algorithms. For both algorithms, the figure shows how the variables are affected by the side force limit. For the largest side force limit the

operation is also affected by the limit on the rudder lift coefficient which are visible by the maximum angle for the rudder. The spread in the rudder angle for a given side force is mainly due to the variability in the propeller thrust which again are dependent on the variability in the sail thrust. For a given side force ratio, there are situations with both large and small amounts of thrust and therefore both small and large thrust loading coefficients. When the max thrust control algorithm is used, there are several occasions where the thrust from the sails is smaller than the sail-induced resistance. With the hydro optimized control algorithm, the angle of attack on the sails is reduced in these situations, so that the thrust is always larger than the sail-induced resistance.

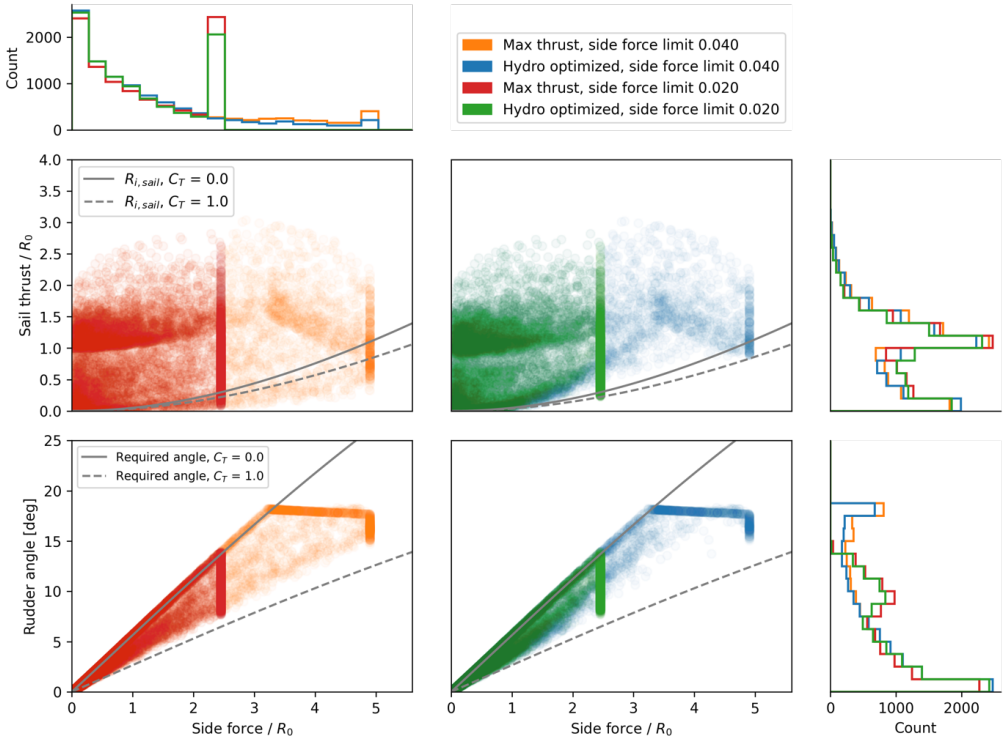


*Figure 33: Overview of sail thrust and rudder angle for a selection of different route simulations with 8 knots ship speed and 3 sails.*

Figure 34 shows scatter plots for the geometric angle of attack averaged over all three sails as a function of the apparent wind angles in the route simulation. Each plot is limited to apparent wind angles between 0 and 30 degrees as the difference between the control algorithms is mostly seen in this range. This is also the range where the sails produce the largest side forces relative to the thrust. The max thrust control algorithm with the largest side force limit is seen in the plot to the left. When lowering the side force limit in the middle plot, the angles of attack are shifted fairly evenly downward. The change is different when the angles of attack are optimized with hydrodynamics in the objective function, as shown to the right. At apparent wind angles less than 10 degrees, the angles of attack of the sails are reduced more with the hydro optimized control algorithm than when reducing the side force limit. For the other apparent wind angles, they are reduced less. There are also clear patterns in the hydro optimized data. This is a result of the discrete jumps of the angles that are tested in the hydro optimized control algorithm, as outlined in Section 6.1.2.

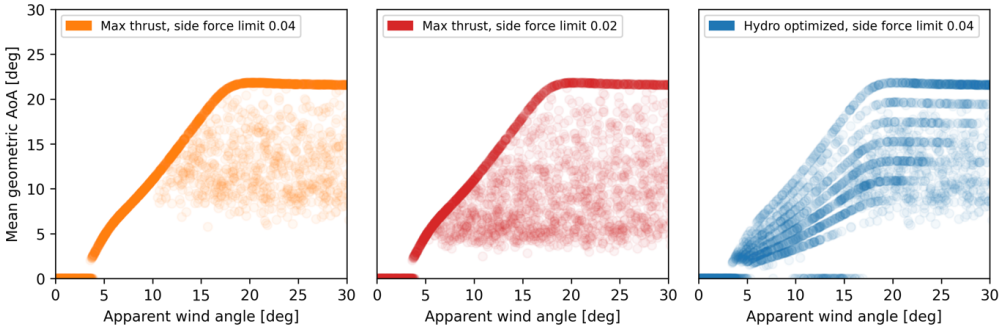


*Figure 34: Average geometric angle of attack for the sails as a function of apparent wind angles in the route simulation.*

# 8 Conclusions

We performed a case study of a wind-powered cargo ship operating on a route in the north Atlantic by combining hydrodynamic CFD simulations, route simulation models based on maneuvering theory, and a discrete lifting line model for the wingsails. The goal was to investigate the magnitude and the source of the sail-induced resistance. We tested four different design configurations and varied both the operational speed, number of sails, and the control algorithm for the sails. The cases tested gave an estimated fuel savings between 17-63%.

The sail-induced resistance for the bare hull was found to be between 4.8 – 14.5% of the total resistance in the route simulations, depending on the ship speed, hydrodynamic design, and number of sails installed. This led to a reduction in the fuel savings that roughly corresponded to the relative increase in resistance. As a comparison, the sail-induced resistance was comparable to the estimated added resistance in waves for the bare hull. At 8 knots – the lowest ship speed tested – the sum of the sail-induced resistance and added resistance in waves accounted for roughly a third of the total resistance on average. This showed that the error in the estimated fuel consumption of a wind-powered cargo ship can be large if only the calm water resistance is used to quantify the energy requirements.

Although both the hull and the rudder contributed significantly to the side force, the rudder was found to be the main source of sail-induced resistance for three of the four design configurations tested. The reason was that the rudder was operating with very large lift-coefficients, which resulted in large lift-induced drag forces. The exception was the design configuration with the dynamic keel. In that case, the keel took over as the main source of both resistance and side force.

The design configurations where first analyzed independently of the sail model and weather data. As a simplified analysis of the sail-induced resistance, they were subjected to a side force with varying magnitude applied at the midship location. This analysis showed that the bilge keels and the static keel would give similar reductions in the sail-induced resistance relative to the bare hull. As an example, the relative reduction was 20% and 26% for the bilge keels and the static keel when the ship was balancing a side force that was 2.9 times the straight-ahead resistance. This was mainly achieved by shifting some of the hydrodynamic side force from the rudder to the hull and keel, and thereby reducing the lift-coefficient on the rudder. The dynamic keel was able to reduce the sail-induced resistance with 61% relative to the bare hull when the same side force was applied. This was achieved by offloading both the rudder and the hull at the same time. The control algorithm for the dynamic keel was optimized to minimize the sail-induced resistance. The optimization result indicated that the keel should balance roughly 50% of the total side force. Although the dynamic keel represents a much more complex solution than the static keels, it could be worth considering for cases where a very large amount of power is to be extracted from the wind.

The amount of side force from the sails in the route simulations was naturally varying depending on the weather, but the average value was close to 0.6 – 1.4 times the straight-ahead resistance, depending on ship speed and number of sails. The bilge keels did not improve the fuel savings from the sails, as the average reduction in sail-induced resistance was about the same as the increase in the frictional resistance. The dynamic keel, on the other hand, was able to improve the fuel savings with 4 percentage points for the case with the largest fuel savings. This was achieved by reducing the average sail-induced resistance with 33%. Since the keel was retractable, it did not increase the straight-ahead resistance for cases with low side forces from the sails.

The tests were done with control algorithms that were designed to include various limits on the angle of attack of the sails to avoid dangerous situations for the ship. This meant that the forces from the sails were reduced in the most extreme weather situations in all tested conditions. The estimated fuel savings were therefore not very dependent on the variations in the different control algorithms tested. However, the sail-induced resistance and the thrust from the sails showed much larger variations. Limiting the side force from the sails through the control algorithm was found to reduce the sail-induced resistance roughly as much as the reduction in the wind generated thrust, depending on the hydrodynamic ship design. The conclusion is therefore that the case study ship in this paper can be operated with strict limits on the side force while still maintain large fuel savings. This means that both the heel and the rudder angle can be kept at low values, without decreasing the performance from the sails. The best control algorithm was the one that optimized the ship with the negative hydrodynamic effects included in the objective function. However, the simpler control algorithm, that primarily maximized the thrust, were found to be almost as good as the hydrodynamically optimized control strategy.

# Acknowledgments

This work was carried out at SFI Smart Maritime (WP2) supported by the Research Council of Norway through the Center for Research- based Innovation (SFI) scheme (Grant number 237917).

# Bibliography


Amini, H., Sileo, L. & Steen, S., 2012. Numerical calculations of propeller shaft loads on azimuth propulsors in oblique inflow. *Journal of Marine Science and Technology,* Volume 17, pp. 403-421.

Anderson, J. D., 1991. *Fundamentals of Aerodynamics.* s.l.:McGraw-Hill.

Bentin, M. et al., 2016. Bentin, Marcus, et al. "A new routing optimization tool-influence of wind and waves on fuel consumption of ships with and without wind assisted ship propulsion systems. *ransportation Research Procedia,* Volume 14, pp. 153-162.

Bertram, V., 2012. *Practical ship hydrodynamics.* Oxford: Elsevier.

Blount, H. & Protell, J. M., 2021. *CFD investigation of wind powered ships under extreme conditions,* Gothenburg, Sweden: Chalmers Univerusty of Technology.

Bøckmann, E., Steen, S. & Myrhaug, D., 2014. *Performance of a ship powered purely by renewable energy.* San Fransisco, California, USA, International Conference on Offshore Mechanics and Arctic Engineering.

Bordogna, G., 2020. *Aerodynamics of Wind-Assisted Ships,* Delt, Netherlands: Delft Univeristy of Technology.

DNV-GL, 2016. *Rules For Classification, Part 3 Hull, Chapter 15 Stability,* s.l.: DNV-GL.

DNV, 2014. *Environmental Conditions and Environmental Loads - Recommended Practice - DNV-RP-C25,* s.l.: DNV.

Duport, C. et al., 2017. *Local Results Verification of a 3D Non-Linear Lifting Line Method for Fluid-Structure Interactions Simulation on a Towing Kite for Vessels.* Zevenwacht, High-Performance Marine Vehicles.

Eca, L. & Hoekstra, M., 2008. The numerical friction line. *Journal of Marine Science and Technology,* Volume 13, pp. 328-345.

Econowind, 2020. *Key wind-assist propulsion installation starts North Sea operations.* [Online]
Available at: https://www.econowind.nl/index.php/2020/03/02/key-wind-assist-propulsion-installation-starts-north-sea-operations/
[Accessed 16 August 2021].

ESI-Group, 2020. *OpenFOAM homepage.* [Online]
Available at: https://www.openfoam.com/
[Accessed 14 October 2020].

Goldstein, S., 1929. On the Vortex Theory of Screw Propellers. *Proceedings of the Royal Society of London. Series A, Containing Papers of a Mathematical and Physical Character,* 123(792), pp. 440-465.

Hersbach, H. et al., 2020. The ERA5 global reanalysis. *Quarterly Journal of the Royal Meteorological Society.*

Hirt, C. W. & Nichols, B. D., 1981. Volume of fluid (VOF) method for the dynamics of free boundaries. *Journal of computational physics,* 39(1), pp. 201-225.

Hunsaker, D. F., 2011. *A Numerical Lifting-Line Method Using Horseshoe Vortex Sheets,* s.l.: Utah State Univeristy.

International Towing Tank Conference (ITTC), 2017. *1978 ITTC Performance Prediction Method,* s.l.: International Towing Tank Conference (ITTC).

International Towing Tank Conference, 2017. *Laboratory Modelling of Multidirectional Irregular Wave Spectra,* s.l.: s.n.

International Towing Tank Conference, 2017. *Uncertainty Analysis in CFD Verification and Validation, Methodology and Procedures,* s.l.: International Towing Tank Conference.

Katz, J. & Plotkin, A., 2001. *Low-Speed Aerodynamics.* s.l.:Cambridge Univeristy Press.

Kramer, J. & Steen, S., 2016. *Drift Forces – Wingsails vs Flettner Rotors.* Cortona, Italy, High-Performance Marine Vehicles.

Kramer, J. V. & Steen, S., 2022. Simplified Test Program for Hydrodynamic CFD Simulations of Wind-Powered Cargo Ships. *Ocean Engineering,* Volume 244.

Kramer, J. V., Godø, J. M. K. & Steen, S., 2018. *Hydrofoil simulations – non-linear lifting line vs CFD.* Cortona, Numerical Towing Tank Symposium.

Lanchester, F. W., 1907. *Aerodynamics: constituting the first volume of a complete work on aerial flight.* s.l.:Constable.

Larsson, L., Eliasson, R. E. & Orych, M., 2000. *Principles of Yach Design.* s.l.:Bloomsbury.

Liu, S. & Papanikolao, A., 2020. Regression analysis of experimental data for added resistance in waves of arbitrary heading and development of a semi-empirical formula. *Ocean Engineering,* Volume 206.

Lu, R. & Ringsberg, J. W., 2020. Ship energy performance study of three wind- assisted ship propulsion technologies including a parametric study of the Flettner rotor technology. *Ships and Offshore structures,* 15(3), pp. 249-258.

Maskew, B., 1987. *VSAERO Theory Document,* s.l.: NASA.

Menter, F., Kuntz, M. & Langtry, R., 2003. Ten years of industrial experience with the SST turbulence model. *Turbulence, heat and mass transfer,* 4(1), pp. 625-632.

Michelin, 2021. *2021 Movin'On: Michelin presents two innovations to accelerate the development of sustainable mobility.* [Online]
Available at: https://www.michelin.com/en/press-releases/2021-movinon-michelin-presents-two-innovations-to-accelerate-the-development-of-sustainable-mobility/
[Accessed 30 December 2021].

Minami, Y., Nimura, T., Fujiwara, T. & Ueno, M., 2003. *Investigation into Underwater Fin Arrangement Effect on Steady Sailing Characteristics of a Sail Assisted Ship.* Honolulu, Hawaii, USA, The Thirteenth International Offshore and Polar Engineering Conference.

Oosterveld, M. W. C. & Oossanen, P. V., 1975. Further computer-analyzed data of the wageningen B-screw series. *International Shipbuilding Progress,* 22(251).

Perić, R. & Abdel-Maksoud, M., 2016. Reliable damping of free-surface waves in numerical simulations. *Ship Technology Research,* 63(1), pp. 1-13.

Phillips, W. F. & Snyder, D. O., 2000. Modern Adaptation of Prandtl's Classic Lifting-Line Theory. *Journal of Aircraft,* 37(4), pp. 662-670.

Popovac, M. & Hanjalic, K., 2007. Compound wall treatment for RANS computation of complex turbulent flows and heat transfer. *Flow, turbulence and combustion,* 78(2), pp. 177-202.

Prandtl, L., 1918. *Tragflügeltheorie.* s.l.:Königliche Gesellschaft der Wissenschaften zu Göttingen.

Rumsey, C. L., Slotnick, J. P. & Sclafani, A. J., 2019. Overview and Summary of the Third AIAA High Lift Prediction Workshop. *Journal of Aircraft,* 56(2).

Schlichting, H., 1979. *Boundary-Layer Theory.* s.l.:McGraw-Hill.

Schneekluth, H. & Bertram, V., 1998. *Ship design for efficiency and economy.* Oxford: Butterworth-Heinemann.

Sheldahl, R. E. & Klimas, P. C., 1981. *Aerodynamic Characteristics of Seven Symmetrical Airfoil Section Through 180-Degree Angle of Attack for Use in Aerodynamic Analysis of Vertical Axis Wind Turbines,* Albuquerque, New Mexico, USA: Sandia National Laboratories.

Ship Technology, 2021. *Norsepower fits first tiltable Rotor Sails on SC Connector.* [Online]
Available at: https://www.ship-technology.com/news/norsepower-rotor-sails-sc-connector/
[Accessed August 2021].

Spalart, P. R. & Rumsey, C. L., 2007. Effective inflow conditions for turbulence models in aerodynamic calculations. *AIAA journal,* 45(10), pp. 2544-2553.

Talluri, L. et al., 2016. Techno economic and environmental assessment of wind assisted marine propulsion systems. *Ocean Engineering,* Volume 121, pp. 301-311.

Talluri, L., Nalianda, D. & Giuliani, E., 2018. Techno economic and environmental assessment of Flettner rotors for marine propulsion. *Ocean Engineering,* Volume 154, pp. 1-15.

Taskar, B. & Andersen, P., 2020. Benefit of speed reduction for ships in different weather conditions. *Transportation Research Part D,* Volume 85.

Tillig, F. & Ringsberg, J. W., 2020. Design, operation and analysis of wind-assisted cargo ships. *Ocean Engineering,* Volume 211.

Traut, M. et al., 2014. Propulsive power contribution of a kite and a Flettner rotor on selected shipping routes. *Applied Energy,* Volume 113, pp. 362-372.

van der Kolk, I., Akkerman, I., Keuning, J. & Huijsmans, R., 2020. Part 2: Simulation methodology and numerical uncertainty for RANS-CFD for the hydrodynamics of wind-assisted ships operating at leeway angles. *Ocean Engineering,* Volume 201.

van der Kolk, N. J., Akkerman, I., Keuning, J. A. & Huijsmans, R. H. M., 2021. Low-aspect ratio appendages for wind-assisted ships. *Journal of Marine Science and Technology,* pp. 1-18.

Virtanen, P. & Al, E., 2020. SciPy 1.0: Fundamental Algorithms for Scientific Computing in Python. *Nat Methods,* Volume 17, p. 261–272.

Wallenius Marien and Alfa Laval, 2021. *The wind-power solution demonstrated in a vessel concept.* [Online]
Available at: https://www.theoceanbird.com/the-vessel/
[Accessed 16 August 2021].

Yasukawa, H. & Yoshimura, Y., 2015. Introduction of MMG standard method for ship maneuvering predictions. *Journal of Marine Science and Technology,* 20(1), pp. 37-52.

Yuankui, L., Yingjun, Z. & Feixiang, Z., 2014. Minimal time route for wind-assisted ships. *Marine Technology Society Journal,* 48(3), pp. 115-124.

van der Kolk, N. J. et al., 2019. *Case study: Wind-assisted ship propulsion performance prediction, routing, and economic modelling.* London, UK, International Conference Power & Propulsion Alternatives for Ships.

Ouchi, K., Uzawa, K. & Kanai, A., 2011. *Huge Hard Wing Sails for the Propulsor of Next Generation Sailing Vessel.* Hamburg, Germany, The Second International Symposium on Marine Propulsors.

Sacher, M., Hauville, F., Bot, P. & Durand, M., 2015. *Sail trimming FSI simulation-comparison of viscous and inviscid flow models to optimise upwind sails trim.* Auckland, New-Zealand, 5th High Performance Yacht Design Conference.

Aubin, N. et al., 2016. *Wind tunnel investigation of dynamic trimming on upwind sail aerodynamics.* s.l., SNAME 22nd Chesapeake Sailing Yacht Symposium.

Ayro, 2022. *OceanWing information page.* [Online]
Available at: https://ayro.fr/oceanwing/

Kramer, J. V., 2021. *Hydrodynamic test programe repository.* [Online]
Available at: https://github.com/jarlekramer/Hydrodynamic-test-program-for-wind-power/blob/main/README.md

Kume, K. a. H. J. a. T. Y., Fujisawa, J., Fukasawa, R. & Hinatsu, M., 2006. Measurements of hydrodynamic forces, surface pressure, and wake for obliquely towed tanker model and uncertainty analysis for CFD validation. *Journal of marine science and technology,* 11(2), pp. 65-75.

# Previous PhD theses published at the Department of Marine Technology

Norwegian University of Science and Technology

**Previous PhD theses published at the Department of Marine Technology (earlier: Faculty of Marine Technology)**
**NORWEGIAN UNIVERSITY OF SCIENCE AND TECHNOLOGY**

| Report No. | Author | Title |
|---|---|---|
| | Kavlie, Dag | Optimization of Plane Elastic Grillages, 1967 |
| | Hansen, Hans R. | Man-Machine Communication and Data-Storage Methods in Ship Structural Design, 1971 |
| | Gisvold, Kaare M. | A Method for non-linear mixed -integer programming and its Application to Design Problems, 1971 |
| | Lund, Sverre | Tanker Frame Optimalization by means of SUMT-Transformation and Behaviour Models, 1971 |
| | Vinje, Tor | On Vibration of Spherical Shells Interacting with Fluid, 1972 |
| | Lorentz, Jan D. | Tank Arrangement for Crude Oil Carriers in Accordance with the new Anti-Pollution Regulations, 1975 |
| | Carlsen, Carl A. | Computer-Aided Design of Tanker Structures, 1975 |
| | Larsen, Carl M. | Static and Dynamic Analysis of Offshore Pipelines during Installation, 1976 |
| UR-79-01 | Brigt Hatlestad, MK | The finite element method used in a fatigue evaluation of fixed offshore platforms. (Dr.Ing. Thesis) |
| UR-79-02 | Erik Pettersen, MK | Analysis and design of cellular structures. (Dr.Ing. Thesis) |
| UR-79-03 | Sverre Valsgård, MK | Finite difference and finite element methods applied to nonlinear analysis of plated structures. (Dr.Ing. Thesis) |
| UR-79-04 | Nils T. Nordsve, MK | Finite element collapse analysis of structural members considering imperfections and stresses due to fabrication. (Dr.Ing. Thesis) |
| UR-79-05 | Ivar J. Fylling, MK | Analysis of towline forces in ocean towing systems. (Dr.Ing. Thesis) |
| UR-80-06 | Nils Sandsmark, MM | Analysis of Stationary and Transient Heat Conduction by the Use of the Finite Element Method. (Dr.Ing. Thesis) |
| UR-80-09 | Sverre Haver, MK | Analysis of uncertainties related to the stochastic modeling of ocean waves. (Dr.Ing. Thesis) |
| UR-81-15 | Odland, Jonas | On the Strength of welded Ring stiffened cylindrical Shells primarily subjected to axial Compression |
| UR-82-17 | Engesvik, Knut | Analysis of Uncertainties in the fatigue Capacity of |

| | | |
|---|---|---|
| | | Welded Joints |
| UR-82-18 | Rye, Henrik | Ocean wave groups |
| UR-83-30 | Eide, Oddvar Inge | On Cumulative Fatigue Damage in Steel Welded Joints |
| UR-83-33 | Mo, Olav | Stochastic Time Domain Analysis of Slender Offshore Structures |
| UR-83-34 | Amdahl, Jørgen | Energy absorption in Ship-platform impacts |
| UR-84-37 | Mørch, Morten | Motions and mooring forces of semi submersibles as determined by full-scale measurements and theoretical analysis |
| UR-84-38 | Soares, C. Guedes | Probabilistic models for load effects in ship structures |
| UR-84-39 | Aarsnes, Jan V. | Current forces on ships |
| UR-84-40 | Czujko, Jerzy | Collapse Analysis of Plates subjected to Biaxial Compression and Lateral Load |
| UR-85-46 | Alf G. Engseth, MK | Finite element collapse analysis of tubular steel offshore structures. (Dr.Ing. Thesis) |
| UR-86-47 | Dengody Sheshappa, MP | A Computer Design Model for Optimizing Fishing Vessel Designs Based on Techno-Economic Analysis. (Dr.Ing. Thesis) |
| UR-86-48 | Vidar Aanesland, MH | A Theoretical and Numerical Study of Ship Wave Resistance. (Dr.Ing. Thesis) |
| UR-86-49 | Heinz-Joachim Wessel, MK | Fracture Mechanics Analysis of Crack Growth in Plate Girders. (Dr.Ing. Thesis) |
| UR-86-50 | Jon Taby, MK | Ultimate and Post-ultimate Strength of Dented Tubular Members. (Dr.Ing. Thesis) |
| UR-86-51 | Walter Lian, MH | A Numerical Study of Two-Dimensional Separated Flow Past Bluff Bodies at Moderate KC-Numbers. (Dr.Ing. Thesis) |
| UR-86-52 | Bjørn Sortland, MH | Force Measurements in Oscillating Flow on Ship Sections and Circular Cylinders in a U-Tube Water Tank. (Dr.Ing. Thesis) |
| UR-86-53 | Kurt Strand, MM | A System Dynamic Approach to One-dimensional Fluid Flow. (Dr.Ing. Thesis) |
| UR-86-54 | Arne Edvin Løken, MH | Three Dimensional Second Order Hydrodynamic Effects on Ocean Structures in Waves. (Dr.Ing. Thesis) |
| UR-86-55 | Sigurd Falch, MH | A Numerical Study of Slamming of Two-Dimensional Bodies. (Dr.Ing. Thesis) |
| UR-87-56 | Arne Braathen, MH | Application of a Vortex Tracking Method to the Prediction of Roll Damping of a Two-Dimension Floating Body. (Dr.Ing. Thesis) |

| | | |
|---|---|---|
| UR-87-57 | Bernt Leira, MK | Gaussian Vector Processes for Reliability Analysis involving Wave-Induced Load Effects. (Dr.Ing. Thesis) |
| UR-87-58 | Magnus Småvik, MM | Thermal Load and Process Characteristics in a Two-Stroke Diesel Engine with Thermal Barriers (in Norwegian). (Dr.Ing. Thesis) |
| MTA-88-59 | Bernt Arild Bremdal, MP | An Investigation of Marine Installation Processes – A Knowledge - Based Planning Approach. (Dr.Ing. Thesis) |
| MTA-88-60 | Xu Jun, MK | Non-linear Dynamic Analysis of Space-framed Offshore Structures. (Dr.Ing. Thesis) |
| MTA-89-61 | Gang Miao, MH | Hydrodynamic Forces and Dynamic Responses of Circular Cylinders in Wave Zones. (Dr.Ing. Thesis) |
| MTA-89-62 | Martin Greenhow, MH | Linear and Non-Linear Studies of Waves and Floating Bodies. Part I and Part II. (Dr.Techn. Thesis) |
| MTA-89-63 | Chang Li, MH | Force Coefficients of Spheres and Cubes in Oscillatory Flow with and without Current. (Dr.Ing. Thesis |
| MTA-89-64 | Hu Ying, MP | A Study of Marketing and Design in Development of Marine Transport Systems. (Dr.Ing. Thesis) |
| MTA-89-65 | Arild Jæger, MH | Seakeeping, Dynamic Stability and Performance of a Wedge Shaped Planing Hull. (Dr.Ing. Thesis) |
| MTA-89-66 | Chan Siu Hung, MM | The dynamic characteristics of tilting-pad bearings |
| MTA-89-67 | Kim Wikstrøm, MP | Analysis av projekteringen for ett offshore projekt. (Licenciat-avhandling) |
| MTA-89-68 | Jiao Guoyang, MK | Reliability Analysis of Crack Growth under Random Loading, considering Model Updating. (Dr.Ing. Thesis) |
| MTA-89-69 | Arnt Olufsen, MK | Uncertainty and Reliability Analysis of Fixed Offshore Structures. (Dr.Ing. Thesis) |
| MTA-89-70 | Wu Yu-Lin, MR | System Reliability Analyses of Offshore Structures using improved Truss and Beam Models. (Dr.Ing. Thesis) |
| MTA-90-71 | Jan Roger Hoff, MH | Three-dimensional Green function of a vessel with forward speed in waves. (Dr.Ing. Thesis) |
| MTA-90-72 | Rong Zhao, MH | Slow-Drift Motions of a Moored Two-Dimensional Body in Irregular Waves. (Dr.Ing. Thesis) |
| MTA-90-73 | Atle Minsaas, MP | Economical Risk Analysis. (Dr.Ing. Thesis) |
| MTA-90-74 | Knut-Aril Farnes, MK | Long-term Statistics of Response in Non-linear Marine Structures. (Dr.Ing. Thesis) |
| MTA-90-75 | Torbjørn Sotberg, MK | Application of Reliability Methods for Safety Assessment of Submarine Pipelines. (Dr.Ing. |

| | | |
|---|---|---|
| | | Thesis) |
| MTA-90-76 | Zeuthen, Steffen, MP | SEAMAID. A computational model of the design process in a constraint-based logic programming environment. An example from the offshore domain. (Dr.Ing. Thesis) |
| MTA-91-77 | Haagensen, Sven, MM | Fuel Dependant Cyclic Variability in a Spark Ignition Engine - An Optical Approach. (Dr.Ing. Thesis) |
| MTA-91-78 | Løland, Geir, MH | Current forces on and flow through fish farms. (Dr.Ing. Thesis) |
| MTA-91-79 | Hoen, Christopher, MK | System Identification of Structures Excited by Stochastic Load Processes. (Dr.Ing. Thesis) |
| MTA-91-80 | Haugen, Stein, MK | Probabilistic Evaluation of Frequency of Collision between Ships and Offshore Platforms. (Dr.Ing. Thesis) |
| MTA-91-81 | Sødahl, Nils, MK | Methods for Design and Analysis of Flexible Risers. (Dr.Ing. Thesis) |
| MTA-91-82 | Ormberg, Harald, MK | Non-linear Response Analysis of Floating Fish Farm Systems. (Dr.Ing. Thesis) |
| MTA-91-83 | Marley, Mark J., MK | Time Variant Reliability under Fatigue Degradation. (Dr.Ing. Thesis) |
| MTA-91-84 | Krokstad, Jørgen R., MH | Second-order Loads in Multidirectional Seas. (Dr.Ing. Thesis) |
| MTA-91-85 | Molteberg, Gunnar A., MM | The Application of System Identification Techniques to Performance Monitoring of Four Stroke Turbocharged Diesel Engines. (Dr.Ing. Thesis) |
| MTA-92-86 | Mørch, Hans Jørgen Bjelke, MH | Aspects of Hydrofoil Design: with Emphasis on Hydrofoil Interaction in Calm Water. (Dr.Ing. Thesis) |
| MTA-92-87 | Chan Siu Hung, MM | Nonlinear Analysis of Rotordynamic Instabilities in Highspeed Turbomachinery. (Dr.Ing. Thesis) |
| MTA-92-88 | Bessason, Bjarni, MK | Assessment of Earthquake Loading and Response of Seismically Isolated Bridges. (Dr.Ing. Thesis) |
| MTA-92-89 | Langli, Geir, MP | Improving Operational Safety through exploitation of Design Knowledge - an investigation of offshore platform safety. (Dr.Ing. Thesis) |
| MTA-92-90 | Sævik, Svein, MK | On Stresses and Fatigue in Flexible Pipes. (Dr.Ing. Thesis) |
| MTA-92-91 | Ask, Tor Ø., MM | Ignition and Flame Growth in Lean Gas-Air Mixtures. An Experimental Study with a Schlieren System. (Dr.Ing. Thesis) |
| MTA-86-92 | Hessen, Gunnar, MK | Fracture Mechanics Analysis of Stiffened Tubular Members. (Dr.Ing. Thesis) |

| | | |
|---|---|---|
| MTA-93-93 | Steinebach, Christian, MM | Knowledge Based Systems for Diagnosis of Rotating Machinery. (Dr.Ing. Thesis) |
| MTA-93-94 | Dalane, Jan Inge, MK | System Reliability in Design and Maintenance of Fixed Offshore Structures. (Dr.Ing. Thesis) |
| MTA-93-95 | Steen, Sverre, MH | Cobblestone Effect on SES. (Dr.Ing. Thesis) |
| MTA-93-96 | Karunakaran, Daniel, MK | Nonlinear Dynamic Response and Reliability Analysis of Drag-dominated Offshore Platforms. (Dr.Ing. Thesis) |
| MTA-93-97 | Hagen, Arnulf, MP | The Framework of a Design Process Language. (Dr.Ing. Thesis) |
| MTA-93-98 | Nordrik, Rune, MM | Investigation of Spark Ignition and Autoignition in Methane and Air Using Computational Fluid Dynamics and Chemical Reaction Kinetics. A Numerical Study of Ignition Processes in Internal Combustion Engines. (Dr.Ing. Thesis) |
| MTA-94-99 | Passano, Elizabeth, MK | Efficient Analysis of Nonlinear Slender Marine Structures. (Dr.Ing. Thesis) |
| MTA-94-100 | Kvålsvold, Jan, MH | Hydroelastic Modelling of Wetdeck Slamming on Multihull Vessels. (Dr.Ing. Thesis) |
| MTA-94-102 | Bech, Sidsel M., MK | Experimental and Numerical Determination of Stiffness and Strength of GRP/PVC Sandwich Structures. (Dr.Ing. Thesis) |
| MTA-95-103 | Paulsen, Hallvard, MM | A Study of Transient Jet and Spray using a Schlieren Method and Digital Image Processing. (Dr.Ing. Thesis) |
| MTA-95-104 | Hovde, Geir Olav, MK | Fatigue and Overload Reliability of Offshore Structural Systems, Considering the Effect of Inspection and Repair. (Dr.Ing. Thesis) |
| MTA-95-105 | Wang, Xiaozhi, MK | Reliability Analysis of Production Ships with Emphasis on Load Combination and Ultimate Strength. (Dr.Ing. Thesis) |
| MTA-95-106 | Ulstein, Tore, MH | Nonlinear Effects of a Flexible Stern Seal Bag on Cobblestone Oscillations of an SES. (Dr.Ing. Thesis) |
| MTA-95-107 | Solaas, Frøydis, MH | Analytical and Numerical Studies of Sloshing in Tanks. (Dr.Ing. Thesis) |
| MTA-95-108 | Hellan, Øyvind, MK | Nonlinear Pushover and Cyclic Analyses in Ultimate Limit State Design and Reassessment of Tubular Steel Offshore Structures. (Dr.Ing. Thesis) |
| MTA-95-109 | Hermundstad, Ole A., MK | Theoretical and Experimental Hydroelastic Analysis of High Speed Vessels. (Dr.Ing. Thesis) |
| MTA-96-110 | Bratland, Anne K., MH | Wave-Current Interaction Effects on Large-Volume Bodies in Water of Finite Depth. (Dr.Ing. Thesis) |
| MTA-96-111 | Herfjord, Kjell, MH | A Study of Two-dimensional Separated Flow by a Combination of the Finite Element Method and |

| | | |
|---|---|---|
| | | Navier-Stokes Equations. (Dr.Ing. Thesis) |
| MTA-96-112 | Æsøy, Vilmar, MM | Hot Surface Assisted Compression Ignition in a Direct Injection Natural Gas Engine. (Dr.Ing. Thesis) |
| MTA-96-113 | Eknes, Monika L., MK | Escalation Scenarios Initiated by Gas Explosions on Offshore Installations. (Dr.Ing. Thesis) |
| MTA-96-114 | Erikstad, Stein O., MP | A Decision Support Model for Preliminary Ship Design. (Dr.Ing. Thesis) |
| MTA-96-115 | Pedersen, Egil, MH | A Nautical Study of Towed Marine Seismic Streamer Cable Configurations. (Dr.Ing. Thesis) |
| MTA-97-116 | Moksnes, Paul O., MM | Modelling Two-Phase Thermo-Fluid Systems Using Bond Graphs. (Dr.Ing. Thesis) |
| MTA-97-117 | Halse, Karl H., MK | On Vortex Shedding and Prediction of Vortex-Induced Vibrations of Circular Cylinders. (Dr.Ing. Thesis) |
| MTA-97-118 | Igland, Ragnar T., MK | Reliability Analysis of Pipelines during Laying, considering Ultimate Strength under Combined Loads. (Dr.Ing. Thesis) |
| MTA-97-119 | Pedersen, Hans-P., MP | Levendefiskteknologi for fiskefartøy. (Dr.Ing. Thesis) |
| MTA-98-120 | Vikestad, Kyrre, MK | Multi-Frequency Response of a Cylinder Subjected to Vortex Shedding and Support Motions. (Dr.Ing. Thesis) |
| MTA-98-121 | Azadi, Mohammad R. E., MK | Analysis of Static and Dynamic Pile-Soil-Jacket Behaviour. (Dr.Ing. Thesis) |
| MTA-98-122 | Ulltang, Terje, MP | A Communication Model for Product Information. (Dr.Ing. Thesis) |
| MTA-98-123 | Torbergsen, Erik, MM | Impeller/Diffuser Interaction Forces in Centrifugal Pumps. (Dr.Ing. Thesis) |
| MTA-98-124 | Hansen, Edmond, MH | A Discrete Element Model to Study Marginal Ice Zone Dynamics and the Behaviour of Vessels Moored in Broken Ice. (Dr.Ing. Thesis) |
| MTA-98-125 | Videiro, Paulo M., MK | Reliability Based Design of Marine Structures. (Dr.Ing. Thesis) |
| MTA-99-126 | Mainçon, Philippe, MK | Fatigue Reliability of Long Welds Application to Titanium Risers. (Dr.Ing. Thesis) |
| MTA-99-127 | Haugen, Elin M., MH | Hydroelastic Analysis of Slamming on Stiffened Plates with Application to Catamaran Wetdecks. (Dr.Ing. Thesis) |
| MTA-99-128 | Langhelle, Nina K., MK | Experimental Validation and Calibration of Nonlinear Finite Element Models for Use in Design of Aluminium Structures Exposed to Fire. (Dr.Ing. Thesis) |
| MTA-99- | Berstad, Are J., MK | Calculation of Fatigue Damage in Ship Structures. |

| | | |
|---|---|---|
| 129 | | (Dr.Ing. Thesis) |
| MTA-99-130 | Andersen, Trond M., MM | Short Term Maintenance Planning. (Dr.Ing. Thesis) |
| MTA-99-131 | Tveiten, Bård Wathne, MK | Fatigue Assessment of Welded Aluminium Ship Details. (Dr.Ing. Thesis) |
| MTA-99-132 | Søreide, Fredrik, MP | Applications of underwater technology in deep water archaeology. Principles and practice. (Dr.Ing. Thesis) |
| MTA-99-133 | Tønnessen, Rune, MH | A Finite Element Method Applied to Unsteady Viscous Flow Around 2D Blunt Bodies With Sharp Corners. (Dr.Ing. Thesis) |
| MTA-99-134 | Elvekrok, Dag R., MP | Engineering Integration in Field Development Projects in the Norwegian Oil and Gas Industry. The Supplier Management of Norne. (Dr.Ing. Thesis) |
| MTA-99-135 | Fagerholt, Kjetil, MP | Optimeringsbaserte Metoder for Ruteplanlegging innen skipsfart. (Dr.Ing. Thesis) |
| MTA-99-136 | Bysveen, Marie, MM | Visualization in Two Directions on a Dynamic Combustion Rig for Studies of Fuel Quality. (Dr.Ing. Thesis) |
| MTA-2000-137 | Storteig, Eskild, MM | Dynamic characteristics and leakage performance of liquid annular seals in centrifugal pumps. (Dr.Ing. Thesis) |
| MTA-2000-138 | Sagli, Gro, MK | Model uncertainty and simplified estimates of long term extremes of hull girder loads in ships. (Dr.Ing. Thesis) |
| MTA-2000-139 | Tronstad, Harald, MK | Nonlinear analysis and design of cable net structures like fishing gear based on the finite element method. (Dr.Ing. Thesis) |
| MTA-2000-140 | Kroneberg, André, MP | Innovation in shipping by using scenarios. (Dr.Ing. Thesis) |
| MTA-2000-141 | Haslum, Herbjørn Alf, MH | Simplified methods applied to nonlinear motion of spar platforms. (Dr.Ing. Thesis) |
| MTA-2001-142 | Samdal, Ole Johan, MM | Modelling of Degradation Mechanisms and Stressor Interaction on Static Mechanical Equipment Residual Lifetime. (Dr.Ing. Thesis) |
| MTA-2001-143 | Baarholm, Rolf Jarle, MH | Theoretical and experimental studies of wave impact underneath decks of offshore platforms. (Dr.Ing. Thesis) |
| MTA-2001-144 | Wang, Lihua, MK | Probabilistic Analysis of Nonlinear Wave-induced Loads on Ships. (Dr.Ing. Thesis) |
| MTA-2001-145 | Kristensen, Odd H. Holt, MK | Ultimate Capacity of Aluminium Plates under Multiple Loads, Considering HAZ Properties. (Dr.Ing. Thesis) |
| MTA-2001-146 | Greco, Marilena, MH | A Two-Dimensional Study of Green-Water |

| | | |
|---|---|---|
| | | Loading. (Dr.Ing. Thesis) |
| MTA-2001-147 | Heggelund, Svein E., MK | Calculation of Global Design Loads and Load Effects in Large High Speed Catamarans. (Dr.Ing. Thesis) |
| MTA-2001-148 | Babalola, Olusegun T., MK | Fatigue Strength of Titanium Risers – Defect Sensitivity. (Dr.Ing. Thesis) |
| MTA-2001-149 | Mohammed, Abuu K., MK | Nonlinear Shell Finite Elements for Ultimate Strength and Collapse Analysis of Ship Structures. (Dr.Ing. Thesis) |
| MTA-2002-150 | Holmedal, Lars E., MH | Wave-current interactions in the vicinity of the sea bed. (Dr.Ing. Thesis) |
| MTA-2002-151 | Rognebakke, Olav F., MH | Sloshing in rectangular tanks and interaction with ship motions. (Dr.Ing. Thesis) |
| MTA-2002-152 | Lader, Pål Furset, MH | Geometry and Kinematics of Breaking Waves. (Dr.Ing. Thesis) |
| MTA-2002-153 | Yang, Qinzheng, MH | Wash and wave resistance of ships in finite water depth. (Dr.Ing. Thesis) |
| MTA-2002-154 | Melhus, Øyvin, MM | Utilization of VOC in Diesel Engines. Ignition and combustion of VOC released by crude oil tankers. (Dr.Ing. Thesis) |
| MTA-2002-155 | Ronæss, Marit, MH | Wave Induced Motions of Two Ships Advancing on Parallel Course. (Dr.Ing. Thesis) |
| MTA-2002-156 | Økland, Ole D., MK | Numerical and experimental investigation of whipping in twin hull vessels exposed to severe wet deck slamming. (Dr.Ing. Thesis) |
| MTA-2002-157 | Ge, Chunhua, MK | Global Hydroelastic Response of Catamarans due to Wet Deck Slamming. (Dr.Ing. Thesis) |
| MTA-2002-158 | Byklum, Eirik, MK | Nonlinear Shell Finite Elements for Ultimate Strength and Collapse Analysis of Ship Structures. (Dr.Ing. Thesis) |
| IMT-2003-1 | Chen, Haibo, MK | Probabilistic Evaluation of FPSO-Tanker Collision in Tandem Offloading Operation. (Dr.Ing. Thesis) |
| IMT-2003-2 | Skaugset, Kjetil Bjørn, MK | On the Suppression of Vortex Induced Vibrations of Circular Cylinders by Radial Water Jets. (Dr.Ing. Thesis) |
| IMT-2003-3 | Chezhian, Muthu | Three-Dimensional Analysis of Slamming. (Dr.Ing. Thesis) |
| IMT-2003-4 | Buhaug, Øyvind | Deposit Formation on Cylinder Liner Surfaces in Medium Speed Engines. (Dr.Ing. Thesis) |
| IMT-2003-5 | Tregde, Vidar | Aspects of Ship Design: Optimization of Aft Hull with Inverse Geometry Design. (Dr.Ing. Thesis) |
| IMT- | Wist, Hanne Therese | Statistical Properties of Successive Ocean Wave |

| | | |
|---|---|---|
| 2003-6 | | Parameters. (Dr.Ing. Thesis) |
| IMT-2004-7 | Ransau, Samuel | Numerical Methods for Flows with Evolving Interfaces. (Dr.Ing. Thesis) |
| IMT-2004-8 | Soma, Torkel | Blue-Chip or Sub-Standard. A data interrogation approach of identity safety characteristics of shipping organization. (Dr.Ing. Thesis) |
| IMT-2004-9 | Ersdal, Svein | An experimental study of hydrodynamic forces on cylinders and cables in near axial flow. (Dr.Ing. Thesis) |
| IMT-2005-10 | Brodtkorb, Per Andreas | The Probability of Occurrence of Dangerous Wave Situations at Sea. (Dr.Ing. Thesis) |
| IMT-2005-11 | Yttervik, Rune | Ocean current variability in relation to offshore engineering. (Dr.Ing. Thesis) |
| IMT-2005-12 | Fredheim, Arne | Current Forces on Net-Structures. (Dr.Ing. Thesis) |
| IMT-2005-13 | Heggernes, Kjetil | Flow around marine structures. (Dr.Ing. Thesis |
| IMT-2005-14 | Fouques, Sebastien | Lagrangian Modelling of Ocean Surface Waves and Synthetic Aperture Radar Wave Measurements. (Dr.Ing. Thesis) |
| IMT-2006-15 | Holm, Håvard | Numerical calculation of viscous free surface flow around marine structures. (Dr.Ing. Thesis) |
| IMT-2006-16 | Bjørheim, Lars G. | Failure Assessment of Long Through Thickness Fatigue Cracks in Ship Hulls. (Dr.Ing. Thesis) |
| IMT-2006-17 | Hansson, Lisbeth | Safety Management for Prevention of Occupational Accidents. (Dr.Ing. Thesis) |
| IMT-2006-18 | Zhu, Xinying | Application of the CIP Method to Strongly Nonlinear Wave-Body Interaction Problems. (Dr.Ing. Thesis) |
| IMT-2006-19 | Reite, Karl Johan | Modelling and Control of Trawl Systems. (Dr.Ing. Thesis) |
| IMT-2006-20 | Smogeli, Øyvind Notland | Control of Marine Propellers. From Normal to Extreme Conditions. (Dr.Ing. Thesis) |
| IMT-2007-21 | Storhaug, Gaute | Experimental Investigation of Wave Induced Vibrations and Their Effect on the Fatigue Loading of Ships. (Dr.Ing. Thesis) |
| IMT-2007-22 | Sun, Hui | A Boundary Element Method Applied to Strongly Nonlinear Wave-Body Interaction Problems. (PhD Thesis, CeSOS) |
| IMT-2007-23 | Rustad, Anne Marthine | Modelling and Control of Top Tensioned Risers. (PhD Thesis, CeSOS) |
| IMT-2007-24 | Johansen, Vegar | Modelling flexible slender system for real-time simulations and control applications |
| IMT-2007-25 | Wroldsen, Anders Sunde | Modelling and control of tensegrity structures. |

| | | |
|---|---|---|
| | | (PhD Thesis, CeSOS) |
| IMT-2007-26 | Aronsen, Kristoffer Høye | An experimental investigation of in-line and combined inline and cross flow vortex induced vibrations. (Dr. avhandling, IMT) |
| IMT-2007-27 | Gao, Zhen | Stochastic Response Analysis of Mooring Systems with Emphasis on Frequency-domain Analysis of Fatigue due to Wide-band Response Processes (PhD Thesis, CeSOS) |
| IMT-2007-28 | Thorstensen, Tom Anders | Lifetime Profit Modelling of Ageing Systems Utilizing Information about Technical Condition. (Dr.ing. thesis, IMT) |
| IMT-2008-29 | Refsnes, Jon Erling Gorset | Nonlinear Model-Based Control of Slender Body AUVs (PhD Thesis, IMT) |
| IMT-2008-30 | Berntsen, Per Ivar B. | Structural Reliability Based Position Mooring. (PhD-Thesis, IMT) |
| IMT-2008-31 | Ye, Naiquan | Fatigue Assessment of Aluminium Welded Box-stiffener Joints in Ships (Dr.ing. thesis, IMT) |
| IMT-2008-32 | Radan, Damir | Integrated Control of Marine Electrical Power Systems. (PhD-Thesis, IMT) |
| IMT-2008-33 | Thomassen, Paul | Methods for Dynamic Response Analysis and Fatigue Life Estimation of Floating Fish Cages. (Dr.ing. thesis, IMT) |
| IMT-2008-34 | Pákozdi, Csaba | A Smoothed Particle Hydrodynamics Study of Two-dimensional Nonlinear Sloshing in Rectangular Tanks. (Dr.ing.thesis, IMT/ CeSOS) |
| IMT-2007-35 | Grytøyr, Guttorm | A Higher-Order Boundary Element Method and Applications to Marine Hydrodynamics. (Dr.ing.thesis, IMT) |
| IMT-2008-36 | Drummen, Ingo | Experimental and Numerical Investigation of Nonlinear Wave-Induced Load Effects in Containerships considering Hydroelasticity. (PhD thesis, CeSOS) |
| IMT-2008-37 | Skejic, Renato | Maneuvering and Seakeeping of a Singel Ship and of Two Ships in Interaction. (PhD-Thesis, CeSOS) |
| IMT-2008-38 | Harlem, Alf | An Age-Based Replacement Model for Repairable Systems with Attention to High-Speed Marine Diesel Engines. (PhD-Thesis, IMT) |
| IMT-2008-39 | Alsos, Hagbart S. | Ship Grounding. Analysis of Ductile Fracture, Bottom Damage and Hull Girder Response. (PhD-thesis, IMT) |
| IMT-2008-40 | Graczyk, Mateusz | Experimental Investigation of Sloshing Loading and Load Effects in Membrane LNG Tanks Subjected to Random Excitation. (PhD-thesis, CeSOS) |
| IMT-2008-41 | Taghipour, Reza | Efficient Prediction of Dynamic Response for Flexible amd Multi-body Marine Structures. (PhD- |

| | | |
|---|---|---|
| | | thesis, CeSOS) |
| IMT-2008-42 | Ruth, Eivind | Propulsion control and thrust allocation on marine vessels. (PhD thesis, CeSOS) |
| IMT-2008-43 | Nystad, Bent Helge | Technical Condition Indexes and Remaining Useful Life of Aggregated Systems. PhD thesis, IMT |
| IMT-2008-44 | Soni, Prashant Kumar | Hydrodynamic Coefficients for Vortex Induced Vibrations of Flexible Beams, PhD thesis, CeSOS |
| IMT-2009-45 | Amlashi, Hadi K.K. | Ultimate Strength and Reliability-based Design of Ship Hulls with Emphasis on Combined Global and Local Loads. PhD Thesis, IMT |
| IMT-2009-46 | Pedersen, Tom Arne | Bond Graph Modelling of Marine Power Systems. PhD Thesis, IMT |
| IMT-2009-47 | Kristiansen, Trygve | Two-Dimensional Numerical and Experimental Studies of Piston-Mode Resonance. PhD-Thesis, CeSOS |
| IMT-2009-48 | Ong, Muk Chen | Applications of a Standard High Reynolds Number Model and a Stochastic Scour Prediction Model for Marine Structures. PhD-thesis, IMT |
| IMT-2009-49 | Hong, Lin | Simplified Analysis and Design of Ships subjected to Collision and Grounding. PhD-thesis, IMT |
| IMT-2009-50 | Koushan, Kamran | Vortex Induced Vibrations of Free Span Pipelines, PhD thesis, IMT |
| IMT-2009-51 | Korsvik, Jarl Eirik | Heuristic Methods for Ship Routing and Scheduling. PhD-thesis, IMT |
| IMT-2009-52 | Lee, Jihoon | Experimental Investigation and Numerical in Analyzing the Ocean Current Displacement of Longlines. Ph.d.-Thesis, IMT. |
| IMT-2009-53 | Vestbøstad, Tone Gran | A Numerical Study of Wave-in-Deck Impact usin a Two-Dimensional Constrained Interpolation Profile Method, Ph.d.thesis, CeSOS. |
| IMT-2009-54 | Bruun, Kristine | Bond Graph Modelling of Fuel Cells for Marine Power Plants. Ph.d.-thesis, IMT |
| IMT 2009-55 | Holstad, Anders | Numerical Investigation of Turbulence in a Sekwed Three-Dimensional Channel Flow, Ph.d.-thesis, IMT. |
| IMT 2009-56 | Ayala-Uraga, Efren | Reliability-Based Assessment of Deteriorating Ship-shaped Offshore Structures, Ph.d.-thesis, IMT |
| IMT 2009-57 | Kong, Xiangjun | A Numerical Study of a Damaged Ship in Beam Sea Waves. Ph.d.-thesis, IMT/CeSOS. |
| IMT 2010-58 | Kristiansen, David | Wave Induced Effects on Floaters of Aquaculture Plants, Ph.d.-thesis, CeSOS. |

| | | |
|---|---|---|
| IMT 2010-59 | Ludvigsen, Martin | An ROV-Toolbox for Optical and Acoustic Scientific Seabed Investigation. Ph.d.-thesis IMT. |
| IMT 2010-60 | Hals, Jørgen | Modelling and Phase Control of Wave-Energy Converters. Ph.d.thesis, CeSOS. |
| IMT 2010- 61 | Shu, Zhi | Uncertainty Assessment of Wave Loads and Ultimate Strength of Tankers and Bulk Carriers in a Reliability Framework. Ph.d. Thesis, IMT/ CeSOS |
| IMT 2010-62 | Shao, Yanlin | Numerical Potential-Flow Studies on Weakly-Nonlinear Wave-Body Interactions with/without Small Forward Speed, Ph.d.thesis,CeSOS. |
| IMT 2010-63 | Califano, Andrea | Dynamic Loads on Marine Propellers due to Intermittent Ventilation. Ph.d.thesis, IMT. |
| IMT 2010-64 | El Khoury, George | Numerical Simulations of Massively Separated Turbulent Flows, Ph.d.-thesis, IMT |
| IMT 2010-65 | Seim, Knut Sponheim | Mixing Process in Dense Overflows with Emphasis on the Faroe Bank Channel Overflow. Ph.d.thesis, IMT |
| IMT 2010-66 | Jia, Huirong | Structural Analysis of Intect and Damaged Ships in a Collission Risk Analysis Perspective. Ph.d.thesis CeSoS. |
| IMT 2010-67 | Jiao, Linlin | Wave-Induced Effects on a Pontoon-type Very Large Floating Structures (VLFS). Ph.D.-thesis, CeSOS. |
| IMT 2010-68 | Abrahamsen, Bjørn Christian | Sloshing Induced Tank Roof with Entrapped Air Pocket. Ph.d.thesis, CeSOS. |
| IMT 2011-69 | Karimirad, Madjid | Stochastic Dynamic Response Analysis of Spar-Type Wind Turbines with Catenary or Taut Mooring Systems. Ph.d.-thesis, CeSOS. |
| IMT - 2011-70 | Erlend Meland | Condition Monitoring of Safety Critical Valves. Ph.d.-thesis, IMT. |
| IMT – 2011-71 | Yang, Limin | Stochastic Dynamic System Analysis of Wave Energy Converter with Hydraulic Power Take-Off, with Particular Reference to Wear Damage Analysis, Ph.d. Thesis, CeSOS. |
| IMT – 2011-72 | Visscher, Jan | Application of Particla Image Velocimetry on Turbulent Marine Flows, Ph.d.Thesis, IMT. |
| IMT – 2011-73 | Su, Biao | Numerical Predictions of Global and Local Ice Loads on Ships. Ph.d.Thesis, CeSOS. |
| IMT – 2011-74 | Liu, Zhenhui | Analytical and Numerical Analysis of Iceberg Collision with Ship Structures. Ph.d.Thesis, IMT. |
| IMT – 2011-75 | Aarsæther, Karl Gunnar | Modeling and Analysis of Ship Traffic by Observation and Numerical Simulation. Ph.d.Thesis, IMT. |

| | | |
|---|---|---|
| Imt – 2011-76 | Wu, Jie | Hydrodynamic Force Identification from Stochastic Vortex Induced Vibration Experiments with Slender Beams. Ph.d.Thesis, IMT. |
| Imt – 2011-77 | Amini, Hamid | Azimuth Propulsors in Off-design Conditions. Ph.d.Thesis, IMT. |
| IMT – 2011-78 | Nguyen, Tan-Hoi | Toward a System of Real-Time Prediction and Monitoring of Bottom Damage Conditions During Ship Grounding. Ph.d.thesis, IMT. |
| IMT- 2011-79 | Tavakoli, Mohammad T. | Assessment of Oil Spill in Ship Collision and Grounding, Ph.d.thesis, IMT. |
| IMT- 2011-80 | Guo, Bingjie | Numerical and Experimental Investigation of Added Resistance in Waves. Ph.d.Thesis, IMT. |
| IMT- 2011-81 | Chen, Qiaofeng | Ultimate Strength of Aluminium Panels, considering HAZ Effects, IMT |
| IMT- 2012-82 | Kota, Ravikiran S. | Wave Loads on Decks of Offshore Structures in Random Seas, CeSOS. |
| IMT- 2012-83 | Sten, Ronny | Dynamic Simulation of Deep Water Drilling Risers with Heave Compensating System, IMT. |
| IMT- 2012-84 | Berle, Øyvind | Risk and resilience in global maritime supply chains, IMT. |
| IMT- 2012-85 | Fang, Shaoji | Fault Tolerant Position Mooring Control Based on Structural Reliability, CeSOS. |
| IMT- 2012-86 | You, Jikun | Numerical studies on wave forces and moored ship motions in intermediate and shallow water, CeSOS. |
| IMT- 2012-87 | Xiang ,Xu | Maneuvering of two interacting ships in waves, CeSOS |
| IMT- 2012-88 | Dong, Wenbin | Time-domain fatigue response and reliability analysis of offshore wind turbines with emphasis on welded tubular joints and gear components, CeSOS |
| IMT- 2012-89 | Zhu, Suji | Investigation of Wave-Induced Nonlinear Load Effects in Open Ships considering Hull Girder Vibrations in Bending and Torsion, CeSOS |
| IMT- 2012-90 | Zhou, Li | Numerical and Experimental Investigation of Station-keeping in Level Ice, CeSOS |
| IMT- 2012-91 | Ushakov, Sergey | Particulate matter emission characteristics from diesel enignes operating on conventional and alternative marine fuels, IMT |
| IMT- 2013-1 | Yin, Decao | Experimental and Numerical Analysis of Combined In-line and Cross-flow Vortex Induced Vibrations, CeSOS |

| | | |
|---|---|---|
| IMT-2013-2 | Kurniawan, Adi | Modelling and geometry optimisation of wave energy converters, CeSOS |
| IMT-2013-3 | Al Ryati, Nabil | Technical condition indexes doe auxiliary marine diesel engines, IMT |
| IMT-2013-4 | Firoozkoohi, Reza | Experimental, numerical and analytical investigation of the effect of screens on sloshing, CeSOS |
| IMT-2013-5 | Ommani, Babak | Potential-Flow Predictions of a Semi-Displacement Vessel Including Applications to Calm Water Broaching, CeSOS |
| IMT-2013-6 | Xing, Yihan | Modelling and analysis of the gearbox in a floating spar-type wind turbine, CeSOS |
| IMT-7-2013 | Balland, Océane | Optimization models for reducing air emissions from ships, IMT |
| IMT-8-2013 | Yang, Dan | Transitional wake flow behind an inclined flat plate-----Computation and analysis, IMT |
| IMT-9-2013 | Abdillah, Suyuthi | Prediction of Extreme Loads and Fatigue Damage for a Ship Hull due to Ice Action, IMT |
| IMT-10-2013 | Ramìrez, Pedro Agustìn Pèrez | Ageing management and life extension of technical systems-<br>Concepts and methods applied to oil and gas facilities, IMT |
| IMT-11-2013 | Chuang, Zhenju | Experimental and Numerical Investigation of Speed Loss due to Seakeeping and Maneuvering. IMT |
| IMT-12-2013 | Etemaddar, Mahmoud | Load and Response Analysis of Wind Turbines under Atmospheric Icing and Controller System Faults with Emphasis on Spar Type Floating Wind Turbines, IMT |
| IMT-13-2013 | Lindstad, Haakon | Strategies and measures for reducing maritime CO2 emissons, IMT |
| IMT-14-2013 | Haris, Sabril | Damage interaction analysis of ship collisions, IMT |
| IMT-15-2013 | Shainee, Mohamed | Conceptual Design, Numerical and Experimental Investigation of a SPM Cage Concept for Offshore Mariculture, IMT |
| IMT-16-2013 | Gansel, Lars | Flow past porous cylinders and effects of biofouling and fish behavior on the flow in and around Atlantic salmon net cages, IMT |
| IMT-17-2013 | Gaspar, Henrique | Handling Aspects of Complexity in Conceptual Ship Design, IMT |
| IMT-18-2013 | Thys, Maxime | Theoretical and Experimental Investigation of a Free Running Fishing Vessel at Small Frequency of Encounter, CeSOS |
| IMT-19-2013 | Aglen, Ida | VIV in Free Spanning Pipelines, CeSOS |

| | | |
|---|---|---|
| IMT-1-2014 | Song, An | Theoretical and experimental studies of wave diffraction and radiation loads on a horizontally submerged perforated plate, CeSOS |
| IMT-2-2014 | Rogne, Øyvind Ygre | Numerical and Experimental Investigation of a Hinged 5-body Wave Energy Converter, CeSOS |
| IMT-3-2014 | Dai, Lijuan | Safe and efficient operation and maintenance of offshore wind farms ,IMT |
| IMT-4-2014 | Bachynski, Erin Elizabeth | Design and Dynamic Analysis of Tension Leg Platform Wind Turbines, CeSOS |
| IMT-5-2014 | Wang, Jingbo | Water Entry of Freefall Wedged – Wedge motions and Cavity Dynamics, CeSOS |
| IMT-6-2014 | Kim, Ekaterina | Experimental and numerical studies related to the coupled behavior of ice mass and steel structures during accidental collisions, IMT |
| IMT-7-2014 | Tan, Xiang | Numerical investigation of ship's continuous- mode icebreaking in leverl ice, CeSOS |
| IMT-8-2014 | Muliawan, Made Jaya | Design and Analysis of Combined Floating Wave and Wind Power Facilities, with Emphasis on Extreme Load Effects of the Mooring System, CeSOS |
| IMT-9-2014 | Jiang, Zhiyu | Long-term response analysis of wind turbines with an emphasis on fault and shutdown conditions, IMT |
| IMT-10-2014 | Dukan, Fredrik | ROV Motion Control Systems, IMT |
| IMT-11-2014 | Grimsmo, Nils I. | Dynamic simulations of hydraulic cylinder for heave compensation of deep water drilling risers, IMT |
| IMT-12-2014 | Kvittem, Marit I. | Modelling and response analysis for fatigue design of a semisubmersible wind turbine, CeSOS |
| IMT-13-2014 | Akhtar, Juned | The Effects of Human Fatigue on Risk at Sea, IMT |
| IMT-14-2014 | Syahroni, Nur | Fatigue Assessment of Welded Joints Taking into Account Effects of Residual Stress, IMT |
| IMT-1-2015 | Bøckmann, Eirik | Wave Propulsion of ships, IMT |
| IMT-2-2015 | Wang, Kai | Modelling and dynamic analysis of a semi-submersible floating vertical axis wind turbine, CeSOS |
| IMT-3-2015 | Fredriksen, Arnt Gunvald | A numerical and experimental study of a two-dimensional body with moonpool in waves and current, CeSOS |
| IMT-4-2015 | Jose Patricio Gallardo Canabes | Numerical studies of viscous flow around bluff bodies, IMT |

| | | |
|---|---|---|
| IMT-5-2015 | Vegard Longva | Formulation and application of finite element techniques for slender marine structures subjected to contact interactions, IMT |
| IMT-6-2015 | Jacobus De Vaal | Aerodynamic modelling of floating wind turbines, CeSOS |
| IMT-7-2015 | Fachri Nasution | Fatigue Performance of Copper Power Conductors, IMT |
| IMT-8-2015 | Oleh I Karpa | Development of bivariate extreme value distributions for applications in marine technology,CeSOS |
| IMT-9-2015 | Daniel de Almeida Fernandes | An output feedback motion control system for ROVs, AMOS |
| IMT-10-2015 | Bo Zhao | Particle Filter for Fault Diagnosis: Application to Dynamic Positioning Vessel and Underwater Robotics, CeSOS |
| IMT-11-2015 | Wenting Zhu | Impact of emission allocation in maritime transportation, IMT |
| IMT-12-2015 | Amir Rasekhi Nejad | Dynamic Analysis and Design of Gearboxes in Offshore Wind Turbines in a Structural Reliability Perspective, CeSOS |
| IMT-13-2015 | Arturo Jesùs Ortega Malca | Dynamic Response of Flexibles Risers due to Unsteady Slug Flow, CeSOS |
| IMT-14-2015 | Dagfinn Husjord | Guidance and decision-support system for safe navigation of ships operating in close proximity, IMT |
| IMT-15-2015 | Anirban Bhattacharyya | Ducted Propellers: Behaviour in Waves and Scale Effects, IMT |
| IMT-16-2015 | Qin Zhang | Image Processing for Ice Parameter Identification in Ice Management, IMT |
| IMT-1-2016 | Vincentius Rumawas | Human Factors in Ship Design and Operation: An Experiential Learning, IMT |
| IMT-2-2016 | Martin Storheim | Structural response in ship-platform and ship-ice collisions, IMT |
| IMT-3-2016 | Mia Abrahamsen Prsic | Numerical Simulations of the Flow around single and Tandem Circular Cylinders Close to a Plane Wall, IMT |
| IMT-4-2016 | Tufan Arslan | Large-eddy simulations of cross-flow around ship sections, IMT |

| | | |
|---|---|---|
| IMT-5-2016 | Pierre Yves-Henry | Parametrisation of aquatic vegetation in hydraulic and coastal research,IMT |
| IMT-6-2016 | Lin Li | Dynamic Analysis of the Instalation of Monopiles for Offshore Wind Turbines, CeSOS |
| IMT-7-2016 | Øivind Kåre Kjerstad | Dynamic Positioning of Marine Vessels in Ice, IMT |
| IMT-8-2016 | Xiaopeng Wu | Numerical Analysis of Anchor Handling and Fish Trawling Operations in a Safety Perspective, CeSOS |
| IMT-9-2016 | Zhengshun Cheng | Integrated Dynamic Analysis of Floating Vertical Axis Wind Turbines, CeSOS |
| IMT-10-2016 | Ling Wan | Experimental and Numerical Study of a Combined Offshore Wind and Wave Energy Converter Concept |
| IMT-11-2016 | Wei Chai | Stochastic dynamic analysis and reliability evaluation of the roll motion for ships in random seas, CeSOS |
| IMT-12-2016 | Øyvind Selnes Patricksson | Decision support for conceptual ship design with focus on a changing life cycle and future uncertainty, IMT |
| IMT-13-2016 | Mats Jørgen Thorsen | Time domain analysis of vortex-induced vibrations, IMT |
| IMT-14-2016 | Edgar McGuinness | Safety in the Norwegian Fishing Fleet – Analysis and measures for improvement, IMT |
| IMT-15-2016 | Sepideh Jafarzadeh | Energy effiency and emission abatement in the fishing fleet, IMT |
| IMT-16-2016 | Wilson Ivan Guachamin Acero | Assessment of marine operations for offshore wind turbine installation with emphasis on response-based operational limits, IMT |
| IMT-17-2016 | Mauro Candeloro | Tools and Methods for Autonomous Operations on Seabed and Water Coumn using Underwater Vehicles, IMT |
| IMT-18-2016 | Valentin Chabaud | Real-Time Hybrid Model Testing of Floating Wind Tubines, IMT |
| IMT-1-2017 | Mohammad Saud Afzal | Three-dimensional streaming in a sea bed boundary layer |
| IMT-2-2017 | Peng Li | A Theoretical and Experimental Study of Wave-induced Hydroelastic Response of a Circular Floating Collar |
| IMT-3-2017 | Martin Bergström | A simulation-based design method for arctic maritime transport systems |

| | | |
|---|---|---|
| IMT-4-2017 | Bhushan Taskar | The effect of waves on marine propellers and propulsion |
| IMT-5-2017 | Mohsen Bardestani | A two-dimensional numerical and experimental study of a floater with net and sinker tube in waves and current |
| IMT-6-2017 | Fatemeh Hoseini Dadmarzi | Direct Numerical Simualtion of turbulent wakes behind different plate configurations |
| IMT-7-2017 | Michel R. Miyazaki | Modeling and control of hybrid marine power plants |
| IMT-8-2017 | Giri Rajasekhar Gunnu | Safety and effiency enhancement of anchor handling operations with particular emphasis on the stability of anchor handling vessels |
| IMT-9-2017 | Kevin Koosup Yum | Transient Performance and Emissions of a Turbocharged Diesel Engine for Marine Power Plants |
| IMT-10-2017 | Zhaolong Yu | Hydrodynamic and structural aspects of ship collisions |
| IMT-11-2017 | Martin Hassel | Risk Analysis and Modelling of Allisions between Passing Vessels and Offshore Installations |
| IMT-12-2017 | Astrid H. Brodtkorb | Hybrid Control of Marine Vessels – Dynamic Positioning in Varying Conditions |
| IMT-13-2017 | Kjersti Bruserud | Simultaneous stochastic model of waves and current for prediction of structural design loads |
| IMT-14-2017 | Finn-Idar Grøtta Giske | Long-Term Extreme Response Analysis of Marine Structures Using Inverse Reliability Methods |
| IMT-15-2017 | Stian Skjong | Modeling and Simulation of Maritime Systems and Operations for Virtual Prototyping using co-Simulations |
| IMT-1-2018 | Yingguang Chu | Virtual Prototyping for Marine Crane Design and Operations |
| IMT-2-2018 | Sergey Gavrilin | Validation of ship manoeuvring simulation models |
| IMT-3-2018 | Jeevith Hegde | Tools and methods to manage risk in autonomous subsea inspection,maintenance and repair operations |
| IMT-4-2018 | Ida M. Strand | Sea Loads on Closed Flexible Fish Cages |
| IMT-5-2018 | Erlend Kvinge Jørgensen | Navigation and Control of Underwater Robotic Vehicles |

| | | |
|---|---|---|
| IMT-6-2018 | Bård Stovner | Aided Intertial Navigation of Underwater Vehicles |
| IMT-7-2018 | Erlend Liavåg Grotle | Thermodynamic Response Enhanced by Sloshing in Marine LNG Fuel Tanks |
| IMT-8-2018 | Børge Rokseth | Safety and Verification of Advanced Maritime Vessels |
| IMT-9-2018 | Jan Vidar Ulveseter | Advances in Semi-Empirical Time Domain Modelling of Vortex-Induced Vibrations |
| IMT-10-2018 | Chenyu Luan | Design and analysis for a steel braceless semi-submersible hull for supporting a 5-MW horizontal axis wind turbine |
| IMT-11-2018 | Carl Fredrik Rehn | Ship Design under Uncertainty |
| IMT-12-2018 | Øyvind Ødegård | Towards Autonomous Operations and Systems in Marine Archaeology |
| IMT-13-2018 | Stein Melvær Nornes | Guidance and Control of Marine Robotics for Ocean Mapping and Monitoring |
| IMT-14-2018 | Petter Norgren | Autonomous Underwater Vehicles in Arctic Marine Operations: Arctic marine research and ice monitoring |
| IMT-15-2018 | Minjoo Choi | Modular Adaptable Ship Design for Handling Uncertainty in the Future Operating Context |
| MT-16-2018 | Ole Alexander Eidsvik | Dynamics of Remotely Operated Underwater Vehicle Systems |
| IMT-17-2018 | Mahdi Ghane | Fault Diagnosis of Floating Wind Turbine Drivetrain- Methodologies and Applications |
| IMT-18-2018 | Christoph Alexander Thieme | Risk Analysis and Modelling of Autonomous Marine Systems |
| IMT-19-2018 | Yugao Shen | Operational limits for floating-collar fish farms in waves and current, without and with well-boat presence |
| IMT-20-2018 | Tianjiao Dai | Investigations of Shear Interaction and Stresses in Flexible Pipes and Umbilicals |
| IMT-21-2018 | Sigurd Solheim Pettersen | Resilience by Latent Capabilities in Marine Systems |
| IMT-22-2018 | Thomas Sauder | Fidelity of Cyber-physical Empirical Methods. Application to the Active Truncation of Slender Marine Structures |
| IMT-23-2018 | Jan-Tore Horn | Statistical and Modelling Uncertainties in the Design of Offshore Wind Turbines |

| | | |
|---|---|---|
| IMT-24-2018 | Anna Swider | Data Mining Methods for the Analysis of Power Systems of Vessels |
| IMT-1-2019 | Zhao He | Hydrodynamic study of a moored fish farming cage with fish influence |
| IMT-2-2019 | Isar Ghamari | Numerical and Experimental Study on the Ship Parametric Roll Resonance and the Effect of Anti-Roll Tank |
| IMT-3-2019 | Håkon Strandenes | Turbulent Flow Simulations at Higher Reynolds Numbers |
| IMT-4-2019 | Siri Mariane Holen | Safety in Norwegian Fish Farming – Concepts and Methods for Improvement |
| IMT-5-2019 | Ping Fu | Reliability Analysis of Wake-Induced Riser Collision |
| IMT-6-2019 | Vladimir Krivopolianskii | Experimental Investigation of Injection and Combustion Processes in Marine Gas Engines using Constant Volume Rig |
| IMT-7-2019 | Anna Maria Kozlowska | Hydrodynamic Loads on Marine Propellers Subject to Ventilation and out of Water Condition. |
| IMT-8-2019 | Hans-Martin Heyn | Motion Sensing on Vessels Operating in Sea Ice: A Local Ice Monitoring System for Transit and Stationkeeping Operations under the Influence of Sea Ice |
| IMT-9-2019 | Stefan Vilsen | Method for Real-Time Hybrid Model Testing of Ocean Structures – Case on Slender Marine Systems |
| IMT-10-2019 | Finn-Christian W. Hanssen | Non-Linear Wave-Body Interaction in Severe Waves |
| IMT-11-2019 | Trygve Olav Fossum | Adaptive Sampling for Marine Robotics |
| IMT-12-2019 | Jørgen Bremnes Nielsen | Modeling and Simulation for Design Evaluation |
| IMT-13-2019 | Yuna Zhao | Numerical modelling and dyncamic analysis of offshore wind turbine blade installation |
| IMT-14-2019 | Daniela Myland | Experimental and Theoretical Investigations on the Ship Resistance in Level Ice |
| IMT-15-2019 | Zhengru Ren | Advanced control algorithms to support automated offshore wind turbine installation |
| IMT-16-2019 | Drazen Polic | Ice-propeller impact analysis using an inverse propulsion machinery simulation approach |
| IMT-17-2019 | Endre Sandvik | Sea passage scenario simulation for ship system performance evaluation |

| | | |
|---|---|---|
| IMT-18-2019 | Loup Suja-Thauvin | Response of Monopile Wind Turbines to Higher Order Wave Loads |
| IMT-19-2019 | Emil Smilden | Structural control of offshore wind turbines – Increasing the role of control design in offshore wind farm development |
| IMT-20-2019 | Aleksandar-Sasa Milakovic | On equivalent ice thickness and machine learning in ship ice transit simulations |
| IMT-1-2020 | Amrit Shankar Verma | Modelling, Analysis and Response-based Operability Assessment of Offshore Wind Turbine Blade Installation with Emphasis on Impact Damages |
| IMT-2-2020 | Bent Oddvar Arnesen Haugaløkken | Autonomous Technology for Inspection, Maintenance and Repair Operations in the Norwegian Aquaculture |
| IMT-3-2020 | Seongpil Cho | Model-based fault detection and diagnosis of a blade pitch system in floating wind turbines |
| IMT-4-2020 | Jose Jorge Garcia Agis | Effectiveness in Decision-Making in Ship Design under Uncertainty |
| IMT-5-2020 | Thomas H. Viuff | Uncertainty Assessment of Wave-and Current-induced Global Response of Floating Bridges |
| IMT-6-2020 | Fredrik Mentzoni | Hydrodynamic Loads on Complex Structures in the Wave Zone |
| IMT-7-2020 | Senthuran Ravinthrakumar | Numerical and Experimental Studies of Resonant Flow in Moonpools in Operational Conditions |
| IMT-8-2020 | Stian Skaalvik Sandøy | Acoustic-based Probabilistic Localization and Mapping using Unmanned Underwater Vehicles for Aquaculture Operations |
| IMT-9-2020 | Kun Xu | Design and Analysis of Mooring System for Semi-submersible Floating Wind Turbine in Shallow Water |
| IMT-10-2020 | Jianxun Zhu | Cavity Flows and Wake Behind an Elliptic Cylinder Translating Above the Wall |
| IMT-11-2020 | Sandra Hogenboom | Decision-making within Dynamic Positioning Operations in the Offshore Industry – A Human Factors based Approach |
| IMT-12-2020 | Woongshik Nam | Structural Resistance of Ship and Offshore Structures Exposed to the Risk of Brittle Failure |
| IMT-13-2020 | Svenn Are Tutturen Værnø | Transient Performance in Dynamic Positioning of Ships: Investigation of Residual Load Models and Control Methods for Effective Compensation |
| IMT-14-2020 | Mohd Atif Siddiqui | Experimental and Numerical Hydrodynamic Analysis of a Damaged Ship in Waves |
| IMT-15-2020 | John Marius Hegseth | Efficient Modelling and Design Optimization of Large Floating Wind Turbines |

| | | |
|---|---|---|
| IMT-16-2020 | Asle Natskår | Reliability-based Assessment of Marine Operations with Emphasis on Sea Transport on Barges |
| IMT-17-2020 | Shi Deng | Experimental and Numerical Study of Hydrodynamic Responses of a Twin-Tube Submerged Floating Tunnel Considering Vortex-Induced Vibration |
| IMT-18-2020 | Jone Torsvik | Dynamic Analysis in Design and Operation of Large Floating Offshore Wind Turbine Drivetrains |
| IMT-1-2021 | Ali Ebrahimi | Handling Complexity to Improve Ship Design Competitiveness |
| IMT-2-2021 | Davide Proserpio | Isogeometric Phase-Field Methods for Modeling Fracture in Shell Structures |
| IMT-3-2021 | Cai Tian | Numerical Studies of Viscous Flow Around Step Cylinders |
| IMT-4-2021 | Farid Khazaeli Moghadam | Vibration-based Condition Monitoring of Large Offshore Wind Turbines in a Digital Twin Perspective |
| IMT-5-2021 | Shuaishuai Wang | Design and Dynamic Analysis of a 10-MW Medium-Speed Drivetrain in Offshore Wind Turbines |
| IMT-6-2021 | Sadi Tavakoli | Ship Propulsion Dynamics and Emissions |
| IMT-7-2021 | Haoran Li | Nonlinear wave loads, and resulting global response statistics of a semi-submersible wind turbine platform with heave plates |
| IMT-8-2021 | Einar Skiftestad Ueland | Load Control for Real-Time Hybrid Model Testing using Cable-Driven Parallel Robots |
| IMT-9-2021 | Mengning Wu | Uncertainty of machine learning-based methods for wave forecast and its effect on installation of offshore wind turbines |
| IMT-10-2021 | Xu Han | Onboard Tuning and Uncertainty Estimation of Vessel Seakeeping Model Parameters |
| IMT-01-2022 | Ingunn Marie Holmen | Safety in Exposed Aquacultrue Operations |
| IMT-02-2022 | Prateek Gupta | Ship Performance Monitoring using In-service Measurements and Big Data Analysis Methods |
| IMT-03-2022 | Sangwoo Kim | Non-linear time domain analysis of deepwater riser vortex-induced vibrations |
| IMT-04-2022 | Jarle Vinje Kramer | Hydrodynamic Aspects of Sail-Assisted Merchant Vessels |
| IMT-05-2022 | | |